
Supermassive black hole spin evolution in cosmological simulations

Luca Sala



München 2024

Supermassive black hole spin evolution in cosmological simulations

Luca Sala

Dissertation
an der Fakultät für Physik
der Ludwig–Maximilians–Universität
München

vorgelegt von
Luca Sala
aus Monza, Italy

München, den 08.04.2024

Erstgutachter: Prof. Dr. Klaus Dolag
Zweitgutachter: Prof. Dr. Eric Emsellem
Tag der mündlichen Prüfung: 07.06.2024

To mom and dad, in loving memory.

Zusammenfassung

Es gibt überzeugende Indizien dafür, dass die meisten Galaxien in unserem Universum ein supermassereiches Schwarzes Loch (SMBH) in ihrem Zentrum beherbergen. Wenn das zentrale SMBH Gas aus seiner Umgebung akkretiert, gibt es große Mengen an Energie an die Umgebung ab. Solche akkretierenden SMBHs werden allgemein als Aktive Galaktische Kerne (AGN) bezeichnet. Es wurde mittlerweile festgestellt, dass sie eine wichtige Rolle bei der Entwicklung von Galaxien spielen, durch das sogenannte AGN-Feedback. Die gemeinsame Entwicklung von SMBHs und ihren Galaxien ist ein komplexes, multi-Skalen Problem und beinhaltet das hochgradig-nichtlineare Zusammenspiel zwischen Akkretion und Feedback, das die kosmische Entwicklung von Strukturen reguliert. Großskalige kosmologische hydrodynamische Simulationen haben sich als grundlegendes Werkzeug erwiesen, um ein solches Zusammenspiel zu untersuchen.

Eine Reihe von Arbeiten in der Literatur hat sich darauf konzentriert, die Details des zentralen Mechanismus, der für die Energieabgabe verantwortlich ist, aus beobachtender und numerischer Sicht zu untersuchen. Seine Eigenschaften sind entscheidend mit der Physik des Akkretionsflusses innerhalb weniger Parsec des schwarzen Lochs verbunden. Diese bestimmt den Kanal der Energieabgabe, der für das Feedback verantwortlich ist, welches in Form von Strahlung oder durch leistungsstarke relativistische Jets auftreten kann. Die Jets spielen eine wichtige Rolle, insbesondere in Galaxienhaufen, wo sie Feedback durch die Einspeisung von Energie in das Intra-Cluster-Medium ausüben und Kühlungsverluste ausgleichen.

Der Spin des schwarzen Lochs wird als Schlüsselkomponente bei der Bildung von Jets betrachtet, da er deren Leistung und Richtung bestimmt. Darüber hinaus bestimmt er die Strahlungseffizienz des Akkretionsprozesses auf SMBHs. Trotz seiner Bedeutung wird der Spin als Eigenschaft von schwarzen Löchern selten in kosmologische Simulationen einbezogen. Diese Arbeit zielt darauf ab, die Entwicklung des Spins des schwarzen Lochs im Laufe der kosmischen Zeit umfassend zu untersuchen und wie dieser die gemeinsame Entwicklung von SMBHs und ihren Galaxien beeinflusst, unter Verwendung kosmologischer hydrodynamischer Simulationen. Um dieses Ziel zu erreichen, habe ich ein Modell implementiert, das Prozesse unter der Auflösungsgrenze beschreibt, insbesondere den Spin des schwarzen Lochs entwickelt und Gasakkretion und Verschmelzungen supermassiver schwarzer Löcher berücksichtigt. Das Modell geht von der Existenz einer ungleichmäßigen, geometrisch dünnen und optisch dicken Akkretionsscheibe aus, die durch die Metrik eines rotierenden schwarzen Lochs gestört wird und den Massentransfer von den aufgelösten Skalen der Simulationen vermittelt. Die Kopplung zwischen dem Akkretionsfluss und der Metrik des schwarzen Lochs übt ein Drehmoment aus, das den Spin des schwarzen Lochs modifiziert. Ich habe untersucht, wie sich der Spin des schwarzen Lochs entwickelt, in-

dem ich eine Reihe von Simulationen verwende, die idealisierte Setups, zoom-in Simulationen und eine kosmologische Box umfasst, die eine große Population von SMBHs produziert. Dies ermöglichte es mir, die gekoppelte Entwicklung von Spinrichtung und -größe, die Auswirkungen des dynamischen Zustands des Gases, das die schwarzen Löcher speist, und die Auswirkungen von Verschmelzungen auf die Verteilung der Spins der schwarzen Löcher als Funktion der Eigenschaften der schwarzen Löcher detailliert zu analysieren.

Die Simulationsergebnisse werden durch die Informationen zum Spin des schwarzen Lochs bereichert. Dies ebnet den Weg für weitere Untersuchungen und Entwicklungen, wie die Analyse der Beziehung zwischen dem Spin des Schwarzen Lochs und Galaxienmorphologie. Am wichtigsten ist, dass die Größe und Richtung des Spin des schwarzen Lochs jetzt mit einer Beschreibung unter der Auflösungsgrenze für Jet-Feedback gekoppelt werden können, die darauf abzielt, ihre Wechselwirkung mit dem umgebenden Medium zu reproduzieren, wie wir es in Radiogalaxien beobachten.

Die Arbeit ist wie folgt strukturiert. In Kap. 1 werde ich den kosmologischen Kontext und das Simulationsrahmenwerk einführen, auf dem das Spin-Entwicklungsmodell basiert. In Kap. 2 werde ich einige beobachtbare Eigenschaften von AGN sowie empirische Beweise für AGN-Feedbackprozesse und wie sie in kosmologischen Simulationen einbezogen werden darstellen. Ich werde auch die Rolle des Spins schwarzer Löcher bei der Erzeugung von Jets und die Techniken diskutieren, die es uns ermöglichen, empirische Einschränkungen darauf zu erhalten. In Kap. 3 werde ich zunächst einige Aspekte der Theorie von Akkretionsscheiben überprüfen und dann die Implementierung des Modells für Spin-Entwicklung in den Code OpenGadget3 vorstellen. In Kap. 4 werde ich die Simulationsreihe beschreiben, die verwendet wurde, um das Modell zu validieren und eine umfassende statistische Studie der Spins von schwarzen Löchern durchzuführen, und ich werde die Ergebnisse dieser Simulationen vorstellen. In Kap. 5 werde ich die Auswirkungen der Ergebnisse diskutieren und mit früheren Arbeiten vergleichen. Schließlich werde ich in Kap. 6 zukünftige Perspektiven aufzeigen und in Kap. 7 die Arbeit zusammenfassen und abschließen.

Abstract

There is compelling evidence that most of the galaxies in our Universe host a supermassive black hole (SMBH) at their centre. When the central SMBH accretes gas from the surroundings it releases large amounts of energy back to the environment. Such massive accreting BHs are commonly referred to as Active Galactic Nuclei (AGN). It has been now established that they have an important role in the evolution of galaxies, through the so-called AGN feedback. This joint evolution is a complex, multi-scale problem and involves the highly non-linear interplay between accretion and feedback, regulating the cosmic evolution of structures. Large-scale cosmological hydrodynamical simulations have proved to be a cornerstone tool to study such interplay.

A number of works in literature have focussed on studying the details of the central engine responsible for the energy release, from the observational and numerical point of view. Its properties are crucially related to the physics of the accretion flow within a few parsecs from the BH. This determines the channel of energy release responsible for feedback, which can occur in the form of radiation or through powerful relativistic jets. The jets are important actors, especially in galaxy clusters where they exert feedback by injecting energy into the intra-cluster medium and offset cooling losses.

The BH spin is thought to be a key ingredient in the formation of jets because it determines their power and direction. Moreover, it determines the radiative efficiency of the accretion process onto BHs. Despite its importance, this property of BHs is seldom included in cosmological simulations. This Thesis aims to comprehensively study the evolution of the BH spin across cosmic time and how it affects the co-evolution of SMBHs and their host galaxies, using cosmological hydrodynamical simulations. To achieve this goal, I implemented a sub-resolution model that evolves the BH spin, accounting for gas accretion and mergers. The model assumes the presence of a misaligned geometrically thin, optically thick accretion disc perturbed by the metric of a spinning BH, mediating the mass transfer from the resolved scales of the simulations. The coupling between the accretion flow and the metric of the BH exerts a torque that modifies the BH spin. I explored how the BH spin evolves using a simulation suite comprising idealised setups, zoomed-in simulations and a cosmological volume, that produces a large simulated population of BHs. This allowed me to analyse in detail the coupled evolution of the spin direction and magnitude, the effect of the dynamical state of the gas fuelling the BHs and the impact of mergers on the distribution of BH spins, as a function of BH properties.

The simulation output is enriched by the information on the BH spin, and this paves the way for further investigation and development, such as the analysis of the relation between BH spin and galaxy morphology. Most importantly, the BH spin magnitude and direction can now be

coupled to a sub-resolution prescription for jet feedback that aims at reproducing their interaction with the surrounding medium, as we observe in features like the radio lobes.

The Thesis is organised as follows. In Ch. 1 I will introduce the cosmological context and the simulation framework upon which the spin evolution model is based. In Ch. 2 I will revise a few observational properties of AGN, as well as the empirical evidence for AGN feedback processes, and how they are included in cosmological simulations. I will also discuss the role of BH spin in the production of jets and the techniques that allow us to get empirical constraints on it. In Ch. 3 I will first review a few aspects of the theory of accretion discs and then present the implementation of the sub-resolution model for spin evolution into the code `OPENGADGET3`. In Ch. 4 I will describe the suite of simulations used to validate the model and conduct a comprehensive statistical study of BH spins and I will present the results of such simulations. In Ch. 5, I will discuss the implications of the results and how they compare to previous works. Finally, in Ch. 6 I will provide future prospects and in Ch. 7 I will summarise and conclude.

Contents

Zusammenfassung	vii
Abstract	ix
List of Acronyms	xii
1 Cosmological simulations	1
1.1 Structure formation in a cosmological context	1
1.2 The cosmological hydrodynamical code <code>OPENGADGET3</code>	9
1.2.1 Collisionless dynamics: the N-body technique	9
1.2.2 The gaseous component: smoothed particle hydrodynamics	12
1.2.3 Additional baryonic processes and sub-resolution models	18
2 Active Galactic Nuclei	23
2.1 Phenomenology	23
2.1.1 Components of an AGN and spectral energy distribution	23
2.1.2 Radiative feedback from AGN and BH-host galaxy correlations	27
2.1.3 Maintenance feedback and AGN in galaxy clusters	29
2.2 The role of BH spin	31
2.2.1 Jet power and rotational energy extraction	31
2.2.2 Jet direction	32
2.2.3 Observational estimates of the BH spin	33
2.3 AGN in cosmological simulations	34
2.3.1 BHs treatment	34
2.3.2 AGN feedback	36
2.3.3 An empirically-motivated model for AGN feedback efficiency	37
3 Black hole spin evolution	43
3.1 Theoretical background	44
3.1.1 The BH metric	44
3.1.2 Circular orbits and ISCO	46
3.1.3 Accretion flows	49
3.1.4 The standard thin disc solution	56

3.1.5	Thin disc around spinning BHs: warps and spin evolution	58
3.2	Implementation in OPENGADGET3	60
3.2.1	Spin evolution algorithm	61
3.2.2	BH mergers	68
3.2.3	AGN feedback	69
4	Applications	71
4.1	The suite of simulations	71
4.1.1	Idealised Milky Way galaxy	71
4.1.2	Idealised galaxy merger	72
4.1.3	Zoom-in simulations	75
4.1.4	Cosmological box	75
4.2	Results	75
4.2.1	Idealised Milky Way galaxy	75
4.2.2	Idealised galaxy merger	77
4.2.3	Zoom-in simulations	79
4.2.4	Cosmological box	86
5	Discussion	95
5.1	Evolution of the BH spin direction	95
5.2	Evolution of the BH spin magnitude	95
5.3	Radiative efficiency	96
5.4	Comparison with previous works	97
6	Outlook	101
6.1	BH spin and galaxy morphology	101
6.2	BH spin and galaxy alignment	101
6.3	BH spin and jet feedback	102
6.4	Accretion flow model	104
7	Summary and conclusions	107
	Bibliography	111
	List of Figures	130
	List of Tables	134
	Acknowledgements	137

List of Acronyms

AGN Active Galactic Nucleus

BH Black hole

CMB Cosmic Microwave Background

DM Dark Matter

GRMHD General-relativistic magneto-hydrodynamics

ICM Intra-Cluster Medium

IMF Initial Mass Function

ISCO Innermost stable circular orbit

ISM Interstellar Medium

SN Supernova

SPH Smoothed-Particle Hydrodynamics

SMBH Supermassive black hole

LOS line-of-sight

LSS Large-Scale Structure

NFW Navarro, Frenk and White

pc Parsec

kpc Kilo-parsec

Mpc Mega-parsec

1 | Cosmological simulations

In this Chapter, I will present the cosmological framework and main concepts and techniques underpinning cosmological hydrodynamical simulations, in which the spin evolution model that I developed is embedded.

1.1 Structure formation in a cosmological context

In this Thesis, I address black hole (BH) spin evolution in a cosmological context, where BHs and galaxies co-evolve during the process of cosmic structure formation and evolution. This process is highly non-linear and it involves the solution of the coupled equations of gravity and hydrodynamics in an expanding Universe, and it cannot be treated analytically. For this reason, in this work, I investigate BH spin evolution using cosmological hydrodynamical simulations. In this Section, based on Ryden (2003), I will review a few essential aspects of the cosmological model and the structure formation theory, that are the underlying framework of such simulations.

Cosmological model

According to our current understanding, the large-scale evolution of the Universe is governed by gravity and is well described by the theory of General Relativity by Albert Einstein. Our Universe is assumed to be *homogeneous* and *isotropic* on scales larger than ~ 100 Mpc, i.e. that intensive properties (such as e.g. the density of matter) are independent of the observer's location or the direction in which they observe. This is the so-called *cosmological principle*. The line element ds^2 of the metric compatible with the assumptions of homogeneity and isotropy, with the spatial part expressed in polar coordinates (r, θ, ϕ) , is

$$ds^2 = -c^2 dt^2 + a^2(t) [dr^2 + S_k^2(r)(d\theta^2 + \sin^2 \theta d\phi^2)], \quad (1.1)$$

where c is the speed of light,

$$S_k(r) = \begin{cases} R_0 \sin(r/R_0) & (k = +1) \\ r & (k = 0) \\ R_0 \sinh(r/R_0) & (k = -1) \end{cases}, \quad (1.2)$$

R_0 is the curvature radius of the metric and $a(t)$ is the *scale factor*. The time evolution of the metric is parameterised by $a(t)$ and is related to the energy content of the Universe. This is also

referred to as the Friedmann-Lemaître-Robertson-Walker (FLRW) metric. The spatial variables take the name of *comoving* coordinates. The metric can have positive, zero or negative curvature, depending on the sign parameter $k = 1, 0, -1$.

The first equation describing its evolution was formalised by Alexander Friedmann and reads

$$\left(\frac{\dot{a}}{a}\right)^2 = \frac{8\pi G}{3c^2}\epsilon - \frac{k}{a^2} \frac{c^2}{R_0^2} \quad (1.3)$$

where ϵ is the energy density, also evolving with time, G is the gravitational constant. The scale factor is normalised such that $a = 1$ at the present day. The quantity $\frac{\dot{a}}{a}$ is commonly referred to as *Hubble parameter*, $H(t)$. Its value at the present day, H_0 , is named for historical reasons the *Hubble constant*. It is customary to define the *density parameter* $\Omega = \epsilon/\epsilon_c$, where the *critical density* ϵ_c (i.e. the density of a spatially flat Universe) is

$$\epsilon_c(t) = \frac{3c^2}{8\pi G}H(t), \quad (1.4)$$

and its present-day value reads

$$\epsilon_c(t=0) = \frac{3c^2 H_0}{8\pi G} \quad (1.5)$$

With these definitions, Eq. 1.3 becomes

$$1 - \Omega(t) = -\frac{kc^2}{R_0^2 a^2(t) H^2(t)}, \quad (1.6)$$

and evaluating it at the present day gives a value for the curvature

$$k = (1 - \Omega_0) \frac{H_0^2 R_0^2}{c^2}. \quad (1.7)$$

Friedmann's equation has two unknowns, $\epsilon(t)$ and $a(t)$. A second equation is needed to be able to solve for both of them. The first law of thermodynamics holds in the form

$$\dot{\epsilon} + 3\frac{\dot{a}}{a}(\epsilon + P) = 0, \quad (1.8)$$

where P is the pressure related to the energy density by the linear equation of state, with proportionality constant w

$$P = w\epsilon. \quad (1.9)$$

Combining Eq. 1.3 with Eq. 1.8 yields an equation for the second derivative of the scale factor, the *acceleration equation*, that reads

$$\frac{\ddot{a}}{a} = -\frac{4\pi G}{3c^2}(\epsilon + 3P). \quad (1.10)$$

Eq. 1.3, 1.8 and 1.10 completely describe the dynamics of the Universe, once the energy content is specified.

The set of observational data available to us (see e.g. Ryden, 2003) strongly supports the cosmological model of *Hot Big Bang*. Our Universe is undergoing an accelerated expansion (i.e. $\ddot{a} > 0$), starting from an initial state of high density and temperature. It is consistent with being geometrically flat ($k = 0$) and has three main constituents contributing to the energy density at the present day: dark energy, dark matter (DM) and ordinary matter. Dark energy is also called "cosmological constant", and was initially introduced by Einstein as a constant energy density term in the equation of the dynamical evolution (see below), to obtain a solution leading to a static Universe. Later, it was reinterpreted as the driver of the acceleration expansion. It is usually associated with the letter Λ . DM is assumed to be a collisionless fluid, with negligible velocity dispersion (hence it is dynamically *cold*). Ordinary matter is constituted by protons, neutrons and electrons, but in a cosmological context the main contributions to the mass density come from protons and neutrons (i.e. baryons), so it is usually referred to as *baryonic matter*. Radiation has a negligible contribution to the present-day energy density, but it was the dominant component in the initial phases of the Universe evolution. On the other hand, DM and dark energy account for around 95% of the current energy density, whereas baryonic matter constitutes around 5%. This cosmological model is referred to as Λ CDM (where CDM stands for cold DM).

Each component of the Universe is characterised by a different value of the proportionality constant for the equation of state w in Eq. 1.8. The pressure of a collisionless fluid (like DM) is zero, while for a collisional fluid of non-relativistic particles (such as gas) is a negligible fraction of its energy density. For these components, $w = 0$. For radiation, $w = 1/3$. Lastly, the cosmological constant is characterised by $w = -1$. By combining Eq. 1.8 and 1.9, it is possible to write for each component

$$\epsilon_w(a) = \epsilon_{w,0} a^{-3(1+w)} \quad (1.11)$$

where $\epsilon_{w,0}$ is the value of its present-day energy density (i.e. when $a = 1$). The total energy density is therefore

$$\epsilon = \sum_w \epsilon_w. \quad (1.12)$$

The set of equations just presented allows us to derive an evolution equation for a Universe with multiple components. Substituting Eq. 1.7 into Eq. 1.3 yields

$$\frac{H(t)^2}{H_0^2} = \frac{\epsilon(t)}{\epsilon_{c,0}} + \frac{1 - \Omega_0}{a(t)^2}, \quad (1.13)$$

and therefore

$$\frac{H^2}{H_0^2} = \frac{\Omega_{r,0}}{a^4} + \frac{\Omega_{m,0}}{a^3} + \Omega_{\Lambda,0} + \frac{1 - \Omega_0}{a^2}, \quad (1.14)$$

where $\Omega_{r,0}$, $\Omega_{m,0}$ and $\Omega_{\Lambda,0}$ are the density parameters of radiation, matter and cosmological constant, respectively, evaluated at the present day. The function $a(t)$ is computed by performing the integral

$$\int_0^a \frac{da}{[\Omega_{r,0}/a^2 + \Omega_{m,0}/a + \Omega_{\Lambda,0}a^2 + (1 - \Omega_0)]^{1/2}} = H_0 t. \quad (1.15)$$

Note that by integrating Eq. 1.1 at a fixed time and on the line-of-sight (i.e. at fixed θ and ϕ), it is possible to recover the result discovered by Edwin Hubble in 1929 (Hubble, 1929) and, independently, by Georges Lemaître in 1927 (Lemaître, 1927), that recessional velocities v of nearby galaxies are proportional to their distances d from us

$$v = H_0 r, \quad (1.16)$$

where H_0 takes the role of proportionality constant. Indeed, consider the light emitted by a distant galaxy, with wavelength λ_{em} . Due to the Universe expansion, the wavelength of the light we receive, λ_{obs} , will be in general different. The *redshift* is defined as

$$z = \frac{\lambda_{\text{obs}} - \lambda_{\text{em}}}{\lambda_{\text{em}}}, \quad (1.17)$$

Hubble and Lemaître measured separately the distances and the redshifts in a sample of galaxies, they interpreted the redshifts as Doppler shifts (i.e. $z = v/c$) and found that they followed a linear relation of the form given by Eq. 1.16. Note that this relation is only valid for $z \ll 1$, or equivalently $v \ll c$ (i.e. local objects). Nonetheless, this represented the first indication that the Universe is not static but is indeed expanding. Their measure of H_0 was largely overestimated, one of the current estimates is $H_0 = 67.4 \pm 0.5$ km/s/Mpc (Planck Collaboration et al., 2020). Finally, it can be shown that the redshift is related to $a(t)$ by the relation

$$1 + z = \frac{1}{a}. \quad (1.18)$$

The redshift does not depend on the detailed evolution of a , but only on its value when the light was emitted at the source.

The most compelling evidence supporting the Hot Big Bang cosmological model is that our Universe is permeated by the Cosmic Microwave Background (CMB), discovered by Arno Penzias and Robert Wilson in 1965. They observed it as an isotropic, unpolarised excess signal in the antenna temperature of the radio telescope, that they could not remove even after carefully calibrating their instrument. By now, several observational campaigns have been conducted to study this ubiquitous radiation background such as the space-based missions COBE, WMAP, and Planck (Boggess et al. 1992, Komatsu et al. 2009, Planck Collaboration et al. 2020). It is found to be characterised by a blackbody spectrum with a temperature $T = 2.725 \pm 0.001$ K. This empirical evidence fits naturally in the Hot Big Bang model. Indeed, in the initial hot and dense state the baryonic matter was completely ionised, opaque and in thermal equilibrium with radiation, and was therefore characterised by a blackbody spectrum. Then, following the expansion of the Universe, density and temperature dropped until electrons and ions were able to recombine. Shortly after, around 0.35 Myr after the Big Bang ($z_{\text{dec}} \sim 1100$), radiation and matter *decoupled*, the medium became transparent and the photons were able to escape and propagate freely (defining a surface of *last scattering*). This produced the signal that we observe now. This is an important tool to gather direct insights into the very early phases of our Universe evolution. The CMB is the most accurate blackbody spectrum observed in nature; in particular, the temperature fluctuations over the average value across the sky is $\delta T/T \sim 10^{-5}$. The temperature fluctuations

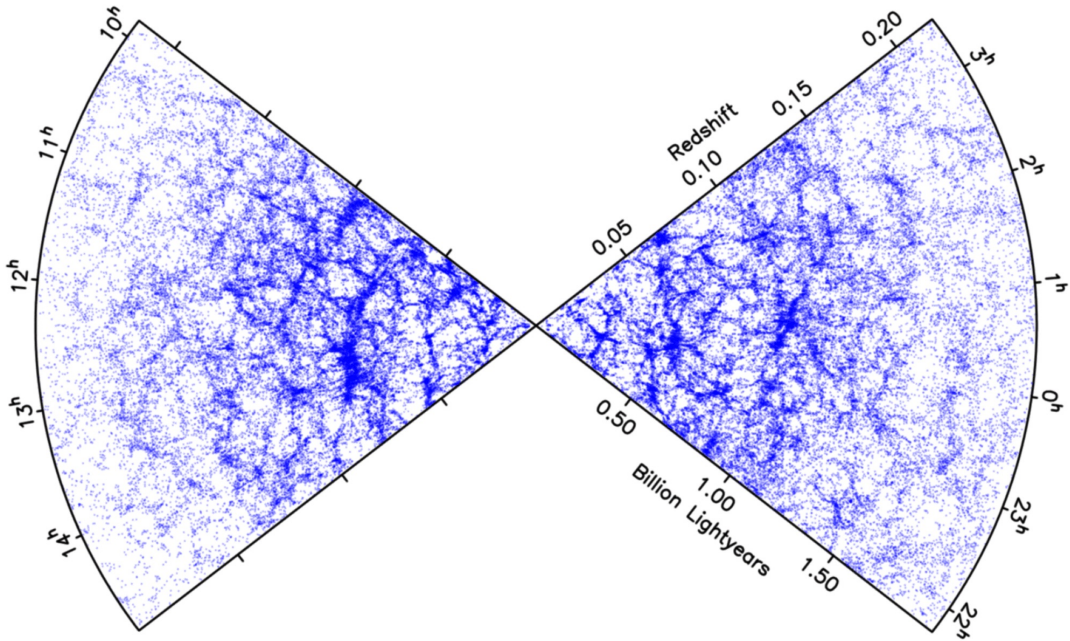


Figure 1.1: The distribution of galaxies in the Two Degree Field Galaxy Redshift Survey (2dFGRS) (Colless et al., 2001).

in the CMB are the imprint of the density fluctuations field (see below) on the radiation field at the time of decoupling. Therefore, they inherently carry important information about the statistical properties of the distribution of DM density and the behaviour of the coupled photon-baryon fluid. In particular, it is possible to put constraints on the parameters of our cosmological model. For example, the most recent results obtained with the Planck satellite (Planck Collaboration et al., 2020) infer $\Omega_{m,0} = 0.315 \pm 0.007$, $\Omega_{\Lambda,0} = 0.685 \pm 0.007$, and $H_0 = 67.4 \pm 0.5$ km/s/Mpc. The age of the Universe is 13.797 ± 0.023 Gyr.

The large-scale structure

Despite their remarkably small amplitude, the fluctuations (also referred to as *anisotropies*) in the CMB are an important indication that the Universe was not indeed perfectly homogeneous when matter and radiation decoupled. Besides, the Universe is remarkably inhomogeneous at the present day, on scales smaller than around 100 Mpc. For instance, planets, stars and galaxies are characterised by densities that are orders of magnitude larger than the average matter density on cosmological scales. With the advent of large spectroscopic surveys, that were able to measure the redshifts of hundreds of thousands of galaxies, it was possible to show that on scales larger than galaxy scales, the matter in the Universe exhibits regions of clustering that are over-dense compared to the background, and regions that are instead under-dense. In particular, the Universe displays an ensemble of filaments, sheets, clusters and voids, collectively referred to as the large-scale structure, illustrated in Fig. 1.1.

If the Universe was perfectly homogeneous and isotropic, we would not be able to observe any

structure. The structure formation process must have originated because of the action of gravity on matter density fluctuations present on top of the homogeneous, average density field that is described by the FLRW metric. In this sense, to describe quantitatively the density distribution of the matter component, it is useful to define the *density contrast* field as

$$\delta(\mathbf{r}, t) = \frac{\rho(\mathbf{r}, t) - \bar{\rho}(t)}{\bar{\rho}(t)} \quad (1.19)$$

where $\bar{\rho}(t)$ is the density averaged over sampling volumes that are larger than the size of the biggest structures in the Universe (i.e. larger than around 100 Mpc). Considering a comoving box with volume V , the statistical properties of the density contrast field are encapsulated in the matter power spectrum,

$$P(k) = \langle |\delta_{\mathbf{k}}|^2 \rangle \quad (1.20)$$

that is the mean square amplitude of the Fourier components is defined as

$$\delta_{\mathbf{k}} = \frac{1}{V} \int \delta(\mathbf{r}) e^{i\mathbf{k}\cdot\mathbf{r}} d^3\mathbf{r}, \quad (1.21)$$

where the average is over all the different orientations of the wavenumber vector \mathbf{k} .

The current cosmological paradigm (see e.g. Liddle & Lyth, 2000; Ryden, 2003) attributes the existence of the density fluctuations, thus the origin of large-scale structure, to the exponential growth in the size of primordial quantum fluctuations during a period named *inflation*, occurred during the first 10^{-32} s after the Big Bang. The inflationary scenario predicts that the resulting density field is a uniform, isotropic *Gaussian field*. This means that at any given point in space, the value of δ is extracted from a Gaussian distribution with a uniform standard deviation σ . Furthermore, the unique characteristic of a Gaussian field lies in the fact that its statistical features are entirely encapsulated in the power spectrum $P(k)$. The inflationary model predicts that immediately after inflation $P(k)$ takes the form of a power-law $P(k) \propto k^n$, with $n \sim 1$.

Once the density fluctuations field is in place, the destiny of each fluctuation depends on the balance between the Universe expansion, the self-gravity of the overdense regions, and the pressure support due to the presence of the gaseous components. For a Universe with multiple components where $H(t)$ is given by Eq. 1.14, a full relativistic, linear perturbations analysis predicts that the δ evolves according to (Ryden (2003))

$$\ddot{\delta} + 2H\dot{\delta} = \frac{3}{2}\Omega_m H^2 \delta. \quad (1.22)$$

as long as $\delta \ll 1$. Since $\Omega_r = \Omega_{r,0} a^{-4}$, while $\Omega_m = \Omega_{m,0} a^{-3}$ (Eq. 1.11), radiation was the dominant component in the very early Universe. In particular, it was dominant until about the radiation-matter equality $z_{r-m} \sim 3500$. During this epoch, the density perturbations could not grow rapidly with time. Eq. 1.22 with $\Omega_m \ll 1$ and $H = 1/(2t)$ (appropriate for a radiation-dominated period), leads to only logarithmically growing perturbations. However, after $z \sim z_{r-m}$, the Universe shifted from radiation-dominated to matter-dominated. Assuming $\Omega_m = 1$ and $H = 2/(3t)$ (appropriate for a matter-dominated era), Eq. 1.22 has a solution of the form

$$\delta(t) \sim D_1 t^{2/3} + D_2 t^{-1}, \quad (1.23)$$

where D_1 and D_2 are integrations constants. The decaying solution eventually becomes negligibly small, while the growing solution has the form

$$\delta(t) \propto t^{2/3} \propto a(t) \propto \frac{1}{1+z}. \quad (1.24)$$

Therefore, the density perturbations in the matter component started growing as soon as the Universe became matter-dominated. In addition, current estimates (e.g. Planck Collaboration et al., 2020) indicate a value for the baryonic density parameter equal to $\Omega_{b,0} \simeq 0.04$ and for the DM equal to $\Omega_{DM,0} \simeq 0.26$, making DM the dominant matter component at all times. For this reason, structure formation was effectively initiated already at $z \sim 3500$, driven by the formation of the potential wells in the DM density field, as a result of the growing overdensities.

After $z \sim z_{r-m}$, photons and baryons were still coupled in a single photon-baryon fluid until decoupling at $z \sim z_{\text{dec}}$. Since DM was the dominant component, the dynamic of the fluid was determined mainly by the potential associated with the dark matter density field. Consider for example a spherical region within the fluid, characterised by a uniform density excess δ . If not supported by pressure, this region would collapse on a timescale of the order of the dynamical timescale t_{dyn}

$$t_{\text{dyn}} \sim \sqrt{\frac{c^2}{G\bar{\epsilon}}} \quad (1.25)$$

where $\bar{\epsilon}$ is the background mean energy density. If gas pressure has time to build up, the region oscillates around a stable equilibrium configuration. An overdense region is stable if its length scale is smaller than the *Jeans length*

$$\lambda_J \sim c_s \sqrt{\left(\frac{c^2}{G\bar{\epsilon}}\right)} \sim c_s t_{\text{dyn}}. \quad (1.26)$$

where $c_s = c\sqrt{dP/d\epsilon} = c\sqrt{w}$ is the fluid sound speed. This is also referred to as the *Jeans criterion*. The photon-baryon fluid was compressed due to gravity in the DM potential wells, while the fluid pressure counter-acted the collapse. For the coupled photon-baryon fluid the Jeans length was larger than the Hubble distance at that time, thus overdense regions were not able to collapse. Instead, standing sound waves were generated inside the potential wells, usually referred to as *baryonic acoustic oscillations*. Eventually, once the baryonic fluid decoupled from radiation, its sound speed reduced by several orders of magnitude, and so did its Jeans length, leading to the collapse of the baryonic component that forms the structures we observe.

It is important to note that the matter power spectrum evolves compared to the primordial power-law spectrum predicted by inflation. Density fluctuations $\delta_{\mathbf{k}}$ characterised by a wavelength $\lambda_k = a(t)2\pi/k$ larger than the Hubble distance $c/H(t)$ (i.e. the Universe horizon at time t) do not follow Eq. 1.22, which is valid only as long as $\lambda_k < c/H(t)$. Therefore, they grow with $\delta \propto a(t)$ both in the radiation- and matter-dominated era. Quantitatively, this means during the radiation-dominated era, for $\lambda_k > a(t)2\pi/k$ perturbations grow and the normalization of the spectrum changes, but the power-law shape is preserved. Conversely, fluctuations at $\lambda_k < a(t)2\pi/k$ are suppressed because they are not able to grow. Therefore, in a radiation-dominated Universe, when

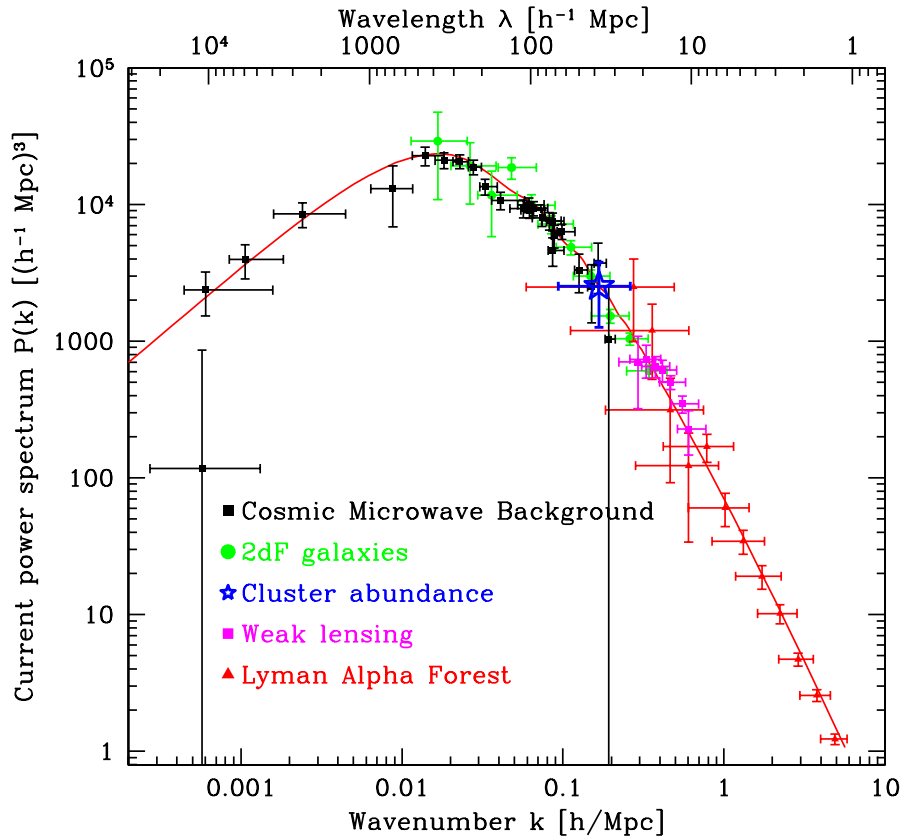


Figure 1.2: Different probes for the matter power spectrum (Tegmark & Zaldarriaga, 2002).

the wavelength of a perturbation becomes smaller than the horizon, it is unable to grow until it reaches z_{r-m} (as discussed earlier). The suppression increases with decreasing wavelengths. In addition, as soon as the perturbations reach the non-linear regime ($\delta > 1$) the shape of the power spectrum is further modified. Fig. 1.2 shows the matter power spectrum as probed at the present day using different tracers. The modes at the largest wavelength, corresponding to structures at large scales, still follow a power-law shape, whereas the amplitude decreases at small scales. This is the basis of the current *hierarchical* structure formation model. The short wavelength modes collapse first, while the largest modes collapse later. Furthermore, baryons may dissipate energy and cool, further sinking towards the centre of the potential wells set by the DM.

So far only the evolution in the linear regime was considered when $\delta \ll 1$. In this regime Eq. 1.24 is valid. However, when an overdense region reaches $\delta \sim 1$, a full treatment of the non-linear evolution requires numerical simulations. This will be the focus of Sec. 1.2.

1.2 The cosmological hydrodynamical code `OPENGADGET3`

Cosmological simulations play a fundamental role in investigating the non-linear evolution of cosmic structures. Moreover, within the cosmological picture of the expanding universe and large-scale structure formation, they enable us to study galaxy formation and evolution, a complex problem that involves multiple physics processes and scales. In this section, I will review the numerical technique and the formalism employed in the code `OPENGADGET3`, serving as the framework for the study undertaken in this Thesis.

The initial conditions (ICs) for cosmological simulations are generated assuming the cosmological model presented in the previous sections. The cosmology is then defined by the set of associated parameters. The ICs specify the density fluctuations field on top of a uniform, expanding background, whose statistical properties are determined by the power spectrum. The parameters for the cosmology and the power spectrum are inferred from the CMB and observations of clustering. First, a uniform or glass-like distribution of particles is generated, which represents the unperturbed, uniform-density field. Then, the required perturbation spectrum is imprinted onto the unperturbed distribution (e.g. Hahn & Abel, 2011; Garrison et al., 2016), by applying displacements and velocities computed using linear perturbation theory (e.g. Bernardeau et al., 2002, for a review). The ICs generated using this method represent a random realisation of the Universe, with statistical properties consistent with observations. The task at hand is to evolve the initial state, defined at a chosen initial redshift (usually around $z \sim 100$), by solving the coupled equations of gravity and hydrodynamics. Additional effective prescriptions are applied when the resolution is insufficient to model essential processes directly from first principles.

1.2.1 Collisionless dynamics: the N-body technique

Dark matter is modelled in the simulations as a collisionless component, whose motion is only affected by the gravitational interaction. For a review of the numerical techniques adopted in literature to simulate the collisionless component, see, for example, Angulo & Hahn (2022). Formally, a collisionless system is described by a distribution function $f(\mathbf{r}, \mathbf{v}, t)$, indicating the probability $f d^3\mathbf{r} d^3\mathbf{v}$ of finding a DM particle with position \mathbf{r} and velocity \mathbf{v} in the phase-space volume $d^3\mathbf{r} d^3\mathbf{v}$. The time evolution of f is described by the collisionless Boltzmann equation

$$\frac{df}{dt} = \frac{\partial f}{\partial t} + \mathbf{v} \cdot \frac{\partial f}{\partial \mathbf{r}} - \frac{\partial \Phi}{\partial \mathbf{r}} \cdot \frac{\partial f}{\partial \mathbf{v}} = 0, \quad (1.27)$$

coupled to Poisson's equation

$$\nabla^2 \Phi(\mathbf{r}, t) = 4\pi G \int f(\mathbf{r}, \mathbf{v}, t) d^3\mathbf{v}, \quad (1.28)$$

where Φ is the gravitational potential.

To solve this coupled system of partial differential equations, a successful approach is to discretise it through the so-called N-body methods. The distribution function is sampled by a set of N points \mathbf{r}_i , where $i = 1 \dots N$ with masses m_i . This sampling can be thought of as

a Monte Carlo estimate, which is therefore subject to Poisson noise. Consider a collisionless system of total mass M ; describing such a system with N particles requires the particle mass to be $m_i = M/N$. The higher the particle number, the better the accuracy of the sampling of the distribution function. Therefore, the mass of the particle used to represent the system is often referred to as *mass resolution*. The particles are tracers of the distribution function and do not represent individual particles. Once this phase-space sampling procedure is adopted, the system of equations to be solved is equivalent to

$$\ddot{\mathbf{r}}_i = -\nabla_i\Phi(\mathbf{r}_i) \quad (1.29)$$

$$\Phi(\mathbf{r}) = -G \sum_{j=1}^N \frac{m_j}{[|\mathbf{r} - \mathbf{r}_j|^2 + \varepsilon^2]^{1/2}}. \quad (1.30)$$

The expression for the Newtonian gravitational force in a pair of interacting particles is singular for null separation. Close particle encounters can produce unphysical accelerations and large-angle scatterings. To prevent such occurrence, as well as the formation of bound particle pairs, gravitational interactions are "softened" on small scales, that is, a correction to the gravitational force for separation $< \varepsilon$ is added. This parameter takes the name of *softening length*. The choice of this value is not trivial, but numerical studies have been conducted to identify a criterion to select an optimal value (e.g. Zhang et al., 2019).

Eq. 1.30 immediately highlights the main computational challenge for N-body methods: how to efficiently compute the gravitational force. Indeed, the potential needs to be computed at the positions of the N particles, and each computation requires summing over N particles. Therefore, this *direct summation* approach has a computational cost of $O(N^2)$. A significant improvement in terms of computational cost can be achieved by introducing some approximations in the force calculation. Since the N-body sampling is noisy in any case, it is possible to trade some of the accuracy to speed up the computation, as long as the force errors are random and small enough.

A useful strategy to improve the computation speed is to use the tree approach (e.g. Barnes & Hut, 1986). The particles are organised into a hierarchical tree structure. The three-dimensional computational domain is recursively partitioned into nodes, each containing a localised group of particles. The most common choice for the tree structure is the octree, in which every node has eight children. This process is illustrated in the left panel of Fig. 1.3 (in 2D for visualisation purposes). To compute the gravitational potential at a given point in space, distant particles are grouped together. An accuracy criterion, typically an opening angle, is used to decide which coarse level of the tree structure is used to group particles (θ in the right panel of Fig. 1.3). The contribution to the potential of each group of particles is then computed using only the lowest-order terms of the multipole expansion of the mass distribution of the group. Usually, the monopole is considered, but further multipole orders can be included if desired. This strategy reduces the computational cost to $O(N \log N)$. An additional speed-up is achieved if the field is expanded symmetrically for pairs of interacting nodes of the tree instead of coupling individual particles and nodes. This method takes the name of fast multipole method (e.g. Dehnen, 2002).

Another approach is to use the *particle-mesh* (PM) method. This method entails four fundamental steps: *i*) a density field is built upon the distribution of the particles using a suitable mesh; *ii*) the potential is computed using the Poisson equation; *iii*) the force is derived from the

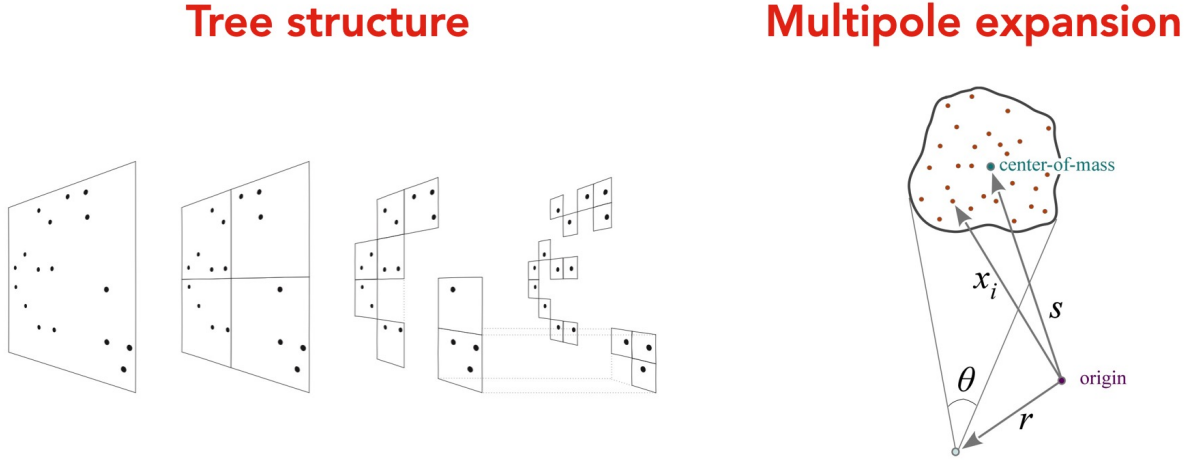


Figure 1.3: On the left, an illustration of the tree technique used to partition the computational domain into nodes, grouping particles recursively. On the right, the criterion to group particles and compute their combined gravitational effect at a given point, using a multipole expansion around their centre of mass. Adapted from Springel et al. (2001b).

potential at the mesh points; *iv*) the forces acting on the particles are interpolated from these points. To solve the Poisson equation over the mesh, a Fourier transform is applied, converting the originally integral problem to an algebraic one, easier to solve (e.g. Hockney & Eastwood, 1981). The force resolution is limited by the mesh size. To overcome this problem, a series of nested meshes can therefore be adopted to increase resolution in clustered regions. Then, an iterative solver that starts with a trial potential and relaxes the solution to convergence is used to solve Poisson equations (e.g. Kravtsov et al., 1997; Teyssier, 2002).

State-of-the-art codes adopt schemes that combine different techniques to achieve the best performance and speed up. The code used to conduct the simulations discussed in this work, `OPENGADGET3`, adopts a strategy commonly referred to as TreePM. The potential is split into two separate contributions in Fourier space, from long- and short-range interactions. Then the Fourier problem for the former contribution is computed using a particle-mesh algorithm, whereas the short-range part is transformed back to real space and the force is computed through a tree-based scheme. This strategy greatly enhances the resolved dynamical range, while efficiently and accurately computing the long-range contributions.

Once the problem of computing the gravitational force has been solved, the particle positions and velocities need to be evolved in time using a suitable integration scheme. While in general several choices are possible (e.g. explicit or implicit Euler, Runge-Kutta, Hermitian integration schemes) the most common choice is the leapfrog integrator, due to its energy conservation properties and good long-term behaviour. The leapfrog integrator is particularly suitable for second-order ordinary differential equations of the form $\ddot{\mathbf{x}} = f(\mathbf{x})$ (such as Eq. 1.29). `OPENGADGET3` in particular adopts the Kick-Drift-Kick scheme, in which the position and velocity of each

particle at timestep n are updated according to the scheme

$$\mathbf{v}_{n+\frac{1}{2}} = \mathbf{v}_n + f(\mathbf{x}_n) \frac{\Delta t}{2} \quad (1.31)$$

$$\mathbf{x}_{n+1} = \mathbf{x}_n + \mathbf{v}_{n+\frac{1}{2}} \Delta t \quad (1.32)$$

$$\mathbf{v}_{n+1} = \mathbf{v}_{n+\frac{1}{2}} + f(\mathbf{x}_{n+1}) \frac{\Delta t}{2} \quad (1.33)$$

where Δt is the timestep of the integration. In this regard, in cosmological simulations, a dynamic range spanning several orders of magnitudes in timescales is typically involved. The dynamical timescale t_{dyn} defined in Eq. 1.25 can also be used as characteristic timescale associated with the orbital motion in a gravitational potential (Binney & Tremaine, 2008); for a star in a typical galaxy $t_{\text{dyn}} \sim 100$ Myr, while in the central parsec of such a galaxy $t_{\text{dyn}} \sim 10^4$ yr, and for a galaxy in a cluster $t_{\text{dyn}} \sim 1$ Gyr. In general, denser regions require smaller timescales to be resolved, for an accurate integration of the trajectory of the particles. However, using the smallest timestep required by the simulation for all the particles would imply to waste computational effort in regions where the time evolution can be integrated faithfully with far larger timesteps. For this reason, adaptive and individual particle timesteps are usually implemented. In `OPENGADGET3`, for instance, each particle evolves on its own timestep, assigned according to criteria that take into account the current particle acceleration (e.g. $t \propto 1/\sqrt{|\mathbf{a}|}$ Springel, 2005) as well as the finite signal velocity of information for the hydrodynamical solver (see Sec. 1.2.2. At any given time only a subset of particles are actually updated, therefore drastically increasing performance.

1.2.2 The gaseous component: smoothed particle hydrodynamics

In the previous Section, I discussed the numerical technique to evolve the collisionless component of our Universe, the DM, which dominates the potential at large scales. However, our universe exhibits a wide diversity of objects, and the mechanism of their formation is contingent on the physics of the baryonic component, namely, gas. For example, as mentioned before the gaseous component can sink to the centre of the potential wells determined by the DM, due to the ability to radiate part of its internal energy (hence "cooling"). From gas, stars are formed. Stars are themselves arranged in systems whose dynamic is determined by the collective gravitational potential, such as galaxies. Gravitational interaction combined with baryonic physical processes drives the dynamical evolution of astrophysical systems and shapes the variety of systems we witness. Therefore, simulating this matter component and its associated processes as comprehensively as possible, given the computational limitations, is essential to achieving our ultimate goal of understanding the galaxy formation process. In this Section, I will revise the method used to include gas dynamics, with the main focus on the one used in `OPENGADGET3`, briefly discussing possible alternative approaches.

The hydrodynamical equations

In an astrophysical context, gas is assumed to be inviscid (i.e. with negligible viscosity), thus following the Euler equations. In a formal sense, it is treated as a collisional fluid, meaning that

particles constituting the fluid are characterized by a mean free path significantly smaller than the length scale of the system under consideration. The Euler equations are a system of hyperbolic PDEs in the *hydrodynamical variables* ρ , the mass density, \mathbf{v} , the velocity of the fluid, P , the pressure, e , the total energy per unit mass, u the internal energy per unit mass. The equations ultimately encode the conservation laws for mass, momentum and energy. The equations are expressed in the *Eulerian formulation* as

$$\frac{\partial \mathbf{U}}{\partial t} + \nabla \cdot (\mathbf{F}) = 0 \quad (1.34)$$

where \mathbf{U} the vector of conserved quantities,

$$\mathbf{U} = \begin{pmatrix} \rho \\ \rho \mathbf{v} \\ \rho e \end{pmatrix} = \begin{pmatrix} \rho \\ \rho \mathbf{v} \\ \rho u + \frac{1}{2} \rho |\mathbf{v}|^2 \end{pmatrix} = \begin{pmatrix} \rho \\ \rho v_x \\ \rho v_y \\ \rho v_z \\ \rho u + \frac{1}{2} \rho |\mathbf{v}|^2 \end{pmatrix} \quad (1.35)$$

and \mathbf{F} the flux of conserved variables

$$\mathbf{F} = \begin{pmatrix} \rho \mathbf{v} \\ \rho \mathbf{v} \mathbf{v}^T + P \mathbb{1} \\ (\rho e + P) \mathbf{v} \end{pmatrix}, \quad (1.36)$$

where $\mathbb{1}$ is the identity tensor. This formulation, conceptually, corresponds to the point of view of an observer who focuses on the time evolution of these quantities at fixed positions.

Alternatively, the equations can be expressed in the *Lagrangian formulation*. In this case, the relevant quantities (such as density, for example) are followed from the reference system of a fluid element. In this case, the system of equations reads

$$\begin{aligned} \frac{D\rho}{Dt} &= -\rho \nabla \cdot \mathbf{v} \\ \frac{D\mathbf{v}}{Dt} &= -\frac{\nabla P}{\rho} \\ \frac{De}{Dt} &= -\frac{P}{\rho} \nabla \cdot \mathbf{v} \end{aligned} \quad (1.37)$$

where $D/Dt \equiv \partial/\partial t + \mathbf{v} \cdot \nabla$ and takes the name of *material* or *convective* derivative. The system of equations is closed with the Equation of State (EoS) for the ideal gas

$$P = (\gamma - 1) \rho u \quad (1.38)$$

where for mono-atomic gas the ratio of specific heats $\gamma = c_P/c_V = 5/3$ and

$$u = \frac{k_B T}{\mu m_p (\gamma - 1)}. \quad (1.39)$$

Here k_B is the Boltzmann constant, μ is the mean molecular weight, m_p is the proton mass.

Eulerian method

Several methods are commonly used to discretise the set of hydrodynamical equations. The most intuitive method is represented by the Eulerian method, which corresponds conceptually to the Eulerian formulation of the equations. Space is discretised in volume elements (cells) defining a mesh, with each cell associated with a mesh-generating point. In the Eulerian approach, each cell is associated with an average over the volume element of each conserved quantity. Using the cell-averaged quantities, a reconstruction step defines how the quantity varies over the cell, determining the value of the quantity at the cell borders. The states can be assumed to be either constant over the cell or with more complex functions (e.g. linear, parabolic, etc.). Then, at each cell border a *Riemann problem* is defined, which determines the fluxes of the conserved quantities across the faces, which are then used to compute their time evolution. The class of methods which make use of Riemann solvers in mesh-based codes are referred to as Godunov methods. As an example, the simplest volume discretisation is a cartesian, regularly spaced grid, characterised by a side length of each cell Δx . The description of a fluid discretised using such a grid cannot capture spatial details smaller than Δx . Therefore, Δx is referred to as *spatial resolution*. The spatial resolution of the simulation determines the smallest structures that can be simulated faithfully, and the level of detail at which the simulation is able to represent physical processes. Achieving sufficient numerical resolution is essential for accurately capturing the complex interplay of physical processes driving structure formation in the universe. However, it often comes at a computational cost, as higher-resolution simulations require more computational resources and longer run times. As mentioned before, in the astrophysical context the collapse of structures under the effect of gravity is an ubiquitous process. Structure formation is characterised by regions reaching densities orders of magnitude higher than the average cosmic density, and strongly clustered. Therefore, cosmological simulations need to deal with a large dynamic range of spatial scales. With a uniform grid, increasing the resolution to properly capture the details of clustered regions implies wasting a significant amount of computational resources on less dense regions where less detail is required. To improve the computational efficiency, *adaptive resolution* can be reached by using a system of nested grids, reducing the cell size only where better resolution is needed. This method is known as Adaptive Mesh Refinement (AMR) schemes (e.g. Berger & Oliger, 1984; Berger & Colella, 1989; Bryan & Norman, 1995; Kravtsov et al., 1997; Teyssier, 2002; Bryan et al., 2014). Often, codes using an AMR scheme for the gravity solver also adopt the same strategy for the hydrodynamical solver, since they couple naturally.

Lagrangian method

Following the approach of the Lagrangian formulation of the hydrodynamics equation, another successful method is *smoothed particle hydrodynamics* (SPH); `OPENGADGET3`, the simulation code adopted in this work, is based on this hydrodynamical solver. For a review of the use of the SPH method in an astrophysical context, see for example Springel (2010b). In the SPH method, the fluid is represented by sampling particles. In this sense, the discretised quantity is mass rather than space. At the core of SPH is the reconstruction of any quantity of interest $A(\mathbf{r})$ using the

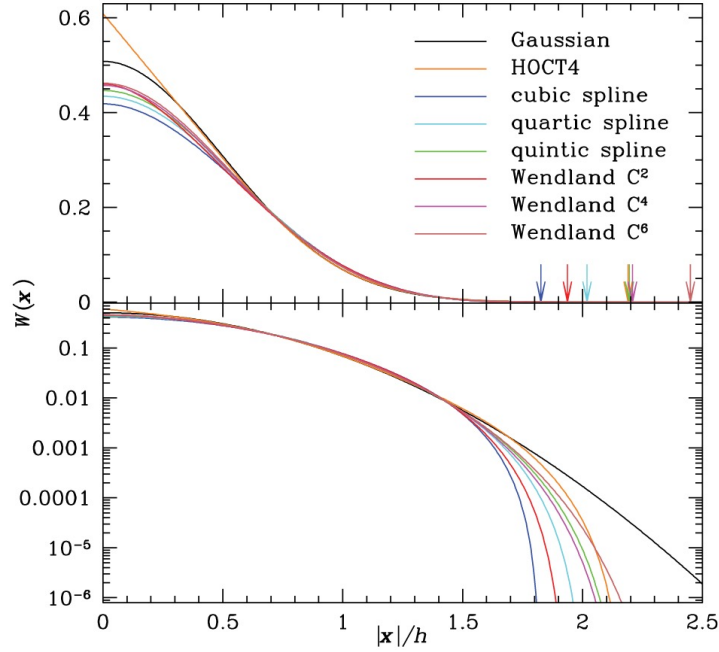


Figure 1.4: Smoothing kernels for SPH estimate. Adopted from Dehnen & Aly (2012).

particles as interpolating points. Any arbitrary function can be represented as

$$\langle A(\mathbf{r}) \rangle = \int W(\mathbf{r} - \mathbf{r}', h) A(\mathbf{r}') d^3 \mathbf{r}', \quad (1.40)$$

where W is the *smoothing kernel* and h is the *smoothing length*. If a function is sampled only at discrete points the integral is approximated by a sum

$$\langle A_i \rangle = \sum_{j=1}^{N_{\text{ngb}}} \frac{m_j}{\rho_j} A_j W(\mathbf{r}_{ij}, h_i). \quad (1.41)$$

For W to be suitable as a kernel, some properties are required, such as normalisation to unity, compact support, differentiability and spherical symmetry. The property of compact support implies that to make an SPH estimate it is not necessary to sum over all particles. This makes it particularly advantageous since it avoids the N^2 scaling when carrying out the sum on a computer. Therefore, a finite number N_{ngb} of neighbouring particles contribute to any SPH estimate at a given point. Eq. 1.41 naturally leads to the SPH estimate of the density at the position of particle i

$$\rho_i = \sum_{j=1}^N m_j W(\mathbf{r}_{ij}, h_i). \quad (1.42)$$

Fig. 1.4 plots the functional form of several choices for the SPH kernels. A commonly used class of kernels that satisfy the aforementioned requirements is represented by the splines (cubic,

quartic, quintic). However, as discussed in Dehnen & Aly (2012), the splines are unstable to the pairing instability, occurring when particles form close bound pairs, effectively reducing N_{ngb} . In this work, they also argue that the reason for this instability is not related to the presence of an inflection point in the kernel, but rather that the necessary condition to avoid this instability is that the Fourier transform of the kernel must be non-negative. The class of Wendland kernels proposed by Dehnen & Aly (2012) has such property.

The modern, fully conservative formulation of SPH that is adopted in this work integrates the entropy as conserved quantity, where the entropy is defined as

$$A_i = \frac{P_i}{\rho^\gamma} \quad (1.43)$$

and is related to the internal energy by

$$u_i = \frac{A_i}{\gamma - 1} \rho^{\gamma-1}. \quad (1.44)$$

The equations of motion (EOM) for the N particles are derived from the discretised Lagrangian

$$L = \frac{1}{2} \sum_{i=1}^N m_i \dot{\mathbf{r}}_i^2 - \frac{1}{\gamma - 1} \sum_{i=1}^N m_i A_i \rho_i^{\gamma-1}, \quad (1.45)$$

where A_i is a constant (i.e. strictly adiabatic) and ρ_i is a function of the positions through Eq. 1.42. Under the constraint that $h_i^3 \rho_i \sim \text{constant}$ the EOM read

$$\frac{d\mathbf{v}_i}{dt} = - \sum_{j=1}^N m_j \left[f_i \frac{P_i}{\rho_i^2} \nabla_i W_{ij}(h_i) + f_j \frac{P_j}{\rho_j^2} \nabla_i W_{ij}(h_j) \right], \quad (1.46)$$

where

$$f_i = \left(1 + \frac{h_i}{3\rho_i} \frac{\partial \rho_i}{\partial h_i} \right)^{-1} \quad (1.47)$$

is a correction factor that accounts for the fact that h_i varies as a function of ρ due to the aforementioned constraint. Since the EOM are derived from a variational principle, SPH manifestly conserves mass, linear and angular momentum, energy and entropy.

One fundamental property that makes SPH particularly suitable for cosmological simulations resides in its naturally adaptive resolution. The kernel smoothing length is adapted to the local density, and the higher-density regions are sampled with a higher number of particles. Moreover, due to its nature, it couples naturally to particle-based gravitational solvers. In this regard, it is also worth noting that in cosmological hydrodynamical codes, the computation of the gravitational force is typically softened. The softening length effectively smoothes the gravitational force over a certain scale, therefore representing the smallest scale at which gravitational interactions are accurately modelled in the simulations. For this reason, in cosmological simulations, the softening length is usually quoted to indicate the smallest resolved spatial scales.

If entropy is conserved, without any further modification this formulation would be unable to handle phenomena that routinely arise in an astrophysical context such as discontinuities and fluid mixing. For this reason, a number of additional ingredients are added to the description. `OPENGADGET3` features an improved formulation of SPH, tailored for accurate simulations of galaxy formation and evolution of cosmic structures. A comprehensive description is provided in Beck et al. (2016), here we summarise the main advancements. To correctly describe discontinuities in the velocity field (e.g. in shocks), a prescription preventing shocked high-velocity particles to unphysically penetrate into unshocked regions is applied; this is referred to as *artificial viscosity*. However, such a prescription might affect also shearing flows and outside shocks (for example suppressing random gas motions in the ICM, see Dolag et al. 2005; Donnert et al. 2013) if applied indiscriminately. The improved formulation features a time-dependent artificial viscosity that correctly detects shocks and is suppressed elsewhere with a shear flow limiter (Balsara, 1995). Moreover, it uses a high-order gradient estimator to compute curl and divergence that enters the computation of such limiter. Another improvement is aimed at counter-acting a spurious surface tension that arises in the entropy formulation of SPH in contact discontinuities (e.g. in mixing problems). For this reason, a time-dependent artificial conductivity is introduced, facilitating heat transport between particles in this case. A numerical limiter is also applied, to suppress the effect of artificial conductivity in gravitationally-induced pressure gradients, where it could foster unphysical heat transport. In some cases, highly dynamical and computationally active particles penetrate into regions of inactive particles. A timestep limiting procedure is thus applied, shortening the timesteps of inactive particles in this situation, to prevent large timestep gradients leading to numerical instability and unphysical results. Finally, the improved scheme adopted in `OPENGADGET3` also features the Wendland kernels as the standard choice and isotropic thermal conduction (Dolag et al., 2004). Such an improved formulation demonstrated much better accuracy and fidelity compared to traditional SPH methods both in an extensive set of hydrodynamical tests and in simulations of galaxy formation and evolution of cosmic structures.

Other methods

The last development in the field of computational astrophysics is represented by methods that try to combine the advantages of both the Eulerian and Lagrangian techniques. In these approaches, the grid velocity can be chosen completely freely and is not forced to be the same of the fluid. Some codes implement this method by defining a Voronoi tessellation to cover the volume, in which the evolution of the cell quantities is computed starting from the fluxes obtained through a Riemann problem in a similar fashion to purely Eulerian codes (e.g. Springel, 2010a; Duffell & MacFadyen, 2011; Vandenbroucke & De Rijcke, 2016). Recently, a new class of mesh-free arbitrary Lagrangian-Eulerian methods have been proposed, in which there is no geometrical mesh, but the fluid is sampled using particles. However, each differential volume d^3x is partitioned fractionally among the nearest particles/cells using a kernel similar to SPH. Then, a quadrature rule is formulated to evolve the conserved quantities associated with each particle, effectively using finite-volume equations of the Godunov type (e.g. Hopkins, 2015; Groth et al., 2023).

1.2.3 Additional baryonic processes and sub-resolution models

A comprehensive model of galaxy formation and evolution requires additional astrophysical processes on top of pure hydrodynamics. The first additional ingredient to consider is *radiative cooling*, the process through which the gas radiates its internal energy through microphysical processes. If cooling is not effective, then compression of the gas results in temperature rise, in turn generating pressure support (see Eq. 1.38). Conversely, if cooling is effective the collapse is able to proceed further. Formally, cooling is represented by a sink term in the energy equation (see Eqs. 1.37). More specifically, a *cooling function* Λ is defined, such that the cooling rate $R = \Lambda n_H^2$ (where n_H is the hydrogen number density) quantifies the amount of energy lost per unit volume and unit time. Several microphysical processes need to be taken into account to compute this function. The relevant ones for galaxy formation entail the emission of a photon after a two-body interaction. Capture of free electrons by ions leads to *recombination* and emission of a photon with the associated ionisation energy. Collisions between the free electrons with ions of elements heavier than Helium (so-called "metals") can induce excitation of the ions, which emit a photon when returning to the ground state (cooling by *collisional excitation*). The electron collision may also ionise the atom, and the freed electron can take part in the recombination and excitation processes (cooling by *collisional ionisation*). Another cooling channel is *bremsstrahlung* (free-free emission), which consists of the emission of radiation following the scattering of free electrons by ions. Finally, inverse Compton cooling occurs when energy is transferred from energetic electrons to lower-energy photons. Each process contributes to the total cooling rate, with a relative importance that depends on the chemical composition, the density and the temperature. Usually, in cosmological simulation codes, the cooling function is pre-computed using detailed radiative transfer codes (e.g. Ferland et al., 2017) and tabulated in the relevant parameter space in density, temperature and metallicity, to be used efficiently on the fly. Nowadays, in most of the cosmological galaxy formation simulations it is assumed that photoionisation equilibrium holds, that is, there is a balance between photoionisation and recombination by electrons and ions. Furthermore, the gas is assumed to be *optically thin*, meaning that once emitted, a photon has a negligible probability of interacting with another particle and is, therefore, able to escape the region. The presence of the CMB as well as the UV and X-ray background produced by quasars (see Ch. 2) and star-forming galaxies is also accounted for by introducing a time-dependent radiation background. In particular, the simulations described in Ch. 4 are carried out with metallicity-dependent radiative cooling, using the procedure described in Wiersma et al. (2009), and account for the presence of a uniform, time-dependent ionising background (Haardt & Madau, 2001).

Starting from the cooling function, it is useful to define the *cooling time*, that is, the time it takes for the gas to radiate its internal energy

$$t_{\text{cool}} \equiv \frac{\rho u}{R} = \frac{\rho u}{n_H^2 \Lambda} = \frac{1}{\gamma - 1} \frac{nk_B T}{n_H^2 \Lambda} \quad (1.48)$$

where the latter equivalence is derived using Eq. 1.39. The impact that cooling has on a gaseous system (e.g. the gas in a DM halo, but the argument holds in general) can be assessed by comparing t_{cool} with the Hubble time $t_H = 1/H(z) \propto 1/(G\bar{\rho})^{1/2}$ (as a proxy for the age of the Universe in the

matter-dominated era), where $\bar{\rho} = \Omega_m \epsilon_c / c^2$, and the dynamical time $t_{\text{dyn}} \propto 1/(G\bar{\rho}_{\text{sys}})^{1/2}$, where $\bar{\rho}_{\text{sys}} = \bar{\rho}_g + \bar{\rho}_{\text{DM}}$. Three scenarios are possible:

- $t_{\text{cool}} > t_{\text{H}}$ - the gas cannot cool in a Hubble time. Cooling is irrelevant and the gas tends to settle in hydrostatic equilibrium.
- $t_{\text{dyn}} < t_{\text{cool}} < t_{\text{H}}$ - the gas contracts slowly while cooling, the system undergoes a sequence of quasi-hydrostatic equilibria.
- $t_{\text{cool}} < t_{\text{dyn}}$ - pressure is lost too quickly for the system to maintain equilibrium. The gas collapses on the dynamical timescale t_{dyn} . Since the density increases as the gas cools, it is a runaway process. It is often referred to as the "cooling catastrophe".

In general, the gas in a DM halo has a density and temperature profile that varies with radius, and the density increases towards the centre. Therefore, the condition also varies accordingly and the innermost region might be able to cool even when the outer part does not.

The gas that is able to cool and collapse towards the centre of the DM halo eventually forms stars and creates the galaxies. The gas that remains distributed between the stars constitutes the *interstellar medium* (ISM). The ISM is composed of coexisting phases of molecular, atomic and ionised gas, with densities between $n \sim 10^{-3} - 10^4 \text{ cm}^{-3}$ and temperatures $T \sim 10 - 10^6 \text{ K}$; it is therefore *multiphase*. The details of the process of star formation are still not completely understood, but in general, it is observed to occur within *molecular clouds*, which are regions within the ISM composed mainly of molecular hydrogen, with masses $10^2 - 10^5 M_{\odot}$ and sizes of the order of $\sim 100 \text{ pc}$. Once the Jeans criterion for the collapse of the cloud is satisfied, the collapse itself can occur if it is possible to channel the gravitational potential energy released into processes that do not generate pressure support, such as separating molecular hydrogen and ionising atomic hydrogen. Part of the energy is also radiated due to molecular cooling. This process ultimately leads to the creation of a protostar, and the whole process continues on scales smaller than $\sim 1 \text{ AU}$. Star formation needs to be included in cosmological simulations, to create and evolve galaxies. However, large-scale simulations typically have a spatial resolution of the order of a kiloparsec (e.g. Hirschmann et al., 2014; Schaye et al., 2015; Dubois et al., 2016) and reach hundreds of parsecs at best (e.g. Pillepich et al., 2019). For this reason, such processes cannot be included from first principles, but rather they need to be implemented in an effective, sub-resolution fashion. This allows us to account for the effects produced by the unresolved physical processes and formulate equations that relate these processes with the resolved scales of the simulations. Generally, a number of free parameters are required, which are set by physical considerations or calibrated against observations. In the simulations used in Ch. 4, the ISM is described in a sub-resolution fashion following Springel & Hernquist (2003). Each gas particle with a hydrogen number density above the threshold $n_{\text{H}} = 0.5 \text{ cm}^{-3}$ is described as a two-phase ISM with a cold, star-forming phase in pressure equilibrium with a hot phase. Multiple generations of star particles are created from gas particles in a stochastic fashion, each representing a simple stellar population described by a Chabrier (2003) initial mass function. Once star particles are created, the evolution of the stellar populations and the metal enrichment of the ISM by ageing and exploding stars is tracked using the detailed chemical evolution model by Tornatore et al.

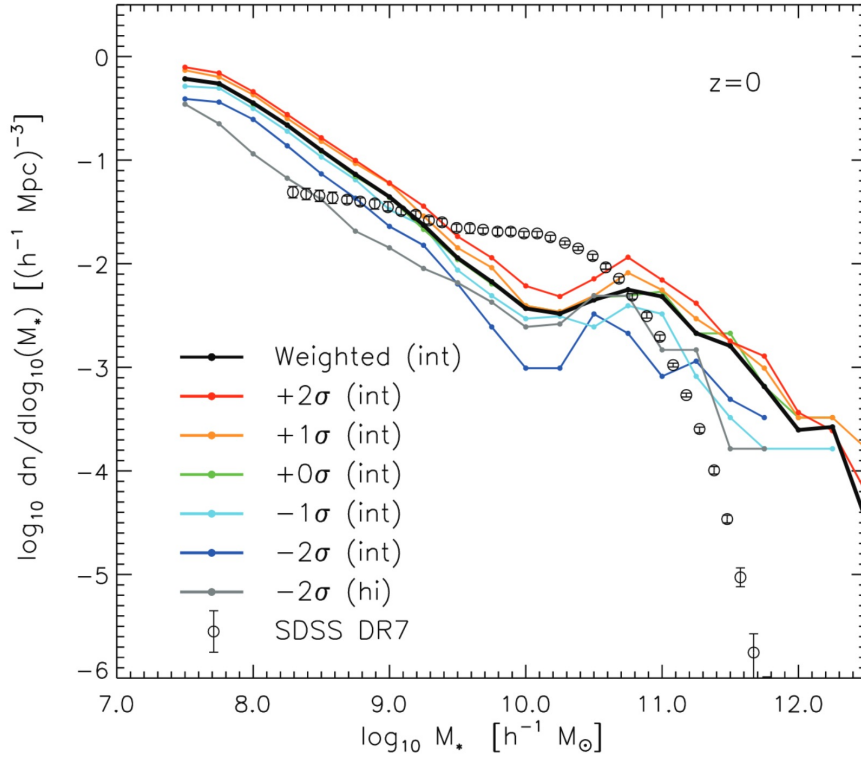


Figure 1.5: Stellar mass function at redshift zero, from the hydrodynamical simulations performed by Crain et al. (2009).

(2004, 2007). The lifetime function by Padovani & Matteucci (1993) is used to compute the age of stars. Finally, the metal enrichment is computed based on the stellar yields for supernovae type Ia by Thielemann et al. (2003), for supernovae type II by Nomoto et al. (2013) and for asymptotic giant branch stars by Karakas & Lattanzio (2007).

In their seminal paper, White & Rees (1978) showed that in a scenario in which gas condenses into the potential wells of DM haloes formed hierarchically, half of it should have formed stars, therefore predicting a ratio between stellar mass M_* and halo mass M_{halo} equal to $M_*/M_{\text{halo}} \sim 0.5\Omega_b/\Omega_m \sim 0.08$ (assuming the results from Planck Collaboration et al. 2020) at the present time. Early cosmological simulations vastly overpredicted the number density of galaxies, at almost all mass scales. For instance, Fig. 1.5 shows the results obtained by Crain et al. (2009), who re-simulated at higher resolution several nearly spherical regions of radius ~ 28 Mpc from the Millennium Simulation Springel et al. (2005b). The regions are characterised by overdensities of $(-2,-1,0,1,2)\sigma$ from the cosmic mean. The stellar mass function (i.e. the number of galaxies per unit volume as a function of stellar mass) for each region is shown as a coloured solid line. The black dots are observational measurements from the Sloan Digital Sky Survey (Abazajian et al., 2009). Furthermore, using abundance matching techniques, Behroozi et al. (2013) predicted the expected ratio M_*/M_{halo} as a function of halo mass calibrated on observations. Fig. 1.6 shows their results (dashed red line), compared to other similar studies in the literature. If star

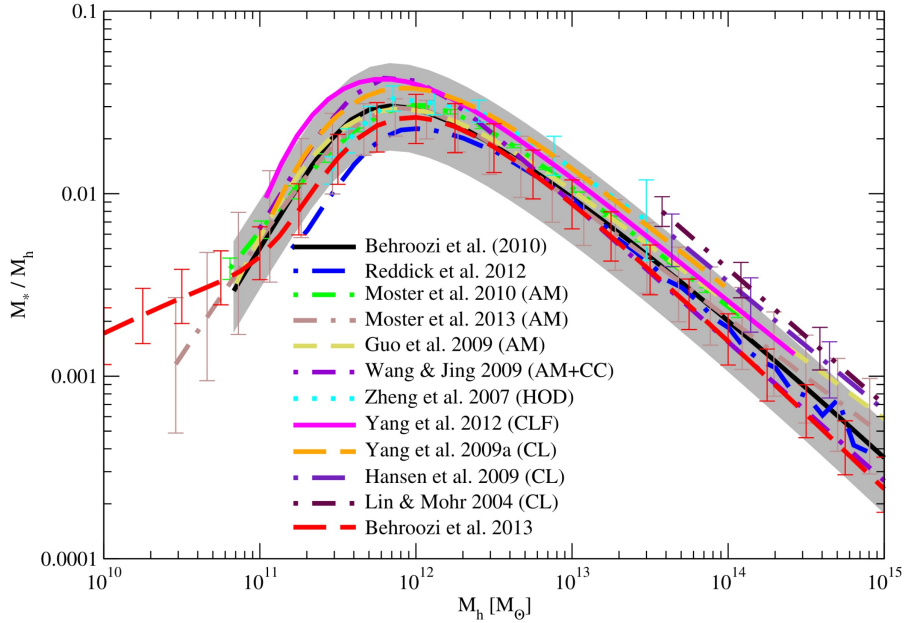


Figure 1.6: M_*/M_{halo} plotted as a function of M_{halo} , as predicted by Behroozi et al. (2013).

formation converted all the available gas into stars, M_*/M_{halo} would be equal to Ω_b/Ω_m . However, comparing to the cosmic baryon fraction $\Omega_b/\Omega_m \sim 0.16$, Fig. 1.6 shows that the star formation efficiency is modulated across different halo mass scales, and in particular is suppressed at the low and high mass scales. As a matter of fact, this is one of the strongest arguments supporting the need for additional processes that heat the gas and prevent the so-called *overcooling*. It has been therefore advocated that feedback from supernovae and Active Galactic Nuclei (AGN) are responsible for this suppression at the low and high masses respectively. In this Thesis, I focus in particular on the role of supermassive BHs (SMBHs) in the context of galaxy formation and evolution, and specifically on a novel method to include into simulations the process powering AGN, that is, accretion onto SMBHs. In general, the problem of a BH accreting in a galaxy and influencing its evolution is characterised by a dynamic range of spatial scales of around 10^{10} . Indeed, the event horizon of a BH (see Sec. 3.1.1), defined as

$$R_{\text{BH}} = \frac{2GM_{\text{BH}}}{c^2} = 10^{-5} \left(\frac{M_{\text{BH}}}{10^8 M_{\odot}} \right) \text{ pc} \sim 3 \times 10^{13} \left(\frac{M_{\text{BH}}}{10^8 M_{\odot}} \right) \text{ cm}, \quad (1.49)$$

has milliparsec scales, whereas the large-scale effect of feedback can be seen on galaxy scales, of tens of kiloparsecs. Therefore, like star formation, BH-related processes need to be included in a sub-resolution fashion. In the next Chapter, I will review some aspects of the observational evidence that supports the role and importance of AGN. Then, I will discuss the details of the treatment of BHs, accretion and feedback in cosmological simulations.

2 | Active Galactic Nuclei

Part of the content of this Chapter is based on Sala et al. (2023).

In the 1960s, the field of radio astronomy witnessed important developments, with pioneering work on interferometry conducted at the University of Cambridge. For the first time a systematic survey of celestial objects at these wavelengths was performed, and the Second and Third Cambridge Catalogues of Radio Sources (2C and 3C, respectively) were published in 1955 and 1959 respectively. In a seminal paper Schmidt (1963) noted that the only optical counterpart seen near the position in the sky of one of the radio sources of the catalogue, 3C 273, was a star-like (unresolved) object of magnitude of about 13. He also realised that the lines of the spectrum had a redshift of 0.16, therefore placing it at a cosmological distance (around 750 Mpc). Such a redshift for a "star" of that magnitude was extremely challenging to interpret. The class of astronomical objects named *quasars* (from *quasi-stellar radio source*) was discovered. It was soon realised that the inferred luminosity cannot be generated by a star but requires a different powering mechanism. It is now known that these objects are *accreting* BHs with masses $10^6 \lesssim M_{\text{BH}}/M_{\odot} \lesssim 10^{10}$ at the centre of massive galaxies; the gravitational energy of gas infalling close to the BH is converted into radiation, and the generated luminosity can often outshine the one of the host galaxy. The phenomenon of a BH releasing a large amount of energy, in different forms, at the centre of a massive galaxy is generally referred to as an Active Galactic Nucleus (AGN). In this Chapter I will focus on presenting a few observational properties of AGN, the importance of AGN feedback and BH spin, and how AGN are included in cosmological simulations. A discussion on the theoretical aspects of accretion physics is presented in Ch. 3.

2.1 Phenomenology

2.1.1 Components of an AGN and spectral energy distribution

The phenomenology of AGN is rich and extensive since it reflects a plethora of astrophysical processes, from details of accretion physics at horizon scales to the interaction of its radiative output and jets with the ISM and, at larger scales, with the intra-cluster medium (ICM). The signatures of an AGN are seen across the whole electromagnetic spectrum, probing different scales and physical conditions, and hence different radiative processes. An extensive review of the multi-wavelength observational view of AGN is provided in Padovani et al. (2017). In this Section I will revise a few essential aspects, based on Ghisellini (2013).

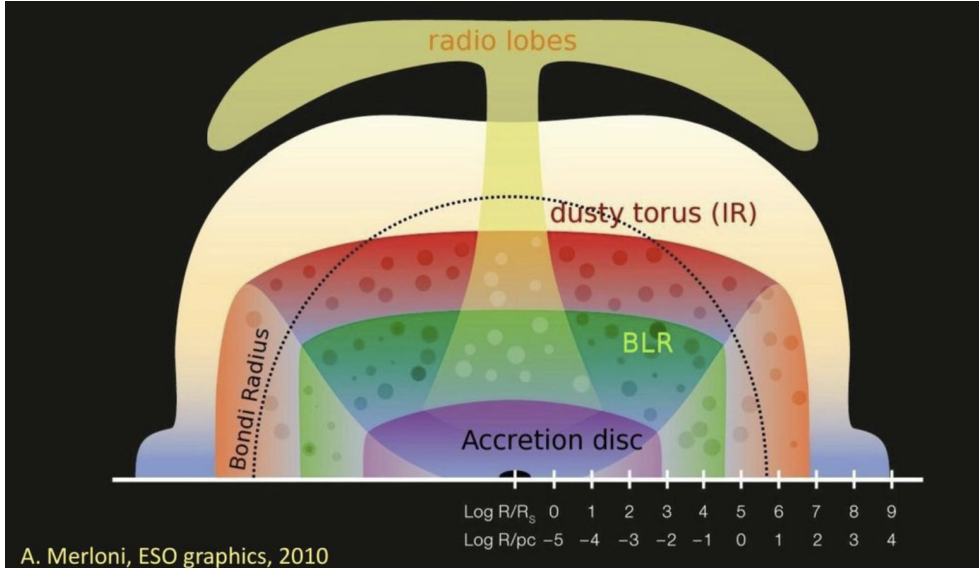


Figure 2.1: Schematic view of the components of an AGN. Credits: A. Merloni, ESO, 2010

According to the current model, an AGN is composed of several different components, illustrated schematically in Fig. 2.1, for an example $10^8 M_{\odot}$ BH. The scales reported in the following are indicative order of magnitudes. The primary emission, in the optical-UV band, is generated by an *accretion disc* between $\sim 10^{-5}$ and $\sim 10^{-2}$ pc, a gaseous structure orbiting the central mass in a disc configuration, in which gas parcels slowly spiral towards the centre due to viscous torques. A hot X-ray-emitting layer, the *X-ray corona*, is thought to be present above and below the accretion disc in the innermost part. At $\sim 0.01 - 1$ pc, in the *broad line region* (BLR) around 10% of the ionising radiation from the disc is reprocessed by a large number of clouds (10^6-8) that re-emit it in the form of emission lines; the lines have widths indicating typical velocities of the clouds of thousands of kilometres per second (see e.g. Peterson, 2006). At $\sim 1 - 100$ pc, a structure rich in dust and molecular gas (the *dusty torus*) absorbs part of the radiation from the central region and re-emits it in the infrared band. Further away, the *narrow line region* (NLR) is present; it is similar to the BLR, but the clouds are moving with lower velocities of around 500 km s^{-1} (hence the associated line widths are narrower). Finally, about 10% of AGN exhibit powerful bipolar relativistic jets, with associated synchrotron emission in the radio band. The jets have been observed to extend up to hundreds of kiloparsecs, sometimes even megaparsecs (for the case of giant radio galaxies, see Dabhade et al., 2020).

A wealth of information about AGN has been gathered by collecting data across different wavelengths and building their *spectral energy distribution* (SED). A prototypical example of the typical SED of a bright quasar without a jet is shown in the black solid line in Fig. 2.2 (see e.g. Elvis et al., 1994). The structure, properties and emission profile of each component of the AGN model were inferred by modelling each specific signature in the SED.

The contribution from the accretion disc to the SED is shown as the blue triple-dot-dashed line in Fig. 2.2. It is typically in the IR-optical-UV band. It is characterised by a low-frequency portion, in which the luminosity (and consequently the flux) per unit frequency L_{ν} is a power-law

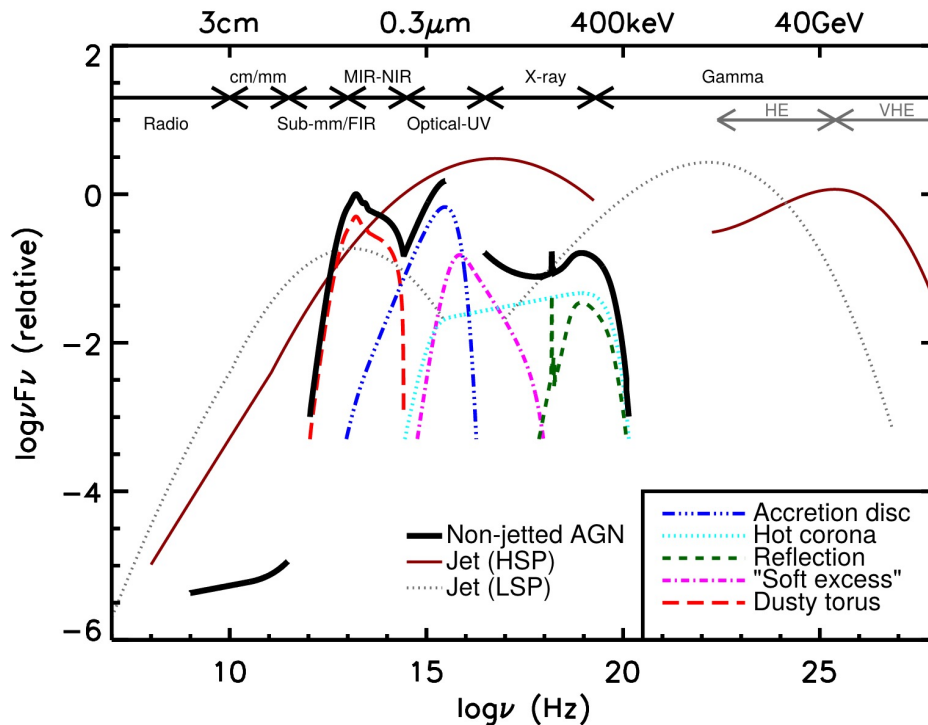


Figure 2.2: Adopted from Padovani et al. (2017), credits C. M. Harrison.

in frequency ν , namely $L_\nu \propto \nu^2$. This power-law transitions to an intermediate portion where $L_\nu \propto \nu^{1/3}$ (e.g. at $\log(\nu) \sim 13.5$ in Fig. 2.2). At higher frequencies, the emission shows a peak followed by an exponential cut-off. These spectral features were successfully explained with the "standard" model of the accretion disc, presented in the seminal paper by Shakura & Sunyaev (1973), which therefore represents an important milestone in our understanding of accretion theory. The shape arises as the result of the combined emission from each cylindrical annulus of the accretion disc. The emission profile is accounted for by assuming an optically thick, geometrically thin disc, that generates a superposition of blackbody spectra. In Sec. 3.1.4 I will discuss this model in further detail from the theoretical point of view.

The X-ray corona is the component that is assumed to be responsible for the strong X-ray emission associated with AGN. Its power-law spectrum (cyan dotted line in Fig. 2.2) is due to thermal Comptonisation by hot electrons. The corona also illuminates the disc, which is colder and not ionised, and produces a reflection component (dashed line in Fig. 2.2). In particular, the Iron $K\alpha$ line at 6.4-6.7 keV also arises as a reflected component and its shape is a very important diagnostic for the conditions of the innermost region of the accretion flow. If the BH has a non-zero angular momentum, the accretion disc extends to smaller radii or larger radii than in a non-rotating BH (see Sec. 3.1.3), and the line is therefore affected measurably, depending on the spin parameter. This effect is the basis for the main technique adopted to measure the BH rotation, that is, its spin (Sec. 2.2.3).

Observationally AGN have different appearances, depending on whether or not they display

broad emission lines. Therefore, there is now a wide consensus that this difference arises for purely geometrical reasons, namely due to the angle of the line of sight with respect to the rotational symmetry axis of the system. When the line of sight intercepts the dusty torus, the broad lines are weak or absent. These objects are named *Type II QSOs*¹, otherwise they are referred to as *Type I QSOs*. Therefore, it was proposed that these different observational classes correspond to the same underlying object, leading to the current model of AGN, referred to as the *unification scheme* (Antonucci, 1993; Urry & Padovani, 1995). It is also worth noting that although there is some consensus on the AGN current working model, several details of the observed features are still unclear, hence recent studies have been dedicated to improving the model of AGN just described, by invoking, for example, disc winds (see e.g. Netzer, 2015, for a review).

As mentioned before, 10% of AGN show bipolar ejection of relativistic matter, the jets. The electromagnetic emission coming from the jets is beamed since the material composing the jet is characterised by a relativistic bulk motion. As I will discuss in Sec. 2.2, jets are powered by accretion and extraction of the rotational energy associated with the spin of the BH. Most of the energy is transferred into sheer kinetic energy of the relativistic material and in the magnetic field that threads the jet (which is therefore a Poynting flux), while a fraction goes into electromagnetic radiation. Even though quasars were initially discovered through their radio emission, this is not the primary band in which this type of AGN emits the most. As can be seen in Fig. 2.2, the largest amount of power is channelled either in the mm-optical or γ -ray bands. At any rate, the observational appearance of jetted AGN depends on whether or not the jet points at us, because relativistic beaming amplifies the emitted power. In particular, objects whose jets point at the Earth are classified as *blazars*, otherwise they are referred to as *radio-galaxies*.

The released energy involved in the process is enough to have a fundamental role in the formation and evolution of galaxies (e.g. Benson et al., 2003; Di Matteo et al., 2005). This occurs despite the direct gravitational influence of central massive BHs being limited to a region of 1 – 100 pc in radius

$$r_{\text{inf}} = \frac{2GM_{\text{BH}}}{\sigma^2} \simeq 8 \left(\frac{M_{\text{BH}}}{10^8 M_{\odot}} \right) \left(\frac{\sigma}{200 \text{ km/s}} \right)^{-2} \text{ pc}, \quad (2.1)$$

the BH *sphere of influence* (e.g. Kormendy & Ho, 2013), much smaller than the size of a galaxy. Here σ is the stellar velocity dispersion in the nuclear region. The same expression also holds as an estimate of the gravitational influence of a BH in a gaseous environment, although in this case σ is the sound speed of the gas and r_{inf} is referred to as the Bondi radius. Hence, it seems counter-intuitive that the BH has an effect on the galaxy as a whole; the effect must be communicated through its energy output. This process is usually dubbed AGN feedback. In the next Sections, I will revise the different flavours in which it is observed and its role in different scenarios.

¹Note that the acronym "QSO" is generally used for AGN with low radio emission, whereas quasar is historically associated with the radio-emitting ones.

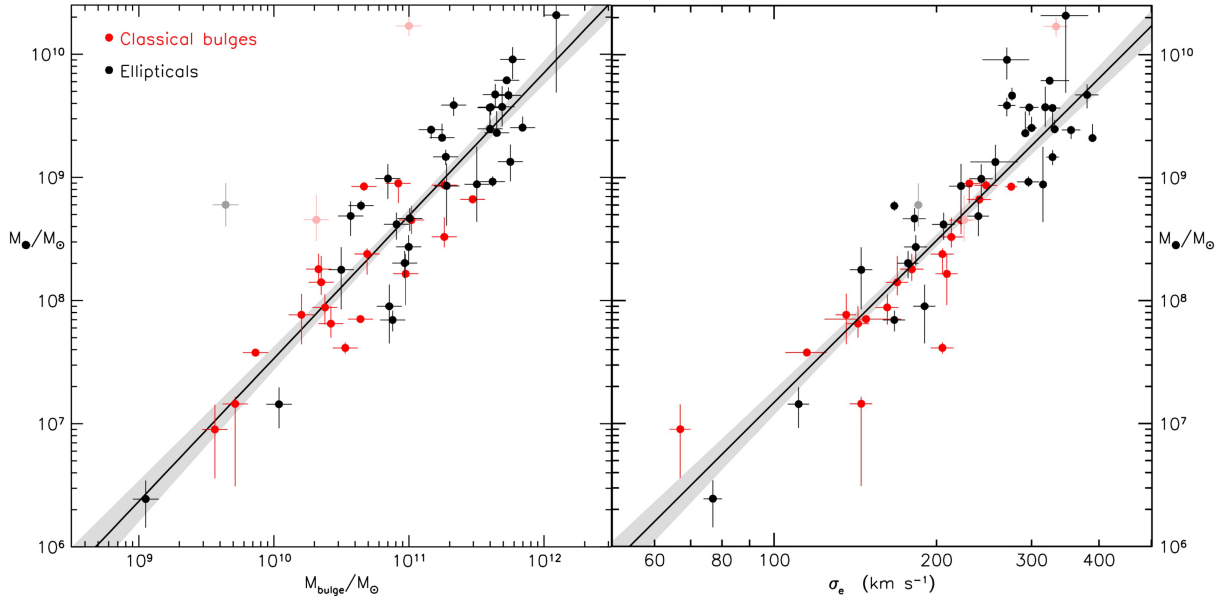


Figure 2.3: Experimental correlations between BH mass and the bulge mass M_{bulge} (left panel) and bulge velocity dispersion (right panel). Adopted from Kormendy & Ho (2013).

2.1.2 Radiative feedback from AGN and BH-host galaxy correlations

Observationally, feedback has been broadly categorized into two modes, depending on the main channel of energy release (Churazov et al., 2005; Sijacki et al., 2007; Fabian, 2012): a so-called quasar mode, associated with luminous AGN, and a maintenance mode (also referred to as kinetic or radio mode), related to AGN with powerful jets. In the quasar mode, operating close to the Eddington limit, most of the energy is released in the form of radiation and winds (Silk & Rees, 1998; Fabian, 1999; Harrison et al., 2018). This mode is prevalent at earlier epochs, at redshift 2-2.5 (e.g. Croton et al., 2006; Fabian, 2012), and has been advocated to explain the emergence of experimental correlations between the BH mass and either the mass of the central spheroid (Magorrian et al., 1998; McConnell & Ma, 2013) or the velocity dispersion (Ferrarese & Merritt, 2000; Gebhardt et al., 2000; Tremaine et al., 2002; Häring & Rix, 2004; Gültekin et al., 2009; Kormendy & Ho, 2013) of the host galaxy. An example of such correlations is shown in Fig. 2.3, from Kormendy & Ho (2013). Several analytical models have suggested a theoretical explanation for these correlations (e.g. Silk & Rees, 1998; Fabian, 1999; King, 2003), by assuming that the luminosity produced by the central object couples with the nearby matter and generates an advancing shell that sweeps up the surrounding medium and expels the gas from the galaxy, suppressing star formation. Considerations on the energetics of a feedback event lead to the prediction $M_{\text{BH}} \propto \sigma^5$ in the energy-conserving and $\propto \sigma^4$ in the momentum-conserving scenario for the expanding shell. The remarkable agreement with the observed correlation (e.g. $M_{\text{BH}} \propto \sigma^{4.38}$ from Kormendy & Ho 2013) suggests that AGN might be a viable mechanism, although it is rather indirect.

The existence of powerful galactic outflows is regarded as a more direct piece of evidence

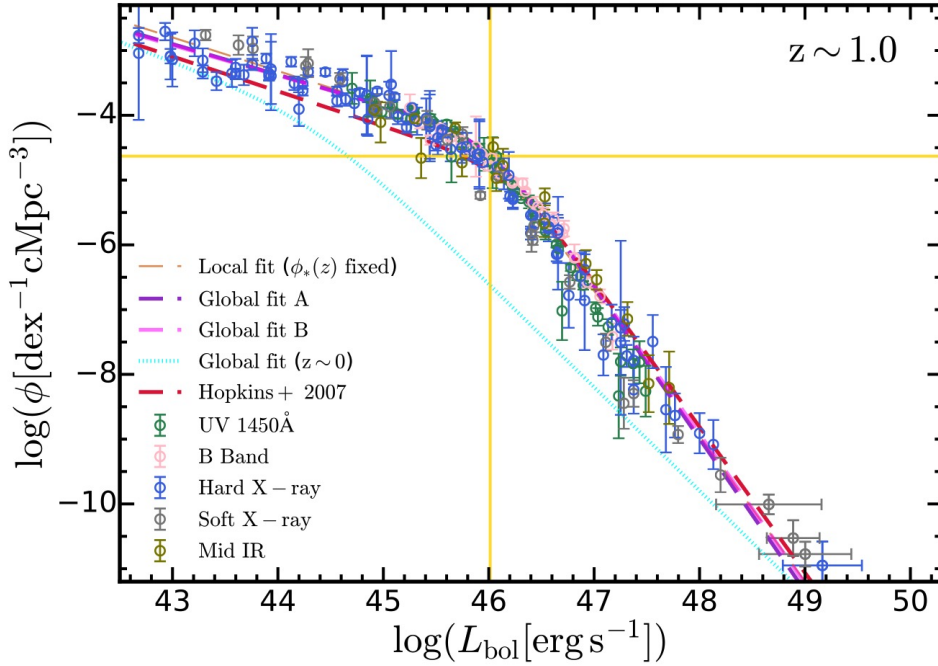


Figure 2.4: Observational determination of the quasar luminosity functions. Adopted from Shen et al. (2020).

indicating AGN feedback at play. The coupling mechanism between the AGN energetic output and the surrounding ISM that drives the shell is thought to be radiation pressure on dust, or a powerful fast wind generated close to the quasar. Such nuclear pc-scale winds (Tombesi et al., 2013; Nardini et al., 2015) as well as kpc-scale outflows (Tremonti et al., 2007; Feruglio et al., 2010; Alexander et al., 2010; Rupke & Veilleux, 2011; Sturm et al., 2011; Greene et al., 2012; Maiolino et al., 2012; Gofford et al., 2015) are indeed found, and cannot be explained by feedback due to a starburst.

By combining surveys of AGN at different wavelengths, it is also possible to compile a luminosity function. Fig. 2.4 shows the experimental determination by Shen et al. (2020). The steep slope, especially at low redshift (cyan dotted line), indicates that less luminous AGN are far more numerous than the brightest ones. This in turn implies that AGN spend more time in a slowly accreting, less luminous phase. Nonetheless, by comparing the total energetic output estimated from the integrated luminosity function or from the X-ray quasar background with the total BH mass density (the Soltan 1982 argument), it is possible to estimate that BHs must have accumulated most of their mass with a high radiative efficiency $\epsilon_r \sim 0.1$, consistent with the standard thin disc paradigm, and therefore while exerting feedback in the quasar mode. In addition, taken at face value, this result also suggests that BH might be *on average* mildly spinning (see Sec. 3.2.1). The self-consistent modelling of BH spin evolution across cosmic time (Ch. 3) provides theoretical constraints on the values of spin and therefore radiative efficiency as a function of BH mass and redshift (see Sec. 4.2). Such predictions help improve upon average

estimates based on global integrated quantities.

2.1.3 Maintenance feedback and AGN in galaxy clusters

A second mode of feedback occurs when energy is channelled mostly into powerful relativistic jets (McNamara & Nulsen, 2007; Cattaneo et al., 2009; McNamara & Nulsen, 2012). This mode often corresponds with highly sub-Eddington accretion rates and is mostly associated with low-luminosity AGN (LLAGN) (Merloni & Heinz, 2007). It is referred to as maintenance or radio mode. However, jets can also be efficient in super-Eddington accretion discs, which are found to become geometrically thick and able to confine the jet (Sądowski et al., 2014; Sądowski & Narayan, 2015; Massonneau et al., 2023b; Lowell et al., 2024).

A class of systems in which relativistic jets have a fundamental role is represented by galaxy clusters and groups. Galaxy clusters are surrounded by hot atmospheres (10^{7-8} K, McNamara & Nulsen 2007), that are detected as extended bright X-ray sources due to thermal bremsstrahlung. The cooling time in their inner regions is found to be much shorter than the Hubble time. In the absence of an additional energy source, the gas should originate a "cooling flow" and abundantly form stars (Fabian, 1994). However, star formation rates in the central brightest cluster galaxies (BCG) are an order of magnitude lower than predicted by the cooling flow model (Crawford et al., 1999; Von Der Linden et al., 2007). Some form of heating is thus required to offset cooling and decrease star formation.

Despite alternative forms of heating have also been suggested (such as thermal conduction or motion of substructures, see McNamara & Nulsen 2007 for a discussion), the most promising mechanism is thought to be the injection of energy from AGN jets (Fabian, 2012; McNamara & Nulsen, 2012; Hlavacek-Larrondo et al., 2022). Indeed, jets are observed to carve out cavities in the ICM, that are visible as depressions in the X-ray brightness (Hlavacek-Larrondo et al., 2022). These cavities are co-spatial with the radio emission from the lobes that mark the termination of the jets (Hlavacek-Larrondo et al., 2015). Fig. 2.5 gives a few stunning examples of such systems. Studies on samples of clusters (Rafferty et al., 2006; Dunn & Fabian, 2006, 2008) have shown that cavities are more frequent when some form of heating is required. Furthermore, the estimates of the mechanical power required to inflate cavities are found to be comparable to the cooling losses in the central regions (Churazov et al., 2002, 2005; McNamara & Nulsen, 2007; Rafferty et al., 2006, 2008). How exactly the jet energy is converted into heat is still a matter of debate (McNamara & Nulsen, 2007; Hlavacek-Larrondo et al., 2022).

It is also worth noting that there are examples of clusters in which cooling losses are not balanced. 10% of the central massive galaxies in clusters at $z \sim 0$ experience star formation in a measure that indicates AGN feedback might not be effective (McNamara & Nulsen, 2007). In addition, the Phoenix cluster (McDonald et al., 2012) exhibits strong features of AGN feedback such as a jet and cavities, but it is still unable to suppress cooling (McDonald et al., 2019). In general, the ability to launch relativistic jets is mainly related to properties of the BH (e.g. spin) or processes occurring in its vicinity (e.g. the structure of the accretion flow, the presence of magnetic fields, etc.; see Davis & Tchekhovskoy 2020 and Sec. 2.2) and overall energetics. Therefore, not all SMBHs in clusters necessarily launch relativistic jets (e.g. Hlavacek-Larrondo et al., 2020).

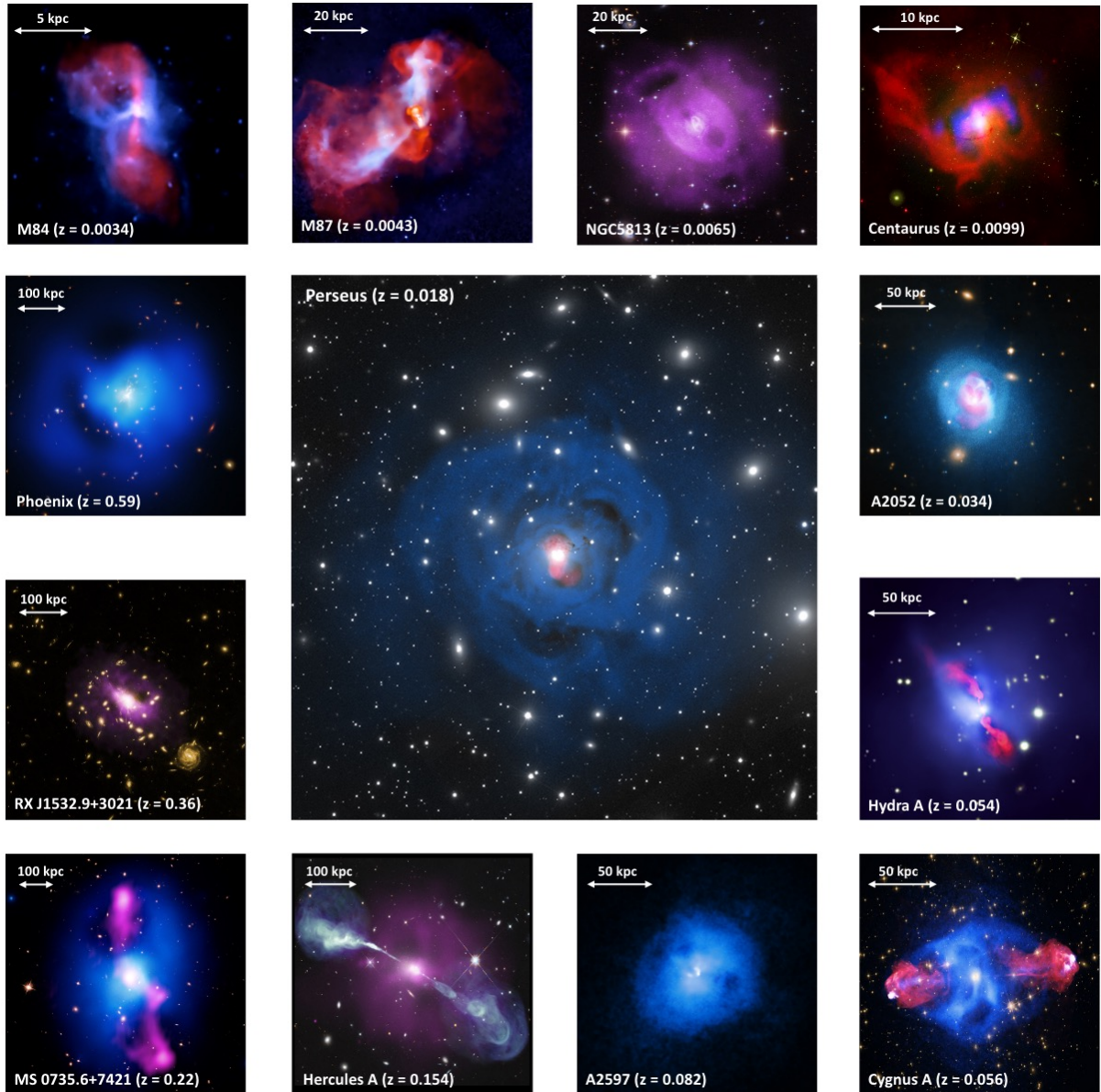


Figure 2.5: Observational collection of AGN feedback from jets. Adopted from Hlavacek-Larrondo et al. (2022).

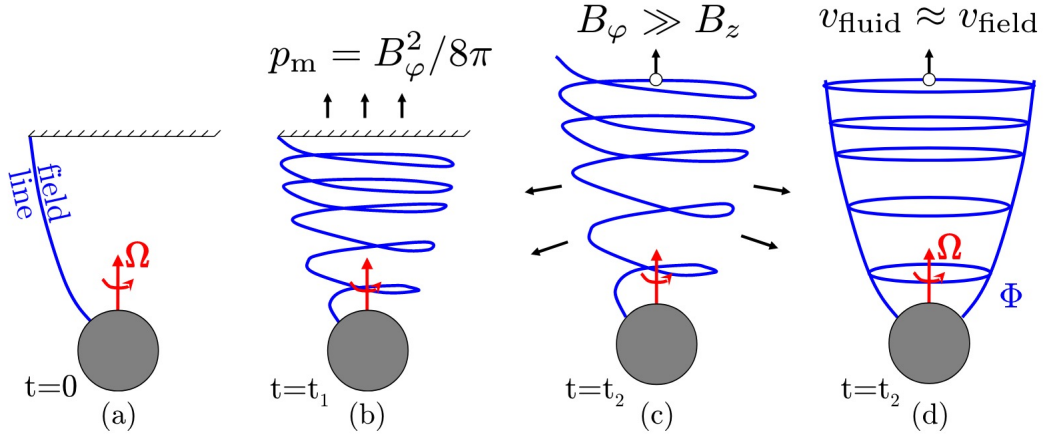


Figure 2.6: Schematic illustration of the process of jet generation. In this analogy, the BH is represented as a perfectly conducting sphere, whose surface rotates with an angular frequency Ω . Moreover, the field lines are anchored to a perfectly conducting "ceiling", representing the ambient medium. From Davis & Tchekhovskoy (2020).

2.2 The role of BH spin

2.2.1 Jet power and rotational energy extraction

It has been advocated that rotating BHs have to have a fundamental role in the formation of jets (Davis & Tchekhovskoy, 2020) and related feedback (McNamara & Nulsen, 2012). The spin J_{BH} of a BH with mass M_{BH} can range from zero to the maximal value $J_{\text{max}} = GM_{\text{BH}}^2/c$. Thus, a BH is characterised by the dimensionless spin parameter $a = J_{\text{BH}}/J_{\text{max}}$. A maximally spinning $10^9 M_{\odot}$ BH can potentially provide $\sim 10^{62}$ erg of rotational energy (McNamara & Nulsen, 2012) that could be injected into the surroundings and offset cooling, once a mechanism to extract this energy is in action. Theoretically, a viable mechanism has been suggested by Blandford & Znajek (1977) (see also Lasota et al., 2014). This process requires poloidal magnetic fields anchored to an accretion flow, surrounding a rotating BH. The accreting matter drags the poloidal field into the BH ergosphere (see Sec. 3.1.1), where the BH rotation twists the field lines, generates a toroidal component of the field (B_{ϕ} in Fig. 2.6) and exerts an effective pressure (p_m in Fig. 2.6); the pressure gradients in the propagation accelerate the plasma (see e.g. Tchekhovskoy, 2015). The power of the jet is therefore crucially dependent on the BH spin magnitude, which is responsible for the frame dragging, and the magnetic field flux threading the BH event horizon. The latter can be maximised in the so-called magnetically-arrested disc state. In this configuration, magnetic flux is accumulated near the event horizon, until it becomes dynamically relevant. In this state, the ratio between jet power and accretion power (i.e. $\eta = P_{\text{jet}}/(\dot{M}c^2)$) can be larger than one (Tchekhovskoy et al., 2011; McKinney et al., 2012; Narayan et al., 2022; Ricarte et al., 2023; Lowell et al., 2024). This is possible by extracting rotational energy from the BH. Launching powerful jets requires the presence of an accretion flow that acts as an anchor for the magnetic

field and drags it inwards. If a jet is created, it is possible to tap into the rotational energy of the BH. Conversely, it is possible to power an AGN by accretion alone (without extracting spin energy) but in this case, the maximum power output can only reach a few tens of percent of the accretion power.

Observationally, a connection between the BH spin and the jet power has been proposed to explain the observed radio-loudness (radio-to-optical flux density ratio, Sikora et al. 2007) in samples of AGN (e.g. Sikora et al., 2007; Martínez-Sansigre & Rawlings, 2011). Ghisellini et al. (2010) found that the power of the most powerful jets in their sample of blazars can exceed the luminosity of the accretion disc by a factor of approximately ten. They argued that the extraction of rotational energy may provide the additional power required. They also argued that if this is the case, the observed correlation between P_{jet} and accretion disc luminosity may arise from a link between the accretion and rotational energy extraction processes (as discussed above). The results published so far by the Event Horizon Telescope (EHT) collaboration have also favoured the extraction of rotational energy as a mechanism to efficiently produce jets (Event Horizon Telescope Collaboration et al., 2021, 2022). Furthermore, although instrumental capabilities have prevented a conclusive confirmation so far, future polarimetry measurements with EHT could provide more direct observational support for this process (Chael et al., 2023).

2.2.2 Jet direction

The direction of the BH spin plays a key role in jet formation. Spinning BHs create an outward Poynting flux in the direction of the BH spin, through the Blandford-Znajek mechanism (Hawley & Krolik, 2006; Nakamura et al., 2008). Several observations of nearby clusters exhibit the presence of multiple pairs of jet-inflated cavities (a few examples are visible in Fig. 2.5), that have distinct angular orientations relative to the central galaxy (e.g. Forman et al., 2007; David et al., 2009; Sanders et al., 2009; Fabian et al., 2011; Hlavacek-Larrondo et al., 2015). This suggests multiple generations of jets propagating along different directions. The observations may be interpreted as spin re-orientation, provided that processes close to the BH manage to modify the BH spin and thus the launching direction of the jet (e.g. accretion proceeding on different planes across subsequent events). A few numerical works have demonstrated that it is possible to recover the observed morphologies by assuming a re-orienting jet (Cielo et al., 2018; Horton et al., 2020; Lalakos et al., 2022).

Using general-relativistic magneto-hydrodynamic (GRMHD) simulations, McKinney et al. (2013) and Liska et al. (2018) demonstrated that thick accretion discs, tilted with respect to the BH spin axis, launch relativistic jets that are aligned with the latter in the innermost region, but as they propagate they re-align with the rotation axis of the disc at large radii. The thick disc undergoes precession as a whole due to Lense-Thirring precession (Fragile et al., 2007), and the jet precesses as a result. However, the disc-jet system ultimately approaches alignment with the BH spin (Liska et al., 2018).

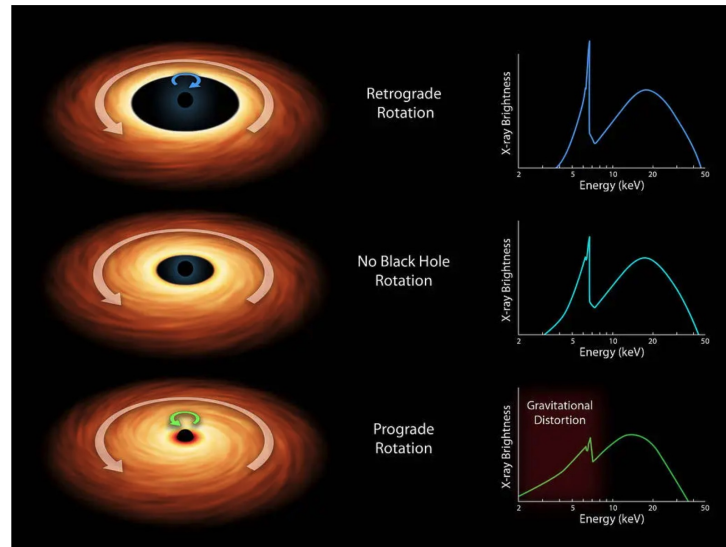


Figure 2.7: Inference of the BH spin from the observed shape of the Fe K lines in the spectra of AGN. Image credit: NASA/JPL-Caltech

2.2.3 Observational estimates of the BH spin

Observational estimates of the BH spin parameter are crucial to gain insight into its role, evolution and relation to the environment. Several methods have been adopted in literature to infer the BH spin of AGN. An extensive review of such methods is presented by Reynolds 2021. Most of the measurements published to date have been based on X-ray reflection spectroscopy based on Fe K lines. These are based on the modelling of the shape of the spectral feature associated with these transitions, taking into account relativistic beaming and gravitational redshift, which depend on the position within the accretion disc of the material responsible for the reflection component. The minimum radius of the accretion disc depends on the innermost stable circular orbit (ISCO), which in turn is determined by the spin parameter a (Ch. 3 for details). Therefore, the reflection feature changes depending on the ISCO and a , because the accretion disc material can reach further inwards. Fig. 2.7 illustrates this concept. Recent works have developed a new class of high-density disc models (Jiang et al., 2019, 2022), which have been used to estimate the spin in low-mass BHs by modelling the X-ray relativistic reflection continuum (Mallick et al., 2022). The observed jet powers can also be used to determine the spin (Daly, 2009, 2011, 2019, 2021). This method is particularly useful because it can be applied to large samples of AGN that exhibit jets. Lastly, interferometric observations with the EHT might provide constraints on the spin of M87*, from the circularity of the shadow (Broderick et al., 2022) or from the phase-twisting of light propagating near the BH (Tamburini et al., 2020) or from the linear polarisation pattern (Palumbo et al., 2020). The former method was only able to infer a clockwise rotation with the current observational capabilities (i.e. spin vector pointing away from Earth). The latter provided an estimate of $a = 0.90 \pm 0.05$ and an angle with respect to the line of sight $i = 163^\circ \pm 2^\circ$.

2.3 AGN in cosmological simulations

As mentioned in Sec. 2.1.1, the processes of BH accretion and feedback involve a dynamic range of approximately 10^{10} in spatial scales, from the $\sim 10^{-5}$ pc scales of the accretion disc to the $\sim 10^5$ pc of jet extent. Therefore they need to be included in cosmological simulations using sub-resolution models, because of limited resolution.

2.3.1 BHs treatment

Generally, BHs are included in cosmological simulations as collisionless particles, coupled to other particles only by gravity, that are able to increase their mass by accretion and mergers. The sub-resolution model for spin evolution described in Sec. 3.2, is built within the broader BH physics module originally described in Springel et al. (2005a), with modifications as in Hirschmann et al. (2014) and Steinborn et al. (2015). An SPH kernel is associated to every BH (with smoothing length h_{BH}) in a similar fashion as for the gas particles, with the same number of neighbours. The gravitational force on the BH is softened using a Plummer-equivalent softening length ε_{BH} . Its value is specific for each simulation presented in Ch. 4 and stated in the corresponding subsections as well as in Table 4.2.

The details of the formation of central massive BHs at early times ($z > 6$), that result in the observed population at redshift zero, are highly debated. A consensus has not been reached yet, although different scenarios have been proposed (see e.g. Volonteri, 2010, for a review). Therefore, in cosmological simulations, BHs are generally placed ("seeded") on haloes that satisfy chosen criteria. In the simulations presented in Ch. 4, to select haloes where to seed new BH particles, a FoF (*Friends-of-Friends*) algorithm is applied to the stellar particles alone. In this way, stellar bulges are identified. A linking length of $l = 0.05$ is adopted, and halos with a stellar mass corresponding to $M_{*,\text{seed}}$ are selected to host a new BH seed. It is also required that the halo has a stellar over dark matter (DM) mass fraction $f_* > 0.05$ and a gas over stellar mass fraction $f_{\text{gas}} > 0.1$, to ensure that the identified stellar bodies are newly forming galaxies and not tidally stripped stellar remains. The seeds are created as soon as a halo satisfies the requirements (at any redshift), at the position of the star particle with the largest binding energy within the group, with an initial mass $M_{\text{BH,seed}}$. The values of $M_{\text{BH,seed}}$ and $M_{*,\text{seed}}$ for each simulation are stated in the corresponding subsections and Table 4.2. Alternatively, BHs with specific properties can be inserted in the initial conditions (ICs) to study a specific configuration of an idealised system (e.g. Sec. 4.1.1 and 4.1.2).

Capturing correctly the dynamics of the BHs is also challenging in cosmological simulations. Some models adopt a scheme in which the BHs are dragged at each timestep towards the most gravitationally bound particle in the BH kernel (Schaye et al., 2015; Sijacki et al., 2015; Weinberger et al., 2017). However, the orbit is not physical and the velocity is ill-defined. Some models instead include some form of drag force onto the BHs, to account for the unresolved dynamical friction process (Hirschmann et al., 2014; Steinborn et al., 2015; Tremmel et al., 2015). In the simulations in Ch. 4, BHs are not pinned to the position of the potential minimum within h_{BH} . Besides, no drag force is applied from the continuous gas accretion onto the BH, whereas the position and velocity of the central BH are kept when BHs merge. Nonetheless, a

sufficient centring of BHs is achieved by 1) seeding the BHs on the star particle with the highest binding energy, which leads to an improved centring from the beginning (compared to seeding on the particle with the highest density as in e.g. Di Matteo et al. (2008)); 2) setting the dynamical mass² of the BH sink particle to the mass of a dark matter particle, mitigating artificial two-body scattering; 3) BHs are seeded only in galaxies which are resolved by a number of star particles of the order of thousands. BHs are allowed to merge if the following criteria are met: (i) their relative velocity is smaller than $0.5c_s$, where c_s is the sound speed of the gas, averaged in a kernel-weighted fashion; (ii) their distance is smaller than 5 times ε_{BH} ; (iii) the binary binding energy is smaller than $0.5c_s^2$ (see Hirschmann et al., 2014, for further details).

Besides mergers, BHs also increase their mass by accreting gas. A full treatment of accretion onto BHs would require resolving gas inflow from galaxy-scale down to the event horizon of the BH, at milliparsec scales. However, this is not feasible in cosmological simulations, reaching hundreds of parsecs at best (see Sec. 1.2.3). To circumvent this issue, an estimate of the accretion rate onto the BH is obtained using an analytical formulation, based on quantities that are resolved in the simulation. In the BH model adopted for Ch. 4, the mass inflow rate onto the BH is computed using the Bondi–Hoyle–Lyttleton prescription (hereafter Bondi; Hoyle & Lyttleton, 1939; Bondi & Hoyle, 1944; Bondi, 1952):

$$\dot{M}_{\text{B}} = \frac{4\pi\alpha_{\text{acc}}G^2M_{\text{BH}}^2\langle\rho\rangle}{(\langle c_s \rangle^2 + \langle v \rangle^2)^{3/2}}, \quad (2.2)$$

where ρ is the gas density, v is the velocity of the BH with respect to the gas and G is the gravitational constant. The properties marked with $\langle \cdot \rangle$ are computed as a kernel-weighted average over the BH neighbouring particles. A maximum radius on h_{BH} is also enforced for the computation, $r_{\text{acc}} = 100$ kpc. α_{acc} is a dimensionless parameter that is often adopted to account for the detailed structure of the interstellar medium (ISM) in the vicinity of the BH (e.g. Springel & Hernquist 2003; Booth & Schaye 2009; but see e.g. Valentini et al. 2020), typically unresolved in cosmological simulations because of the limited spatial resolution (\sim kpc). In Ch. 4, two different Bondi rates are computed (motivated by e.g. Gaspari et al. 2013, as thoroughly discussed in Steinborn et al. 2015), using $\alpha_{\text{acc,hot}} = 10$ and $\alpha_{\text{acc,cold}} = 100$ (unless stated otherwise) for the hot and cold gas phases³ respectively. The accretion rate onto the BH is given by

$$\dot{M}_{\text{BH}} = \min(\dot{M}_{\text{B,hot}} + \dot{M}_{\text{B,cold}}, \dot{M}_{\text{Edd}}) \quad (2.3)$$

where $\dot{M}_{\text{Edd}} = 4\pi GM_{\text{BH}}m_{\text{p}}/(\sigma_{\text{T}}\epsilon_{\text{r}}c)$ is the Eddington (1916) accretion rate, m_{p} the proton mass, σ_{T} the Thomson cross section, c the speed of light and ϵ_{r} the radiative efficiency. The latter depends on the BH dimensionless spin parameter in our simulations, as explained in Sec. 3.2.1.

²In our code BHs are characterised by two masses, a dynamical mass used to compute gravitational interactions and a physical mass used in all the BH sub-resolution models.

³The hot phase is composed by particles with a temperature $T > 2 \times 10^5$ K. The cold phase is composed of star-forming particles (see Sec. 4.1) and gas particles that have a temperature $T < 2 \times 10^5$ K.

2.3.2 AGN feedback

In cosmological simulations, AGN feedback is implemented by prescriptions that are aimed at mimicking in an effective way the channels with which SMBHs affect their surroundings, namely by including the effects associated with radiation and quasar-mode feedback (Sec. 2.1.2) or with the presence of jets and maintenance-mode feedback (Sec. 2.1.3). Although AGN feedback is a complex, multiscale problem, and in principle, several physical processes should be taken into account (such as magnetic fields, radiative transfer, cosmic rays, etc.), it is usually modelled by injecting either thermal energy, kinetic energy, momentum, or a combination of them in the surrounding of the BH, due to resolution limitations.

In the model by Springel et al. (2005b) and Di Matteo et al. (2005), pure thermal energy is injected in the neighbouring region of the BH in an isotropic fashion. The accretion rate is obtained by the Bondi formula (Eq. 2.2), and the rate of energy injection is

$$\dot{E} = \epsilon_f \epsilon_r \dot{M}_{\text{BH}} c^2, \quad (2.4)$$

where ϵ_r is the radiative efficiency and ϵ_f is the efficiency with which the energy radiated from the BH is coupled to the ISM (Springel et al., 2005a; Booth & Schaye, 2009). A single thermal channel is also the prescription adopted in the EAGLE simulation (Schaye et al., 2015) and in the reference model of the FLAMINGO simulation (Schaye et al., 2023). In the Illustris simulation (Sijacki et al., 2015), two modes of AGN feedback are introduced, to mimic the quasar mode at high Eddington ratios ($f_{\text{Edd}} = \dot{M}/\dot{M}_{\text{Edd}} > 0.05$), and the maintenance mode (i.e. aimed at modelling the effect of relativistic jets propagating in the ICM) at low Eddington ratios. In the "radio" mode the energy is injected in symmetric bubbles at 100 kpc from the BH, in a random direction. In Illustris-TNG and Millennium-TNG (Weinberger et al., 2018; Pakmor et al., 2022), the transition f_{Edd} is made BH mass-dependent, and the low-accretion-rates channel is implemented as kinetic energy injection in a random direction, isotropic on average. In Horizon-AGN (Dubois et al., 2016), a thermal energy injection channel is active at $f_{\text{Edd}} < 0.01$, while at high f_{Edd} feedback is exerted through mass, momentum and kinetic energy injection in a cylinder centred on the BH, to mimic a bipolar jet.

In the Magneticum simulation model (Hirschmann et al., 2014), two separate feedback channels are adopted, in which feedback is always exerted by injecting thermal energy. However, feedback is made 4 times more efficient at $f_{\text{Edd}} < 0.01$, such that the total heating efficiency of the ICM amounts to 0.1, as suggested by Churazov et al. (2005). Improving upon this model, Steinborn et al. (2015) developed a prescription where the AGN feedback energy is split into two separate contributions, based on Churazov et al. (2005), who argue that at low accretion rates most of the accretion power is used to generate an outflow, with high coupling efficiency, while at high accretion rates the outflow power decreases and the accretion power is released into radiation, with relatively low coupling efficiency. This is formulated in terms of efficiencies, such that

$$\dot{E} = (\epsilon_o + \epsilon_f \epsilon_r) \dot{M}_{\text{BH}} c^2, \quad (2.5)$$

where ϵ_o and ϵ_r are the outflow and radiative efficiencies respectively, and ϵ_f is the coupling efficiency of the radiation to the ISM. These efficiencies depend on f_{Edd} and on M_{BH} (see Eq. 19

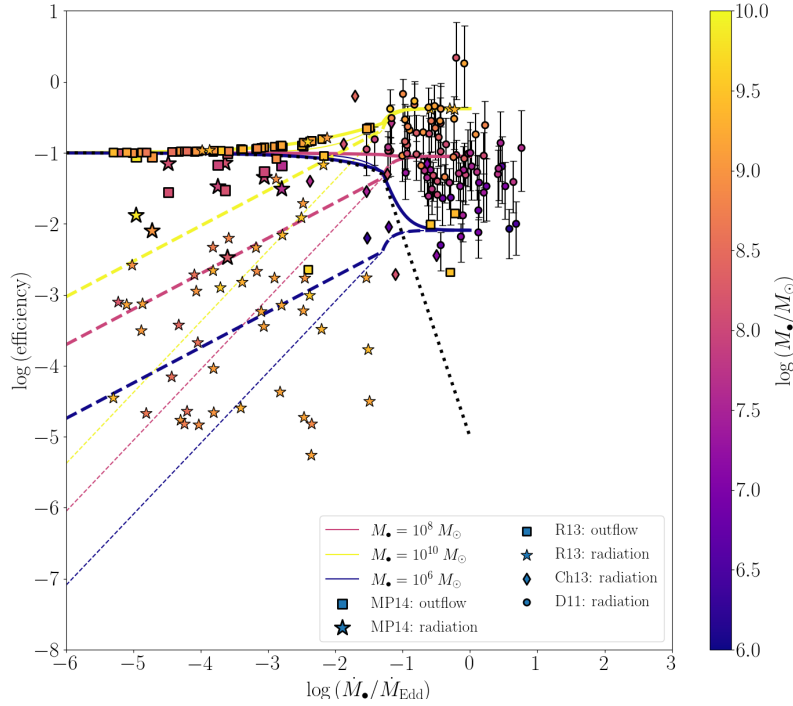


Figure 2.8: Efficiencies model adopted in Steinborn et al. (2015).

and 20 in Steinborn et al. 2015)

$$\epsilon_{r,o} = \epsilon_{r,o}(f_{\text{Edd}}, M_{\text{BH}}). \quad (2.6)$$

and calibrated against observations, as shown in Fig. 2.8. At $f_{\text{Edd}} < 0.05$, the total efficiency is set to 0.1, and the radiative efficiency (dashed lines) is low. Above the threshold, the outflow efficiency (dotted lines) decreases, and the radiative efficiency is high. Moreover, higher BH masses correspond to higher efficiencies.

2.3.3 An empirically-motivated model for AGN feedback efficiency

Before including a physically-motivated prescription for spin evolution, in which the radiative efficiency varies self-consistently in the sub-resolution model (see Ch. 3), I developed an empirically-motivated prescription to determine the radiative efficiency, building upon the model by Steinborn et al. (2015). In this model, the radiative efficiency is parametrised as

$$\epsilon_r = \epsilon_r(\dot{M}_{\text{BH}}, M_{\text{BH}}) = A \dot{M}_{\text{BH}}^\alpha M_{\text{BH}}^\beta, \quad (2.7)$$

namely, the efficiency depends on the *physical* accretion rate \dot{M}_{BH} . A , α and β are parameters constrained using the observational catalogue adopted by Steinborn et al. (2015) (data from Davis & Laor, 2011; Chelouche, 2013; Russell et al., 2013; Mezcua & Prieto, 2014), merged with the database by Liu et al. (2021). The latter database extends in particular the range of measured accretion rates to the super-Eddington regime. In the analysis, the subset of observations that

allows two independent estimates of the accretion rate and the bolometric luminosity L_{bol} were considered, namely Davis & Laor (2011), Chelouche (2013) and Liu et al. (2021). For this subset of the observations, however, only the radiative component of the feedback energy is available, therefore a separate outflow feedback channel is not included. From the independent values of L_{bol} and \dot{M}_{BH} provided in the aforementioned datasets, the efficiency is obtained using $\epsilon_r = L_{\text{bol}}/(\dot{M}_{\text{BH}}c^2)$. The dataset and the power-law fit to the data are shown in Figure 2.9. Note that we also cap the efficiency to a maximum of 0.42, which is the theoretical limit imposed by maximally spinning BHs.

The choice of \dot{M}_{BH} , physical accretion rate, as independent quantity instead of the dimensionless Eddington ratio $f_{\text{Edd}} \equiv \dot{M}_{\text{BH}}/\dot{M}_{\text{Edd}}$ is motivated by two reasons. The first is that \dot{M}_{BH} is directly available in the simulations, without any a priori assumption on the efficiency. In addition, care needs to be taken when inferring $\dot{M}_{\text{BH}}/\dot{M}_{\text{Edd}}$ from the observed $L_{\text{bol}}/L_{\text{Edd}}$. If

$$L_{\text{Edd}} \equiv \epsilon_{\text{Edd}}\dot{M}_{\text{BH}}c^2, \quad (2.8)$$

then $\dot{M}_{\text{BH}}/\dot{M}_{\text{Edd}} \equiv L_{\text{bol}}/L_{\text{Edd}}$ only under the assumption that $\epsilon_{\text{Edd}} \equiv \epsilon_r$, at all accretion rates. The Eddington luminosity L_{Edd} is defined as

$$L_{\text{Edd}} = 4\pi Gm_p c M_\bullet / \sigma_T. \quad (2.9)$$

However, with this assumption, effects like e.g. radiation trapping could lead to infer from $L_{\text{bol}}/L_{\text{Edd}}$ a lower value for $\dot{M}_{\text{BH}}/\dot{M}_{\text{Edd}}$ than the actual one. Indeed, if $\epsilon_r < \epsilon_{\text{Edd}}$, an observed $L_{\text{bol}}/L_{\text{Edd}}$ should correspond to a higher actual value of f_{Edd} :

$$f_{\text{Edd}} = \frac{\dot{M}_{\text{BH}}}{\dot{M}_{\text{Edd}}} = \frac{L_{\text{bol}}}{L_{\text{Edd}}} \frac{\epsilon_{\text{Edd}}}{\epsilon_r}. \quad (2.10)$$

Using directly \dot{M}_{BH} removes this ambiguity and avoids the circular dependence that arises if ϵ_r is made dependent on an f_{Edd} that is itself dependent on ϵ_r . Moreover, the new formulation allows us to test the model without limiting the accretion rate in terms of the Eddington ratio with a fixed assumed radiative efficiency. Conversely, the physical accretion rate is capped to a value determined by the maximum extent in accretion rates reached by the observed sample, namely $50 M_\odot/\text{yr}$.

The model was tested with our fiducial prescription for AGN feedback (i.e. Hirschmann et al., 2014) and without the spin evolution model, on the cosmological volume with $L_{\text{box}} = 48 h^{-1} \text{ cMpc}$ of the Magneticum⁴ simulations suite. It assumes a flat ΛCDM model, with $\Omega_m = 0.272$, $\Omega_b = 0.0456$ and $h = 0.704$, $n = 0.963$ and $\sigma_8 = 0.809$. It also assumes the following parameters: $\epsilon_f = 0.0775$; $M_{\text{BH,seed}} = 4 \times 10^5 M_\odot/h$; $M_{*,\text{seed}} = 1.6 \times 10^{10} M_\odot/h$; DM particle mass $m_{\text{DM}} = 6.9 \times 10^8 M_\odot/h$; initial gas particle mass $m_g = 1.4 \times 10^8 M_\odot/h$; star particle mass $m_* = 3.5 \times 10^7 M_\odot/h$; $\epsilon_{\text{DM}} = 3.75 \text{ kpc/h}$, $\epsilon_g = 3.75 \text{ kpc/h}$, and $\epsilon_* = 2 \text{ kpc/h}$ for the DM, gas, and stellar and BH softening lengths, respectively.

In this test, the BH physical accretion rates are naturally always below $50 M_\odot/\text{yr}$. Fig. 2.10 shows the entire set of BHs at $z = 0$ within the BH mass-stellar mass ($M_{\text{BH}} - M_*$) plane. Each BH

⁴<http://www.magneticum.org>

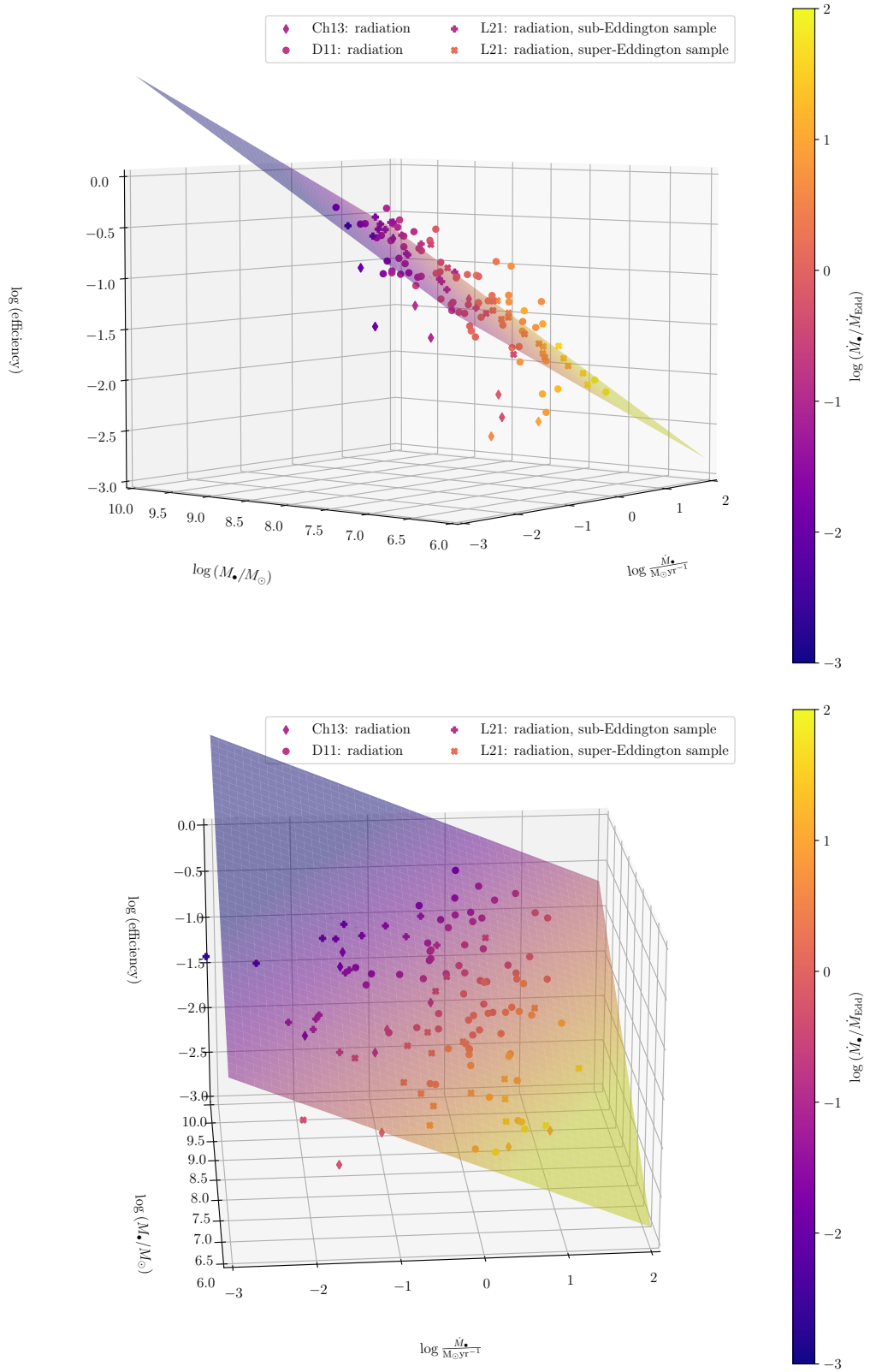


Figure 2.9: Dataset for the new efficiency prescription, with the power-law fit superimposed to the data.

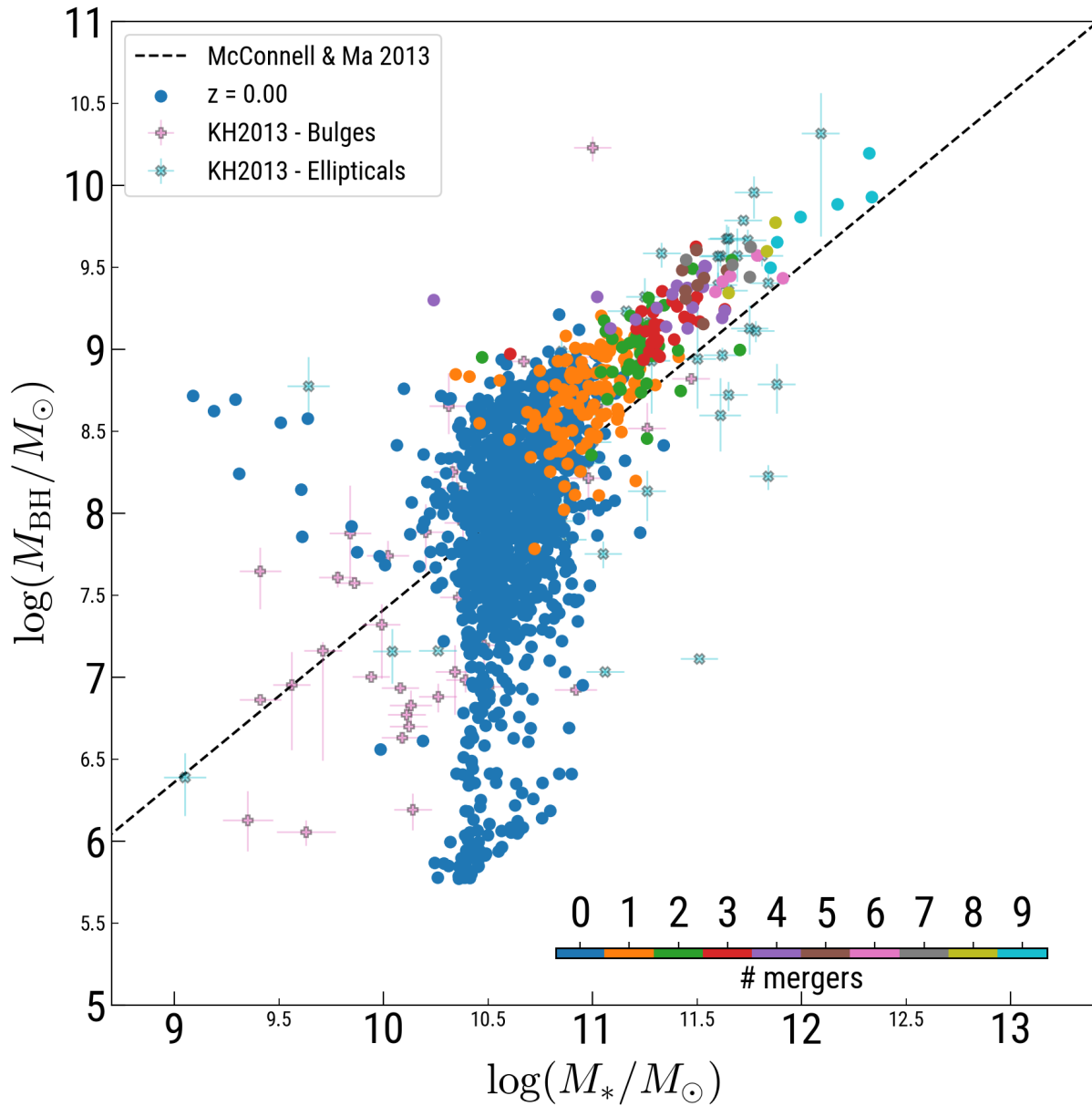


Figure 2.10: M_{BH} as a function of stellar mass M_{*} , at $z = 0$, for the BH sample in the simulation using the empirically-motivated model for efficiencies. Each point is colour-coded according to the number of mergers of the BH (including their progenitors). The dashed line shows the experimental fit by McConnell & Ma (2013), while crosses with associated uncertainties show data from Kormendy & Ho (2013).

is associated to a subhalo identified with the sub-structure finder algorithm SUBFIND (Springel et al., 2001a; Dolag et al., 2009) based on particle ID matching. Whenever more than one BH is associated to the same subhalo, the closest to the subhalo centre is chosen. M_* is the stellar mass as computed by SUBFIND. The dashed line shows the experimental fit by McConnell & Ma (2013), while crosses with associated uncertainties show observations from Kormendy & Ho (2013). The model broadly reproduces the observed BH mass-stellar mass relation, although it is systematically above the observed fit by McConnell & Ma (2013).

The model includes new and updated observational constraints on the efficiencies, but the underlying sub-resolution description of accretion is analogous to previous models. In the next Chapter, I present the model for BH spin evolution, that enables a self-consistent variability of the radiative efficiency.

3 | Black hole spin evolution

Part of the content of this Chapter has been published in Sala et al. (2023):

Luca Sala, Milena Valentini, Veronica Biffi, Klaus Dolag:
Supermassive black hole spin evolution in cosmological simulations with OPENGADGET3
accepted for publication in *Astronomy & Astrophysics*

Black hole spins evolve across cosmic time due to accretion and mergers. From the theoretical standpoint, several analytical studies have been focussed on investigating the mechanism driving spin evolution that is linked to the coupling between the accretion disc and the BH spin (Bardeen, 1970; Pringle, 1981; Scheuer & Feiler, 1996; Natarajan & Pringle, 1998; Natarajan & Armitage, 1999; King et al., 2005; Martin et al., 2007; Perego et al., 2009). If a geometrically thin, optically thick disc is misaligned with respect to the BH spin rotation axis, the innermost part aligns with the BH spin and is connected to the unperturbed outermost part through a smooth warp (Bardeen-Petterson effect). The flow through this region exerts a torque on the BH spin, modifying its direction. Recently, full GRMHD simulations performed by Liska et al. (2019b) were able to reproduce this effect in magnetised thin discs.

Further works have focussed on building upon the analytical theory to understand the evolution of BH spin as a response to accretion and mergers, as well as the relative contribution between the two channels. A number of works adopted a semi-analytical treatment in a hierarchical cosmological context, with various recipes for the drivers of gas accretion and its effect on spin evolution (Volonteri et al., 2005; Berti & Volonteri, 2008; Lagos et al., 2009; Fanidakis et al., 2011; Izquierdo-Villalba et al., 2020; Sesana et al., 2014; Griffin et al., 2020). Other studies focused on simulating evolutionary histories of BHs under the assumption of a fixed fuelling angular momentum distribution and analysed how it affects the distribution of BH spins (Volonteri et al., 2007; King et al., 2008; Dotti et al., 2013; Zhang & Lu, 2019). Going a step further, some works developed models suitable to be used on the fly in hydrodynamical simulations (Maio et al., 2013; Fiacconi et al., 2018), to study isolated systems at high resolution. The model by Fiacconi et al. (2018) was also coupled to novel feedback recipes for winds (Cenci et al., 2020; Sala et al., 2020) and jets (Talbot et al., 2021). Recently, using the same model, Bollati et al. (2023) studied the dynamics of massive BH binaries in the presence of spin-dependent radiative feedback, whereas Talbot et al. (2023) focused on the effect of jets in gas-rich galaxy mergers. While all of the above-mentioned works assumed a thin accretion disc, Huško et al. (2022) developed a spin evolution model that assumes a thick disc and applied it to study jet feedback in galaxy clusters. Dubois et al. (2014a) made a further step forward and developed a model suited to cosmological,

hydrodynamical simulations, built upon the work of Volonteri et al. (2007) and King et al. (2005, 2008). The model was used to perform zoom-in simulations (Dubois et al., 2014a) and later updated to include jets, with a BH spin-dependent direction and power (Beckmann et al., 2019; Dubois et al., 2021; Dong-Páez et al., 2023; Massonneau et al., 2023a; Koudmani et al., 2023; Peirani et al., 2024).

Comparatively fewer works have been dedicated to the study of spin evolution in a cosmological box and have used a large statistical sample of BHs. Dubois et al. (2014b) ran their spin evolution model, although only in post-processing, on the output of the HORIZON-AGN simulation. Bustamante & Springel (2019) performed a set of simulations of a cosmological volume, evolving the spin on the fly with a similar model, although with a few differences at the sub-resolution level with respect to our implementation (see Sec. 3.2.1 and 5.4).

In this work, we focus on studying SMBH spin evolution with a sub-resolution model that follows the latter two works. In this Chapter I will revise a few key concepts of accretion theory, necessary for the spin evolution model, and will describe its implementation in `OPENGADGET3`.

3.1 Theoretical background

In this Section I will review the underlying theoretical concepts concerning accretion disc theory, at the basis of my spin evolution model.

3.1.1 The BH metric

From the theoretical point of view, a BH is a solution of Einstein's field equations presenting a singularity in the metric tensor that is not possible to eliminate by a change of coordinates. This is signalled in the theory by the presence of a mathematical singularity in, for example, a diverging scalar quantity that is invariant under a coordinate transformation. The first solution was found by Karl Schwarzschild, in 1916, and describes the stationary, isotropic metric tensor produced by a point mass in empty space. By appropriately taking advantage of the symmetries of the system, it is possible to derive from the field equations the metric $g_{\mu\nu}$, such that the line element ds^2 reads

$$ds^2 = g_{\mu\nu} dx^\mu dx^\nu = - \left(1 - \frac{R_{\text{BH}}}{R} \right) dt^2 + \frac{1}{1 - \frac{R_{\text{BH}}}{R}} dR^2 + R^2 (d\theta^2 + \sin^2 \theta d\phi^2), \quad (3.1)$$

where the spatial part is expressed in polar coordinates (R, θ, ϕ) (where capital R indicates dimensional units), and the *Schwarzschild radius* is defined as $R_{\text{BH}} = \frac{2GM}{c^2}$. Note that formally the components of the metric have a singularity at $R = R_{\text{BH}}$ and $R = 0$. However, the former is not physical because it can be removed by an appropriate coordinate change. The surface at $R = R_{\text{BH}}$ is also referred to as *event horizon*. An invariant quantity such as the Kretschmann scalar allows us to identify the true physical singularities. For a Schwarzschild BH it takes the form (e.g. D'Inverno, 1992)

$$K = \frac{48G^2 M^2}{c^4 R^6} = \frac{12R_{\text{BH}}^2}{R^6}. \quad (3.2)$$

The invariant is singular only at $r = 0$, that is indeed the unique point in space where the metric is singular regardless of the coordinate system.

There are other BH solutions to Einstein's field equation, and according to the no-hair theorem, the most general BH is completely characterised by three parameters: mass, angular momentum and electric charge. Despite being a solution of the field equations of general relativity coupled to electromagnetism, electrically charged BHs would rapidly attract an opposite charge until they reach neutrality. Therefore, they are not believed to be astrophysically relevant Cardoso et al. (2016). On the other hand, most astronomical objects have at least some angular momentum. Moreover, stellar-mass BHs are formed as the final stage of the evolutions of stars, which are generally rotating. For angular momentum conservation, it is plausible to expect BHs to spin at formation. Moreover, as discussed in Chap. 2, there is compelling evidence that rotating SMBHs are required to account for specific features in the spectra of AGN, as well as to explain the production of powerful jets. Therefore, BHs with angular momentum are astrophysically relevant; astrophysical BHs are usually referred to as BHs defined by two parameters, spin and mass.

I will now revise a few properties of the solution for an uncharged BH with angular momentum, that was found by Roy Kerr, in 1963. The metric is axisymmetric, and it has two free parameters, M and $\tilde{a} = J/M$, corresponding to the mass and angular momentum per unit mass, respectively (where we assumed geometrised units – i.e. $G = c = 1$ – for simplicity). The Boyer–Lindquist coordinates are a possible (but not unique) choice to represent the metric of this spacetime (Boyer & Lindquist, 1967). The spatial part of the spacetime, in this case, is described by oblate spheroidal coordinates (r, θ, ϕ) (where r is in geometrised units), which relate to the common cartesian coordinate as:

$$x = \sqrt{r^2 + \tilde{a}^2} \sin \theta \cos \phi \quad (3.3)$$

$$y = \sqrt{r^2 + \tilde{a}^2} \sin \theta \sin \phi \quad (3.4)$$

$$z = r \cos \theta. \quad (3.5)$$

In this coordinate system, the metric takes the form (e.g. Enderlein, 1997)

$$ds^2 = -\frac{\Delta}{\rho^2} \left(dt - \tilde{a} \sin^2 \theta d\phi \right)^2 + \frac{\sin^2 \theta}{\rho^2} \left(\left(r^2 + \tilde{a}^2 \right) d\phi - \tilde{a} dt \right)^2 + \frac{\rho^2}{\Delta} dr^2 + \rho^2 d\theta^2, \quad (3.6)$$

where

$$\Delta = r^2 + \tilde{a}^2 - 2Mr \quad (3.7)$$

$$\rho^2 = r^2 + \tilde{a}^2 \cos^2 \theta \quad (3.8)$$

The metric is not static (the off-diagonal elements in t, ϕ are non-zero), but does not depend explicitly on the time, therefore it is said to be stationary. Moreover, it is possible to identify a few interesting surfaces, that are presented in Fig. 3.1. The metric is singular for $\Delta = 0$. The solution for this equation is the locus $r = 0$ and $\theta = \pi/2$, that according to Eq. 3.5 corresponds to

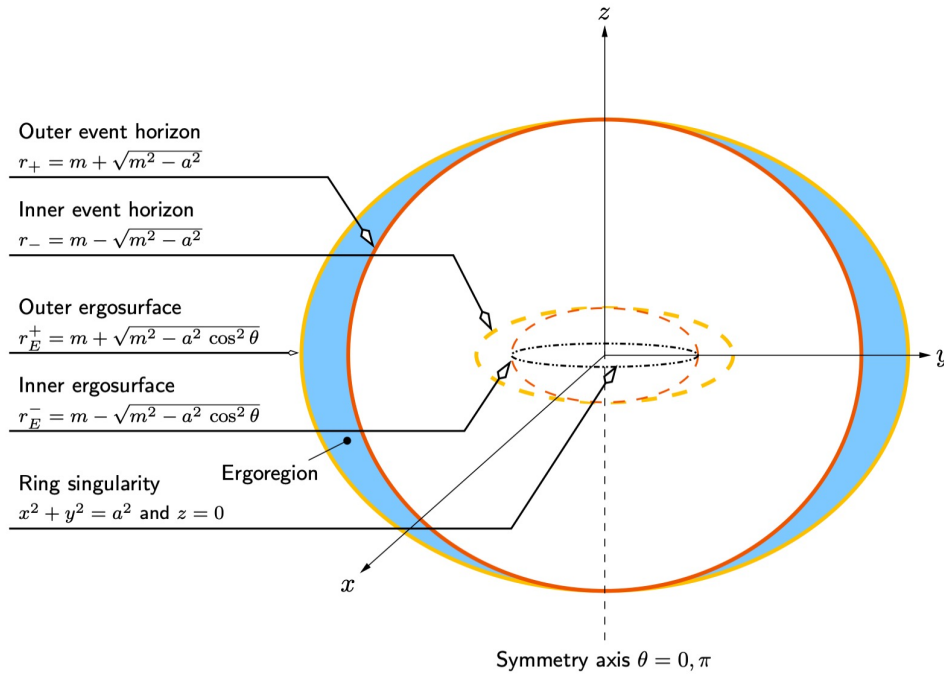


Figure 3.1: Horizons and ergosurfaces of a rotating BH, in the Boyer–Lindquist coordinates. From Visser (2008).

the ring $x^2 + y^2 = \tilde{a}^2$ and $z = 0$. It can be shown that this is a physical singularity. Furthermore, $\rho^2 = 0$ implies two event horizons at

$$r_{\pm} = m \pm \sqrt{m^2 - \tilde{a}^2}. \quad (3.9)$$

A rotating BH presents an additional feature with respect to a Schwarzschild one, named the ergosphere. It is the region of space enclosed between the surfaces at r_E^- and r_E^+ in Fig. 3.1. An object located inside the ergosphere cannot appear stationary from the perspective of an external observer positioned far away (Visser, 2008). The term ergosphere (from the Greek "érgon", "work") was adopted because particles with specific trajectories and crossing r_E^+ could in principle make it possible to extract rotational energy from the BH (Shapiro & Teukolsky, 1983). Finally, as mentioned in Visser (2008), the inner horizon r_- and the inner ergosurface r_E^- should not be physically trusted.

3.1.2 Circular orbits and ISCO

The equations of motion of a particle (massive or mass-less) can be derived from the BH metric. In this section I will restrict my discussion to massive particles, relevant to understand the dynamics of gaseous accretion discs. By analysing the conserved quantities that arise naturally from the symmetries of the metric it is possible to distinguish some qualitatively different types of orbits. For the Schwarzschild solution, these conserved quantities are the energy (per unit

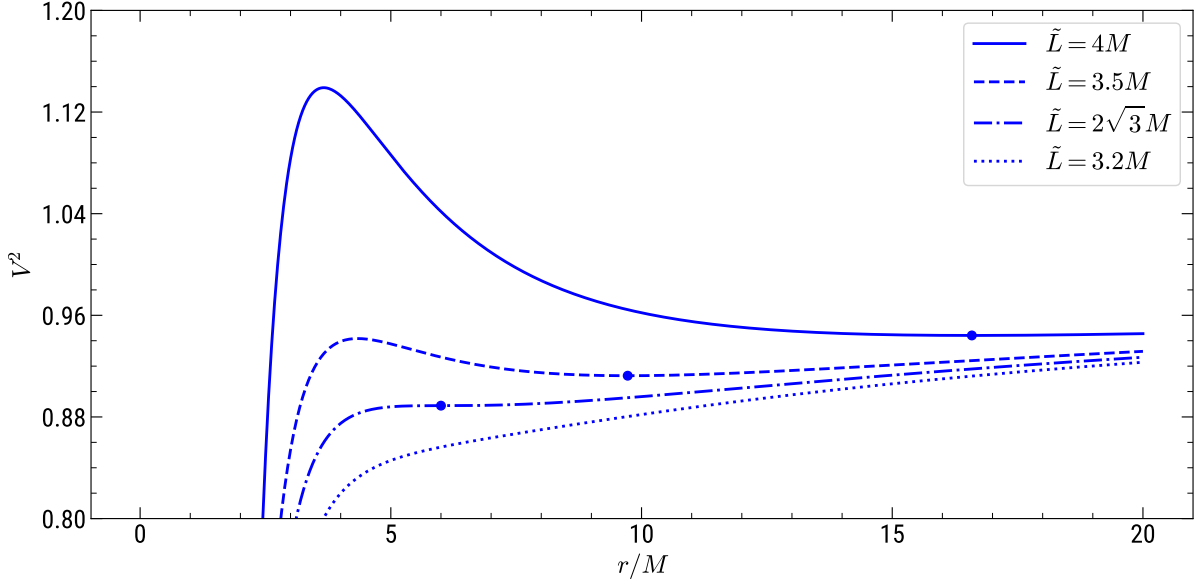


Figure 3.2: Effective potential for a Schwarzschild BH. Each curve shows the potential for a different value of \tilde{L} .

mass) $\tilde{E} = E/m$ and the angular momentum (per unit mass) $\tilde{L} = L/m$. The equations of motion are (Shapiro & Teukolsky, 1983)

$$\left(\frac{dr}{d\tau}\right)^2 = \tilde{E}^2 - \left(1 - \frac{2M}{r}\right) \left(1 + \frac{\tilde{L}^2}{r^2}\right) \quad (3.10)$$

$$\frac{d\phi}{d\tau} = \frac{\tilde{L}}{r^2} \quad (3.11)$$

$$\frac{dt}{d\tau} = \frac{\tilde{E}}{1 - \frac{2M}{r}}. \quad (3.12)$$

where τ is the proper time and the convention of $G = c = 1$ is applied for convenience. This set of equations in principle allows us to integrate the specific trajectories with appropriate initial conditions. However, more intuitive insights are drawn by defining the effective potential

$$\tilde{V}^2(r) = \left(1 - \frac{2M}{r}\right) \left(1 + \frac{\tilde{L}^2}{r^2}\right), \quad (3.13)$$

illustrated in Fig. 3.2. A test particle with $\tilde{E}^2 > \tilde{V}_{max}^2$ is inevitably captured by the BH. A particle with $1 < \tilde{E}^2 < \tilde{V}_{max}^2$ undergoes a hyperbolic orbit, while one with $\tilde{E}^2 = 1$ undergoes a parabolic orbit. If $\tilde{V}_{min}^2 < \tilde{E}^2 < 1$ the orbit is bound. Finally, $\tilde{E}^2 = \tilde{V}_{min}^2$ corresponds to a circular orbit.

The extremal points of the potential, defining the circular orbits, are

$$r_{\pm} = \frac{\tilde{L}^2}{2M} \left[1 \pm \sqrt{1 - \frac{12M^2}{\tilde{L}^2}} \right]. \quad (3.14)$$

Eq. 3.14 highlights that a potential minimum (marked by the point in Fig. 3.2) exists only for $\tilde{L} > \tilde{L}_{ISCO} = 2\sqrt{3}M$. Below this value, it is not possible to find a stable circular orbit, i.e. a particle with such an angular momentum will plunge into the BH on a very short timescale. Now, if the BH is accreting from an accretion disc, the gas undergoes radial infall in subsequent circular orbits because of some form of viscosity (as I will discuss in Sec. 3.1.3), dissipating energy in the process. The energy released in the process is, effectively, the binding energy at the ISCO. For a circular orbit $dr/d\tau = 0$, so $\tilde{E}^2 = \tilde{V}^2$. By evaluating Eq. 3.13 for $r_{ISCO}(L_{ISCO}) = 6M$, we obtain $\tilde{E}_{ISCO}^2 = 8/9$ and therefore an accretion efficiency

$$\epsilon_r = 1 - \tilde{E}_{ISCO} = 1 - \sqrt{\frac{8}{9}} \sim 5.7\% \quad (3.15)$$

A similar analysis for the Kerr metric leads to analogous integrals and equations of motion, as well as expressions for the circular energy and angular momentum, with the key difference that they depend on \tilde{a} and M (Shapiro & Teukolsky, 1983):

$$\left(\frac{dr}{d\tau}\right)^2 = \frac{1}{r^3} R(\tilde{E}, \tilde{L}, r, \tilde{a}) \quad (3.16)$$

where

$$R = \tilde{E}^2 (r^3 + \tilde{a}^2 r + 2Ma^2) - 4aM\tilde{E}\tilde{L} - (r - 2M)\tilde{L}^2 - m^2 r \Delta, \quad (3.17)$$

and

$$\begin{aligned} \tilde{E} &= \frac{r^2 - 2Mr \pm \tilde{a}\sqrt{Mr}}{r (r^2 - 3Mr \pm 2\tilde{a}\sqrt{Mr})^{1/2}}, \\ \tilde{L} &= \pm \frac{\sqrt{Mr} (r^2 \mp 2\tilde{a}\sqrt{Mr} + \tilde{a}^2)}{r (r^2 - 3Mr \pm 2\tilde{a}\sqrt{Mr})^{1/2}}. \end{aligned} \quad (3.18)$$

The minimum of the potential must satisfy

$$1 - \tilde{E}^2 = \frac{2M}{3r} \quad (3.19)$$

which combined with Eq. 3.18 leads to the expression of r_{ISCO} for a rotating BH (Bardeen et al., 1972). In physical units, it reads

$$r_{ISCO} = R_{ISCO}/R_g = (3 + Z_2 \pm [(3 - Z_1)(3 + Z_1 + 2Z_2)]^{1/2}), \quad (3.20)$$

where the positive (negative) sign is for counter(co)-rotating orbits and $R_g = R_{BH}/2 = GM_{BH}/c^2$ is the gravitational radius. Z_1 and Z_2 are defined as:

$$Z_1 = 1 + \left(1 - \frac{\tilde{a}^2}{M^2}\right)^{1/3} \left[\left(1 + \frac{\tilde{a}}{M}\right)^{1/3} + \left(1 - \frac{\tilde{a}}{M}\right)^{1/3} \right], \quad (3.21)$$

$$Z_2 = \left(3 \frac{\tilde{a}^2}{M^2} + Z_1^2 \right)^{1/2}. \quad (3.22)$$

The radiative efficiency is $\epsilon_r = 1 - \tilde{E}(r_{\text{ISCO}})$, computed by combining Eq. 3.18 and Eq. 3.19

$$\epsilon_r = 1 - \sqrt{1 - \frac{2}{3r_{\text{ISCO}}}}. \quad (3.23)$$

Note that in this Section \tilde{a} represents the *angular momentum per unit mass* in geometrised units ($G = c = 1$). \tilde{a} varies from 0 to M . Alternatively, a *dimensionless spin parameter* $a = J/(GM^2/c)$ can be defined. This is also the choice adopted in Sec. 3.2. The equations above are equivalent, after the substitution $\tilde{a} = aM$.

3.1.3 Accretion flows

As we have seen in Ch. 2, observations strongly support the idea that accretion onto the central SMBH is the only process efficient enough to account for the large energy release occurring in AGN. The theory of accretion physics is vast, thus in what follows I will summarise selected topics of the background theory for the specific case of AGN, relevant to my work, referring often to Frank et al. (2002), Yuan & Narayan (2014) and Armitage (2022).

There is convincing evidence (see Ch. 2) that the engine that powers AGN is an accretion disc, where gas orbits the central SMBH in an axisymmetrical configuration. However, for the gas to flow towards the BH in the accretion flow, some form of angular momentum dissipation and/or redistribution must be present. Indeed, consider the angular momentum per unit mass of a parcel of gas at distance R from the SMBH of mass M , in Newtonian gravity,

$$h_K = R^2 \Omega_K = \sqrt{GMR}, \quad (3.24)$$

where

$$\Omega_K = \sqrt{\frac{GM}{R^3}}. \quad (3.25)$$

is the Keplerian angular frequency. This frequency also defines a dynamical timescale for the accretion disc (e.g. Davis & Tchekhovskoy, 2020)

$$t_{\text{dyn}} = \frac{1}{\Omega_K} \sim 1 \text{ day} \frac{M}{10^8 M_\odot} \left(\frac{R}{30R_g} \right)^{3/2} \quad (3.26)$$

for typical parameters in an AGN. Since h_K increases with radius, a gas parcel at r must lose angular momentum to move to an orbit at a smaller r . The mechanism that allows a gas parcel to move inwards and be accreted is viscosity. The differential rotation of nearby gas annuli produces a shear stress and therefore a torque, such that gas parcels can transfer part of their angular momentum to larger radii and move to smaller orbits. It is possible to define a *viscous timescale* (e.g. Frank et al., 2002) as

$$t_v = \frac{R^2}{\nu} \quad (3.27)$$

where ν is the kinematic viscosity, with units $\text{cm}^2 \text{s}^{-1}$. This can be understood as the timescale over which a gas parcel at radius R is accreted onto the BH. This can also be written as

$$t_\nu = \frac{R^2}{\nu} = \frac{R}{v_\phi} \frac{R v_\phi}{\nu} = \Omega^{-1} \text{Re} \quad (3.28)$$

where v_ϕ is the tangential velocity within the disc and Re is the Reynolds number associated with the flow. If we assume the ν is a *microphysical viscosity* (i.e. associated with the random motions of particles in a fluid), the Reynolds number can be expressed in terms of M , the density, the temperature and the radius within the accretion disc. Moreover, for typical parameters for binary stellar systems place it in the range $\text{Re} \gtrsim 10^{14}$. In AGN, the estimate can be several orders of magnitude larger (Frank et al., 2002). Assuming $\Omega = \Omega_K$, for typical parameters for an AGN this leads to $t_\nu \gg 13.7 \text{ Gyr}$. In conclusion, microphysical viscosity is not sufficient to provide the necessary amount of viscous torque that would lead to accretion within the age of the Universe. More likely, processes such as the magneto-rotational instability (MRI, Balbus & Hawley, 1991, 1998), gravitational instabilities due to self-gravity (Shlosman et al., 1990), or disc winds (Blandford & Payne, 1982) are good candidates for such a mechanism. Understanding how these processes lead to angular momentum transport from first principles is subject to intense study with the help of numerical simulations. However, significant progress has been made by using an *effective viscous theory*, developed to treat accretion flows analytically. The viscosity is not modelled from first principles by resolving, for example, the MRI. Rather, the stresses that arise due to turbulence are parameterised in the same fashion as a fluid viscosity in the equations, which encapsulates all the details. This parametrisation, commonly referred to as " α -prescription", was first introduced by Shakura & Sunyaev (1973) and reads

$$\nu \equiv \alpha c_s H = \alpha \frac{c_s^2}{\Omega_K} \quad (3.29)$$

where H is the disc scale height, related to c_s , the sound speed of the gas, and Ω_k :

$$H \equiv \frac{c_s}{\Omega_k} \quad (3.30)$$

The parameter α must be in general $\lesssim 1$. With this prescription for viscosity, the viscous timescale is given by (e.g. Davis & Tchekhovskoy, 2020)

$$t_\nu = \frac{1}{\alpha \Omega} \left(\frac{H}{R} \right)^{-2} \sim 260 \text{ year} \frac{M}{10^8 M_\odot} \frac{0.1}{\alpha} \left(\frac{H/R}{0.01} \right)^2 \left(\frac{R}{30 R_g} \right)^{3/2} \quad (3.31)$$

The parameter H/R is the aspect ratio of the disc scale height to radius. A disc characterised by $H/R \ll 1$ is said to be *thin disc*. If $H/R \lesssim 1$ it is referred to as *thick disc*.

The equations for the time evolution of an accretion flow around a BH are derived from the general fluid dynamics equations. To treat accretion discs analytically, several approximations and simplifications are assumed and the equations are generally manipulated to produce a height-integrated version of them (or rather shell-integrated in the case of thick discs). The equations

for a stationary axisymmetric accretion flow read (e.g. Yuan & Narayan, 2014)

$$\begin{aligned}
\frac{d}{dR}(\rho R H v_R) &= 0, \\
v_R \frac{dv_R}{dR} - \Omega^2 R &= -\Omega_K^2 R - \frac{1}{\rho} \frac{d}{dR}(\rho c_s^2), \\
v_R \frac{d(\Omega R^2)}{dR} &= \frac{1}{\rho R H} \frac{d}{dR} \left(v \rho R^3 H \frac{d\Omega}{dR} \right), \\
\rho v_R \frac{de}{dR} - q^c &= q^+ - q^- \equiv q^{\text{adv}},
\end{aligned} \tag{3.32}$$

corresponding to *mass*, *radial momentum*, *angular momentum* and *energy* conservation. Here, ρ is the density in the mid-plane of the disc, R is the radial coordinate, v_R is the radial velocity, Ω the angular velocity, p is the pressure, e the specific internal energy. Furthermore,

$$c_s \equiv \sqrt{p/\rho} \tag{3.33}$$

$$\rho \equiv \Sigma/H. \tag{3.34}$$

Also note that the equation of mass conservation can be integrated radially, yielding the following important relation between mass accretion \dot{M} and surface density Σ

$$\dot{M} = -2\pi R v_R \Sigma. \tag{3.35}$$

The energy equation contains several terms, defined as such:

$$\begin{aligned}
\rho v_R \frac{de}{dR} & \text{rate of change of internal energy} \\
q^c \equiv \frac{p v_R}{\rho} \frac{d\rho}{dR} & \text{compressive work} \\
q^+ \equiv \rho v_R R^2 \left(\frac{d\Omega}{dR} \right)^2 & \text{rate of entropy injection by viscous dissipation} \\
q^- & \text{radiative cooling rate.}
\end{aligned}$$

Eqs. 3.32 are quite general, and from them, it is possible to find solutions dependent on different physical conditions. An important factor is the optical thickness of the gas τ , also known as optical depth, a measure of how much the gas attenuates or absorbs light as it passes through. In general, the increment in optical depth $d\tau$ by a layer of gas with length dz is given by $d\tau = \kappa dz$, where κ is the opacity, with units $\text{cm}^2 \text{g}^{-1}$. Opacity depends on the density, temperature, and composition of the gas. The gas is optically thin if $\tau \ll 1$ or thick if $\tau \gg 1$. The regime of optical thickness determines the radiative transport within the disc and therefore the redistribution of energy and the importance of radiation pressure. Moreover, another essential property in determining the disc structure is the amount of radiative cooling. These conditions combined determine the magnitude of the terms in the energy equation. The two sources of heating, viscous (q^+) and compressional (q^c), compete with the two terms that act to transport energy away, namely energy advection

(q^{adv}) and radiative cooling (q^-). The types of accretion flow that are theoretical solutions of Eqs. 3.32, can be understood by analysing the relative importance of each term. Therefore, we have (e.g. Abramowicz & Fragile, 2013; Yuan & Narayan, 2014):

- **Shakura & Sunyaev (1973) thin accretion disc (SSD):** $H/R \ll 1$; the gas is cool, far from the virial temperature (the temperature is $\sim 10^6$ K for typical AGN parameters – e.g. Frank et al. 2002 –, while $T_{\text{vir}} \simeq 10^{12}(R_{\text{BH}}/R)$ K¹.); the gas is optically thick; the advection term is zero by construction ($q^{\text{adv}} \equiv 0$), and the viscously dissipated energy is radiated locally.
- **Slim disc (Abramowicz et al., 1988):** $H/R \sim 1$; the gas is still cool and optically thick; however it is denser and optically thicker than the thin disc, such that a significant fraction of the energy is advected inwards ($q^{\text{adv}} \sim q^+$).
- **Shapiro, Lightman, Eardley (SLE) solution (Shapiro et al., 1976):** the gas is hot, optically thin, radiatively cooled and advection is absent ($q^{\text{adv}} \equiv 0$). This solution is thermally unstable, therefore it is believed to be unphysical.
- **"Advection-dominated" hot accretion flow (ADAF):** $H/R \lesssim 1$; the gas is hot, optically thin, and advection dominated ($q^{\text{adv}} \sim q^+$). A small fraction of the viscously dissipated energy is radiated, therefore they are radiatively inefficient.
- **Luminous hot accretion flow (LHAF):** $H/R \lesssim 1$; the gas is hot and optically thin. However, contrary to the previous case, the flow is radiatively efficient. Despite this fact, the gas remains hot due to compressional heating ($q^{\text{adv}} < 0$) or, in other words, due to the advection of energy dissipated at larger radii.

Note that the slim disc is still technically "advection-dominated". However, in literature, the term "ADAF" has traditionally been reserved for the hot accretion flow solutions. Another interesting property to note is that when energy is trapped and pressure is larger, discs tend to become geometrically thick ($H/R \sim 1$), which occurs in hot accretion flows but also in slim discs.

It is useful to plot the solutions on the parameter space spanned by $(\dot{M} - \Sigma)$, which also shows their viscous stability (the positive slope branches are stable, see Frank et al., 2002). Fig. 3.4 displays such a plot, taken from Yuan & Narayan (2014). As said, the SLE solution is thermally unstable, whereas the branch between SSD and slim disc is viscously unstable. From this plot, it is possible to appreciate visually that at fixed Σ or at fixed \dot{M} , there are multiple ways to satisfy Eqs. 3.32, depending on the physical condition. For example, an Eddington ratio $f_{\text{Edd}} \sim 10^{-3}$ would be perfectly consistent with both an ADAF or an SSD, although an ADAF would be characterised by a five orders of magnitude lower surface density. Therefore, it is worth stressing that Eddington ratios and type of accretion flows are not associated one-to-one. Moreover, it is not at all obvious which solutions should be preferred in nature, although e.g. Narayan & Yi (1995) argue that a thin disc would transition to an ADAF whenever it is locally allowed.

¹The virial temperature is defined as $T_{\text{vir}} = GMm_p/(3k_bR)$, (see e.g. Yuan & Narayan, 2014). The gas in an accretion flow would reach $2T_{\text{vir}}$ if its gravitational potential energy were completely converted into thermal energy, without radiating part of it.

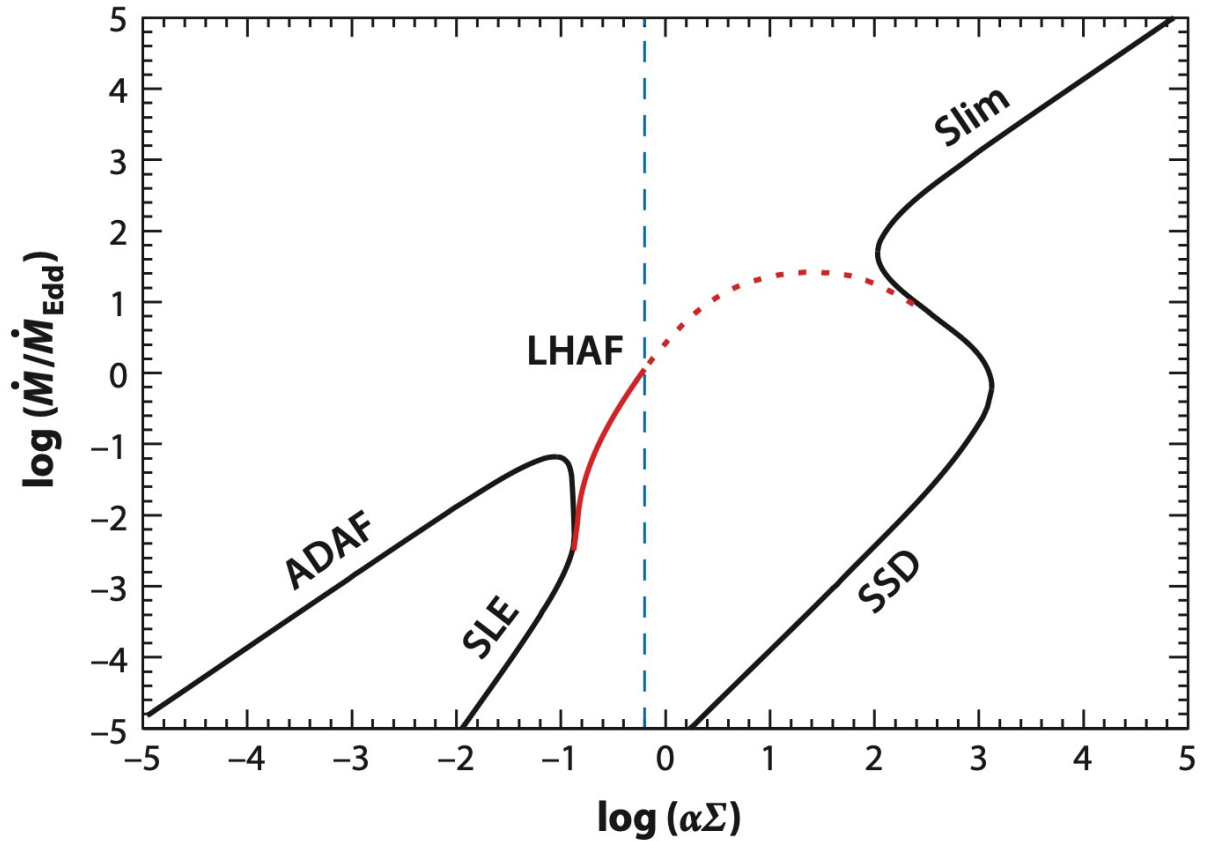
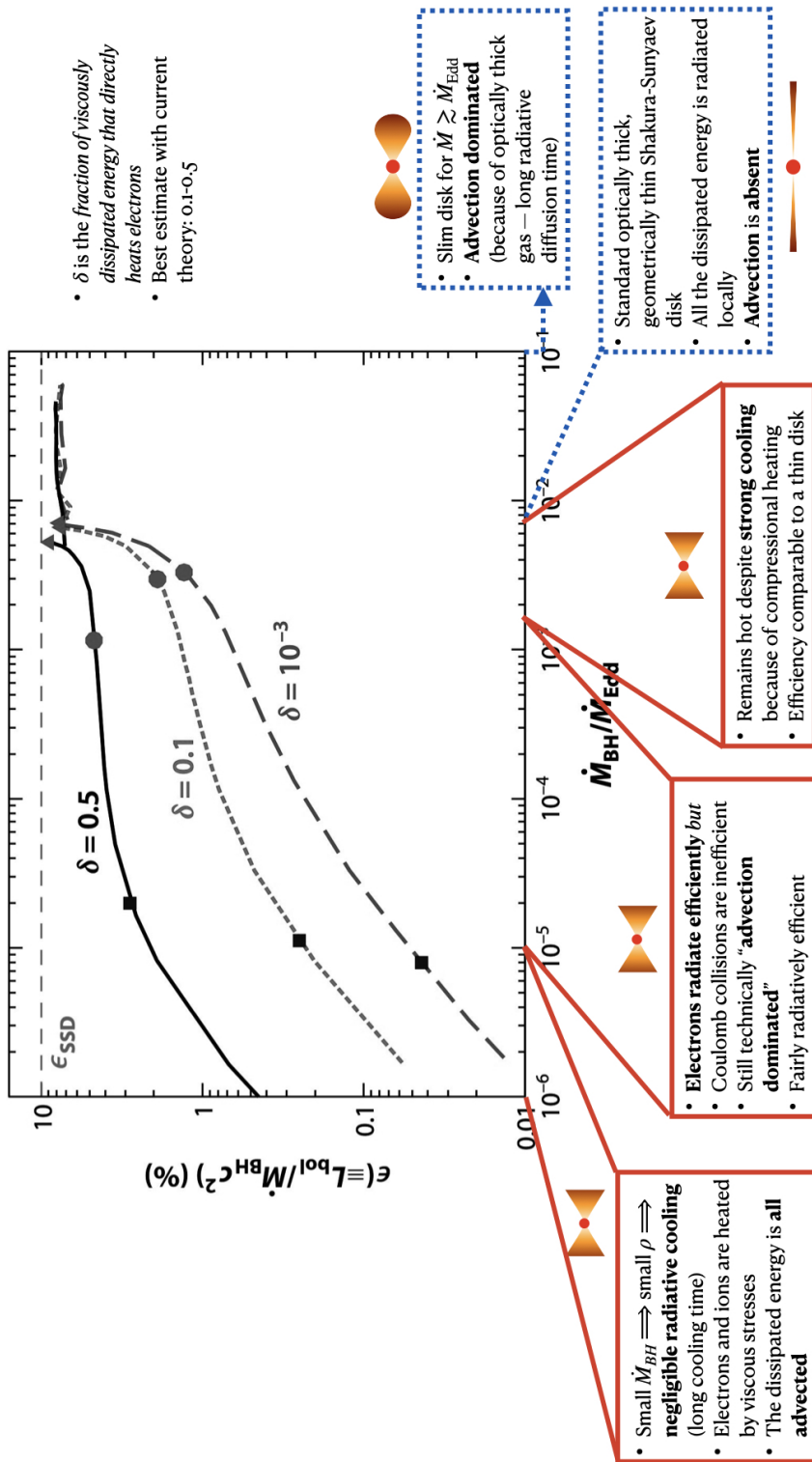


Figure 3.3: Curves of accretion rate \dot{M} versus Σ , defining different solutions for the accretion disc equations, plotted for a BH of $M_{\text{BH}} = 10 M_{\odot}$, $a = 0.1$ and $r/R_{\text{BH}} = 5$. Solutions on the left (right) of the dashed line are optically thin (thick). The LHAF is found to be internally inconsistent in the optically thick case (hence the dashed line). From Yuan & Narayan (2014).

Overall, this qualitative picture assumes that it is possible to model the accretion disc as a one-temperature fluid, in which electrons and ions exchange energy efficiently. However, it has been shown that in hot accretion flows this might not be the case. Nonetheless, the qualitative picture should be correct (e.g. Chen et al., 1995; Yuan & Narayan, 2014).

As discussed earlier, some types of accretion flow are radiatively efficient, while others are not. Ultimately, this is determined by the amount of advection and the ability to cool. For a thin disc, *the entire* dissipated energy is radiated away while the gas spirals inwards in the accretion disc. Therefore, the radiative efficiency of the process is fully defined by the binding energy at the last stable orbit (see Eq. 3.19). The radiative efficiency depends on the magnitude of the BH spin. When advection becomes important, however, some radiation is trapped in the accretion flow and is able to reach the last stable orbit before being radiated. Overall, the radiative efficiency is lower, at a fixed Eddington ratio, compared to the thin disc solution. Fig. 3.4 illustrates this important concept. Plotted is the radiative efficiency of a hot accretion flow, as a function of f_{Edd} . Moreover, the insets on the bottom illustrate qualitatively the various regimes of accretion flows described earlier in this section. The figure is adapted from Yuan & Narayan (2014), although the original work is by Xie & Yuan (2012). Since the authors use a two-temperature accretion disc model, the curves shown depend on the parameter δ , which quantifies the fraction of dissipated energy that directly heats the electron in the accretion disc plasma. This plot further shows that the efficiency increases with the accretion rate, and there is even a regime where it is comparable to the thin disc. As a final note, since advection plays an important role in the slim disc regime, this model presents a *decreasing* efficiency with increasing accretion rate, in the super-Eddington regime (e.g. Madau et al., 2014).



3.1.4 The standard thin disc solution

The most general solution of the fluid equations for an accretion flow requires numerical simulations, especially to include magnetic fields and make physical processes arise self-consistently, without ad-hoc treatments. This is the approach adopted for example in studies of MRI-induced shear stresses, or radiative transport. However, with a few further assumptions, it is possible to obtain *algebraic* equations from Eqs. 3.32, in the case of a geometrically thin, circular and planar disc. This is the idea behind the seminal work by Shakura & Sunyaev (1973). In this Section, I present the features of this disc solution, which is the one assumed in the spin evolution model.

One of the defining features of such a geometrically thin disc is that the mid-plane sound speed is small compared to the orbital velocity (i.e. $c_s/v_K = H/R \ll 1$). The vertical and radial structure of the disc are decoupled because the disc is rotationally-supported radially, and pressure-supported and in hydrostatic equilibrium vertically. Furthermore, the sub-dominant radial pressure gradients do not modify the angular velocity profile of the disc to leading order. If we further assume that we are dealing with an accretion disc around a point mass and the potential is dominated by the central mass, then the angular velocity profile is approximately Keplerian, such that $\Omega = \Omega_K$. Eqs. 3.32 are fairly general, as discussed in Sec. 3.1.3, because they only assume axisymmetry, a static potential from a central mass, and that the torque is provided by an effective fluid viscosity. However, by noting that the accretion rate (Eq. 3.35) must be constant along the disc in a steady solution, and integrating the angular momentum equation (the third of Eqs. 3.32) it is possible to obtain the following defining relation (e.g. Frank et al., 2002)

$$v\Sigma = \frac{\dot{M}}{3\pi} \left[1 - \sqrt{\frac{R_{\text{ISCO}}}{R}} \right]. \quad (3.36)$$

This equation further assumes a *zero-torque* boundary conditions at the ISCO; i.e., the angular momentum at the innermost radius of the accretion disc is exactly defined by the angular momentum of the corresponding circular orbit at R_{ISCO} .

The thin disc model further assumes that advection is identically zero, such that the energy is radiated locally, and that the disc is optically thick. For this reason, the radiation emitted by each annulus is characterised by a blackbody spectrum. Under these assumptions, it is possible to relate the energy released by viscous dissipation q^+ (e.g. Armitage, 2022)

$$q^+ = \frac{9}{4} v\Sigma\Omega_K^2, \quad (3.37)$$

to the blackbody radiative flux from the surface of the accretion discs

$$F = 2\sigma T_{\text{eff}}^4, \quad (3.38)$$

where the factor two accounts for the surface above and below the midplane. Here σ is the Stefan-Boltzmann constant and T_{eff} is the effective temperature of the disc surface. This leads to another algebraic equation in the case of a Keplerian velocity profile:

$$T_{\text{eff}}^4 = 3 \frac{GM\dot{M}}{8\pi\sigma R^3} \left[1 - \sqrt{\frac{R_{\text{ISCO}}}{R}} \right]. \quad (3.39)$$

This equation shows that the temperature profile depends neither on the disc structure nor on the viscosity. This means that a precise knowledge of these two aspects is not necessary, from the point of view of comparing an observed temperature profile with the theoretical one. The resulting spectrum is a superposition of blackbody spectra at different temperatures, whose dependence on the radius is given by Eq. 3.39. The flux emitted by the disc as a function of frequency can be obtained by integrating the blackbody intensity over the radial extent of the disc, producing the characteristic shape presented in Sec. 2.1.1.

Since the disc is in vertical hydrostatic equilibrium, it is possible to solve the energy transport locally at a fixed radius, with a treatment akin to stellar structures. Under the assumption that the energy is transported from the mid-plane at temperature T_c to the surface of the disc radiatively, the optical depth τ is (Armitage, 2022)

$$T_c/T_{\text{eff}} \simeq 3/4\tau \quad (3.40)$$

where the optical thickness assumption translates to the requirement that

$$\tau = \rho H \kappa_R = \Sigma \kappa_R \quad (3.41)$$

where κ_R is the wavelength-averaged Rosseland opacity, which in general depends on T_c and ρ_c . Eq. 3.39 therefore becomes

$$T_c^4 = \frac{9\dot{M}\Omega_k^2}{32\pi\sigma} \left[1 - \sqrt{\frac{r_{\text{ISCO}}}{r}} \right] \tau. \quad (3.42)$$

An equation of state including gas pressure and radiation

$$p = \frac{k_B}{\mu m_p} \rho_c T_c + \frac{4\sigma}{3c} T_c^4 \quad (3.43)$$

is adopted to close the system of equations.

In conclusion, the system of equations 3.29, 3.33, 3.36, 3.41, 3.42 and 3.43 can be used to solve for the unknown ρ_c , Σ , H , c_s , p , T_c , τ , ν . The solution of Shakura & Sunyaev (1973) can be readily derived from this system of algebraic equations, and each unknown is expressed as a power-law in α , \dot{M} , M and R . They are also referred to as *similarity solutions*. Different scalings are obtained for different dominant contributions for pressure and opacity, as mentioned before. In particular, three regimes are relevant for AGN:

- **inner region:** *radiation pressure* and *electron scattering opacity*;
- **middle region:** *gas pressure* and *electron scattering opacity*;
- **external region:** *gas pressure* and *free-free opacity*.

For example, the external region solutions, for typical AGN properties, reads (e.g. Frank et al., 2002):

$$\begin{aligned} \Sigma &= 5.2 \times 10^6 \alpha^{-4/5} \left(\frac{\dot{M}}{10^{26} \text{ g/s}} \right)^{7/10} \left(\frac{M}{10^8 M_\odot} \right)^{1/4} \left(\frac{R}{10^{14} \text{ cm}} \right)^{-3/4} f^{14/5} \text{ g cm}^{-2} \\ T_c &= 1.4 \times 10^6 \alpha^{-1/5} \left(\frac{\dot{M}}{10^{26} \text{ g/s}} \right)^{3/10} \left(\frac{M}{10^8 M_\odot} \right)^{1/4} \left(\frac{R}{10^{14} \text{ cm}} \right)^{-3/4} f^{6/5} \text{ K} \end{aligned} \quad (3.44)$$

where in this case $r' = r/(3r_{\text{BH}})$, and $f = (1 - r'^{-1/2})$. The full expressions for each region can be retrieved in the original Shakura & Sunyaev (1973) work, or in Frank et al. (2002). However, the treatment just presented is fully Newtonian; general relativistic extensions are provided, for example, in Novikov & Thorne (1973). In any case, the corrections are supposed to be important in the regime of strong gravity, close to the event horizon, where also the standard thin disc solution is no longer valid. Indeed, in the innermost region, the disc might become geometrically thick, due to the increasingly important contribution of radiation pressure. Therefore, when dealing with effects that occur far away from the inner region (such as the one presented in this work) the Shakura & Sunyaev (1973) solution is an adequate approximation.

As a final comment, it is worth noting that Eq. 3.36 allows us to directly compute the dependence of ν on the disc structure. In particular, $\nu \propto 1/\Sigma \propto R^{-\beta}$. In the spin evolution model (Sec. 3.2.1), the resulting expression for ν is adopted in every equation that depends explicitly on viscosity.

3.1.5 Thin disc around spinning BHs: warps and spin evolution

So far we dealt with completely flat discs and derived their structure in the thin discs regime. Consider now an accretion disc around a BH with angular momentum vector \mathbf{J}_{BH} as

$$\mathbf{J}_{\text{BH}} = J_{\text{BH}} \cdot \mathbf{j}_{\text{BH}} = a \frac{GM_{\text{BH}}^2}{c} \mathbf{j}_{\text{BH}}, \quad (3.45)$$

where \mathbf{j}_{BH} is the unit vector encoding its direction and J_{BH} is its magnitude. The dimensionless spin parameter a is $0 \leq a \leq 1$. In what follows, a negative sign encodes counter-rotating conditions on a BH with spin parameter a . Orbits around a Kerr BH whose orbital planes are misaligned with respect to the equatorial plane of the metric itself, undergo *Lense-Thirring precession* due to the torque that the metric exerts on the orbit. Each annulus orbital plane precesses independently, with a precession frequency that depends on the radius

$$\omega_{\text{LT}} = \frac{2GJ_{\text{BH}}}{c^2 R^3}. \quad (3.46)$$

As a consequence, annuli at different radii have different precession frequencies. This differential precession induces adjacent annuli to have a mutual inclination with respect to each other and therefore a vertical shear stress. In an initially flat but tilted disc around a Kerr BH the Lense-Thirring torque induces the disc profile to evolve towards a *warped* configuration (Bardeen & Petterson, 1975), illustrated in Fig. 3.5. In the *viscous regime*, that occurs if (Papaloizou & Pringle, 1983)

$$\alpha \gtrsim \frac{H}{R}, \quad (3.47)$$

the perturbation propagates diffusively. The viscosity responsible for the propagation of vertical perturbation is in general different from ν_1 . In particular it can be related to the one responsible for radial inward drift (e.g. Armitage, 2022; Ogilvie, 1999)

$$\nu_2 \sim \frac{\nu_1}{2\alpha^2} \quad (3.48)$$

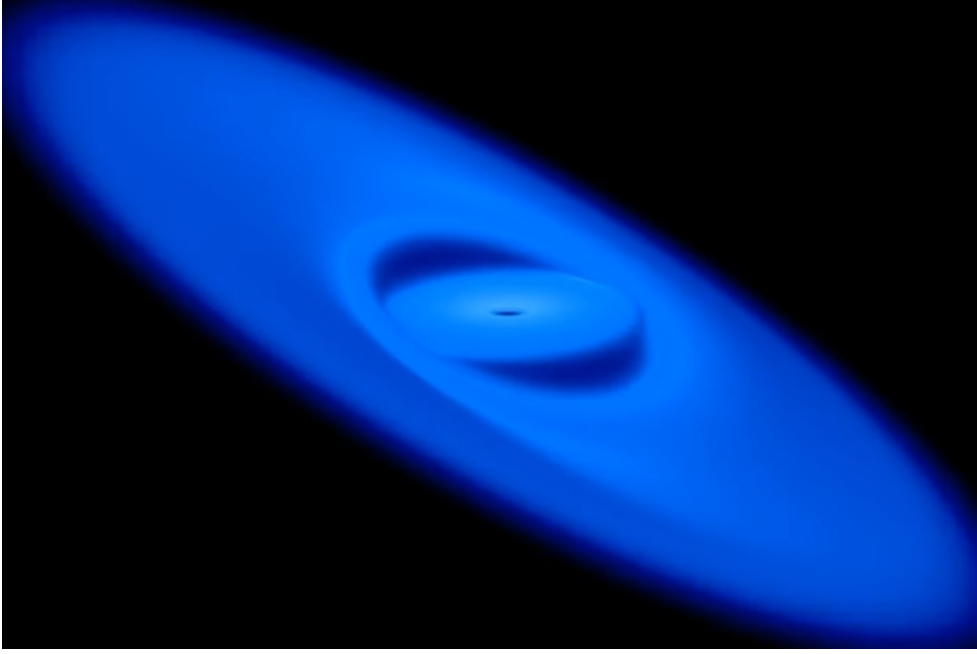


Figure 3.5: Illustration of the structure of a warped thin disc. From Nealon et al. (2015).

and is therefore generally much larger than ν_1 . At small radii the disc plane is aligned (or anti-aligned) with the BH equatorial plane, at large radii is essentially unperturbed. In thin discs around a SMBH, condition 3.47 is expected to be verified for a wide range of radii. In the viscous regime, the warp reaches a steady state; while the gas flows through the region of maximal warp, misaligned both with the BH and the external disc region, it experiences a torque. This requires an opposite torque to act onto the BH, such that (for an isolated system, i.e. without inflow on the disc)

$$\frac{d\mathbf{J}_{\text{BH}}}{dt} = -\frac{d\mathbf{J}_{\text{d}}}{dt}, \quad (3.49)$$

where \mathbf{J}_{d} is the total angular momentum of the disc. This effect ultimately leads to spin evolution and is the motivation behind the prescription described in this work. In general, the torque responsible for modifying the BH spin direction reads

$$\frac{d\mathbf{J}_{\text{BH}}}{dt} = \frac{4\pi G}{c^2} \int_{\text{disc}} \frac{\Sigma \mathbf{L} \times \mathbf{J}_{\text{BH}}}{R^2} dR \quad (3.50)$$

The torque depends on the surface density $\Sigma(R)$ and the angular momentum profile $\mathbf{L}(R)$. Martin et al. (2007) computed it under the assumption of a power-law viscosity law, as the one mentioned in Sec. 3.1.4. The total torque on the BH can thus be expressed in the form (King et al., 2005; Fiacconi et al., 2018):

$$\begin{aligned} \frac{d\mathbf{J}_{\text{BH}}}{dt} = & \dot{M} L_{\text{ISCO}} \text{sign}(\mathbf{j}_{\text{BH}} \cdot \mathbf{j}_{\text{d}}) \mathbf{j}_{\text{BH}} - \\ & \mathbf{J}_{\text{BH}} \left\{ \frac{\sin(\pi/7)}{\tau_{\text{align}}} [\mathbf{j}_{\text{BH}} \times \mathbf{j}_{\text{d}}] + \frac{\cos(\pi/7)}{\tau_{\text{align}}} [\mathbf{j}_{\text{BH}} \times (\mathbf{j}_{\text{BH}} \times \mathbf{j}_{\text{d}})] \right\}, \end{aligned} \quad (3.51)$$

where τ_{align} is the *alignment timescale* (e.g. Armitage, 2022)

$$\tau_{\text{align}} \sim \frac{1}{\Sigma_{\infty}} \sqrt{\frac{acM}{Gv_2}} \quad (3.52)$$

and Σ_{∞} is the surface density at large radii. The first part in Eq. 3.51 represents the torque in the same direction as the BH angular momentum, which modifies its magnitude. The term in parenthesis expresses precession (left) and alignment (right) of the BH with the disc angular momentum at large radii. The timescale t_{al} can be understood as the time required for an e-folding reduction of the angle of misalignment between the BH spin and the disc at large radii (Perego et al., 2009). In general, the details of the disc structure (such as the one discussed in Sec. 3.1.4) are encapsulated in the definition of τ_{align} . For example, assuming an external region solution, a numerical value is (e.g. Fiacconi et al., 2018)

$$\tau_{\text{al}} \sim 0.13 \left(\frac{M_{\text{BH}}}{10^8 M_{\odot}} \right)^{-2/35} \left(\frac{f_{\text{Edd}}}{\eta_{0.1}} \right)^{-\frac{32}{35}} a^{5/7} \text{Myr}. \quad (3.53)$$

Eq. 3.51 in principle can be integrated directly in time to evolve \mathbf{J}_{BH} , \mathbf{J}_{d} and account also for possible inflow onto the disc, as done for example by Fiacconi et al. (2018). However, this would require timesteps as low as 10^{-3} Myr, which are achievable in high-resolution simulations of isolated objects or in zoom-in simulations but can severely hinder performance in cosmological simulations. In our prescription, described in depth in Sec. 3.2, we account for the first term in Eq. 3.51 explicitly, while the second is modelled in subsequent accretion episodes where precession and alignment are not explicitly integrated, but rather the BH spin direction aligns with the total angular momentum in each episode, according to King et al. (2005). In the modelling, it is assumed that the main contribution to the integral in Eq. 3.50 comes from the region where the warp has the largest amplitude, corresponding to the warp radius R_{w} (see Sec. 3.2.1).

Finally, it is worth noting that the timescale of alignment of the BH spin with the disc angular momentum at large radii over one accretion episode is short compared to the timescale over which the BH spin changes in magnitude and direction due to the continuous accretion process, that occurs instead on the Salpeter timescale, $\tau_{\text{S}} = \sigma_{\text{T}}c / (4\pi Gm_{\text{p}}) \sim 4.5 \times 10^8$ yr.

3.2 Implementation in `OPENGADGET3`

In this Section, I will present the sub-resolution model for spin evolution due to gas accretion onto BHs and mergers and its coupling to the resolved scales, as described in Sala et al. (2023). The model is implemented in the `TREEPM` code `OPENGADGET3` (see Groth et al., 2023), descendant of a non-public evolution of the `GADGET-3` code (originally from Springel, 2005). The code features a modern smoothed particle hydrodynamics (SPH) description (Beck et al., 2016) and adopts a bias-corrected, sixth-order Wendland kernel (Dehnen & Aly, 2012) with 295 neighbours.

3.2.1 Spin evolution algorithm

Our model is designed for simulations whose spatial resolution ranges from few tens of pc to a few kpc (see Sec. 4.1), several orders of magnitudes larger than the physical size of an accretion disc around a BH (< 1 pc, Frank et al. 2002). In the approach often adopted in cosmological simulations, an accretion disc is not included in the modelling (e.g. Springel et al., 2005a; Booth & Schaye, 2009). In our implementation, we introduce a sub-grid accretion disc as an intermediate step in the mass transfer between the resolved scales and the BH. We then assume that the mass transfer rate from the resolved scales onto the accretion disc is equal to the mass rate from the accretion disc onto the BH. The mass rate is defined by Eqs. (2.2) and (2.3). We also assume that the gas maintains the angular momentum direction it has at the resolved scales. The inclusion of an accretion disc is necessary to model the physical effects that modify the spin due to gas accretion, as explained in the following.

Accretion disc and spin evolution

\mathbf{J}_{BH} evolves because of its interaction with the distribution of matter in a surrounding accretion disc, whose angular momentum is misaligned with respect to \mathbf{J}_{BH} . Our model assumes an optically thick, geometrically thin Shakura & Sunyaev (1973) accretion disc.

If we start from a completely flat disc surrounding a spinning BH, Lense-Thirring precession forces the fluid elements close to the BH to precess and induces them to rotate in the BH equatorial plane. If viscosity is sufficiently high, the shear stresses propagate the perturbation diffusively until a warped steady state of the disc is reached (Bardeen & Petterson, 1975; Martin et al., 2007). The largest deviation from a flat profile – i.e. disc annuli where the gas angular momentum is misaligned with respect to both the unperturbed outer region of the disc and the BH spin – occurs at the warp radius. The latter is defined as the radius R_w at which the Lense-Thirring precession timescale $t_{\text{LT}} = R_w^3 c^2 / (2GJ_{\text{BH}})$ (Wilkins, 1972) is equal to the warp propagation timescale $t_w \sim R_w^2 / \nu_2$ (Pringle, 1981; Perego et al., 2009). ν_2 is the vertical shear viscosity governing the propagation of vertical perturbations (e.g. Volonteri et al., 2007; Perego et al., 2009; Dotti et al., 2013; Dubois et al., 2014b). Following Dubois et al. (2014b) we compute

$$\frac{R_w}{R_{\text{BH}}} \simeq 4 \times 10^2 a^{5/8} M_{\text{BH},8}^{1/8} \left(\frac{f_{\text{Edd}}}{\epsilon_{r,01}} \right)^{-1/4} \left(\frac{\nu_2/\nu_1}{85} \right)^{-5/8} \alpha_{\nu_1,01}^{-1/2}, \quad (3.54)$$

where $M_{\text{BH},8} = M_{\text{BH}} / (10^8 M_{\odot})$, $\epsilon_{r,01} = \epsilon_r / 0.1$ and we define the Eddington ratio $f_{\text{Edd}} = \dot{M}_{\text{BH}} / \dot{M}_{\text{Edd}}$. ν_1 is the radial shear viscosity, responsible for the radial inward drift of gas across the disc. We also assume that the viscosity α -parameter (Shakura & Sunyaev, 1973) is $\alpha_{\nu_1,01} = \alpha_{\nu_1} / 0.1 \equiv 1$, following King et al. (2005), and $\nu_2/\nu_1 = 2(1 + 7\alpha_{\nu_1}) / (4 + \alpha_{\nu_1}^2) / \alpha_{\nu_1}^2$, following Ogilvie (1999), leading to a fiducial value for the ratio $\nu_2/\nu_1 = 85$.

The flow of matter through the warp is responsible to exert a torque that modifies only the direction of the BH spin. Indeed, matter flowing from the unperturbed outermost region to the aligned innermost region through the warp changes its angular momentum direction, therefore forcing the BH spin orientation to change and ensure conservation of the total angular momentum (King et al., 2005; Dotti et al., 2013). Since the torque acting to modify the direction of the BH spin

is produced by matter flowing through the warped region at R_w , we adopt the same assumption as Volonteri et al. (2007) and Dubois et al. (2014b) and define $\mathbf{J}_d = J_d \mathbf{j}_d$ as the angular momentum of the disc within R_w . King et al. (2005) showed that starting from a configuration where \mathbf{J}_{BH} and \mathbf{J}_d are initially misaligned, the torque resulting from the warped configuration always leads the BH spin to align with the total angular momentum \mathbf{J}_{tot} of the system disc+BH

$$\mathbf{J}_{\text{tot}} = \mathbf{J}_{\text{BH}} + \mathbf{J}_d. \quad (3.55)$$

Moreover, the torque acts dissipatively on the disc, whose angular momentum ends up either aligned or counter-aligned with the BH spin, depending on the ratio between the angular momentum magnitudes. Namely, the counter-aligned configuration is possible if and only if

$$\cos \theta_{\text{BH-d}} < -\frac{J_d}{2J_{\text{BH}}} \quad (3.56)$$

where $\theta_{\text{BH-d}}$ is the angle subtended by the initial angular momentum directions \mathbf{j}_{BH} and \mathbf{j}_d , i.e. $\cos \theta_{\text{BH-d}} = \mathbf{j}_{\text{BH}} \cdot \mathbf{j}_d$. Only the (counter-) aligned innermost – i.e. within R_w – region can effectively transfer its angular momentum to the BH, once the matter enclosed within this region is eventually accreted (Volonteri et al., 2007). Therefore, R_w is also the relevant radial scale to estimate the variation of the BH spin magnitude as a result of the accretion of this innermost part. Since the radial shear viscosity ν_1 is responsible for the inward drift of matter across the disc, the region within R_w is accreted on a timescale $t_{\nu_1}(R_w) \sim R_w^2/\nu_1$ (King et al., 2005; Perego et al., 2009; Dubois et al., 2014b). We follow Dubois et al. (2014b) and compute

$$t_{\nu_1}(R_w) \sim 3.4 \times 10^5 a^{7/8} M_{\text{BH},8}^{11/8} \left(\frac{f_{\text{Edd}}}{\epsilon_{r,01}} \right)^{-3/4} \left(\frac{\nu_2/\nu_1}{85} \right)^{-7/8} \alpha_{\nu_1,01}^{-3/2} \text{yr}. \quad (3.57)$$

Note that $\nu_1 \ll \nu_2$ and the warp propagation timescale t_w is thus much shorter than the radial drift timescale t_{ν_1} . As a consequence, the timescale on which the warp forms is much shorter than that over which the spin magnitude and direction change. We then estimate the mass enclosed within the warped region M_d as

$$M_d \simeq \dot{M}_{\text{BH}} t_{\nu_1}(R_w). \quad (3.58)$$

where \dot{M}_{BH} is given by Eq. (2.3). When M_d is accreted onto the BH, the BH spin magnitude a changes due to the accretion of its ISCO angular momentum, according to the expression derived in Bardeen (1970)

$$a_f = \frac{1}{3} \frac{r_{\text{ISCO}}^{1/2}}{M_{\text{ratio}}} \left[4 - \left(3 \frac{r_{\text{ISCO}}}{M_{\text{ratio}}^2} - 2 \right)^{1/2} \right], \quad (3.59)$$

where

$$M_{\text{ratio}} = \frac{M_{\text{BH}}^i + M_d(1 - \epsilon_r)}{M_{\text{BH}}^i}. \quad (3.60)$$

and, normalising to the gravitational radius $R_g = R_{\text{BH}}/2 = GM_{\text{BH}}/c^2$,

$$r_{\text{ISCO}} = R_{\text{ISCO}}/R_g = 3 + Z_2 \pm [(3 - Z_1)(3 + Z_1 + 2Z_2)]^{1/2}, \quad (3.61)$$

where the positive (negative) sign is for counter(co)-rotating orbits. Z_1 and Z_2 are functions of the BH dimensionless spin parameter only:

$$Z_1 = 1 + (1 - a^2)^{1/3} [(1 + a)^{1/3} + (1 - a)^{1/3}], \quad (3.62)$$

$$Z_2 = (3a^2 + Z_1^2)^{1/2}. \quad (3.63)$$

R_{ISCO} ranges from 1 to $9 R_g$, for co- and counter-rotating orbits on a maximally spinning BH respectively, as illustrated in the bottom panel of Fig. 3.6. Physical sizes are therefore between $\sim 5 \times 10^{-6} M_{\text{BH},8} \text{ pc}$ and $\sim 5 \times 10^{-5} M_{\text{BH},8} \text{ pc}$. The mass accreted is also corrected for the radiated energy, where

$$\epsilon_r = 1 - \sqrt{1 - \frac{2}{3r_{\text{ISCO}}}}. \quad (3.64)$$

The top panel of Fig. 3.6 shows the value of ϵ_r as a function of a .

Finally, as mentioned before, we estimate the angular momentum J_d of the accreted disc region that determines the spin variation in magnitude and direction (and is also used to evaluate condition 3.56) as

$$J_d \simeq M_d(R_w) \omega_k(R_w) R_w^2 = M_d(R_w) (GM_{\text{BH}} R_w)^{1/2}, \quad (3.65)$$

where $\omega_k = \sqrt{GM_{\text{BH}}/R^3}$ is the keplerian angular frequency. While $R_{\text{ISCO}} \sim 1-9R_g$, the warped region is at hundreds of gravitational radii (see Eq. 3.54), thus a few orders of magnitude larger. Therefore, the BH spin direction changes on a shorter timescale than its magnitude (Scheuer & Feiler, 1996; Perego et al., 2009; Dotti et al., 2013).

BH spin update iteration

The algorithm that we adopt to update BH mass and spin in our simulations models the above-mentioned processes, and makes sure that the BH mass grows consistently with the rate given by Eq. (2.3). Following Dubois et al. (2014b), BH mass and spin are updated in iterations (hereafter *accretion episodes*) composed of the following steps:

1. we assume that an accretion disc forms around the BH, characterised by the accretion rate given by Eq. 2.3. We further assume that the initial angular momentum direction of the disc \mathbf{j}_d is set by the resolved scales of the simulation, i.e. parallel to the direction of the angular momentum of the gas within the BH kernel \mathbf{j}_g :

$$\mathbf{j}_d = \mathbf{j}_g \equiv \mathbf{L}_{\text{BH,kernel}} / |\mathbf{L}_{\text{BH,kernel}}|, \quad (3.66)$$

where

$$\mathbf{L}_{\text{BH,kernel}} = \sum_j m_j (\mathbf{r}_j - \mathbf{r}_{\text{BH}}) \times (\mathbf{v}_j - \mathbf{v}_{\text{BH}}) w(\mathbf{r}_j - \mathbf{r}_{\text{BH}}, h_{\text{BH}}). \quad (3.67)$$

$\mathbf{L}_{\text{BH,kernel}}$ is computed considering only the cold gas particles – i.e. the component that is able to settle into an accretion disc. w is the dimensionless SPH kernel function. This is the initial misaligned configuration illustrated on the left in Fig. 3.7.

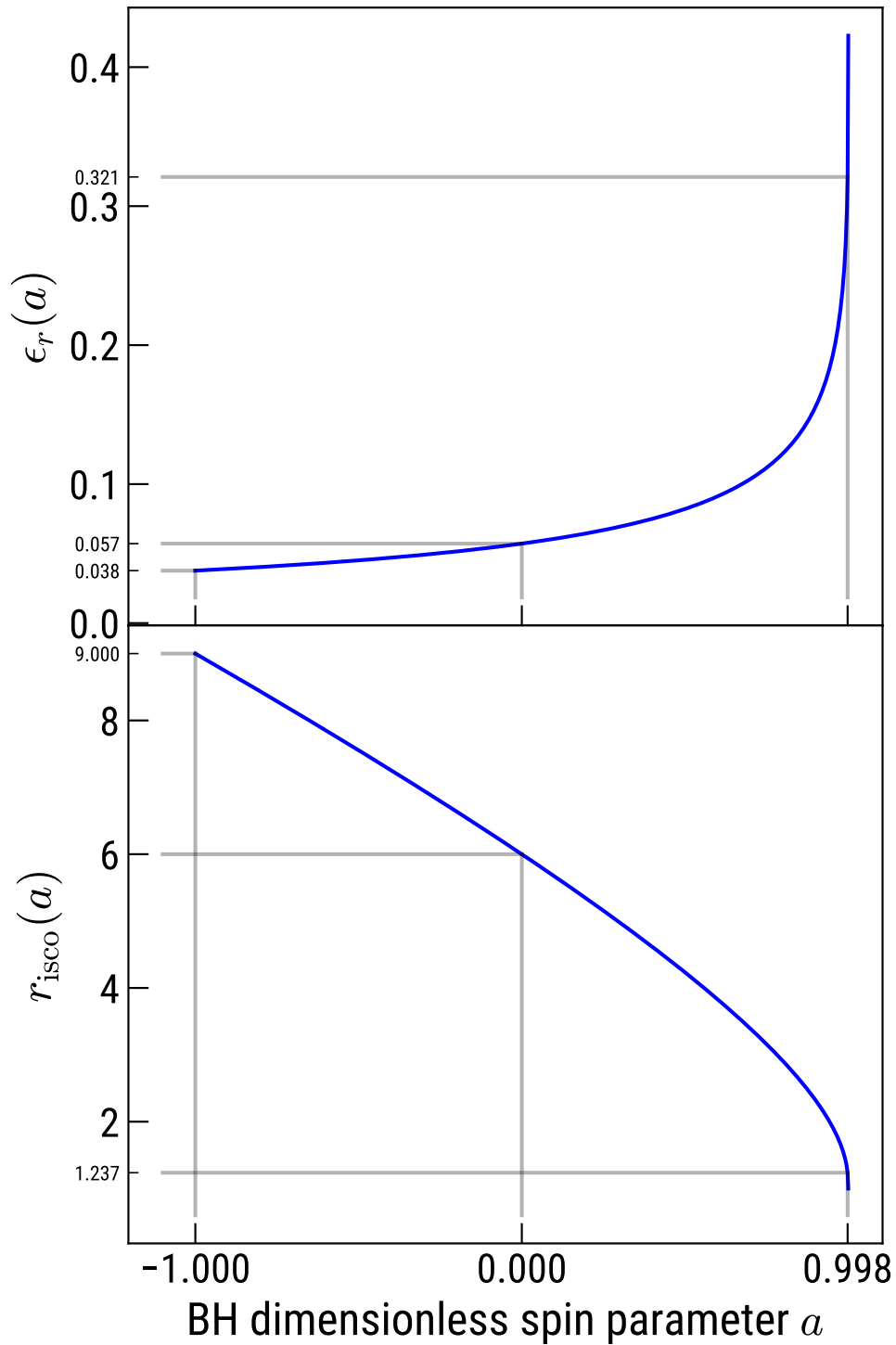


Figure 3.6: Radiative efficiency – Eq. (3.64) – (top panel) and radius of the innermost stable circular orbit – Eq. (3.61) – (bottom panel), as a function of the BH dimensionless spin parameter. Some reference values of these quantities are also highlighted: $a = -1$, for a counter-rotating orbit around a maximally spinning BH; $a = 0$, for a non-spinning BH; $a = 0.998$, for the maximum spin allowed in our simulations.

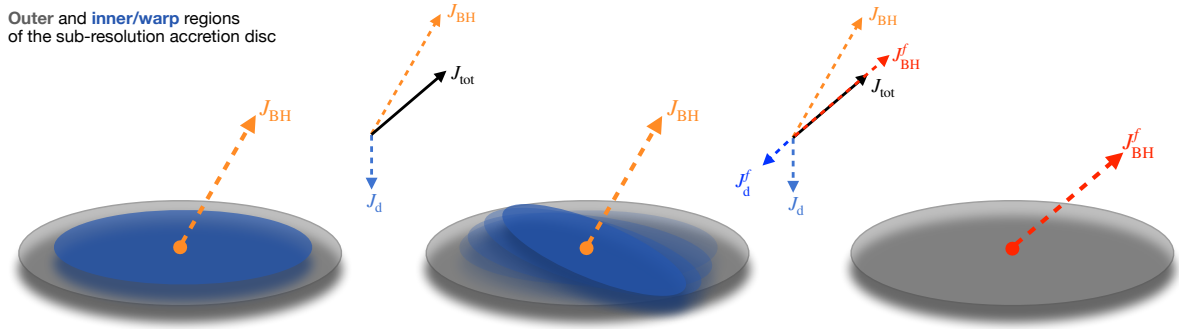


Figure 3.7: Schematic of the steps that compose a single accretion episode. The vector schemes in the upper part of the figure represent the initial and final configurations of the angular momenta, in a case similar to the one shown in Fig. 1b by King et al. (2005). *Left*: an accretion disc settles around the BH, in a misaligned configuration. *Centre*: a warp develops, and the innermost part is forced to rotate in the BH equatorial plane and either co- or counter-align. *Right*: the BH spin changes in magnitude when gas is accreted at the innermost stable orbit.

2. we compute R_w using Eq. 3.54. This defines the region of the disc (marked in blue in Fig. 3.7) that exerts the alignment torque on the BH spin and whose gas is eventually accreted by the end of the accretion episode.
3. we compute M_d and J_d , using Eq. 3.58 and 3.65 respectively. This defines the total angular momentum of the accretion episode $\mathbf{J}_{\text{tot}} = \mathbf{J}_{\text{BH}} + \mathbf{J}_d = \mathbf{J}_{\text{BH}} + J_d \mathbf{j}_d$ (black solid vector in Fig. 3.7). Note that we are assuming that the warped distribution that defines the innermost aligned region of the disc (central panel in Fig. 3.7) develops on a timescale shorter than those over which the BH spin direction and magnitude change, as explained in Sec. 3.2.1.
4. we establish whether the innermost part of the disc is co- or counter-rotating using Eq. (3.56), by computing

$$\frac{J_d}{2J_{\text{BH}}} \simeq \frac{M_d(R_w)}{aM_{\text{BH}}} \left(\frac{R_w}{R_g} \right)^{1/2} \quad (3.68)$$

$$\sim 6.8 \times 10^{-2} a^{3/16} M_{\text{BH},8}^{23/16} \left(\frac{f_{\text{Edd}}}{\epsilon_{r,01}} \right)^{1/8} \left(\frac{v_2/v_1}{85} \right)^{-19/16} \alpha_{v_1,01}^{-7/4}. \quad (3.69)$$

In case of counter-rotating conditions, r_{ISCO} and ϵ_r are computed with a negative sign in front of a .

5. the final BH spin direction changes as a result of the alignment torque and ends up parallel to the total angular momentum (vector scheme on the right in Fig. 3.7), i.e. $\mathbf{J}_{\text{BH}}^f \parallel \mathbf{J}_{\text{tot}}$.
6. the disc within R_w is consumed and the BH spin magnitude changes according to Eq. (3.59) (right panel in Fig. 3.7), with M_d computed in step 3. Counter-alignment is taken into consideration as described in step 4. We also cap the spin parameter to 0.998, which is

the maximum spin allowed if photon trapping is assumed (Thorne, 1974). The BH mass is increased by $\Delta M_{\text{BH}} = M_d(1 - \epsilon_r)$.

We stress that it is possible to update the BH magnitude and direction separately because the latter changes over a shorter timescale than the former, i.e. first the BH spin aligns with the total angular momentum, then the magnitude changes because of accretion at the ISCO (for a detailed discussion on the impact of relevant timescales, see Perego et al., 2009; Dotti et al., 2013). Moreover, Eq. (3.59) does not depend on the direction, because it models angular momentum accretion from the innermost disc region, that is (counter-)aligned with the equatorial plane of the spinning BH due to the Bardeen-Petterson effect.

We also note that the mass per accretion episode M_d might be smaller or larger than the amount of mass required to be accreted during the simulation timestep Δt . Therefore, we follow Bustamante & Springel (2019) and adopt the following strategy:

- if $M_d < \dot{M}_{\text{BH}}\Delta t$, multiple accretion episodes occur over one BH simulation timestep Δt . We allow for timestep sub-cycles indexed with a counter variable, therefore executing $N = \dot{M}_{\text{BH}}\Delta t / M_d$ accretion episodes. All the sub-cycles share the same accretion rate, computed at the beginning of the timestep. At the end of each sub-cycle (i.e. accretion episode) we update BH spin and mass.
- if $M_d > \dot{M}_{\text{BH}}\Delta t$, we adopt the same strategy extending the counter across multiple timesteps. The code executes $N = M_d / (\dot{M}_{\text{BH}}\Delta t)$ timesteps, then the accretion episode ends and the BH mass and spin are updated using averages for the accretion rate necessary in Eqs. (3.54), (3.58), and (3.68), i.e.

$$\langle \dot{M}_{\text{BH}} \rangle_t = \frac{\sum_{i=1}^N \dot{M}_{\text{BH},i} \Delta t_i}{\sum_{i=1}^N \Delta t_i}, \quad (3.70)$$

Fig. 3.8 illustrates how the final value of a after a *single accretion episode* depends on M_{ratio} , for a few example values of initial a , assuming no misalignment is present. Note that the plotted lines do not correspond to evolutionary tracks of the BH in our simulations, the latter ones being defined instead by a succession of multiple accretion episodes, each one characterised by different initial directions and different values for M_{ratio} and r_{ISCO} . The solid and dotted lines correspond to counter-rotating events. Fig. 3.8 shows that a single counter-rotating accretion episode on a maximally spinning BH (solid line) would be able to spin it down to $a = 0$, if the accreted mass per episode were $\simeq 25\%$ of the BH initial mass. It would require an accreted mass of $\simeq 2$ times the BH mass to spin it up to $a = 1$, in a direction opposite to the initial one. Similarly, a counter-rotating accretion episode on a BH with $a = 0.5$ (dotted line) would require $\simeq 0.1M_{\text{BH}}$ and $1.75M_{\text{BH}}$ to achieve the same results, respectively. An accretion episode on a non-spinning BH (dashed line) needs to be $1.5M_{\text{BH}}$ to spin it up to its maximal value, whereas it needs to be equal to $\simeq M_{\text{BH}}$ to obtain the same result on a BH with $a = 0.5$ in co-rotating conditions (dash-dotted line).

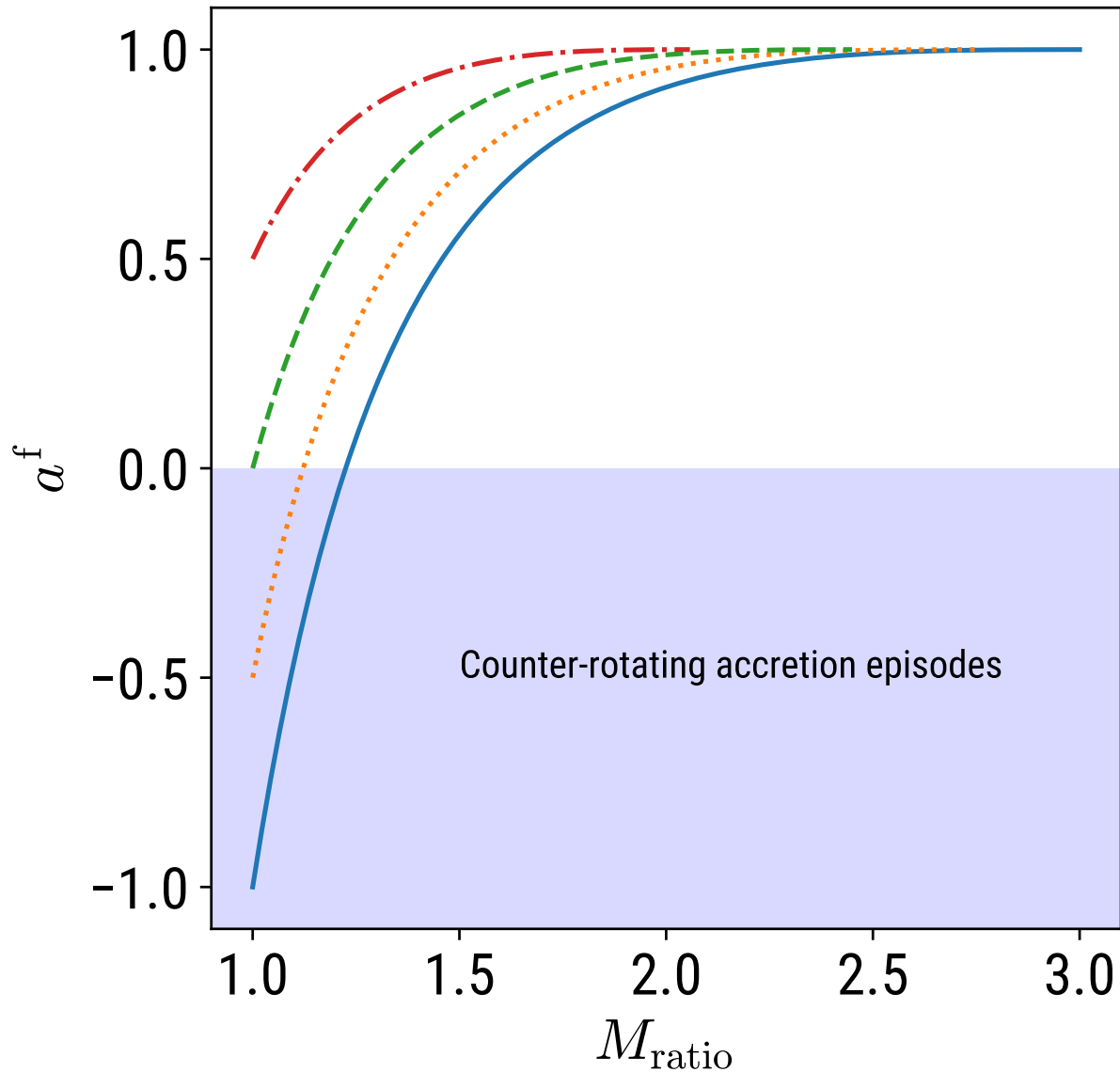


Figure 3.8: Final BH spin dimensionless parameter after a single accretion episode as a function of M_{ratio} as defined in Eq. (3.60). The solid, dotted, dashed and dot-dashed lines represent a^f for the initial spin values -1, -0.5, 0, and 0.5 respectively. The solid and dotted lines represent the event of an accretion episode in which the accretion disc is counter-rotating with respect to the BH.

Self-gravity regime

Depending on the physical conditions, parts of the accretion disc could become unstable because of their own self-gravity (Dotti et al., 2013). This occurs at radii that are beyond

$$\frac{R_{\text{sg}}}{R_{\text{BH}}} \simeq 5 \times 10^2 M_{\text{BH},8}^{-52/45} \left(\frac{f_{\text{Edd}}}{\epsilon_{r,01}} \right)^{-22/45} \alpha_{v_1,01}^{28/45}. \quad (3.71)$$

The mass stable against fragmentation (see Dotti et al., 2013) is then

$$M_{\text{sg}} \simeq 6 \times 10^5 M_{\text{BH},8}^{34/45} \left(\frac{f_{\text{Edd}}}{\epsilon_{r,01}} \right)^{4/45} \alpha_{v_1,01}^{-1/45} M_{\odot}. \quad (3.72)$$

Under this condition, only the region of the disc within R_{sg} can be accreted. Therefore, if $R_{\text{sg}} < R_{\text{w}}$ we set $M_{\text{d}} = M_{\text{sg}}$ and substitute R_{w} with R_{sg} in Eqs. (3.65) and (3.68). In this case,

$$\frac{J_{\text{d}}}{2J_{\text{BH}}} \simeq 9.4 \times 10^{-2} a^{-1} M_{\text{BH},8}^{-37/45} \left(\frac{f_{\text{Edd}}}{\epsilon_{r,01}} \right)^{-7/45} \alpha_{v_1,01}^{13/45}. \quad (3.73)$$

Whenever a BH is seeded, its spin is set to zero. As soon as $\dot{M}_{\text{BH}} > 0$, a disc is initialised with an angular momentum equal to

$$J_{\text{d}} = M_{\text{sg}} (GM_{\text{BH}} R_{\text{sg}})^{1/2}, \quad (3.74)$$

since we assume that only the portion of the disc that is stable against fragmentation can eventually accrete on the BH. The rest of the algorithm proceeds as before. M_{sg} and R_{sg} are computed using Eqs. (3.71) and (3.72) respectively.

3.2.2 BH mergers

We implement a prescription to account for spin evolution in the case of BH mergers. In what follows, we adopt the same strategy as Dubois et al. (2014b) and Bustamante & Springel (2019). We use equations retrieved in a full general-relativistic framework by Rezzolla et al. (2008a) to compute the final spin after a merger event. Following their notation, we define $\mathbf{a} = a \mathbf{j}_{\text{BH}}$. Once two BHs characterised by masses M_1 , M_2 and spins a_1 , a_2 have been selected to merge according to the criteria described in Sec. 2.3, the final spin vector of the remnant BH \mathbf{a}^f is given by

$$\mathbf{a}^f = \frac{1}{(1+q)^2} \left(\mathbf{a}_1 + \mathbf{a}_2 q^2 + \ell q \right), \quad (3.75)$$

where $q = M_2/M_1$, with $M_1 \geq M_2$. In this formula, M_1 and M_2 are the BH physical masses. $\ell = \ell'/(M_1 M_2)$ where ℓ' is the binary orbital angular momentum that cannot be radiated away in gravitational waves before coalescence. The magnitude of ℓ is provided by Rezzolla et al. (2008a) and reads

$$\begin{aligned} \ell = & \frac{s_4}{(1+q^2)^2} \left(a_1^2 + a_2^2 q^4 + 2\mathbf{a}_1 \cdot \mathbf{a}_2 q^2 \right) \\ & + \left(\frac{s_5 \mu + t_0 + 2}{1+q^2} \right) \left(a_1 \cos \phi_1 + a_2 q^2 \cos \phi_2 \right) \\ & + 2\sqrt{3} + t_2 \mu + t_3 \mu^2. \end{aligned} \quad (3.76)$$

Here, $\cos \phi = \mathbf{a} \cdot \boldsymbol{\ell} / (a\ell)$ depicts the angle subtended by the spin vector of BH with $\boldsymbol{\ell}$, $\mu = q/(1+q)^2$. $s_4 = -0.129$, $s_5 = -0.384$, $t_0 = -2.686$, $t_2 = -3.454$, $t_3 = 2.353$ are the parameters of the fit to their numerical results. We assume that $\boldsymbol{\ell}$ is parallel to the binary angular momentum $\mathbf{L} = \mathbf{L}_1 + \mathbf{L}_2$ (Rezzolla et al., 2008a). $\mathbf{L}_{i=1,2}$ is the angular momentum vector of BH i with respect to the binary centre of mass (CM), computed as $\mathbf{L}_i = M_i(\mathbf{r}_i - \mathbf{r}_{\text{CM}}) \times (\mathbf{v}_i - \mathbf{v}_{\text{CM}})$. The values for the radii \mathbf{r}_i and velocities \mathbf{v}_i are retrieved when the BHs are selected to merge.

3.2.3 AGN feedback

Our AGN feedback model assumes that a fraction ϵ_f of the radiated energy is coupled to the local ISM (refer to Table 4.2 and following sections for values), as often adopted in cosmological simulations (see e.g. Springel et al., 2005a; Di Matteo et al., 2008; Booth & Schaye, 2009). The total rate of coupled energy is thus:

$$\dot{E} = \epsilon_f \epsilon_r \dot{M}_{\text{BH}} c^2, \quad (3.77)$$

where ϵ_f is the coupling efficiency of the feedback energy to the surrounding ISM. An amount of energy $\Delta E = \dot{E} \Delta t$ is distributed among the particles surrounding each BH in a weighted fashion, using the SPH kernel. Moreover, we follow Hirschmann et al. (2014) and implement a transition from quasar- to maintenance-mode feedback by assuming a coupling efficiency ϵ_f larger by a factor of 4 when $f_{\text{Edd}} < 0.01$. In our model, the radiative efficiency ϵ_r depends on a through Eq. (3.64). This is at variance with other implementations where ϵ_r is either kept fixed (e.g., Springel et al., 2005a; Booth & Schaye, 2009; Hirschmann et al., 2014) or depends on the accretion rate and BH mass using a phenomenological prescription (e.g., Steinborn et al., 2015).

4 | Applications

The content of this chapter has been published in Sala et al. (2023):

Luca Sala, Milena Valentini, Veronica Biffi, Klaus Dolag:
Supermassive black hole spin evolution in cosmological simulations with OPENGADGET3
accepted for publication in *Astronomy & Astrophysics*

4.1 The suite of simulations

In the following sections we present our suite of simulations. We consider two idealised cases, a galaxy in isolation (Sec. 4.1.1) and a galaxy merger (Sec. 4.1.2), to test the model in a simple setup and study the evolution of the BH spin in a well-controlled environment. We also consider three setups in a full cosmological context (Sec. 4.1.3 and 4.1.4), which is key to capture the effects that the complex interplay between accretion and feedback can have on BH spin evolution. All the tests are performed including cooling, as well as star formation and evolution. The cosmological simulations include AGN and stellar feedback, whereas the idealised tests are performed with stellar feedback but no AGN feedback.

4.1.1 Idealised Milky Way galaxy

The first test we present is based upon the setup described in Steinwandel et al. (2019) aimed at modelling a Milky Way-like galaxy with total halo mass of $M_{200} = 10^{12} M_{\odot}$ in isolation with a BH at the potential minimum. M_{200} is the mass enclosed within the spherical region whose average density is 200 times the critical density of the Universe. We defer the reader to their paper for the detailed procedure used to generate the ICs.

Table 4.1 summarises the initial properties of the central BH in our tests. We consider a fiducial case (IdealGal-fid), initialised with $M_{\text{BH},0} = 5 \cdot 10^6 M_{\odot}$, $a_0 = 0.5$, $\theta_{z,0} = 170^{\circ}$ and $f_{\text{Edd}} = 1$. θ_z is the angle subtended by the BH spin and the z-axis. We perform further tests modifying one parameter at a time with respect to the fiducial run. Each simulation is labelled according to the value of the modified parameter, as in Table 4.1. Each test assumes a fixed Eddington fraction f_{Edd} for the duration of the simulation.

The resolution is the same for all the tests. Masses of DM, gas and star particles are: $m_{\text{DM}} = 9.6 \times 10^5 M_{\odot}$, $m_{\text{g}} = m_{*} = 4.8 \times 10^4 M_{\odot}$, respectively; the softening lengths are: $\varepsilon_{\text{DM}} = 218 \text{ pc}$ and $\varepsilon_{\text{g}} = \varepsilon_{*} = \varepsilon_{\text{BH}} = 50 \text{ pc}$.

Table 4.1: Parameter summary for the idealised tests. $M_{\text{BH},0}$ is the BH mass in the ICs, $\theta_{z,0}$ is the angle subtended by the initial BH spin direction and the positive z axis, $f_{\text{Edd}} = \dot{M}_{\text{BH}}/\dot{M}_{\text{Edd}}$ is the Eddington ratio.

Idealised Milky Way galaxy			
	$\theta_{z,0}$ [°]	$M_{\text{BH},0}$ [M_{\odot}]	f_{Edd}
IdealGal-fid	170	5×10^6	1
IdealGal-120	120	5×10^6	1
IdealGal-30	30	5×10^6	1
IdealGal-5e5	170	5×10^5	1
IdealGal-5e7	170	5×10^7	1
IdealGal-0.3	170	5×10^6	0.3

4.1.2 Idealised galaxy merger

The second set of ICs describes a galaxy merger with a mass ratio of 1:1, initialised following the procedure described in Karademir et al. (2019).

The setup consists of two identical Milky Way-like galaxies, each with mass $M_{200} = 1.89 \cdot 10^{12} M_{\odot}$. Each of them is embedded in a DM halo and has a spherical stellar bulge component, as well as an exponential stellar and gas discs. The initial separation of their CMs is 80 kpc and they rotate one around the other in the same direction in which they complete their revolution. The angle between the line connecting the two galaxy centres and their initial velocity vectors is equal to 40° . Fig. 4.1 shows the setup. The BHs are initialised with $a = 0$ and $M_{\text{BH}} = 2 \times 10^5 M_{\odot}$.

In this setup, $m_{\text{DM}} = 3.22 \times 10^6 M_{\odot}$, $m_{\text{g}} = m_{*} = 1.86 \times 10^6 M_{\odot}$, $\varepsilon_{\text{DM}} = 83$ pc and $\varepsilon_{\text{g}} = \varepsilon_{*} = \varepsilon_{\text{BH}} = 20$ pc.

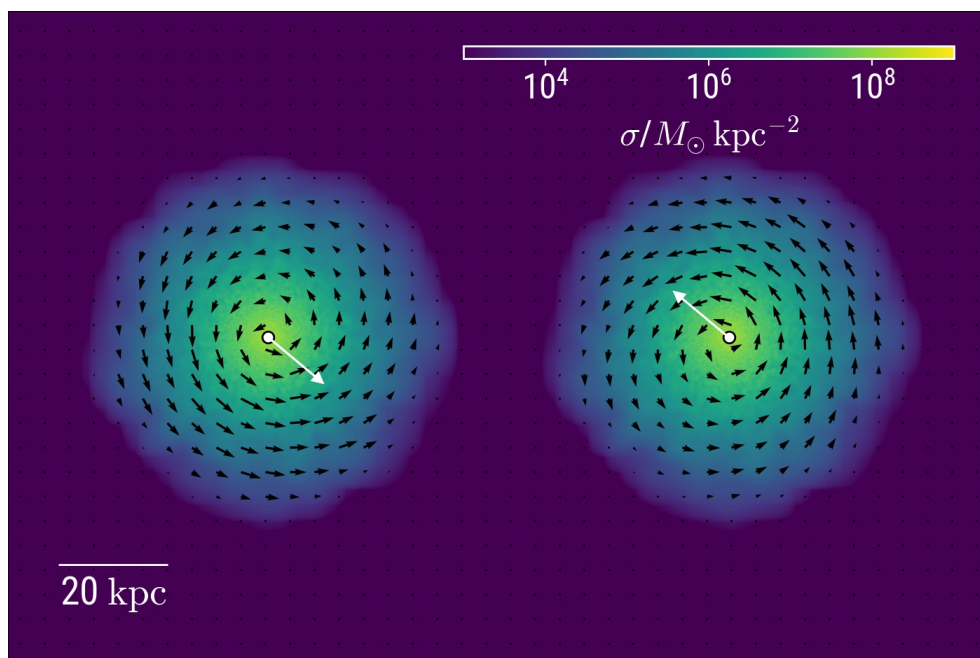


Figure 4.1: Gas density map of the ICs for the galaxy merger. The black arrows trace the local gas projected velocity field, while the white arrows indicate the initial direction of the CM of each galaxy. The arrows are scaled arbitrarily for visualisation purposes.

Table 4.2: Parameter summary of the cosmological simulations. a_{seed} is the BH spin parameter at seeding; ϵ_f is the feedback coupling efficiency (Sec. 3.2.3); $M_{\text{BH,seed}}$ is the BH mass at seeding; $M_{*,\text{seed}}$ is the stellar mass considered for BH seeding (Sec. 2.3); m_{DM} is the DM particle mass; m_g is the initial gas particle mass; m_* is the star particle mass; ϵ_{DM} , ϵ_g , and ϵ_* are the DM, gas, and stellar and BH softening length, respectively.

	a_{seed}	ϵ_f	$M_{\text{BH,seed}}$	$M_{*,\text{seed}}$	m_{DM}	m_g	m_*	ϵ_{DM}	ϵ_g	$\epsilon_{*,\text{BH}}$
			$[\text{M}_{\odot}/h]$	$[\text{M}_{\odot}/h]$	$[\text{M}_{\odot}/h]$	$[\text{M}_{\odot}/h]$	$[\text{M}_{\odot}/h]$	$[\text{kpc}/h]$	$[\text{kpc}/h]$	$[\text{kpc}/h]$
Zoom-in simulations										
ASIN/DFROGIN	0	0.05	2×10^5	1×10^9	3.3×10^7	6.25×10^7	1.6×10^7	1	1	0.25
Cosmological box										
Box4	0	0.0775	4×10^5	1.6×10^{10}	6.9×10^8	1.4×10^8	3.5×10^7	3.75	3.75	2.0

4.1.3 Zoom-in simulations

We perform our zoom-in simulations starting from ICs generated with the procedure described in Bonafede et al. (2011). We consider two halos: a region with target mass $M_{200} \simeq 10^{12} h^{-1} M_{\odot}$, dubbed ASIN; a region with target mass $M_{200} \simeq 10^{13} h^{-1} M_{\odot}$, dubbed DFROGIN. They are selected from a parent DM-only simulation of a periodic box with side length $L_{\text{box}} = 1 h^{-1} \text{ cGpc}$ and resolution $m_{\text{DM}} = 10^9 h^{-1} M_{\odot}$. The final resolution is quoted in Table 4.2, together with the properties and parameters of each simulation. This set of simulations adopts a flat Λ CDM cosmological model, with a matter density parameter $\Omega_{\text{m}} = 0.24$, a baryon density parameter $\Omega_{\text{b}} = 0.04$ and $h = 0.72$. The initial power spectrum follows $n = 0.96$ and is normalised to $\sigma_8 = 0.8$.

4.1.4 Cosmological box

We carry out a simulation starting from the ICs of the cosmological volume with $L_{\text{box}} = 48 h^{-1} \text{ cMpc}$ (hereafter Box4) of the Magneticum¹ simulations suite. Such a simulation, that contains $\sim 10^3$ BHs at redshift $z = 0$, allows us to analyse the properties of a statistically significant BH population, rather than focussing only on the specific behaviour of a few BHs.

Table 4.2 summarises the properties and parameters of the simulation. It assumes a flat Λ CDM model, with $\Omega_{\text{m}} = 0.272$, $\Omega_{\text{b}} = 0.0456$ and $h = 0.704$, $n = 0.963$ and $\sigma_8 = 0.809$.

4.2 Results

4.2.1 Idealised Milky Way galaxy

Fig. 4.2 presents the BH spin evolution in the tests listed in Table 4.1. Top left panel shows the time evolution of θ_z , the angle between \mathbf{j}_{BH} and the unit vector indicating the positive z-axis \mathbf{j}_z . The isolated galaxy is initialised with the angular momentum of the accreting gas along \mathbf{j}_z (i.e. $\theta_z = \pi$ refers to the BH spin direction being anti-parallel to the galaxy angular momentum, while $\theta_z = 0$ refers to complete alignment). According to condition (3.56), counter-rotating accretion requires both $\mathbf{j}_d \cdot \mathbf{j}_{\text{BH}} > \pi/2$ and $J_d < 2J_{\text{BH}}$. In IdealGal-fid, IdealGal-120, IdealGal-5e5, IdealGal-5e7 and IdealGal-0.3 both conditions are satisfied at the beginning. However, the accreting gas in the BH surroundings keeps the same direction across the entire simulation, i.e. \mathbf{j}_g remains constant. As a result, the initial sub-grid disc direction \mathbf{j}_d for every accretion episode is also constant (Eq. 3.66, $\mathbf{j}_g = \mathbf{j}_d$). Therefore, each of them induces the BH spin to tilt towards the angular momentum direction of the large-scale external reservoir. Note that also J_d/J_{BH} is approximately constant in these runs (a and ϵ_r vary slightly, but J_d/J_{BH} depends weakly on them, see Eq. 3.69). Whether or not condition (3.56) is verified in these tests depends only on $\mathbf{j}_d \cdot \mathbf{j}_{\text{BH}}$ (actually only on \mathbf{j}_{BH} , since \mathbf{j}_d is constant). Each vertical dotted line marks the first instant in which accretion becomes co-rotating (from counter-rotating; i.e., condition (3.56) is no longer verified after this instant). In IdealGal-fid the BH spin completes its alignment with the external reservoir in $\sim 2 \text{ Myr}$. If

¹<http://www.magneticum.org>

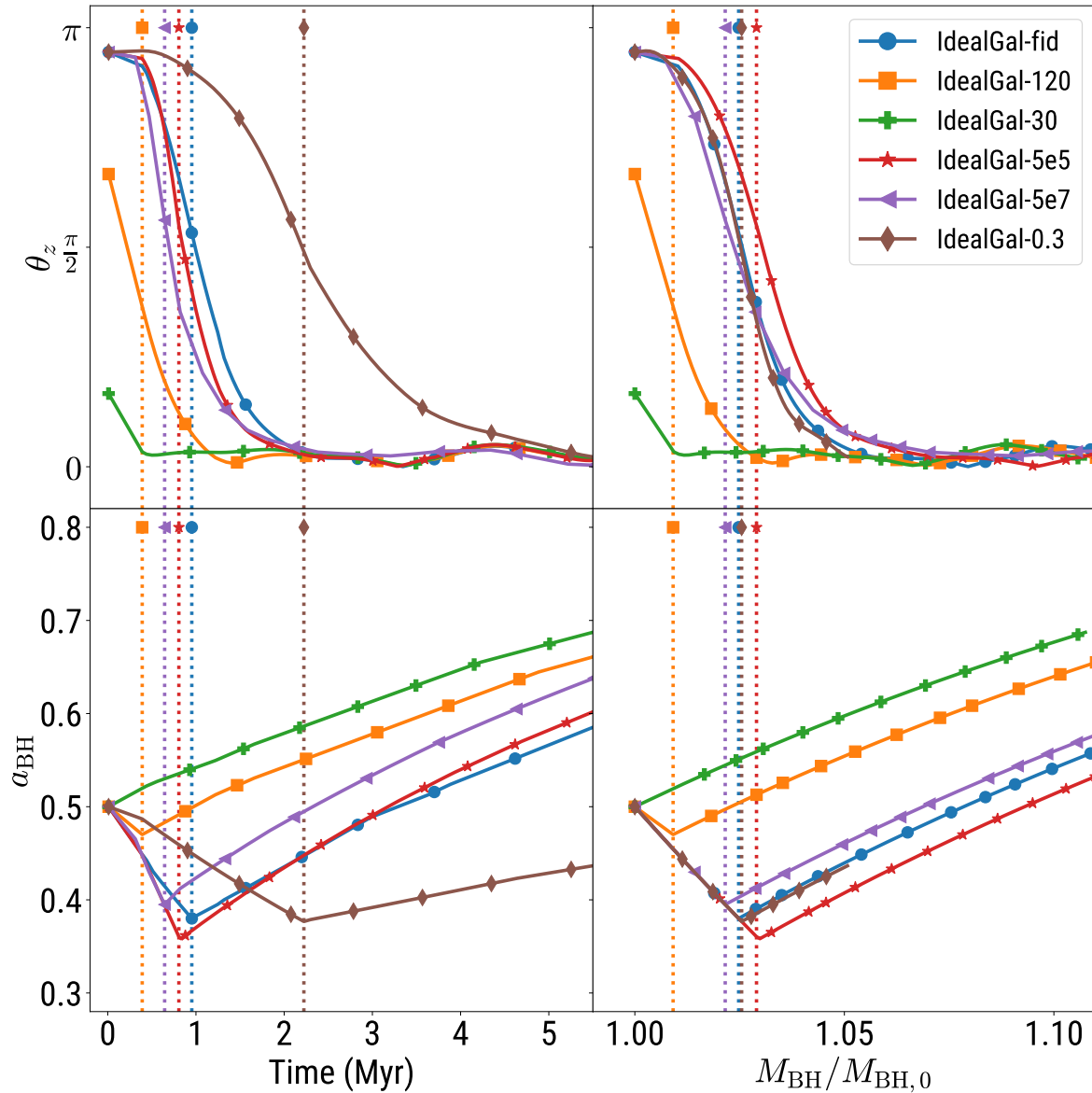


Figure 4.2: Spin alignment process in the idealised Milky Way galaxy. Top panels: angle subtended by the BH angular momentum and the z-axis θ_z . Bottom panels: BH spin parameter a . Quantities are plotted as a function of time (left panels) and of the ratio between accreted and initial BH mass $M_{\text{BH}}/M_{\text{BH},0}$ (right). Each line represents one simulation of the set summarised in Table 4.1. Dotted lines represent the instant after which condition (3.56) is no longer satisfied.

we keep the same Eddington ratio but change the BH mass (IdealGal-5e5 and IdealGal-5e7, respectively), alignment takes the same time. On the other hand, alignment takes longer (~ 5 Myr) to complete with the same mass but a lower Eddington ratio (IdealGal-0.3). At fixed BH mass and Eddington ratio (IdealGal-fid, -120, and -30), the alignment timescale depends weakly on the initial misalignment angle. A smaller $\theta_{z,0}$ leads to a faster alignment.

The bottom left panel of Fig. 4.2 illustrates the time evolution of the BH spin parameter a . Since IdealGal-fid, IdealGal-120, IdealGal-5e5, IdealGal-5e7 and IdealGal-0.3 start with counter-rotating accretion conditions, a decreases. At $t \simeq 1$ Myr co-rotating conditions take over and a starts increasing. The turnaround point occurs in correspondence of the dotted line, after which condition (3.56) is no longer verified. In IdealGal-30, a monotonically increases as condition (3.56) is not verified from the very beginning.

The top right panel of Fig. 4.2 shows θ_z as a function of the ratio $M_{\text{BH}}/M_{\text{BH},0}$. At fixed $\theta_{z,0}$ (IdealGal-fid, -5e5, -5e7, and -0.3), the same ratio of accreted mass over BH mass ($M_{\text{BH}} \sim 5\% M_{\text{BH},0}$) is needed for complete alignment to occur, regardless of other parameters. The actual time it takes to align depends on how fast the BH accretion proceeds. BHs whose spin starts with smaller $\theta_{z,0}$ (IdealGal-120 and -30) require less time.

The bottom right panel of Fig. 4.2 presents a as a function of the ratio $M_{\text{BH}}/M_{\text{BH},0}$. Similarly to the bottom left panel, the turnaround point occurs in correspondence of the dotted line, when accretion switches from counter- to co-rotating. This plot further shows that it occurs at about the same value of $M_{\text{BH}}/M_{\text{BH},0}$ at fixed $\theta_{z,0}$. Finally, for smaller $\theta_{z,0}$ a smaller ratio is required to reach the turnaround point.

The behaviour of both θ_z and a as a function of $M_{\text{BH}}/M_{\text{BH},0}$ is similar for simulations assuming the same $\theta_{z,0}$ because f_{Edd} is fixed. Indeed, the BH grows according to the following differential equation

$$\frac{dM_{\text{BH}}}{dt} = (1 - \epsilon_r) f_{\text{Edd}} \dot{M}_{\text{Edd}} = f_{\text{Edd}} \frac{1 - \epsilon_r}{\epsilon_r} \frac{M_{\text{BH}}}{\tau_S}, \quad (4.1)$$

where $\tau_S = \sigma_{\text{TC}}/(4\pi G m_p) \sim 4.5 \times 10^8$ yr is the Salpeter time. As a result,

$$\frac{M_{\text{BH}}}{M_{\text{BH},0}} = \exp\left(f_{\text{Edd}} \frac{1 - \epsilon_r}{\epsilon_r} \frac{t}{\tau_S}\right). \quad (4.2)$$

Therefore, the evolution of θ_z and a as a function of time is different depending on f_{Edd} (compare IdealGal-fid and IdealGal-0.3). On the other hand, the curves overlap if we consider $M_{\text{BH}}/M_{\text{BH},0}$ as the independent variable (and they are independent of $M_{\text{BH},0}$ – see IdealGal-fid, IdealGal-5e5, IdealGal-5e7).

4.2.2 Idealised galaxy merger

Fig. 4.3 presents the evolution of the spins of the two BHs (one identified with the solid blue lines and the other with the dashed orange lines) in the idealised merger simulation. The left panel shows the evolution of quantities for the entire simulated timespan, whereas the right panel shows a 2 Myr window, centred on the merger instant, marked in both panels by the vertical grey dotted line.

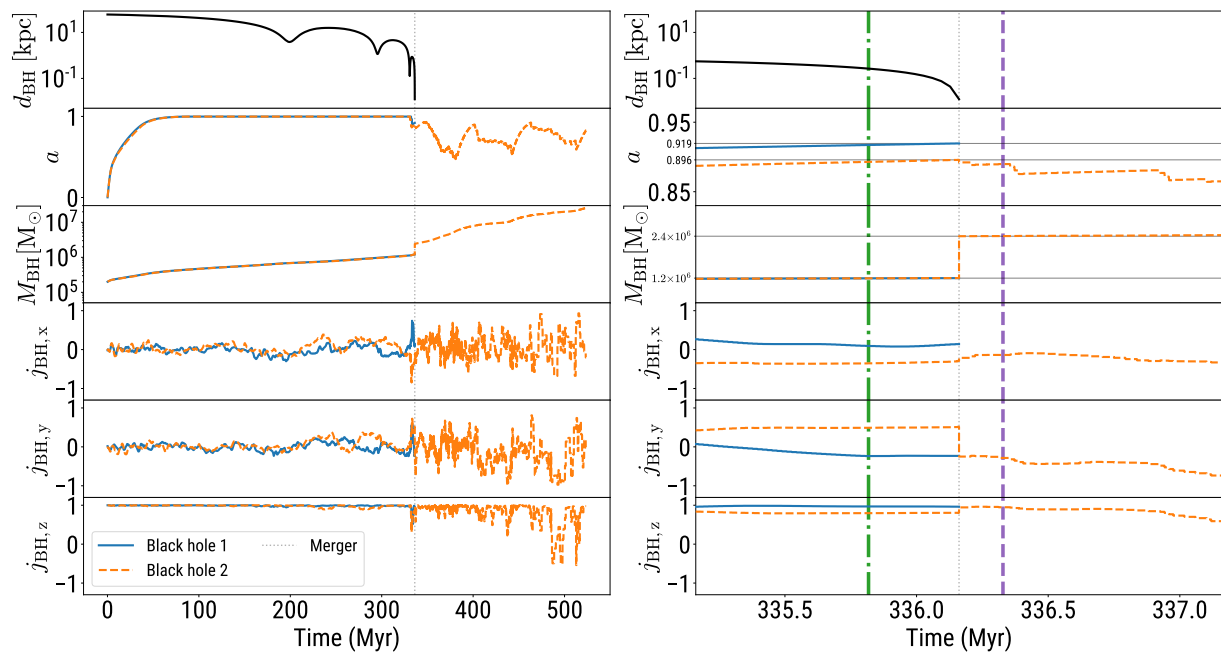


Figure 4.3: Time evolution of a few properties of the two BHs (each of them is depicted by either blue solid or orange dotted lines) in the idealised galaxy merger simulation. From top to bottom: separation distance between the two BHs; BH dimensionless spin parameter; BH mass; x, y, z component of the unit vector of the BH angular momentum. *Left panel*: entire simulated timespan. *Right panel*: timespan of 2 Myr, centred on the time of the merger (grey, dotted vertical line). The vertical green dash-dotted and purple dashed lines mark the instants in time illustrated in the top and bottom panel of Fig. 4.4, respectively.

The first row from the top of Fig. 4.3 shows the separation distance between the BHs. The galaxies undergo three pericentre passages before the BHs merge (left panel), at ~ 336.15 Myr (right panel).

The second row of Fig. 4.3 follows the evolution of the spin parameter a . The left panel shows that both BHs follow an identical path from zero spin to maximal within 50 Myr (the two galaxies of the pair are identical). They are kept at maximal spin by accretion occurring consistently on the same plane, until the third pericentre passage. At this stage accretion becomes less coherent – i.e. the direction of the local angular momentum has larger variability – and a decreases slightly due to counter-rotating accretion conditions. In the right panel, second row, just before the merger instant we identify two progenitors with $a \sim 0.9$. The final remnant has $a \sim 0.9$.

The third row of Fig. 4.3 shows the evolution of M_{BH} . On the left, we see that the mass increases steadily and identically for the two BHs. The right panel allows us to identify two equal-mass progenitors with $M_{\text{BH}} = 1.2 \times 10^6 M_{\odot}$ merging into a remnant of $M_{\text{BH}} = 2.4 \times 10^6 M_{\odot}$.

Rows 4 to 6 of Fig. 4.3 show the three components of the BH spin direction. In the left panel we see that the two BHs consistently accrete from the same plane, hence their spins are kept very well aligned with the angular momentum direction of the host galaxies, which is along \mathbf{j}_z . The pericentre passages create some disturbance in the gas close to the BH, temporarily inducing the BH spin to tilt. This effect is more prominent close to the merger. In the right panel, we see that the BH spin components immediately before the merger are close to \mathbf{j}_z , although with some disturbances induced by the local environment. Furthermore, the spin of the remnant is also aligned with \mathbf{j}_z .

Fig. 4.4 represents visually the process just described, using a volume rendering of the gas density in the simulation, for two simulation snapshots. The field of view depicted in the figure spans a width of 55 kpc and a height of 31 kpc, as measured along a plane that intersects the centre of the rendering volume, offering a perspective view of the merging galaxies. The arrows represent the instantaneous directions of the BH spins. The top panel of Fig. 4.4 corresponds to the instant marked by the green dash-dotted line in the right panel of Fig. 4.3, showing the pre-merger configuration. The bottom panel of Fig. 4.4 corresponds to the time marked by the purple dashed line, displaying the post-merger configuration.

The idealised galaxy merger test enables a simplified computation of the expected BH spin of the merger remnant to validate the result obtained. The pre-merger configuration (as shown in the right panels of Fig. 4.3 and in the top panel of Fig. 4.4) can be approximated to the idealised configuration of an equal-mass BH binary with aligned spins treated in Rezzolla et al. (2008b). In this configuration, the final spin magnitude a_f depends only on the initial spin magnitudes a_1 and a_2 (and the final direction is equal to the initial one). Two BHs with $a \sim 0.9$ and spins in the same direction are indeed expected to end up in a merger remnant with $a \sim 0.9$ and spin along the original, common rotation axis, as observed in our test.

4.2.3 Zoom-in simulations

Fig. 4.5 presents projected gas density maps at $z = 0$ of ASIN (top) and DFROGIN (bottom). The white dots mark the positions of the BHs in the simulation. In what follows, we consider only the BHs that lie within a spherical region of radius $5R_{200}$ at $z = 0$, centred on the target halo

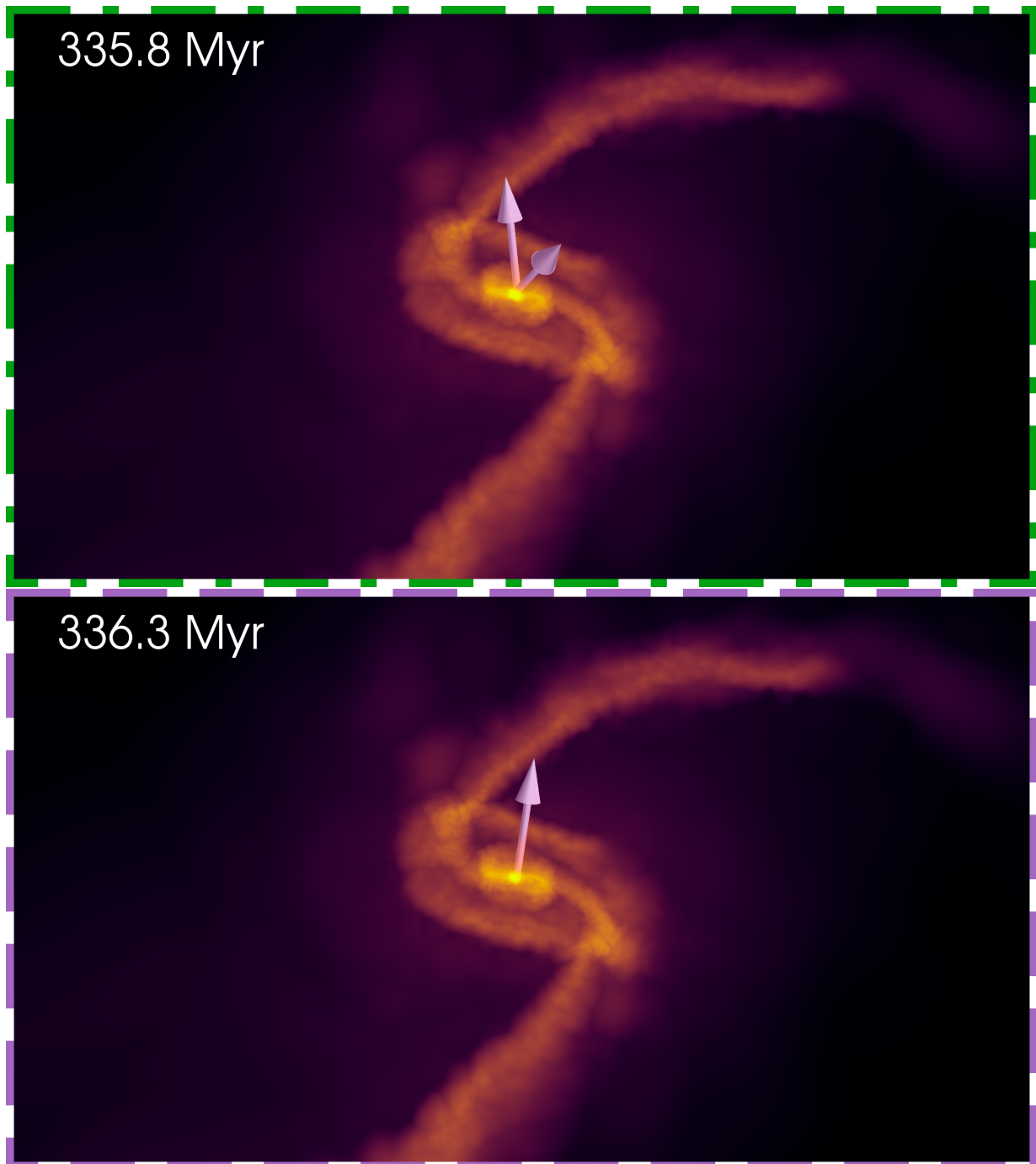


Figure 4.4: 3D perspective volumetric rendering of the gas density in the idealised galaxy merger simulation. The field of view depicted in the figure spans a width of 55 kpc and a height of 31 kpc, as measured along a plane that intersects the centre of the rendering volume. *Top panel*: last snapshot before the merger. *Bottom panel*: first snapshot after merger. The arrows mark the instantaneous direction of the BH spin vector.

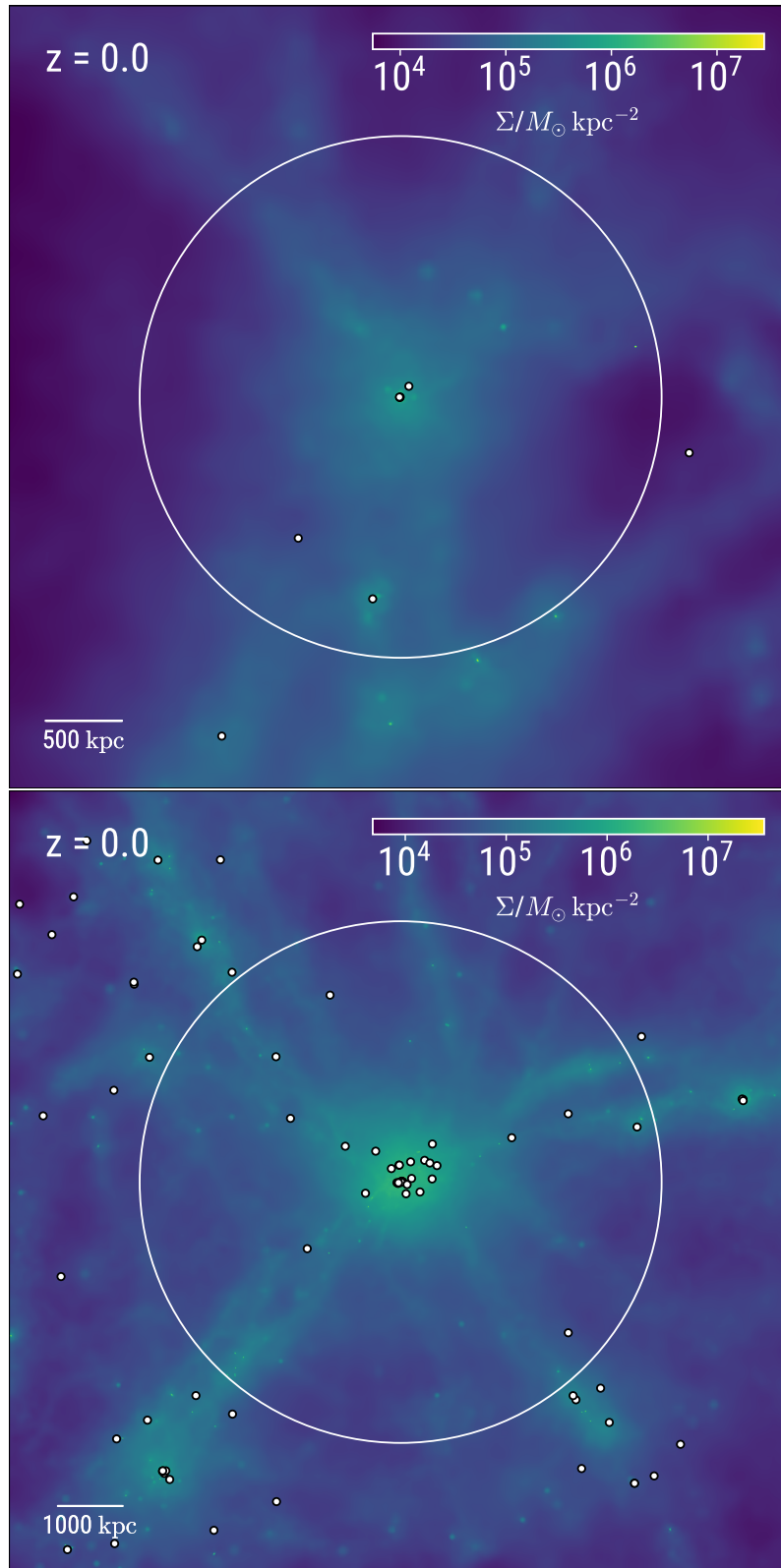


Figure 4.5: Gas surface density maps at $z = 0$ for the ASIN (top) and DFROGIN (bottom) runs. The white circle indicates a spherical region of radius $5R_{200}$, centred on the target halo of the zoom-in region (i.e. the most massive at $z = 0$). The white dots mark the positions of the BHs in the simulation.

of interest of the zoom-in region (i.e. the most massive one at $z = 0$). R_{200} is the radius of the spherical volume, centred on the subhalo, whose average density is 200 times the critical density of the Universe. The region is marked by the white circle in Fig. 4.5. The main purpose of this selection is to exclude BHs that are close to the border of the high-resolution region.

Fig. 4.6 shows the BH sample at $z = 0$ in `ASIN` (diamonds) and `DFROGIN` (stars) in the BH mass-stellar mass ($M_{\text{BH}} - M_*$) plane. The BHs are selected according to the criterion explained above; the sample is composed by 4 BHs in `ASIN` with $10^{6.5} \lesssim M_{\text{BH}}/M_{\odot} \lesssim 10^8$ and 21 BHs in `DFROGIN`, with $10^6 \lesssim M_{\text{BH}}/M_{\odot} \lesssim 10^9$. Each BH is associated to a subhalo identified with the sub-structure finder algorithm `SUBFIND` (Springel et al., 2001a; Dolag et al., 2009) based on particle ID matching. Whenever more than one BH is associated to the same subhalo, the closest to the subhalo centre is chosen. M_* is the stellar mass as computed by `SUBFIND`. The dashed line shows the experimental fit by McConnell & Ma (2013), while crosses with associated uncertainties show observations from Kormendy & Ho (2013).

Fig. 4.7 presents the spin parameters of the BHs in the simulated regions as a function of M_{BH} at $z = 0$, with the same symbols used in Fig. 4.6. We compare our simulation output to the available observations that provide estimates of a and BH mass, with associated uncertainties. We include the collection by Reynolds (2021), with updates by Bambi et al. (2021) as described in Sisk-Reynés et al. 2022, as well as the low-mass sample by Mallick et al. (2022). We also include the spin estimate by Walton et al. (2021). In particular, we include the result by Sisk-Reynés et al. (2022), who provide a well-defined constraint of the spin of a $\sim 3 \times 10^9 M_{\odot}$ BH, the most massive for which such a measure has been obtained to date. We observe a range of BH masses ($10^6 \lesssim M_{\text{BH}}/M_{\odot} \lesssim 5 \times 10^7$) where BH spins tend to be larger than $a \sim 0.70$, in both the simulated regions. Several of them are maximally spinning. For masses above $5 \times 10^7 M_{\odot}$, there are no maximally spinning BHs, whereas the most massive BH in each region systematically has a lower spin, $a \simeq 0.25$ in `ASIN` and $a \simeq 0.1$ in `DFROGIN`.

Fig. 4.8 shows the time evolution of a few BH properties predicted by the sub-resolution model. We restrict our analysis to the most massive BH of the sample in `DFROGIN`, and focus on the relationship between BH spin and gas accretion as they evolve with time. The evolutionary tracks of the other BHs in the sample display features which are similar to those of our reference, most massive BH as for the interplay between the BH spin and the fuelling gas. The upper axis of Fig. 4.8 marks the time since the Big Bang, while the lower axis shows the redshift z . Across the panels, the vertical dashed lines mark the occurrence of mergers.

The top panel of Fig. 4.8 shows the z -components of \mathbf{j}_{BH} (black, solid line) and \mathbf{j}_{g} (orange, dashed line). Before 1.7 Gyr, \mathbf{j}_{g} varies gradually with time, with a clear, average trend and limited scatter. From $\simeq 1.7$ to $\simeq 2.6$ Gyr a trend in \mathbf{j}_{g} is still present but the scatter increases. \mathbf{j}_{BH} follows the average evolution of \mathbf{j}_{g} . From $\simeq 2.6$ to $\simeq 6$ Gyr, \mathbf{j}_{g} exhibits drastic and sudden changes, whereas \mathbf{j}_{BH} remains stable with minimal variations. After $\simeq 6$ Gyr, \mathbf{j}_{BH} often undergoes abrupt variations due to the erratic behaviour of \mathbf{j}_{g} .

The second row of Fig. 4.8 shows $\cos \theta_{\text{BH-d}}$ (black solid line), i.e. the left-hand-side term of Eq. (3.56), as a function of time. The orange dashed line shows $-J_{\text{d}}/(2J_{\text{BH}})$, i.e. the right-hand side of Eq. (3.56). Before $\simeq 1.7$ Gyr each accretion episode is characterised by consistently small misalignment. Between $\simeq 1.7$ and $\simeq 2.6$ Gyr several accretion episodes display $\theta_{\text{BH-d}}$ close to $\pi/2$. After $\simeq 2.6$ Gyr accretion episodes are mostly misaligned. This panel also allows us to

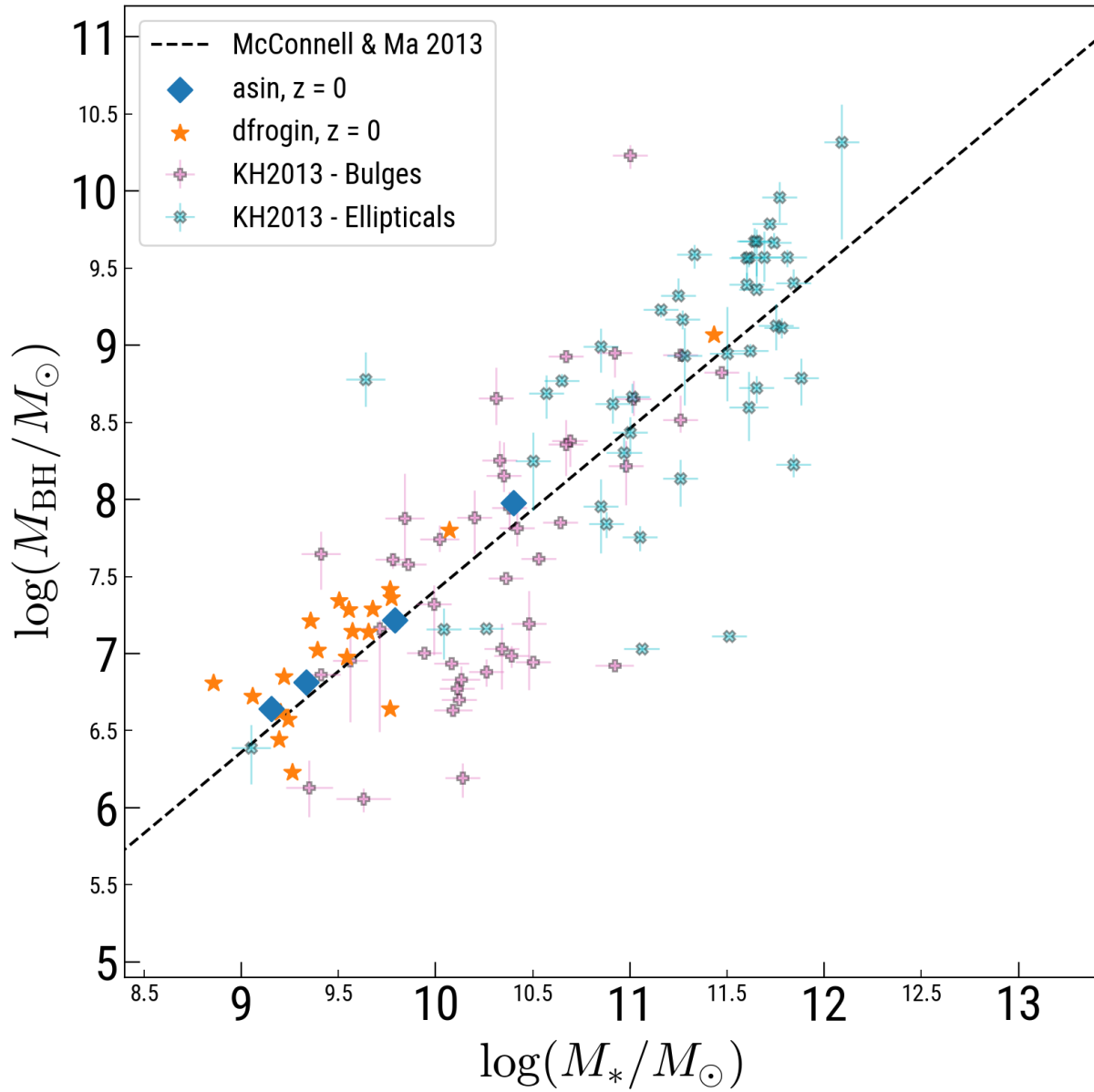


Figure 4.6: M_{BH} as a function of stellar mass M_* , at $z = 0$. Diamonds and stars represent BHs in ASIN and DFROGIN, respectively. The dashed line shows the experimental fit by McConnell & Ma (2013), while crosses with associated uncertainties show data from Kormendy & Ho (2013).

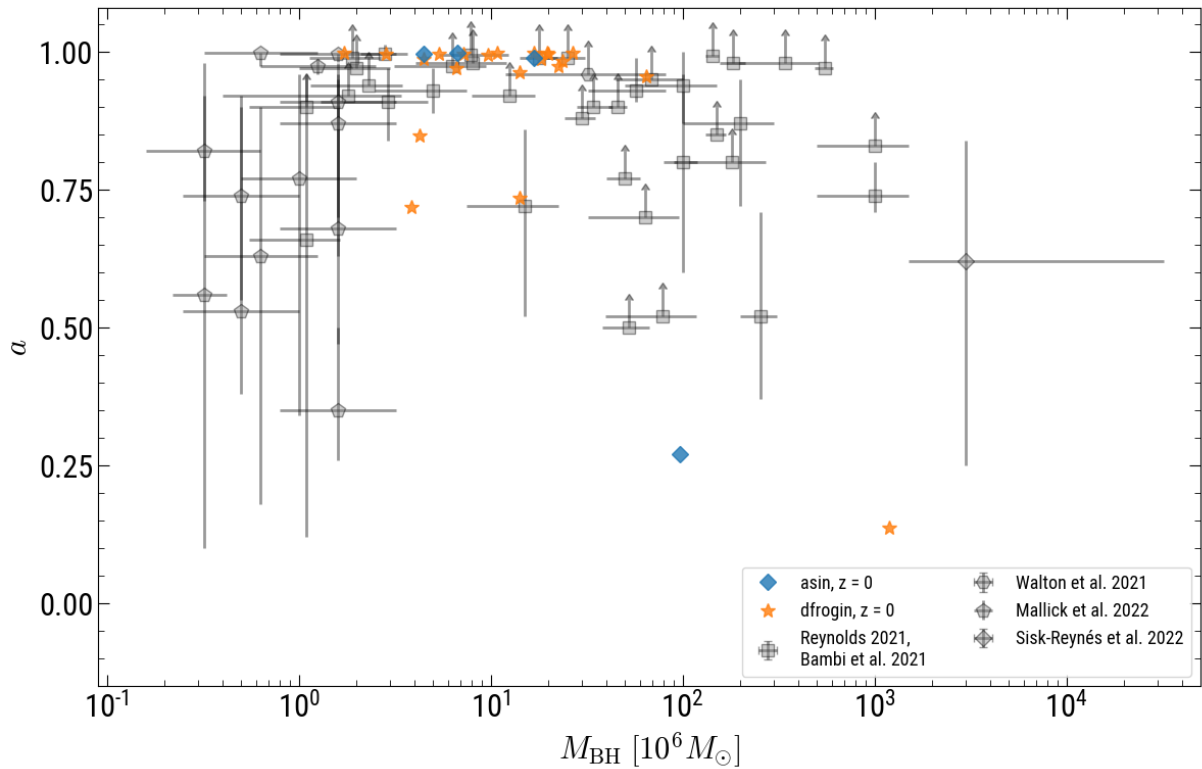


Figure 4.7: BH spin parameters a of the selected BH sample in ASIN (diamonds) and DFROGIN (stars) as a function of M_{BH} , at $z = 0$. The squares and pentagons show the collection of observational measurements of the BH spin parameter by Reynolds (2021) (with updates from Bambi et al. 2021) and Mallick et al. (2022), respectively. The hexagon represents the spin estimate reported by Walton et al. (2021) and the diamond represents the measurement obtained by Sisk-Reynés et al. (2022).

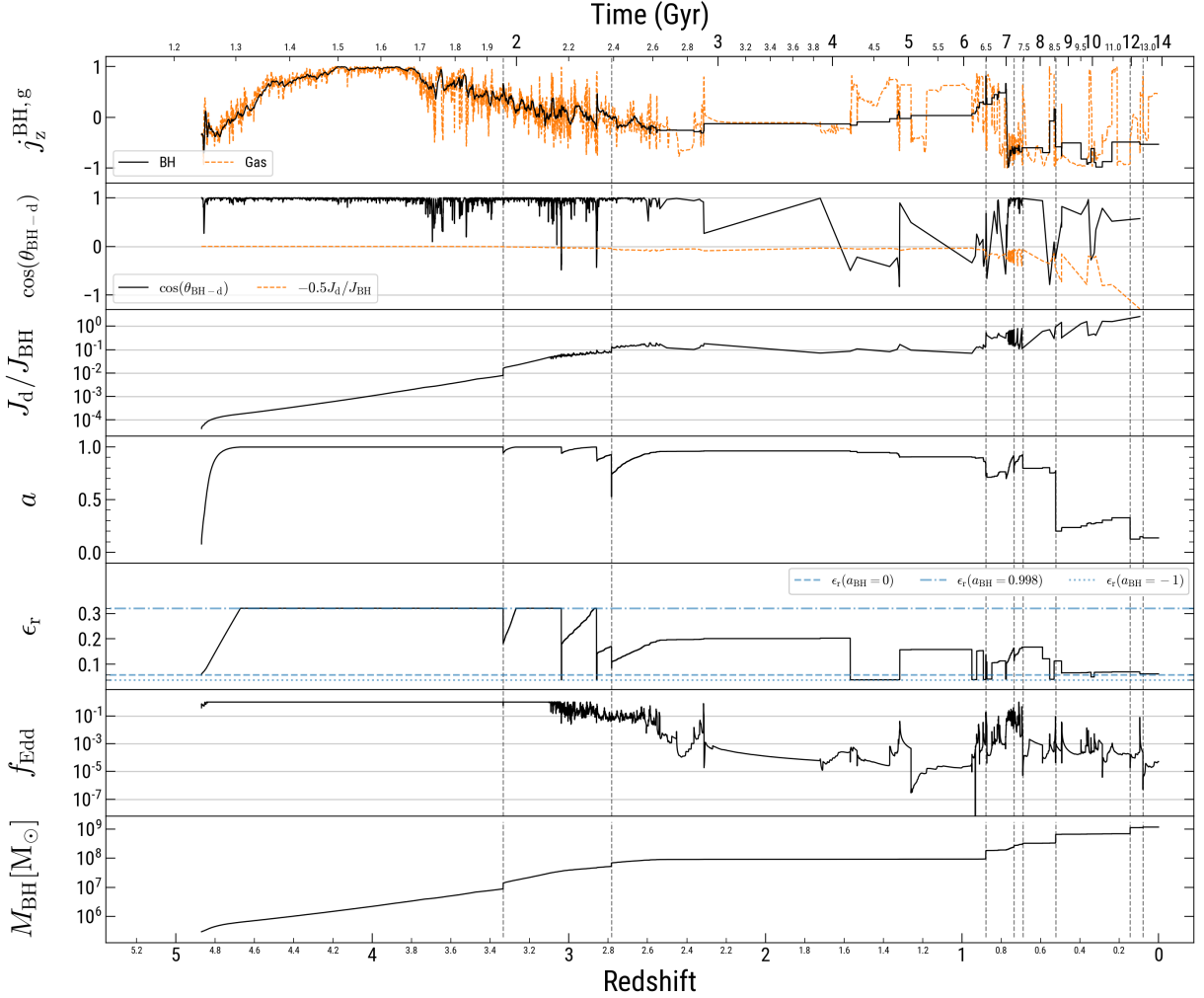


Figure 4.8: Summary of properties related to the most massive BH in the `dfrogin` run, as they evolve across time. From top to bottom: z -component of the BH spin direction $j_{\text{BH},z}$ (black, solid line) and direction of the angular momentum of the gas in the BH kernel $j_{g,z}$ (orange, dashed line); cosine of the angle between the accretion disc and the BH spin at the beginning of each accretion episode $\cos \theta_{\text{BH-d}}$ (i.e. left-hand side of Eq. (3.56), black solid line) and $-J_d/(2J_{\text{BH}})$ (i.e. right-hand side of Eq. (3.56), orange dashed line); ratio of the magnitudes of the disc and BH angular momenta J_d/J_{BH} ; BH dimensionless spin parameter a ; radiative efficiency of the accretion disc ϵ_r ; Eddington ratio f_{Edd} ; BH mass M_{BH} .

easily identify counter-rotating accretion episodes, when $\cos(\theta_{\text{BH-d}}) < -J_{\text{d}}/(2J_{\text{BH}})$ (e.g. around 2.2 Gyr and 4.5 Gyr).

The third row of Fig. 4.8 shows $J_{\text{d}}/J_{\text{BH}}$, the ratio between the accretion disc and the BH angular momentum per accretion episode. This quantity controls how much a single accretion episode is able to modify the direction of the BH spin and ultimately determines to which degree the BH spin is able to follow the variations of \mathbf{j}_{g} . Being the BH spin direction \mathbf{j}_{BH}^f after an accretion episode parallel to $\mathbf{J}_{\text{tot}} = \mathbf{J}_{\text{d}} + \mathbf{J}_{\text{BH}}$, if $J_{\text{d}} \ll J_{\text{BH}}$, then $\mathbf{j}_{\text{BH}}^f \sim \mathbf{j}_{\text{tot}} \sim \mathbf{j}_{\text{BH}}$ (i.e. the direction change is negligible; Sec. 3.2.1). Conversely, if $J_{\text{d}} \gg J_{\text{BH}}$, then $\mathbf{j}_{\text{BH}}^f \sim \mathbf{j}_{\text{d}}$, i.e. \mathbf{j}_{BH} aligns with the direction imparted by \mathbf{j}_{d} (and hence \mathbf{j}_{g}). In an intermediate configuration \mathbf{j}_{BH} only partially aligns with \mathbf{j}_{d} . The latter situation is expected to occur before $\simeq 6$ Gyr, when $J_{\text{d}}/J_{\text{BH}} \lesssim 0.1$. However, at $t \gtrsim 6$ Gyr $J_{\text{d}}/J_{\text{BH}}$ sometimes approaches 1; as a result, \mathbf{j}_{BH} exhibits larger variations as a response to large changes in \mathbf{j}_{g} . Although here we inspect the evolution of $J_{\text{d}}/J_{\text{BH}}$ and $\theta_{\text{BH-d}}$ for one BH as an example, we properly quantify how the change \mathbf{j}_{BH} depends on these two quantities by analysing accretion episodes statistically in the cosmological box (Sec. 4.2.4).

The fourth row of Fig. 4.8 shows the BH dimensionless spin parameter a . Its evolution is characterised by a maximally spinning phase until $t \simeq 1.95$ Gyr ($z \gtrsim 3.3$). The largest spin-downs occur because of mergers, although we also observe counter-rotating phases that decrease the spin due to gas accretion (e.g. at $t \simeq 2.2$ and $\simeq 2.35$ Gyr, as well as around 4.5 Gyr).

The fifth row of Fig. 4.8 plots the radiative efficiency, which depends on a (see Eq. 3.64). The dash-dotted, dashed and dotted lines mark the values of efficiency for $a = 0.998$, 0 and for a counter-rotating episode on a BH with $a = 1$, respectively. The maximally spinning period before $z \sim 3.5$ corresponds to a maximal efficiency of 0.32, whereas later times are characterised by a lower efficiency. Counter-rotating accretion conditions are clearly visible as a drastic decrease in efficiency, close to the minimum theoretical value marked by the dotted line.

The sixth row of Fig. 4.8 illustrates the Eddington ratio f_{Edd} . Accretion is Eddington-limited soon after the BH is seeded ($z \sim 4.9$). f_{Edd} is typically $\gtrsim 10^{-1}$ until $z \sim 2.6$. Between $0.9 \lesssim z \lesssim 2.6$, $f_{\text{Edd}} \ll 10^{-1}$ for most of the time. A few highly accreting ($f_{\text{Edd}} \simeq 10^{-1}$) episodes occur in proximity of the mergers at $z \sim 0.9$ and $z \sim 0.7$, and lead to significant reorientation of the BH spin (see first row of Fig. 4.8). After $z \sim 0.7$ f_{Edd} is mostly $\lesssim 10^{-3}$. Comparing with the evolution of a (fourth row of Fig. 4.8), we observe that the largest f_{Edd} , the largest is the change induced in a .

The last row of Fig. 4.8 plots M_{BH} . The BH increases its mass by three orders of magnitude during the highly accreting phase at $z \gtrsim 2.6$. After $z \sim 2.6$, the BH gets more massive (by about one order of magnitude) mostly due to mergers.

4.2.4 Cosmological box

For the analysis of Box4 we consider all the BHs in the cosmological volume and we select them at $z = 0$. We associate each BH to a subhalo based on particle ID matching using SUBFIND and whenever more than one BH is associated to the same subhalo, the closest to the subhalo centre is chosen. The sample includes 1790 BHs, in a mass range between 6×10^6 and $2 \times 10^{10} M_{\odot}$.

Fig. 4.9 frames the Box4 BH sample at $z \sim 0$ in the $M_{\text{BH}} - M_{*}$ plane. M_{*} corresponds to

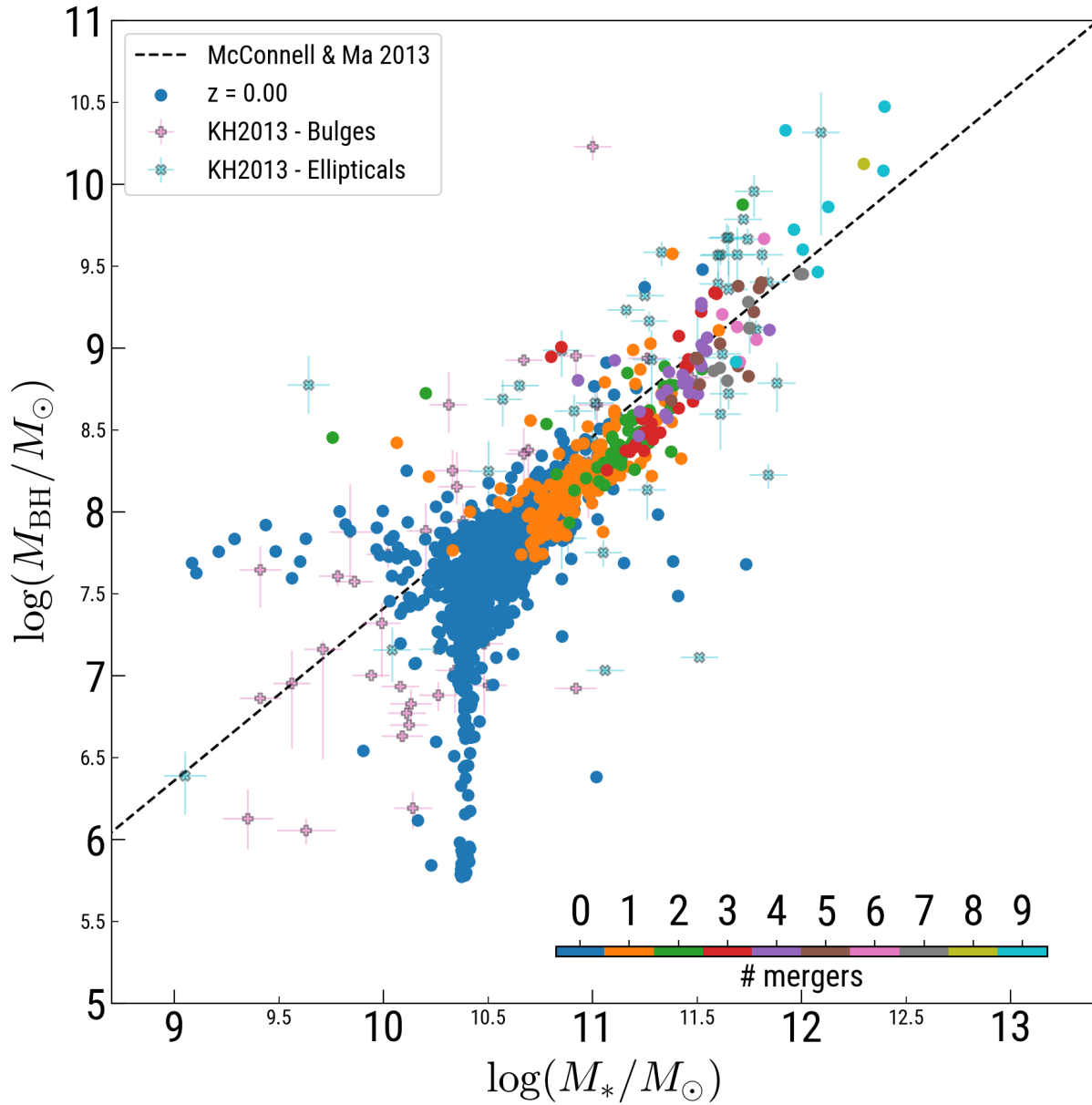


Figure 4.9: M_{BH} as a function of stellar mass M_{*} for the Box4 run. Circles represent the simulated sample at $z = 0$, while the observational points are as in Fig. 4.6. The points are colour-coded according to the number of mergers BH have undergone.

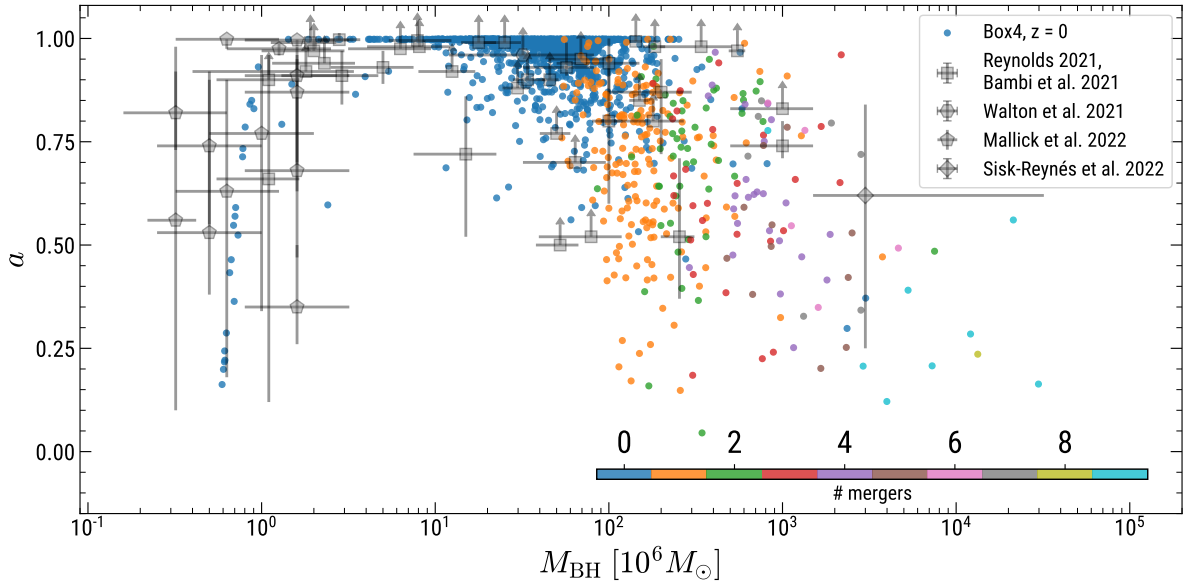


Figure 4.10: Distribution of BH spin parameters as a function of the BH mass in Box4 (circles), at $z = 0$. The points are colour-coded according to the number of mergers BH have undergone. The squares and pentagons show the collection of observational measurements of the BH spin parameter by Reynolds (2021) (with updates from Bambi et al. 2021) and Mallick et al. (2022), respectively. The hexagon represents the spin estimate reported by Walton et al. (2021) and the diamond represents the measurement obtained by Sisk-Reynés et al. (2022).

the subhalo stellar mass as computed by SUBFIND. We compare our sample to observations by McConnell & Ma (2013) and Kormendy & Ho (2013) (as in Fig. 4.6). Each point is colour-coded according to the number of mergers of the BH (including their progenitors). The number increases with increasing BH mass.

In Fig. 4.10 we show how BH spin parameters change as a function of M_{BH} in Box4 (similar to Fig. 4.7). The simulated BHs are indicated by circles, and are colour-coded according to the number of mergers they have undergone. We compare our simulation output to the observational data by Reynolds (2021); Bambi et al. (2021); Walton et al. (2021); Sisk-Reynés et al. (2022); Mallick et al. (2022) (as in Fig. 4.7). We compare our simulation output to the observational data by Reynolds (2021) and Mallick et al. (2022). The BH sample is much more numerous than in the zoom-in regions and the mass range extends further on the high-end, up to $2 \sim 10^{10} M_{\odot}$. We identify three mass ranges in which we observe different distributions of a . Close to the seeding mass ($\sim 5.5 \times 10^5 M_{\odot}$), we can see a steep increase of a with M_{BH} . We caution that the match with observations in this region is due to the choice of the seeding mass, which determines at which mass scale this regime of steep increase occurs. The BH population characterised by $10^6 \lesssim M_{\text{BH}}/M_{\odot} \lesssim 2 \times 10^7$ shows a systematic tendency for highly spinning BHs ($a \gtrsim 0.85$), with most of them close to the maximal value. BHs with masses above $2 \times 10^7 M_{\odot}$ display a wider range of a , extending as low as $a \sim 0.1$. Moreover, we observe a sharp transition at

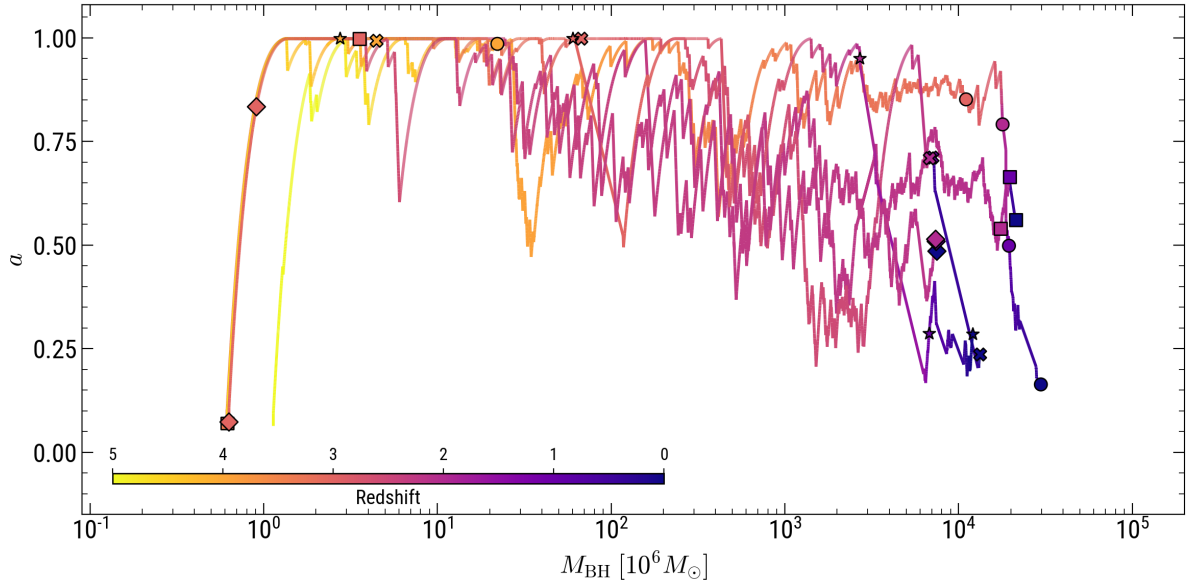


Figure 4.11: BH dimensionless spin parameter a as a function of M_{BH} , for the five most massive BHs at $z = 0$, for the Box4 run. Each line corresponds to one BH and is colour-coded by redshift. The symbols mark the position of each BH in the plot at a few specific instants in time, corresponding to $z = 0, 1, 2, 3, 4$, colour-coded accordingly.

$M_{\text{BH}} \sim 10^8 M_{\odot}$, associated clearly with the regime where mergers start to occur. This mass range also corresponds to the largest scatter in a . The robustness of this result is consolidated by the larger number of BHs probing this high-mass regime with respect to the zoom-in simulations. We also note that for $M_{\text{BH}} \gtrsim 5 \times 10^8 M_{\odot}$ there are no maximally spinning BHs.

Fig. 4.11 shows the evolution of a of the five most massive BHs in the sample as a function of mass. The redshift is encoded in the colour gradient of each curve. The symbols mark the position of each BH in the plot at a few specific instants in time, corresponding to $z = 0, 1, 2, 3, 4$, colour-coded accordingly. As soon as the BHs are seeded, they undergo a phase of rapid increase of a , then they reach and maintain a maximally spinning state. We also notice that when M_{BH} is between 10^6 and $2 \times 10^7 M_{\odot}$, BHs undergo short transitory periods of spin-down due to counter-rotating accretion or mergers. On the other hand, a reaches again the maximal state afterwards, highlighting that co-rotating accretion is dominant. After the BHs overcome the $2 \times 10^7 M_{\odot}$ mass scale, a exhibits a tendency to decrease. In addition, we observe large and sudden changes due to mergers (when also the mass increases significantly at the same time). A binary with BH spins oriented towards opposite directions results in a severe spin-down of the remnant compared to the state immediately before the merger. The wider distribution of a at the highest masses in Fig. 4.10 suggests that spin-down due to counter-rotating accretion and mergers occurs frequently.

In Fig. 4.12 we carry out a statistical analysis of a few key properties of the accretion episodes occurred in the Box4 run, to gain insight on the mechanisms with which gas accretion drives the trends observed in Fig. 4.10 and 4.11. For the analysis, the entire set of accretion episodes

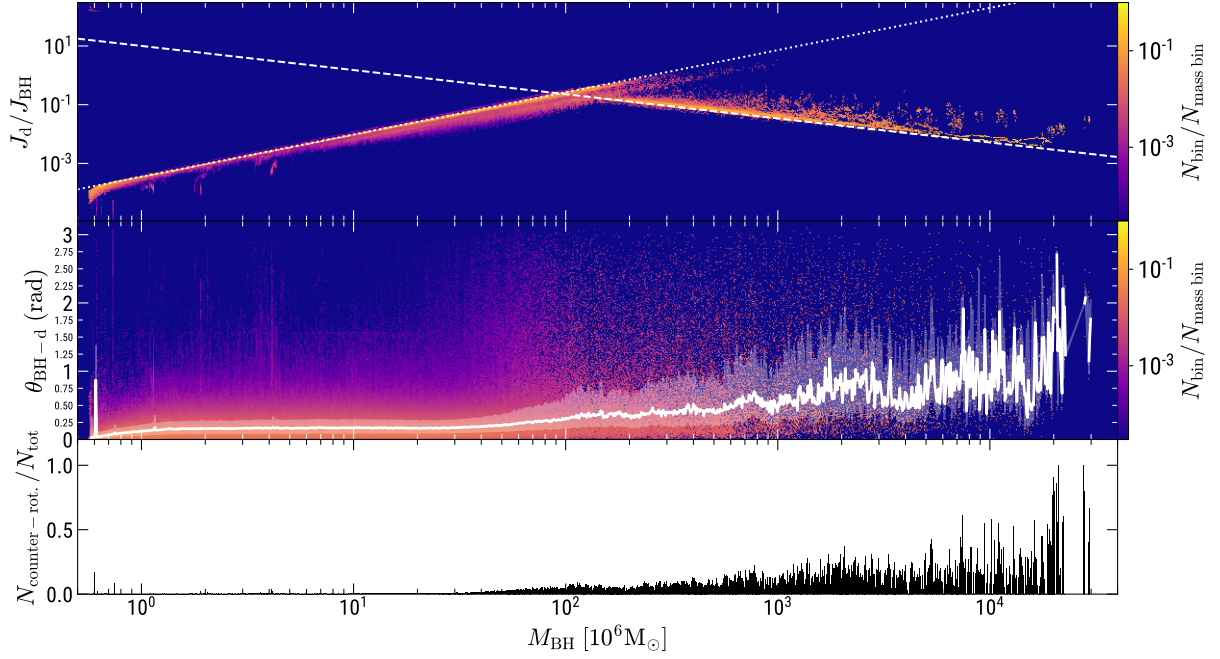


Figure 4.12: Statistical analysis of a few key properties of the accretion episodes occurred in the Box4 run. The entire set of accretion episodes occurred during the simulation has been considered (i.e. for every BH and at every redshift). The top (middle) panel shows a 2D histogram of the values of J_d/J_{BH} ($\theta_{\text{BH-d}}$) as a function of mass. Each bin is colour-coded by the number of accretion episodes in that bin (N_{bin}), normalised to the total number of episodes per mass bin ($N_{\text{mass bin}}$). In the top panel, the dashed line pinpoints $J_d/J_{\text{BH}} \propto M_{\text{BH}}^{-37/45}$ (for the self-gravitating case, Eq. 3.73); the dotted line shows $J_d/J_{\text{BH}} \propto M_{\text{BH}}^{23/16}$ (non self-gravitating case, Eq. 3.69). $a = 0.998$ and $f_{\text{Edd}} = 1$ are assumed to plot these reference lines. The bottom panel shows the fraction of counter-rotating accretion episodes over the total, per BH mass bin.

occurred during the simulation is considered (i.e. for every BH at every redshift). The top panel of Fig. 4.12 shows a 2D histogram where accretion episodes are binned according to their values of J_d/J_{BH} and M_{BH} . Each 2D bin is colour-coded by the number of accretion episodes in that bin. The dashed and dotted lines represent the dependence of J_d/J_{BH} on mass from Eq. 3.68 (i.e. $\propto M_{\text{BH}}^{-37/45}$ for the self-gravitating case and $\propto M_{\text{BH}}^{23/16}$ for the standard case), assuming $a = 0.998$ and $f_{\text{Edd}} = 1$. The distribution observed in J_d/J_{BH} at fixed mass bin is due to different values of a and f_{Edd} . However, J_d/J_{BH} depends weakly on the latter two quantities, while it depends on M_{BH} quite strongly (see Eq. 3.69). Above $M_{\text{BH}} \sim 10^8 M_{\odot}$ accretion occurs mostly in the self-gravitating regime (i.e. $R_{\text{sg}} < R_w$). The middle panel of Fig. 4.12 shows a 2D histogram where accretion episodes are binned according to their values of $\theta_{\text{BH-d}}$ and M_{BH} . The solid white line indicates the median value of $\theta_{\text{BH-d}}$ per BH mass bin, whereas the shaded region represents the 25th and 75th percentile of the distribution of $\theta_{\text{BH-d}}$ in that BH mass bin. We observe that accretion episodes are characterised predominantly by small misalignment (75% of them has $\theta_{\text{BH-d}} \lesssim 0.25 \text{ rad} \sim 15^\circ$) below $M_{\text{BH}} \sim 10^8 M_{\odot}$. Above this mass threshold, the distribution broadens with increasing mass, showing that large misalignment is increasingly more probable. However, we caution that in this regime less accretion episodes occur, therefore the significance of this trend is limited by low-number statistics. Note that when $J_d \ll J_{\text{BH}}$, the minimum angle required for an episode to satisfy condition (3.56) is $\theta_{\text{BH-d}} = \pi/2$. The minimum angle is larger for larger J_d/J_{BH} , whereas for $J_d \geq 2J_{\text{BH}}$ accretion will be always co-rotating regardless the initial misalignment. Since a large misalignment is more probable at high BH masses (middle panel of Fig. 4.12) whereas J_d/J_{BH} decreases with mass above $M_{\text{BH}} \sim 10^8 M_{\odot}$ (top panel of Fig. 4.12), counter-rotating accretion episodes are more likely. In the bottom panel of Fig. 4.12 we plot the fraction of accretion episodes that are counter-rotating with respect to the total number per BH mass bin. This fraction increases with increasing mass and it is as high as 0.5 for the highest mass bins. Note that if the self-gravity prescription were not in place, $J_d/J_{\text{BH}} \gtrsim 1$ above $M_{\text{BH}} \sim 10^8 M_{\odot}$, co-rotating conditions would be prevalent at all masses, and the gas accretion channel of spin evolution would have generally larger probability of increasing the spin.

It is now possible to assess the contribution of gas accretion to the trends discussed in Fig. 4.10 and 4.11 in light of the results shown in Fig. 4.12. Below $M_{\text{BH}} \sim 10^8 M_{\odot}$, most of the accretion episodes are co-rotating, therefore spin-up is favoured. Counter-rotating accretion episodes do occur, but the decrease in spin is transitory and co-rotating accretion leads the spin back to maximal. Conversely, above $M_{\text{BH}} \sim 10^8 M_{\odot}$ the probability of counter-rotating accretion (and hence spin-down) increases as a function of mass.

In Fig. 4.13 we quantify the direction variation imparted to the BH spin as a function of the properties of each accretion episode. The plot shows the angle $\Delta\theta_{\text{BH}}$ between the direction of the BH spin before and after each accretion episode (i.e. $\mathbf{j}_{\text{BH}} \cdot \mathbf{j}_{\text{BH}}^f$) in the Box4 run, as a function of J_d/J_{BH} . The accretion episodes (circles) are colour-coded by $\theta_{\text{BH-d}}$, i.e. the BH spin-disc misalignment at the beginning of the episode. The dashed lines indicate the analytical dependence computed using Eq. (3.55) and expressing $\mathbf{j}_{\text{BH}} \cdot \mathbf{j}_{\text{BH}}^f$ as a function of J_d/J_{BH} , at fixed $\theta_{\text{BH-d}}$. If $J_d \ll J_{\text{BH}}$ then $\Delta\theta_{\text{BH}} \sim 0$, regardless $\theta_{\text{BH-d}}$. If $J_d \gg J_{\text{BH}}$, then $\Delta\theta_{\text{BH}} \sim \theta_{\text{BH-d}}$. Increasing values of J_d/J_{BH} induce larger alignment of \mathbf{j}_{BH} with \mathbf{j}_d per accretion episode. Fig. 4.13 also shows that, overall, $J_d/J_{\text{BH}} \gtrsim 1$ is rare. Therefore complete alignment of \mathbf{j}_{BH} with \mathbf{j}_d ($\Delta\theta_{\text{BH}} = \theta_{\text{BH-d}}$) never

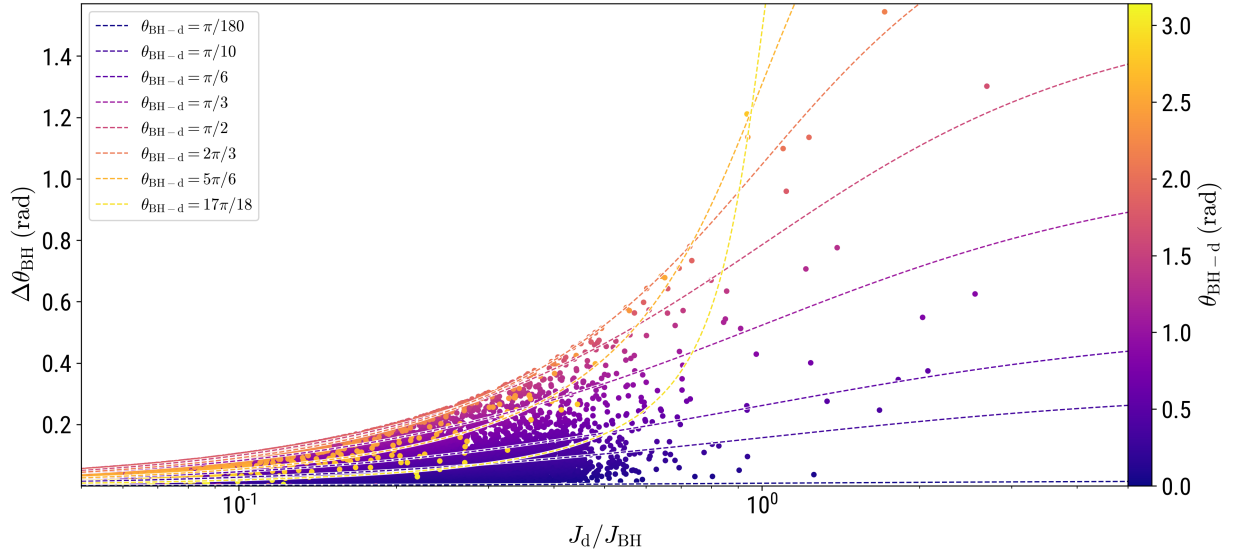


Figure 4.13: BH spin direction variation per accretion episode (i.e. $\Delta\theta_{\text{BH}} = \mathbf{j}_{\text{BH}} \cdot \mathbf{j}_{\text{BH}}^f$) as a function of J_d/J_{BH} , colour-coded by $\theta_{\text{BH-d}}$, the misalignment angle between disc and BH angular momenta at the beginning of the episode. The dashed lines illustrate the analytical dependence of $\mathbf{j}_{\text{BH}} \cdot \mathbf{j}_{\text{BH}}^f$ on J_d/J_{BH} , computed using Eq. 3.55.

occurs in a single accretion episode, i.e. accretion episodes lead at most to partial alignment with the instantaneous direction of the accreting gas.

Fig. 4.14 shows the radiative efficiency ϵ_r across the BH sample at $z = 0$, as a function of M_{BH} . The trends shown in Fig. 4.10 are reflected in the distribution of ϵ_r . Indeed, each BH has its own value of ϵ_r at each instant, dependent on a (see Fig. 3.6). We observe predominantly high efficiency (~ 0.32) at intermediate BH masses ($10^6 \lesssim M_{\text{BH}}/M_{\odot} \lesssim 2 \times 10^7$). A lower efficiency value becomes more likely at higher masses (above $4 \times 10^7 M_{\odot}$), whereas at the highest masses (above $5 \times 10^8 M_{\odot}$) efficiencies have systematically lower values ($\sim 0.06 - 0.1$). The radiative efficiency also depends on whether, at a given instant, accretion is proceeding in co- or counter-rotating accretion conditions. Points with ϵ_r below the dashed line correspond to BHs that are accreting in counter-rotating conditions. Indeed, the probability of having counter-rotating conditions increases with mass above $4 \times 10^7 M_{\odot}$ (bottom panel of Fig. 4.12). We also compare our simulated sample with a collection of radiative efficiency factors provided in Daly (2021). Since the simulation points refer to the sample at $z = 0$, we consider all the sources in the observational catalogue that have $z < 0.2^2$.

²Note that we exclude the sources catalogued as LINERs.

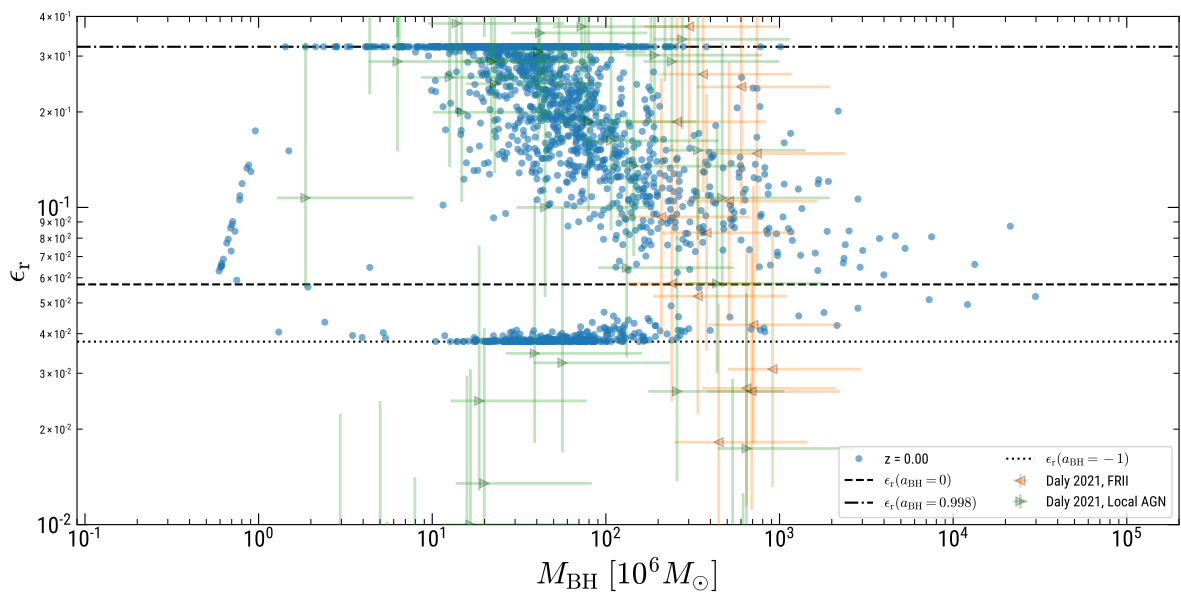


Figure 4.14: Radiative efficiencies of the BH populations at redshift $z = 0$, as a function of mass, for the Box4 run. The triangles show the collection of empirical estimates of the radiative efficiency by Daly (2021). The dotted, dashed and dash-dotted lines mark the values of the efficiency corresponding to $a = -1, 0, 0.998$, respectively, for reference. The population in the bottom part of the figure represents the BH that are accreting in counter-rotating conditions.

5 | Discussion

The content of this chapter has been published in Sala et al. (2023):

Luca Sala, Milena Valentini, Veronica Biffi, Klaus Dolag:
Supermassive black hole spin evolution in cosmological simulations with OPENGADGET3
accepted for publication in *Astronomy & Astrophysics*

5.1 Evolution of the BH spin direction

Our algorithm for spin evolution proceeds through accretion episodes that modify \mathbf{j}_{BH} as an effect of the external change in \mathbf{j}_{g} . As shown in Fig. 4.13, only if $J_{\text{d}} \gg J_{\text{BH}}$ a single accretion episode is able to induce complete alignment with \mathbf{j}_{d} and therefore with \mathbf{j}_{g} . Conversely, if $J_{\text{d}} \ll J_{\text{BH}}$, then J_{BH} is insensitive to external change. We observe that in our simulations accretion episodes are in general characterised by $J_{\text{d}}/J_{\text{BH}} \lesssim 1$ (Fig. 4.13), therefore accretion episodes induce only partial alignment of \mathbf{j}_{BH} with \mathbf{j}_{d} . Larger values of $J_{\text{d}}/J_{\text{BH}}$ reduce the misalignment between \mathbf{j}_{BH} and \mathbf{j}_{g} to a larger degree. The relation between \mathbf{j}_{BH} and \mathbf{j}_{d} (and hence \mathbf{j}_{g}) on timescales longer than a single accretion episode depends on $J_{\text{d}}/J_{\text{BH}}$ and on the variability of \mathbf{j}_{g} . For the reference BH considered in `DFROGIN`, the top panel of Fig. 4.8 shows that before $t \sim 2.6$ Gyr \mathbf{j}_{g} varies gradually with time, although with some variability on short (i.e. $\lesssim 1$ Myr) timescales. On the other hand, \mathbf{j}_{g} changes erratically after $t \sim 2.6$ Gyr. In the former case \mathbf{j}_{BH} manages to follow the average evolution of \mathbf{j}_{g} , whereas the two directions are decoupled in the latter. The middle panel of Fig. 4.12 shows that statistically such large misalignment is more probable at the highest masses. Combined with low values of $J_{\text{d}}/J_{\text{BH}}$, it results in counter-rotating accretion conditions to be more frequent with increasing mass (bottom panel of Fig. 4.12).

5.2 Evolution of the BH spin magnitude

The BH spin magnitude evolution via gas accretion is driven by the amount of accreted mass and by the radius of the ISCO (Eq. 3.59). Therefore, it evolves more rapidly in high accretion rate phases. Furthermore, counter-rotating accreting gas is characterised by a larger ISCO (bottom panel of Fig. 3.6), thus a larger angular momentum per unit mass. The same amount of accreted mass induces a larger (negative) change in a than if it were accreted in co-rotating conditions. At fixed mass, if co- and counter-rotating episodes occurred in equal number, the net effect would

actually be a decrease in a (Dotti et al., 2013). Whether there is a trend to increase or decrease the spin magnitude depends on the accretion rate and on how frequent co- or counter-rotating accretion is. Moreover, mergers also contribute to influence a . In Figs. 4.7 and 4.10 we analyse the trends of a with BH mass and observe that BHs with $M_{\text{BH}} \lesssim 2 \times 10^7 M_{\odot}$ show systematic spin-up. This effect is attributed to the prevalence of co-rotating accretion conditions (bottom panel of Fig. 4.12). Mergers do not occur in this range of masses (see Fig. 4.10), hence the trend is exclusively due to gas accretion. For $M_{\text{BH}} \gtrsim 2 \times 10^7 M_{\odot}$ we observe a wide distribution of a , indicating that the behaviour strongly depends on the detailed history, and there is no systematic behaviour. In this mass regime, several elements contribute to the trend: *i*) the fraction of counter-rotating episodes increases with mass (bottom panel of Fig. 4.12) but it remains generally lower than 50%; *ii*) co-rotating conditions and hence spin-up still occur; *iii*) only the BHs in the highest mass bins ($\gtrsim 5 \times 10^9 M_{\odot}$) reach a fraction $\gtrsim 0.5$ and exhibit systematically low spins ($a \simeq 0.2 - 0.3$). We also note that above $M_{\text{BH}} \gtrsim 10^8 M_{\odot}$ BHs undergo several mergers (Fig. 4.10) and Eddington ratios are generally highly sub-Eddington (e.g. second to last panel of Fig. 4.8). Therefore, mergers significantly contribute to the variation of the spin. Moreover, mergers with misaligned directions tend to significantly decrease a (e.g. fourth panel of Fig. 4.8). From Fig. 4.10, we infer that the widening of the distribution at the high masses is associated with the increasing importance of mergers and a more likely counter-rotating accretion.

In Fig. 4.10 we also note that BHs close to the seeding mass ($M_{\text{BH}} \simeq 5.5 \times 10^5 M_{\odot}$) are characterised by a steep increase of a with mass. The region in the $a - M_{\text{BH}}$ plane that these BHs occupy is mostly determined by $M_{\text{BH,seed}}$. However, the initial value of a does not affect the following evolution, since any initial spin value is quickly evolved to maximal due to large accretion rates.

Overall, the trends in a as a function of M_{BH} are consistent between the zoom-in simulations (Fig. 4.7) and the Box4 (Fig.4.10), which even have different resolutions. The distribution of a is compatible with the observations within the uncertainties, across the entire mass range.

5.3 Radiative efficiency

The radiative efficiency plays an important role. First of all, it enters the computation of the Eddington accretion rate. Since the BH accretion rate cannot exceed this rate in our model, the efficiency directly affects the Eddington-limited growth phases. According to Eq. 4.2, the e -folding timescale

$$\tau_{\text{MBH}} = \frac{\epsilon_r \tau_S}{f_{\text{Edd}}(1 - \epsilon_r)} \quad (5.1)$$

depends on the efficiency. Eddington-limited co-rotating accretion on a maximally spinning BH (i.e. $\epsilon_r \sim 0.32$) implies $\tau_{\text{MBH}} \sim 210$ Myr, whereas in counter-rotating conditions ($\epsilon_r \sim 0.038$) $\tau_{\text{MBH}} \sim 18$ Myr. A lower efficiency leads to a significantly faster BH growth. In our simulations, Eddington-limited phases are characterised by maximally spinning BHs and co-rotating accretion, thus growth proceeds with $\epsilon_r \sim 0.32$ (see e.g. ϵ_r panel in Fig. 4.8).

The efficiency also controls the amount of feedback energy released to the surroundings, at a given \dot{M}_{BH} (see Eq. 3.77). A lower efficiency implies less released energy and subsequent

increased accretion. It also means a faster increase in M_{BH} (because of the factor $1 - \epsilon_r$ in Eq. 3.60). This in turn boosts \dot{M}_{BH} (due to the $\propto M_{\text{BH}}$ dependence in Eddington-limited phases or $\propto M_{\text{BH}}^2$ otherwise, see Eq. 2.2), leading to stronger feedback outbursts that hinder accretion. In addition, since the Eddington accretion rate depends on the efficiency, the switch to maintenance mode feedback is also affected. Overall, the effects just discussed contribute in a non-trivial way to modify the evolutionary path of a BH through the feedback loop. Our simulations – where all these processes are self-consistently taken into account – show that BHs are on the observed correlation between BH mass and stellar mass (Figs. 4.9 and 4.6). While the detailed evolutionary path along the plane $M_{\text{BH}} - M_*$ changes, each BH is eventually able to approach the correlation, implying that the BHs still grow in an overall self-regulated scenario.

Fig. 4.14 highlights that ϵ_r tends to decrease with increasing mass at the high-mass end. We also find that the distribution of our simulated sample is compatible with the distribution of empirical estimates by Daly (2021), within the uncertainties. Note that the empirical sample is obtained with a method that does not rely on a specific accretion disc model. Therefore, while our sample has an upper and lower limit for the efficiency determined by our theoretical assumption on the disc structure, the interpretation of the empirical estimates is not bound to such an assumption. On the other hand, assuming for the accretion disc a different model based on e.g. hot accretion flow (Yuan & Narayan, 2014) would imply lower efficiencies than in the thin disc theory.

5.4 Comparison with previous works

Dubois et al. (2014b) and Bustamante & Springel (2019) perform a statistical study similar to ours. The former simulate a cosmological volume with size and resolution comparable to Box4 and the latter a smaller box with higher resolution ($L_{\text{box}} = 25 h^{-1} \text{ cMpc}$ and $m_{\text{DM}} = 8.4 \times 10^6 M_{\odot}$). Our spin evolution model follows Dubois et al. (2014b), although we track the spin on-the-fly whereas in their work the spin is tracked in post-processing. ϵ_r is assumed to be fixed to 0.1. They include a thermal feedback channel for $f_{\text{Edd}} > 0.01$ and a bipolar outflow launched in the direction of the local gas otherwise, but both do not depend on a . Bustamante & Springel (2019) adopt an on-the-fly spin update algorithm similar to ours, with a variable ϵ_r affecting the thermal feedback mode. However, below a mass-dependent f_{Edd} threshold, BHs inject purely kinetic energy, with a fixed efficiency and random direction, isotropic on average. Moreover, when the sub-grid accretion disc is affected by self-gravity the angular momentum direction of each accretion episode is extracted from a chosen angular distribution. In our implementation we assume it is fixed and equal to the gas angular momentum direction at all times. Interestingly, the trends we find in Fig. 4.10 are in agreement with both works, regardless of whether or not ϵ_r depends on a or whether the spin is evolved in post-processing rather than on-the-fly. This indicates that the variability of the radiative efficiency does not play a significant role in setting these trends. On the other hand, ϵ_r does affect AGN feedback and BH growth (Sec. 3.2.3). As a result, a different prescription for ϵ_r changes the detailed time evolution of BH mass and stellar mass, leading to a different path towards the $M_{\text{BH}} - M_*$ relation and more scatter around it (Bustamante & Springel, 2019). Nonetheless, Fig. 4.9 shows that the self-regulated scenario is

still present and eventually leads the BHs on the relation.

We find that the dynamical state of the feeding material, combined with the key parameter J_d/J_{BH} , plays a significant role in the evolution of the BH spin due to gas accretion (Fig. 4.12 and 4.13). Dotti et al. (2013) conclude that when $J_d/J_{\text{BH}} \ll 1$ (as it occurs in our simulations, see Fig. 4.12), the feeding angular momentum distribution determines whether a increases or decreases. Our findings regarding the behaviour of the spin in response to the feeding conditions are in agreement with theirs, as well as with Dubois et al. (2014b) and Bustamante & Springel (2019). When the gas angular momentum direction varies slowly and its misalignment with respect to the BH spin is small (indicating a preferential direction), the BHs are maximally spinning. This generally occurs at $M_{\text{BH}} \lesssim 10^8 M_{\odot}$ (see Fig. 4.8, 4.11, 4.12). Conversely, uncorrelated gas angular momentum directions lead to increasingly probable counter-rotating accretion and BH spin-down (bottom panel of Fig. 4.12, Sec. 4.2.4). We note that the large scatter in a at high masses (Fig. 4.10) is found also by Dubois et al. (2014a) and Bustamante & Springel (2019), despite the different prescriptions for AGN feedback. This might indicate that its effect is to generally induce loss of coherence in the angular momentum distribution (middle panel of Fig. 4.12), regardless of the specific channel.

In contrast to our model, Bustamante & Springel (2019) introduce stochasticity in \mathbf{j}_d (Eq. 3.66) at the sub-resolution level, on top of the resolved variability in the simulation. Such a prescription can be thought as a way to account for turbulent structures in the ISM that are not resolved in cosmological simulations (see e.g., Murchikova et al. 2019; Ressler et al. 2020 for our Galactic centre). They assume that in the self-gravity regime \mathbf{j}_d is extracted from a distribution that ranges from random (isotropic) to concentrated around the preferential axis set by the local gas angular momentum (anisotropic). As a result, they observe a more pronounced decoupling between \mathbf{j}_d and \mathbf{j}_{BH} compared to us, in case of an isotropic distribution. On the other hand, they find the same widening of the distribution of a at high BH masses, regardless of the degree of anisotropy. Dubois et al. (2014a) also explore the effect of varying the distribution of \mathbf{j}_d at the sub-resolution level. However, they introduce stochasticity in all accretion regimes. They find that even a slight anisotropy leads to results that are very similar to the completely coherent case (i.e. when the gas preserves the angular momentum direction as measured by the simulation). Only if the gas angular momentum is randomly oriented at all masses, then BHs settle on $a \sim 0.2 - 0.3$ (King et al., 2008) and an increasing trend of spin with mass is found (Fanidakis et al., 2011) (in those conditions the trend is produced by mergers, that tend to bring slowly spinning BHs to values around 0.7 for $M_{\text{BH}} \gtrsim 10^9 M_{\odot}$). One possibility to explain these results is that when gas accretion is sub-dominant, the trend is mainly driven by mergers. However, we observe that above $M_{\text{BH}} \gtrsim 10^8 M_{\odot}$ gas accretion does contribute to spin evolution, inducing both spin-up and spin-down (Fig. 4.11). The net effect depends crucially on the accretion rate, the BH environment and the level of anisotropy of the feeding gas. This level varies widely over time and across the BH population. Mergers also contribute to modifying the spin value, but the relative contribution of gas accretion and mergers to spin evolution is different depending on the detailed cosmological history. We postpone a systematic study to future work.

Finally, we note that we do not integrate the full differential equation that describes the precession and alignment process, due to the coupling between the gas distribution in the accretion disc and the BH spin (at variance with, e.g., Fiacconi et al., 2018). Rather, we assume that the

process is discretised in accretion episodes and is globally taken into account, while the total angular momentum is conserved (Sec. 3.2.1), following King et al. (2005). Fiacconi et al. (2018) developed an algorithm that includes the full detailed treatment, although it requires high temporal and spatial resolution. In fact, timesteps as low as 10^{-3} Myr are required in some cases to meaningfully integrate the differential equation, which are prohibitive in a full cosmological context. Moreover, their model measures directly the inflow properties as resolved by the simulation at the sub-resolution boundary, rather than using an effective prescription such as the Bondi parametrisation. Therefore, it is suitable for high-resolution simulations (e.g. approximately a parsec scale). In contrast, we assume that the mass rate through the sub-resolution accretion disc is equal to the mass accretion rate onto the BH and it is identical to the Bondi accretion rate at all times. We further note that Fiacconi et al. (2018) model spin evolution only due to gas accretion, although mergers are expected to contribute to spin evolution for $M_{\text{BH}} \gtrsim 10^8 M_{\odot}$ (Fanidakis et al., 2011; Dubois et al., 2014a) and the low-redshift growth of massive BHs is dominated by mergers in several models (e.g. Weinberger et al., 2018; Pacucci & Loeb, 2020). Although they do not produce a statistical sample of BHs, they perform a suite of simulations aimed at mimicking a range of realistic conditions. Despite the approach being different in a number of numerical aspects, the expected effect of the gas accretion channel on spin evolution is in line with ours: systematic spin-up for $M_{\text{BH}} \lesssim 10^7 M_{\odot}$ and a wider distribution of a at higher masses.

6 | Outlook

In this Thesis, I have shown that hydrodynamical simulations of cosmological structure formation, equipped with a sub-resolution model tailored to evolve the BH spin, can provide constraints on the distribution of BH spins and to gain insights on the influence of the dynamical state of the gas surrounding the BH. Specifically, it was possible to investigate the level of coherence of the angular momentum of the inflowing gas, and its dependence on the system and period of cosmic history. The simulations contain the properties of BHs and those of their associated host galaxies, and with the spin evolution model, they are now enriched with the time-evolution of the BH spin vector and the radiative efficiency. This opens several future avenues for further investigation and development.

6.1 BH spin and galaxy morphology

The extended information now provided by the simulations can be used to investigate the relation between the value of the magnitude of the BH spin a and the galaxy morphology. Such a relation was previously investigated, for instance, by Sesana et al. (2014), using a semi-analytical approach. In their work, they linked the dynamical state of the gas feeding the BH and driving spin evolution to the morphological type of the host galaxy. They find that BHs hosted in ellipticals tend to have lower spins than spirals. Moreover, a comparison to observations of BHs hosted in spirals favours a model in which the gas feeding the BH generally shares the coherent dynamics of the kpc-scales disc, except for merger-driven accretion events in which the angular momentum is reshuffled and significantly loses coherence. In the cosmological simulations run with my model the kinematics of the accreted gas arise from the hydrodynamics and evolved self-consistently (on scales larger than the spatial resolution). Therefore, a connection with morphology and/or mergers is not imposed a priori. On the other hand, higher resolution simulations than the ones presented in Ch. 4 are likely required to better resolve the morphological features and carry out a similar analysis to assess whether an association between spin and morphology is present and its impact on the distribution of BH spins.

6.2 BH spin and galaxy alignment

The three-dimensional information of the BH spin vector can also be used to assess statistically its level of alignment with the host galaxy stellar component. For instance, using the results of

the Horizon-AGN simulations (Dubois et al., 2014a) in which the spin evolution was computed in post-processing, Beckmann et al. (2023) found that BHs whose growth is dominated by mergers are more likely to have their spins misaligned with the host galaxy. Moreover, BHs that do not undergo mergers tend to have higher spins. With the model presented in this work, in which the spin is evolved on the fly, it will be possible to further test these results. It is also worth noting that an investigation of the observed misalignment in specific systems can provide interesting insights into their evolutionary history; for example, EHT measurements of the spin axis of its central SMBH Sgr A* indicate a significant misalignment with respect to the Milky Way plane (Palumbo et al., 2020), that may be used to infer the occurrence of a past SMBH merger (Wang & Zhang, 2024).

6.3 BH spin and jet feedback

As mentioned in Sec. 3.2.3, the spin evolution model so far was coupled to a single channel of energy injection, namely purely thermal, aimed at reproducing the radiative feedback. Moreover, in my model, the radiative efficiency is no longer a free parameter but is linked to the BH spin magnitude. Nonetheless, the remaining free parameters are still calibrated against observational properties. However, in the case of AGN feedback, the injection of thermal energy isotropically close to the BH might be a poor representation of reality in some cases (i.e. it might inject energy at the wrong scales). In such cases, the calibration of free parameters does not help in obtaining a better agreement with observations. Moreover, increasing the resolution might require revisiting the numerical implementation to avoid producing unphysical results (see e.g. Anglés-Alcázar et al., 2021). Therefore, a more realistic modelling of AGN feedback, especially relevant for low-luminosity sources and in galaxy clusters, requires to include an additional mechanism, in which large-scale jets (tens to hundreds of kiloparsecs) are the key actors. In addition, jets could also be coupled to cosmic rays models (Guo & Mathews, 2011; Böss et al., 2023), further improving the realism of the simulations.

As discussed in Sec. 2.2, the BH spin plays an important role in the launching of jets. A self-consistent treatment of spin evolution is therefore a key ingredient to properly include AGN feedback from jets in cosmological simulations. The sub-resolution model presented in this work represents a natural framework upon which a jet model can be developed, based on the BH spin magnitude and direction. Previous attempts to include feedback from jets in cosmological simulations include the injection of energy far from the BHs to mimic the inflation of bubbles (Sijacki et al., 2007, 2015), or the directional injection of momentum, kinetic energy or both (Dubois et al., 2012, 2016; Weinberger et al., 2018; Davé et al., 2019). However, few models so far have taken the BH spin into account in the sub-resolution model for jet feedback. In one of the model variation simulations of the FLAMINGO simulation suite (Schaye et al., 2023), particles are kicked along the BH spin axis with a fixed velocity, to mimic jet-like kinetic feedback. In the NEWHORIZON simulations (Dubois et al., 2021), mass, momentum and energy are injected in a cylindrical region close to the BH, with the same model as in Dubois et al. (2016). The cylinder axis is along the BH spin direction, and the jet power $P = \eta \dot{M}_{\text{BH}} c^2$ depends on the BH spin magnitude through the efficiency η , according to an interpolated function based on the results of

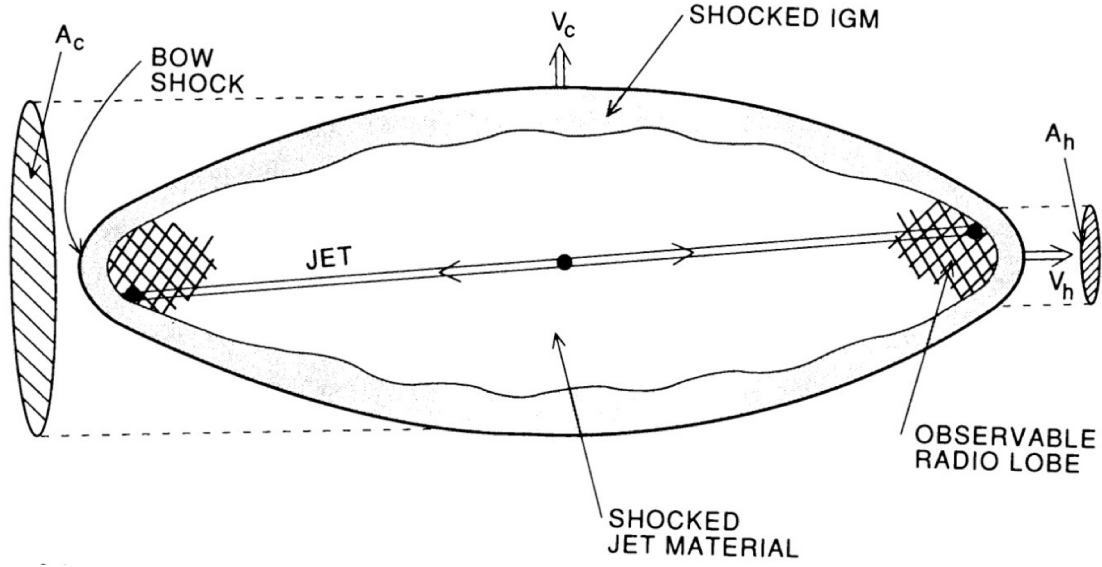


Figure 6.1: Schematic representation of jet propagation in an ambient medium. Adopted from Begelman & Cioffi (1989).

GRMHD simulations of magnetically arrested discs by McKinney et al. (2012).

Even though significant progress has been made in the inclusion of jets in high-resolution simulations of isolated systems (e.g. Talbot et al., 2021; Huško et al., 2022), properly resolving the physics of jet propagation is prohibitive in cosmological simulations. Improved models of jet feedback might require a different strategy and an effective description. Analytical models of jet propagation in an ambient medium are available in literature (e.g. Begelman & Cioffi, 1989; Bromberg et al., 2011), whose solutions have also been verified with numerical simulations (Mizuta & Ioka, 2013; Harrison et al., 2018). The basic picture of jet propagation (see Begelman & Cioffi 1989 and Fig. 6.1), envisage the balance of the jet thrust \dot{p}_j (i.e. its momentum flux)

$$\dot{p}_j = \dot{M}_j v_j \quad (6.1)$$

where \dot{M}_j is the mass flux of the jet, and v_j is the velocity of the jet material, against the force due to the ram pressure of the ambient medium towards the jet head

$$F_{ram} = \rho_a v_h^2 A_h \quad (6.2)$$

where ρ_a is the density of the ambient medium, v_h is the head velocity (which is different from v_j) and A_h is the working surface area of the jet head. The jet produces an expanding over-pressurised cocoon, that acts to collimate the jet itself. Setting $\dot{p}_j/2 = F_{ram}$ ¹, the evolution equation for the jet head velocity in its simplest form (Begelman & Cioffi, 1989) is derived:

$$v_h = \left(\frac{\dot{p}_j}{2\rho_a A_h} \right)^{1/2}, \quad (6.3)$$

¹The factor 1/2 comes from considering that each side of the jet gets half of the total momentum flux.

where \dot{p}_j , ρ_a and A_h are assumed constant. In the model by Begelman & Cioffi (1989), the jet head cross-section A_h is estimated phenomenologically. Bromberg et al. (2011), building upon this work, computed a time evolution equation for the jet dynamical properties (e.g. the jet head velocity and cross-section) in an arbitrary density profile. The key improvement of their work is a proper treatment of the collimation shock at the jet base that allows them to determine self-consistently the jet head cross-section and velocity. The jet evolution depends only on three parameters: the jet power, the density profile of the ambient medium and the initial jet opening angle. They also find that the jet behaviour can manifest as either collimated or uncollimated, and provide the specific conditions regarding the jet parameters dictating which regime it will follow. An avenue worth exploring can be to connect the spin evolution model to a prescription for the jet propagation based on tracer particles, that integrates on the fly the evolution equation to determine where the jet terminates and deposits energy, producing the observed lobes. Using an analytical evolution equation would circumvent the need to resolve the full details of jet propagation. The spin magnitude can be used to specify the time-dependent jet power (see e.g. McKinney et al. 2012), whereas the density of the ambient medium during the propagation can be inferred directly from the simulation. Constraints on the launching opening angle can be drawn from observations; high-resolution observations in the radio band provide constraints on the expansion profile of jets at parsec scales (e.g. Boccardi et al., 2021). Moreover, Bromberg et al. (2011) have shown that powerful jets from AGN are collimated at distances larger than 10 kpc, considering the observed jet powers and ambient medium densities. Nevertheless, it is also worth noting that in general a consensus has not been reached yet on why some jets develop instabilities and disrupt before escaping their host galaxies since the details of the interaction of jets with the local ISM are still a subject of debate (see Davis & Tchekhovskoy, 2020, for a discussion).

6.4 Accretion flow model

Another aspect that deserves further exploration concerns the modelling of the accretion flow. The model adopted in this work assumes that accretion proceeds in a thin accretion disc at all accretion rates. From the theoretical point of view, a thin disc is not inconsistent with low accretion rates, as discussed in Sec. 3.1.3. However, observations of the SED of local LLAGN indicate that the accretion flow in these objects is substantially modified compared to the standard thin disc model. The SED lacks the typical signature of thermal emission from the innermost part of an optically thick accretion disc, suggesting that these sources might be better described by a "truncated disc", composed of an outermost cool thin disc and an innermost radiatively inefficient hot accretion flow (see e.g. Ho, 2008; Nemmen et al., 2014). The transition radius between the two regions increases for decreasing \dot{M}_{BH} (e.g. Yuan & Narayan, 2004). However, the results in Ch. 4 highlight that the spin magnitude and direction change significantly when the accretion rate is high. Therefore, from the point of view of spin evolution, even if the accretion flow structure departs from the standard model at low f_{Edd} , the effect on spin evolution is not expected to be large. On the other hand, jet formation does depend on the properties of the accretion flow, although a realistic investigation of discs around SMBHs requires the inclusion of radiative transfer (Davis & Tchekhovskoy, 2020). Therefore, an improvement in our understanding of the conditions

leading to jet launching requires GRMHD simulations. The results of these simulations improve our understanding of the disc-jet connection and can provide the efficiency of jet generation $\eta = P_{\text{jet}}/(\dot{M}_{\text{BH}}c^2)$. The work by McKinney et al. (2012) represents a remarkable example. The inclusion of jets in cosmological simulations necessarily needs to rely on sub-resolution models, that can be built upon the input provided by these simulations.

It is also worth noting that recent state-of-the-art GRMHD simulations have led to interesting results, that defeat previous expectations and provide new elements to our understanding of accretion flows onto BHs. For instance, while the present work assumes that the BH torques on the disc produce a smooth warp, Liska et al. (2019a) demonstrated that thin discs heavily misaligned with the BH spin axis can tear up in multiple individually precessing discs, that induce additional angular momentum transport on top of the local MRI stresses (Liska et al., 2022; Kaaz et al., 2022). The different accretion disc structure could have far-reaching implications also on the process of spin evolution. Moreover, Liska et al. (2019b) showed that not only thick discs but also thin discs can launch a powerful relativistic jet with $\eta \sim 20 - 50\%$, perhaps providing an explanation for the 10% of luminous quasars which exhibit radio jets.

Finally, this work and many other cosmological simulations adopt the Bondi prescription as an estimator for the BH accretion rate, even though with strategies to account for limited resolution (i.e. the α_{acc} factor). Remarkably, recent works have started providing insights on the missing link between the scales of the Bondi radius and the accretion disc scales (Guo et al., 2022; Hopkins et al., 2023a,b; Cho et al., 2023). These works can provide the basis for future improvement of the sub-resolution description of accretion onto BHs suitable for cosmological simulations, whose implications are worth exploring.

7 | Summary and conclusions

Part of the content of this Chapter has been published in Sala et al. (2023).

The goal of this Thesis was to conduct a comprehensive statistical study of the evolution of the spins of SMBHs across cosmic time due to gas accretion and mergers.

The general framework for the study was the use of large-scale cosmological simulations; in Ch. 1 I described the fundamental concepts underpinning these simulations, namely the current cosmological model of structure formation, the code adopted for solving the equations of hydrodynamics and gravity in this context, and the importance of sub-resolution models.

In Ch. 2 I introduced the concept of Active Galactic Nuclei, that is, accreting SMBHs at the centre of massive galaxies. I revised a few key observational properties and described the mechanisms with which AGN are thought to influence their host galaxies, which play an important role in galaxy evolution. Then, I discussed the importance of BH spin for the formation of jets, the main channel of feedback in galaxy clusters. Finally, I discussed how AGN are included in cosmological simulations and presented an empirical model for variable AGN feedback efficiency.

In Ch. 3 I presented the theoretical background underlying the process of spin evolution; namely, the theory of accretion flows around BHs, with a particular focus on the thin disc solution, and the evolution of warped discs. Then, I presented the sub-resolution model that made it possible to include the treatment of BH spins in cosmological simulations, published in Sala et al. (2023). The model entails the presence of a misaligned thin accretion disc perturbed by the metric of a spinning BH mediating the mass transfer from the resolved scales of the simulations onto the BH. The BH radiative efficiency and Eddington accretion rate were made dependent on the BH spin and thus variable across cosmic time. Their impact on accretion and feedback was therefore captured self-consistently. The model also takes into account spin evolution in the case of BH mergers, with a prescription derived from the results of detailed general-relativistic simulations.

In Ch. 4 I presented the simulation suite described in Sala et al. (2023), featuring idealised, isolated systems (Sec. 4.2.1 and 4.2.2) to validate the sub-resolution model and cosmological setups (Sec. 4.2.3 and 4.2.4) to investigate statistical properties of the BH population, and the results from the simulations. In Ch. 5 I discussed their implications, and I summarise here the conclusions from the work.

- The ability of a single accretion episode to modify the BH spin depends on the amount of mass and angular momentum it carries with respect to the BH (J_d/J_{BH} , Fig. 4.13). An

accretion episode with larger J_d/J_{BH} induces the BH spin direction \mathbf{j}_{BH} to tilt more towards the gas angular momentum direction \mathbf{j}_{g} .

- The evolution of the direction and the magnitude of the spin are tightly coupled. When $J_d/J_{\text{BH}} \lesssim 1$ (Fig. 4.12), the feeding distribution of the gas angular momentum directions determines whether a preferably increases or decreases. If accretion occurs consistently along the same plane (e.g. Fig. 4.2), spin-up is expected. Conversely, if \mathbf{j}_{g} changes direction erratically, counter-rotating conditions and spin-down can occur (Fig. 4.8 and 4.12).
- In a cosmological context, we identified two regimes, depending on the distribution of a with BH mass (Fig. 4.10). BHs with $M_{\text{BH}} \lesssim 2 \times 10^7 M_{\odot}$ tend to be highly spinning ($a \gtrsim 0.85$). At the high-mass range ($M_{\text{BH}} \gtrsim 2 \times 10^7 M_{\odot}$), a exhibits a broad range of values.
- We observed a wide variety of evolutionary histories for a (Fig. 4.11), depending on the dynamical state of the gas feeding the BH and the occurrence of coalescences. This indicates that the level of anisotropy of \mathbf{j}_{g} and the relative contribution of mergers and accretion varies across the BH population.
- When \mathbf{j}_{g} exhibits some degree of coherence and varies slowly (generally at $z \gtrsim 2$ and $M_{\text{BH}} \lesssim 2 \times 10^7 M_{\odot}$), \mathbf{j}_{BH} follows the average evolution of \mathbf{j}_{g} and small misalignment is observed (Fig. 4.12). At late times ($z \lesssim 2$), \mathbf{j}_{g} shows large and abrupt changes, while \mathbf{j}_{BH} is stable over long periods (hundreds of millions of years, e.g. Fig. 4.8). Indeed, since $J_d/J_{\text{BH}} \lesssim 1$, accretion episodes are not able to modify significantly \mathbf{j}_{BH} . This frequently leads to large misalignment.
- The tendency for maximal spin in the low-mass range is due to the accretion of co-rotating gas with small misalignment (Fig. 4.12). The wide range of values of a in the high-mass range is due to mergers and more isotropically distributed \mathbf{j}_{g} , and this results in a probability of counter-rotating accretion that increases with mass (Figs. 4.11 and 4.12). The distribution of \mathbf{j}_{g} arises self-consistently, as measured from the simulation.
- Including a self-consistent ϵ_{r} has an important effect on determining the BH growth rate in the Eddington-limited phases. A higher efficiency during these phases implies a lower growth rate. Our statistical sample shows that BHs with $M_{\text{BH}} \lesssim 4 \times 10^7 M_{\odot}$ always have efficiencies around 0.32, whereas the most massive BHs generally have lower efficiencies (Fig. 4.14).
- Although the variable ϵ_{r} modifies the detailed path on the $M_{\text{BH}} - M_{\ast}$ plane, BHs eventually approach the observed correlation, indicating self-regulated growth.
- The spin with which BHs are initialised is erased quickly after they are seeded. Massive BHs can retain some information on the dynamical state of the gas they recently accreted (Figs. 4.11 and 4.12).

In Ch. 6 I presented exciting future extensions of the work presented in the Thesis, that are worth exploring for their relevance to multiple aspects of galaxy formation and evolution. The relation between BH spin and galaxy properties can shed some light on the relevance of the former as a tracer for the past accretion and merger history. Most importantly, the spin evolution model enhances the realism of the simulations by constituting the basis for the future incorporation of jets in cosmological simulations, whose power and direction are coupled to the BH spin.

Bibliography

- Abazajian, K. N., Adelman-McCarthy, J. K., Agüeros, M. A., et al. (2009), *The Seventh Data Release of the Sloan Digital Sky Survey*, *The Astrophysical Journal Supplement Series*, 182, 543
- Abramowicz, M. A., Czerny, B., Lasota, J. P., and Szuszkiewicz, E. (1988), *Slim Accretion Disks*, *The Astrophysical Journal*, 332, 646
- Abramowicz, M. A. and Fragile, P. C. (2013), *Foundations of Black Hole Accretion Disk Theory*, *Living Reviews in Relativity*, 16(1), 1
- Alexander, D. M., Swinbank, A. M., Smail, I., et al. (2010), *Searching for Evidence of Energetic Feedback in Distant Galaxies: A Galaxy Wide Outflow in a $z \sim 2$ Ultraluminous Infrared Galaxy*, *Monthly Notices of the Royal Astronomical Society*, 402, 2211
- Anglés-Alcázar, D., Quataert, E., Hopkins, P. F., et al. (2021), *Cosmological Simulations of Quasar Fueling to Subparsec Scales Using Lagrangian Hyper-refinement*, *The Astrophysical Journal*, 917, 53
- Angulo, R. E. and Hahn, O. (2022), *Large-Scale Dark Matter Simulations*, *Living Reviews in Computational Astrophysics*, 8, 1
- Antonucci, R. (1993), *Unified Models for Active Galactic Nuclei and Quasars.*, *Annual Review of Astronomy and Astrophysics*, 31, 473
- Armitage, P. J. (2022), *Lecture Notes on Accretion Disk Physics*
- Balbus, S. A. and Hawley, J. F. (1991), *A Powerful Local Shear Instability in Weakly Magnetized Disks. I. Linear Analysis*, *The Astrophysical Journal*, 376, 214
- Balbus, S. A. and Hawley, J. F. (1998), *Instability, Turbulence, and Enhanced Transport in Accretion Disks*, *Reviews of Modern Physics*, 70, 1
- Balsara, D. S. (1995), *Von Neumann Stability Analysis of Smooth Particle Hydrodynamics—Suggestions for Optimal Algorithms*, *Journal of Computational Physics*, 121, 357
- Bambi, C., Brenneman, L. W., Dauser, T., et al. (2021), *Towards Precision Measurements of Accreting Black Holes Using X-Ray Reflection Spectroscopy*, *Space Science Reviews*, 217, 65

- Bardeen, J. M. (1970), *Kerr Metric Black Holes*, Nature, 226(5240), 64
- Bardeen, J. M. and Petterson, J. A. (1975), *The Lense-Thirring Effect and Accretion Disks around Kerr Black Holes*, The Astrophysical Journal, 195, L65
- Bardeen, J. M., Press, W. H., and Teukolsky, S. A. (1972), *Rotating Black Holes: Locally Nonrotating Frames, Energy Extraction, and Scalar Synchrotron Radiation*, The Astrophysical Journal, 178, 347
- Barnes, J. and Hut, P. (1986), *A Hierarchical $O(N \log N)$ Force-Calculation Algorithm*, Nature, 324, 446
- Beck, A. M., Murante, G., Arth, A., et al. (2016), *An Improved SPH Scheme for Cosmological Simulations*, Monthly Notices of the Royal Astronomical Society, 455(2), 2110
- Beckmann, R. S., Dubois, Y., Guillard, P., et al. (2019), *Dense Gas Formation and Destruction in a Simulated Perseus-like Galaxy Cluster with Spin-Driven Black Hole Feedback*, Astronomy & Astrophysics, 631, A60
- Beckmann, R. S., Smethurst, R. J., Simmons, B. D., et al. (2023), *Supermassive Black Holes in Merger-Free Galaxies Have Higher Spins Which Are Preferentially Aligned with Their Host Galaxy*, Monthly Notices of the Royal Astronomical Society, stad1795
- Begelman, M. C. and Cioffi, D. F. (1989), *Overpressured Cocoons in Extragalactic Radio Sources*, The Astrophysical Journal, 345, L21
- Behroozi, P. S., Wechsler, R. H., and Conroy, C. (2013), *The Average Star Formation Histories of Galaxies in Dark Matter Halos from $z = 0-8$* , The Astrophysical Journal, 770, 57
- Benson, A. J., Bower, R. G., Frenk, C. S., et al. (2003), *What Shapes the Luminosity Function of Galaxies?*, The Astrophysical Journal, 599, 38
- Berger, M. and Colella, P. (1989), *Local Adaptive Mesh Refinement for Shock Hydrodynamics*, Journal of Computational Physics, 82(1), 64
- Berger, M. J. and Oliger, J. (1984), *Adaptive Mesh Refinement for Hyperbolic Partial Differential Equations*, Journal of Computational Physics, 53(3), 484
- Bernardeau, F., Colombi, S., Gaztañaga, E., and Scoccimarro, R. (2002), *Large-Scale Structure of the Universe and Cosmological Perturbation Theory*, Physics Reports, 367, 1
- Berti, E. and Volonteri, M. (2008), *Cosmological Black Hole Spin Evolution by Mergers and Accretion*, The Astrophysical Journal, 684, 822
- Binney, J. and Tremaine, S. (2008), *Galactic Dynamics: Second Edition*
- Blandford, R. D. and Payne, D. G. (1982), *Hydromagnetic Flows from Accretion Disks and the Production of Radio Jets.*, Monthly Notices of the Royal Astronomical Society, 199, 883

- Blandford, R. D. and Znajek, R. L. (1977), *Electromagnetic Extraction of Energy from Kerr Black Holes.*, Monthly Notices of the Royal Astronomical Society, 179, 433
- Boccardi, B., Perucho, M., Casadio, C., et al. (2021), *Jet Collimation in NGC 315 and Other Nearby AGN*, Astronomy & Astrophysics, 647, A67
- Boggess, N. W., Mather, J. C., Weiss, R., et al. (1992), *The COBE Mission: Its Design and Performance Two Years after Launch*, The Astrophysical Journal, 397, 420
- Bollati, F., Lupi, A., Dotti, M., and Haardt, F. (2023), *Dynamical Evolution of Massive Black Hole Pairs in the Presence of Spin-Dependent Radiative Feedback*, Monthly Notices of the Royal Astronomical Society, 520, 3696
- Bonafede, A., Dolag, K., Stasyszyn, F., et al. (2011), *A Non-Ideal Magnetohydrodynamic GADGET: Simulating Massive Galaxy Clusters*, Monthly Notices of the Royal Astronomical Society, 418, 2234
- Bondi, H. (1952), *On Spherically Symmetrical Accretion*, Monthly Notices of the Royal Astronomical Society, 112(2), 195
- Bondi, H. and Hoyle, F. (1944), *On the Mechanism of Accretion by Stars*, Monthly Notices of the Royal Astronomical Society, 104(5), 273
- Booth, C. M. and Schaye, J. (2009), *Cosmological Simulations of the Growth of Supermassive Black Holes and Feedback from Active Galactic Nuclei: Method and Tests*, Monthly Notices of the Royal Astronomical Society, 398(1), 53
- Böss, L. M., Steinwandel, U. P., Dolag, K., and Lesch, H. (2023), *CRESCENDO: An on-the-Fly Fokker-Planck Solver for Spectral Cosmic Rays in Cosmological Simulations*, Monthly Notices of the Royal Astronomical Society, 519, 548
- Boyer, R. H. and Lindquist, R. W. (1967), *Maximal Analytic Extension of the Kerr Metric*, Journal of Mathematical Physics, 8, 265
- Broderick, A. E., Tiede, P., Pesce, D. W., and Gold, R. (2022), *Measuring Spin from Relative Photon-ring Sizes*, The Astrophysical Journal, 927(1), 6
- Bromberg, O., Nakar, E., Piran, T., and Sari, R. (2011), *The Propagation of Relativistic Jets in External Media*, The Astrophysical Journal, 740, 100
- Bryan, G. L. and Norman, M. L. (1995), *Simulating X-ray Clusters with Adaptive Mesh Refinement*, 187, 95.04
- Bryan, G. L., Norman, M. L., O'Shea, B. W., et al. (2014), *ENZO: An Adaptive Mesh Refinement Code for Astrophysics*, The Astrophysical Journal Supplement Series, 211, 19

- Bustamante, S. and Springel, V. (2019), *Spin Evolution and Feedback of Supermassive Black Holes in Cosmological Simulations*, Monthly Notices of the Royal Astronomical Society, 490(3), 4133
- Cardoso, V., Macedo, C. F., Pani, P., and Ferrari, V. (2016), *Black Holes and Gravitational Waves in Models of Minicharged Dark Matter*, Journal of Cosmology and Astroparticle Physics, 2016(05), 054
- Cattaneo, A., Faber, S. M., Binney, J., et al. (2009), *The Role of Black Holes in Galaxy Formation and Evolution*, Nature, 460, 213
- Cenci, E., Sala, L., Lupi, A., et al. (2020), *Black Hole Spin Evolution in Warped Accretion Discs*, Monthly Notices of the Royal Astronomical Society, 500(3), 3719
- Chabrier, G. (2003), *Galactic Stellar and Substellar Initial Mass Function*, Publications of the Astronomical Society of the Pacific, 115(809), 763
- Chael, A., Lupsasca, A., Wong, G. N., and Quataert, E. (2023), *Black Hole Polarimetry I: A Signature of Electromagnetic Energy Extraction*
- Chelouche, D. (2013), *THE CASE FOR STANDARD IRRADIATED ACCRETION DISKS IN ACTIVE GALACTIC NUCLEI*, The Astrophysical Journal, 772(1), 9
- Chen, X., Abramowicz, M. A., Lasota, J.-P., et al. (1995), *Unified Description of Accretion Flows around Black Holes*, The Astrophysical Journal, 443, L61
- Cho, H., Prather, B. S., Narayan, R., et al. (2023), *Bridging Scales in Black Hole Accretion and Feedback: Magnetized Bondi Accretion in 3D GRMHD*, The Astrophysical Journal, 959, L22
- Churazov, E., Sazonov, S., Sunyaev, R., et al. (2005), *Supermassive Black Holes in Elliptical Galaxies: Switching from Very Bright to Very Dim*, Monthly Notices of the Royal Astronomical Society, 363, L91
- Churazov, E., Sunyaev, R., Forman, W., and Bohringer, H. (2002), *Cooling Flows as a Calorimeter of Active Galactic Nucleus Mechanical Power*, Monthly Notices of the Royal Astronomical Society, 332(3), 729
- Cielo, S., Babul, A., Antonuccio-Delogu, V., et al. (2018), *Feedback from Reorienting AGN Jets: I. Jet-ICM Coupling, Cavity Properties and Global Energetics*, Astronomy & Astrophysics, 617, A58
- Colless, M., Dalton, G., Maddox, S., et al. (2001), *The 2dF Galaxy Redshift Survey: Spectra and Redshifts*, Monthly Notices of the Royal Astronomical Society, 328, 1039
- Crain, R. A., Theuns, T., Dalla Vecchia, C., et al. (2009), *Galaxies-Intergalactic Medium Interaction Calculation - I. Galaxy Formation as a Function of Large-Scale Environment*, Monthly Notices of the Royal Astronomical Society, 399, 1773

- Crawford, C. S., Allen, S. W., Ebeling, H., et al. (1999), *The ROSAT Brightest Cluster Sample - III. Optical Spectra of the Central Cluster Galaxies*, Monthly Notices of the Royal Astronomical Society, 306, 857
- Croton, D. J., Springel, V., White, S. D. M., et al. (2006), *The Many Lives of Active Galactic Nuclei: Cooling Flows, Black Holes and the Luminosities and Colours of Galaxies*, Monthly Notices of the Royal Astronomical Society, 365(1), 11
- Dabhade, P., Röttgering, H. J. A., Bagchi, J., et al. (2020), *Giant Radio Galaxies in the LOFAR Two-metre Sky Survey: I. Radio and Environmental Properties*, Astronomy & Astrophysics, 635, A5
- Daly, R. A. (2009), *Bounds on Black Hole Spins*, The Astrophysical Journal, 696, L32
- Daly, R. A. (2011), *Estimates of Black Hole Spin Properties of 55 Sources*, Monthly Notices of the Royal Astronomical Society, 414, 1253
- Daly, R. A. (2019), *Black Hole Spin and Accretion Disk Magnetic Field Strength Estimates for More Than 750 Active Galactic Nuclei and Multiple Galactic Black Holes*, The Astrophysical Journal, 886, 37
- Daly, R. A. (2021), *Black Hole Mass Accretion Rates and Efficiency Factors for over 750 AGN and Multiple GBH*, Monthly Notices of the Royal Astronomical Society, 500, 215
- Davé, R., Anglés-Alcázar, D., Narayanan, D., et al. (2019), *SIMBA: Cosmological Simulations with Black Hole Growth and Feedback*, Monthly Notices of the Royal Astronomical Society, 486, 2827
- David, L. P., Jones, C., Forman, W., et al. (2009), *Isotropic Active Galactic Nucleus Heating with Small Radio-quiet Bubbles in the NGC 5044 Group*, The Astrophysical Journal, 705, 624
- Davis, S. W. and Laor, A. (2011), *THE RADIATIVE EFFICIENCY OF ACCRETION FLOWS IN INDIVIDUAL ACTIVE GALACTIC NUCLEI*, The Astrophysical Journal, 728(2), 98
- Davis, S. W. and Tchekhovskoy, A. (2020), *Magnetohydrodynamics Simulations of Active Galactic Nucleus Disks and Jets*, Annual Review of Astronomy and Astrophysics, 58(1), 407
- Dehnen, W. (2002), *A Hierarchical $O(N)$ Force Calculation Algorithm*, Journal of Computational Physics, 179, 27
- Dehnen, W. and Aly, H. (2012), *Improving Convergence in Smoothed Particle Hydrodynamics Simulations without Pairing Instability: SPH without Pairing Instability*, Monthly Notices of the Royal Astronomical Society, 425(2), 1068
- Di Matteo, T., Colberg, J., Springel, V., et al. (2008), *Direct Cosmological Simulations of the Growth of Black Holes and Galaxies*, The Astrophysical Journal, 676(1), 33

- Di Matteo, T., Springel, V., and Hernquist, L. (2005), *Energy Input from Quasars Regulates the Growth and Activity of Black Holes and Their Host Galaxies*, *Nature*, 433(7026), 604
- D’Inverno, R. A. (1992), *Introducing Einstein’s Relativity*
- Dolag, K., Borgani, S., Murante, G., and Springel, V. (2009), *Substructures in Hydrodynamical Cluster Simulations*, *Monthly Notices of the Royal Astronomical Society*, 399(2), 497
- Dolag, K., Jubelgas, M., Springel, V., et al. (2004), *Thermal Conduction in Simulated Galaxy Clusters*, *The Astrophysical Journal*, 606(2), L97
- Dolag, K., Vazza, F., Brunetti, G., and Tormen, G. (2005), *Turbulent Gas Motions in Galaxy Cluster Simulations: The Role of Smoothed Particle Hydrodynamics Viscosity*, *Monthly Notices of the Royal Astronomical Society*, 364(3), 753
- Dong-Páez, C. A., Volonteri, M., Beckmann, R. S., et al. (2023), *Black Hole Mergers as Tracers of Spinning Massive Black Hole and Galaxy Populations in the Obelisk Simulation*, *Astronomy & Astrophysics*, 673, A120
- Donnert, J., Dolag, K., Brunetti, G., and Cassano, R. (2013), *Rise and Fall of Radio Haloes in Simulated Merging Galaxy Clusters*, *Monthly Notices of the Royal Astronomical Society*, 429(4), 3564
- Dotti, M., Colpi, M., Pallini, S., et al. (2013), *ON THE ORIENTATION AND MAGNITUDE OF THE BLACK HOLE SPIN IN GALACTIC NUCLEI*, *The Astrophysical Journal*, 762(2), 68
- Dubois, Y., Beckmann, R., Bournaud, F., et al. (2021), *Introducing the NEWHORIZON Simulation: Galaxy Properties with Resolved Internal Dynamics across Cosmic Time*, *Astronomy and Astrophysics*, 651, A109
- Dubois, Y., Devriendt, J., Slyz, A., and Teyssier, R. (2012), *Self-Regulated Growth of Supermassive Black Holes by a Dual Jet-Heating Active Galactic Nucleus Feedback Mechanism: Methods, Tests and Implications for Cosmological Simulations: AGN Feedback for Cosmological Simulations*, *Monthly Notices of the Royal Astronomical Society*, 420(3), 2662
- Dubois, Y., Peirani, S., Pichon, C., et al. (2016), *The Horizon-AGN Simulation: Morphological Diversity of Galaxies Promoted by AGN Feedback*, *Monthly Notices of the Royal Astronomical Society*, 463(4), 3948
- Dubois, Y., Volonteri, M., and Silk, J. (2014a), *Black Hole Evolution - III. Statistical Properties of Mass Growth and Spin Evolution Using Large-Scale Hydrodynamical Cosmological Simulations*, *Monthly Notices of the Royal Astronomical Society*, 440, 1590
- Dubois, Y., Volonteri, M., Silk, J., et al. (2014b), *Black Hole Evolution – II. Spinning Black Holes in a Supernova-Driven Turbulent Interstellar Medium*, *Monthly Notices of the Royal Astronomical Society*, 440(3), 2333

- Duffell, P. C. and MacFadyen, A. I. (2011), *TESS: A RELATIVISTIC HYDRODYNAMICS CODE ON A MOVING VORONOI MESH*, The Astrophysical Journal Supplement Series, 197(2), 15
- Dunn, R. J. H. and Fabian, A. C. (2006), *Investigating AGN Heating in a Sample of Nearby Clusters*, Monthly Notices of the Royal Astronomical Society, 373, 959
- Dunn, R. J. H. and Fabian, A. C. (2008), *Investigating Heating and Cooling in the BCS and B55 Cluster Samples*, Monthly Notices of the Royal Astronomical Society, 385, 757
- Eddington, A. S. (1916), *On the Radiative Equilibrium of the Stars*, Monthly Notices of the Royal Astronomical Society, 77(1), 16
- Elvis, M., Wilkes, B. J., McDowell, J. C., et al. (1994), *Atlas of Quasar Energy Distributions*, The Astrophysical Journal Supplement Series, 95, 1
- Enderlein, J. (1997), *A Heuristic Way of Obtaining the Kerr Metric*, American Journal of Physics, 65, 897
- Event Horizon Telescope Collaboration, Akiyama, K., Alberdi, A., et al. (2022), *First Sagittarius A* Event Horizon Telescope Results. VI. Testing the Black Hole Metric*, The Astrophysical Journal, 930, L17
- Event Horizon Telescope Collaboration, Akiyama, K., Algaba, J. C., et al. (2021), *First M87 Event Horizon Telescope Results. VIII. Magnetic Field Structure near The Event Horizon*, The Astrophysical Journal, 910, L13
- Fabian, A. (2012), *Observational Evidence of Active Galactic Nuclei Feedback*, Annual Review of Astronomy and Astrophysics, 50(1), 455
- Fabian, A. C. (1994), *Cooling Flows in Clusters of Galaxies*, Annual Review of Astronomy and Astrophysics, 32(1), 277
- Fabian, A. C. (1999), *The Obscured Growth of Massive Black Holes*, Monthly Notices of the Royal Astronomical Society, 308, L39
- Fabian, A. C., Sanders, J. S., Allen, S. W., et al. (2011), *A Wide Chandra View of the Core of the Perseus Cluster*, Monthly Notices of the Royal Astronomical Society, 418, 2154
- Fanidakis, N., Baugh, C. M., Benson, A. J., et al. (2011), *Grand Unification of AGN Activity in the Λ CDM Cosmology*, Monthly Notices of the Royal Astronomical Society, 410, 53
- Ferland, G. J., Chatzikos, M., Guzmán, F., et al. (2017), *The 2017 Release Cloudy*, Revista Mexicana de Astronomía y Astrofísica, 53, 385
- Ferrarese, L. and Merritt, D. (2000), *A Fundamental Relation between Supermassive Black Holes and Their Host Galaxies*, The Astrophysical Journal, 539(1), L9

- Feruglio, C., Maiolino, R., Piconcelli, E., et al. (2010), *Quasar Feedback Revealed by Giant Molecular Outflows*, *Astronomy and Astrophysics*, 518, L155
- Fiacconi, D., Sijacki, D., and Pringle, J. E. (2018), *Galactic Nuclei Evolution with Spinning Black Holes: Method and Implementation*, *Monthly Notices of the Royal Astronomical Society*, 477(3), 3807
- Forman, W., Jones, C., Churazov, E., et al. (2007), *Filaments, Bubbles, and Weak Shocks in the Gaseous Atmosphere of M87*, *The Astrophysical Journal*, 665, 1057
- Fragile, P. C., Blaes, O. M., Anninos, P., and Salmonson, J. D. (2007), *Global General Relativistic Magnetohydrodynamic Simulation of a Tilted Black Hole Accretion Disk*, *The Astrophysical Journal*, 668, 417
- Frank, J., King, A., and Raine, D. J. (2002), *Accretion Power in Astrophysics: Third Edition*
- Garrison, L. H., Eisenstein, D. J., Ferrer, D., et al. (2016), *Improving Initial Conditions for Cosmological N-body Simulations*, *Monthly Notices of the Royal Astronomical Society*, 461, 4125
- Gaspari, M., Ruszkowski, M., and Oh, S. P. (2013), *Chaotic Cold Accretion on to Black Holes*, *Monthly Notices of the Royal Astronomical Society*, 432, 3401
- Gebhardt, K., Bender, R., Bower, G., et al. (2000), *A Relationship between Nuclear Black Hole Mass and Galaxy Velocity Dispersion*, *The Astrophysical Journal*, 539, L13
- Ghisellini, G. (2013), *Radiative Processes in High Energy Astrophysics*, *Lecture Notes in Physics*, Berlin Springer Verlag, 873
- Ghisellini, G., Tavecchio, F., Foschini, L., et al. (2010), *General Physical Properties of Bright Fermi Blazars*, *Monthly Notices of the Royal Astronomical Society*, 402, 497
- Gofford, J., Reeves, J. N., McLaughlin, D. E., et al. (2015), *The Suzaku View of Highly Ionized Outflows in AGN - II. Location, Energetics and Scalings with Bolometric Luminosity*, *Monthly Notices of the Royal Astronomical Society*, 451, 4169
- Greene, J. E., Zakamska, N. L., and Smith, P. S. (2012), *A Spectacular Outflow in an Obscured Quasar*, *The Astrophysical Journal*, 746, 86
- Griffin, A. J., Lacey, C. G., Gonzalez-Perez, V., and Lagos, C. d. P. (2020), *The Evolution of Radio Jets across Cosmic Time*
- Groth, F., Steinwandel, U. P., Valentini, M., and Dolag, K. (2023), *The Cosmological Simulation Code OpenGadget3 – Implementation of Meshless Finite Mass*
- Gültekin, K., Richstone, D. O., Gebhardt, K., et al. (2009), *The M - σ and M - L Relations in Galactic Bulges, and Determinations of Their Intrinsic Scatter*, *The Astrophysical Journal*, 698, 198

- Guo, F. and Mathews, W. G. (2011), *COSMIC-RAY-DOMINATED AGN JETS AND THE FORMATION OF X-RAY CAVITIES IN GALAXY CLUSTERS*, *The Astrophysical Journal*, 728(2), 121
- Guo, M., Stone, J. M., Kim, C.-G., and Quataert, E. (2022), *Toward Horizon-scale Accretion Onto Supermassive Black Holes in Elliptical Galaxies*
- Haardt, F. and Madau, P. (2001), *Modelling the UV/X-ray Cosmic Background with CUBA*, arXiv, eprint: arXiv:astro-ph/0106018
- Hahn, O. and Abel, T. (2011), *Multi-Scale Initial Conditions for Cosmological Simulations*, *Monthly Notices of the Royal Astronomical Society*, 415, 2101
- Häring, N. and Rix, H.-W. (2004), *On the Black Hole Mass-Bulge Mass Relation*, *The Astrophysical Journal*, 604(2), L89
- Harrison, C. M., Costa, T., Tadhunter, C. N., et al. (2018), *AGN Outflows and Feedback Twenty Years On*, *Nature Astronomy*, 2(3), 198
- Hawley, J. F. and Krolik, J. H. (2006), *Magnetically Driven Jets in the Kerr Metric*, *The Astrophysical Journal*, 641, 103
- Hirschmann, M., Dolag, K., Saro, A., et al. (2014), *Cosmological Simulations of Black Hole Growth: AGN Luminosities and Downsizing*, *Monthly Notices of the Royal Astronomical Society*, 442(3), 2304
- Hlavacek-Larrondo, J., Li, Y., and Churazov, E. (2022), *AGN Feedback in Groups and Clusters of Galaxies*, in *Handbook of X-ray and Gamma-ray Astrophysics* {*Handbook of X-ray and Gamma-ray Astrophysics*, 1–66, Springer
- Hlavacek-Larrondo, J., McDonald, M., Benson, B. A., et al. (2015), *X-Ray Cavities in a Sample of 83 SPT-selected Clusters of Galaxies: Tracing the Evolution of AGN Feedback in Clusters of Galaxies out to $Z=1.2$* , *The Astrophysical Journal*, 805, 35
- Hlavacek-Larrondo, J., Rhea, C. L., Webb, T., et al. (2020), *Evidence of Runaway Gas Cooling in the Absence of Supermassive Black Hole Feedback at the Epoch of Cluster Formation*, *The Astrophysical Journal*, 898, L50
- Ho, L. C. (2008), *Nuclear Activity in Nearby Galaxies.*, *Annual Review of Astronomy and Astrophysics*, 46, 475
- Hockney, R. W. and Eastwood, J. W. (1981), *Computer Simulation Using Particles*
- Hopkins, P. F. (2015), *A New Class of Accurate, Mesh-Free Hydrodynamic Simulation Methods*, *Monthly Notices of the Royal Astronomical Society*, 450, 53
- Hopkins, P. F., Grudic, M. Y., Su, K.-Y., et al. (2023a), *FORGE'd in FIRE: Resolving the End of Star Formation and Structure of AGN Accretion Disks from Cosmological Initial Conditions*

- Hopkins, P. F., Squire, J., Su, K.-Y., et al. (2023b), *FORGE'd in FIRE II: The Formation of Magnetically-Dominated Quasar Accretion Disks from Cosmological Initial Conditions*
- Horton, M., Krause, M., and Hardcastle, M. (2020), *3D Hydrodynamic Simulations of Large-Scale Precessing Jets: Radio Morphology*, Monthly Notices of the Royal Astronomical Society, 499(4), 5765
- Hoyle, F. and Lyttleton, R. A. (1939), *The Effect of Interstellar Matter on Climatic Variation*, Mathematical Proceedings of the Cambridge Philosophical Society, 35(3), 405
- Hubble, E. (1929), *A Relation between Distance and Radial Velocity among Extra-Galactic Nebulae*, Proceedings of the National Academy of Science, 15, 168
- Huško, F., Lacey, C. G., Schaye, J., et al. (2022), *Spin-Driven Jet Feedback in Idealised Simulations of Galaxy Groups and Clusters*
- Izquierdo-Villalba, D., Bonoli, S., Dotti, M., et al. (2020), *From Galactic Nuclei to the Halo Outskirts: Tracing Supermassive Black Holes across Cosmic History and Environments*, Monthly Notices of the Royal Astronomical Society, 495(4), 4681
- Jiang, J., Abdikamalov, A. B., Bambi, C., and Reynolds, C. S. (2022), *Black Hole Spin Measurements Based on a Thin Disc Model with Finite Thickness - I. An Example Study of MCG-06-30-15*, Monthly Notices of the Royal Astronomical Society, 514, 3246
- Jiang, J., Fabian, A. C., Dauser, T., et al. (2019), *High Density Reflection Spectroscopy - II. The Density of the Inner Black Hole Accretion Disc in AGN*, Monthly Notices of the Royal Astronomical Society, 489, 3436
- Kaaz, N., Liska, M. T. P., Jacquemin-Ide, J., et al. (2022), *Nozzle Shocks, Disk Tearing and Streamers Drive Rapid Accretion in 3D GRMHD Simulations of Warped Thin Disks*
- Karademir, G. S., Remus, R.-S., Burkert, A., et al. (2019), *The Outer Stellar Halos of Galaxies: How Radial Merger Mass Deposition, Shells, and Streams Depend on Infall-Orbit Configurations*, Monthly Notices of the Royal Astronomical Society, 487, 318
- Karakas, A. and Lattanzio, J. C. (2007), *Stellar Models and Yields of Asymptotic Giant Branch Stars*, Publications of the Astronomical Society of Australia, 24(3), 103
- King, A. (2003), *Black Holes, Galaxy Formation, and the M_{BH} - Relation*, The Astrophysical Journal, 596(1), L27
- King, A. R., Lubow, S. H., Ogilvie, G. I., and Pringle, J. E. (2005), *Aligning Spinning Black Holes and Accretion Discs*, Monthly Notices of the Royal Astronomical Society, 363(1), 49
- King, A. R., Pringle, J. E., and Hofmann, J. A. (2008), *The Evolution of Black Hole Mass and Spin in Active Galactic Nuclei*, Monthly Notices of the Royal Astronomical Society, 385, 1621

- Komatsu, E., Dunkley, J., Nolta, M. R., et al. (2009), *Five-Year Wilkinson Microwave Anisotropy Probe Observations: Cosmological Interpretation*, The Astrophysical Journal Supplement Series, 180, 330
- Kormendy, J. and Ho, L. C. (2013), *Coevolution (Or Not) of Supermassive Black Holes and Host Galaxies*, Annual Review of Astronomy and Astrophysics, 51(1), 511
- Koudmani, S., Somerville, R. S., Sijacki, D., et al. (2023), *A Unified Accretion Disc Model for Supermassive Black Holes in Galaxy Formation Simulations: Method and Implementation*
- Kravtsov, A. V., Klypin, A. A., and Khokhlov, A. M. (1997), *Adaptive Refinement Tree: A New High-Resolution N-Body Code for Cosmological Simulations*, The Astrophysical Journal Supplement Series, 111, 73
- Lagos, C. D. P., Padilla, N. D., and Cora, S. A. (2009), *Black Hole Spin and Radio Loudness in a Cold Dark Matter Universe*, Monthly Notices of the Royal Astronomical Society, 395, 625
- Lalakos, A., Gottlieb, O., Kaaz, N., et al. (2022), *Bridging Bondi and Event Horizon Scales: 3D GRMHD Simulations Reveal X-Shaped Radio Galaxy Morphology*, The Astrophysical Journal Letters, 936(1), L5
- Lasota, J.-P., Gourgoulhon, E., Abramowicz, M., et al. (2014), *Extracting Black-Hole Rotational Energy: The Generalized Penrose Process*, Physical Review D, 89(2), 024041
- Lemaître, G. (1927), *Un Univers Homogène de Masse Constante et de Rayon Croissant Rendant Compte de La Vitesse Radiale Des Nébuleuses Extra-Galactiques*, Annales de la Société Scientifique de Bruxelles, 47, 49
- Liddle, A. R. and Lyth, D. H. (2000), *Cosmological Inflation and Large-Scale Structure*
- Liska, M., Chatterjee, K., Tchekhovskoy, A., et al. (2019a), *H-AMR: A New GPU-accelerated GRMHD Code for Exascale Computing with 3D Adaptive Mesh Refinement and Local Adaptive Time-Stepping*
- Liska, M., Hesp, C., Tchekhovskoy, A., et al. (2018), *Formation of Precessing Jets by Tilted Black Hole Discs in 3D General Relativistic MHD Simulations*, Monthly Notices of the Royal Astronomical Society: Letters, 474(1), L81
- Liska, M., Tchekhovskoy, A., Ingram, A., and van der Klis, M. (2019b), *Bardeen–Peterson Alignment, Jets, and Magnetic Truncation in GRMHD Simulations of Tilted Thin Accretion Discs*, Monthly Notices of the Royal Astronomical Society, 487(1), 550
- Liska, M. T. P., Kaaz, N., Musoke, G., et al. (2022), *Radiation Transport Two-Temperature GRMHD Simulations of Warped Accretion Disks*
- Liu, H., Luo, B., Brandt, W. N., et al. (2021), *On the Observational Difference between the Accretion Disk-Corona Connections among Super- and Sub-Eddington Accreting Active Galactic Nuclei*, The Astrophysical Journal, 910, 103

- Lowell, B., Jacquemin-Ide, J., Tchekhovskoy, A., and Duncan, A. (2024), *Rapid Black Hole Spin-down by Thick Magnetically Arrested Disks*, *The Astrophysical Journal*, 960, 82
- Madau, P., Haardt, F., and Dotti, M. (2014), *SUPER-CRITICAL GROWTH OF MASSIVE BLACK HOLES FROM STELLAR-MASS SEEDS*, *The Astrophysical Journal*, 784(2), L38
- Magorrian, J., Tremaine, S., Richstone, D., et al. (1998), *The Demography of Massive Dark Objects in Galaxy Centers*, *The Astronomical Journal*, 115, 2285
- Maio, U., Dotti, M., Petkova, M., et al. (2013), *EFFECTS OF CIRCUMNUCLEAR DISK GAS EVOLUTION ON THE SPIN OF CENTRAL BLACK HOLES*, *The Astrophysical Journal*, 767(1), 37
- Maiolino, R., Gallerani, S., Neri, R., et al. (2012), *Evidence of Strong Quasar Feedback in the Early Universe*, *Monthly Notices of the Royal Astronomical Society*, 425, L66
- Mallick, L., Fabian, A. C., García, J. A., et al. (2022), *High-Density Disc Reflection Spectroscopy of Low-Mass Active Galactic Nuclei*, *Monthly Notices of the Royal Astronomical Society*, 513(3), 4361
- Martin, R. G., Pringle, J. E., and Tout, C. A. (2007), *Alignment and Precession of a Black Hole with a Warped Accretion Disc*, *Monthly Notices of the Royal Astronomical Society*, 381(4), 1617
- Martínez-Sansigre, A. and Rawlings, S. (2011), *Observational Constraints on the Spin of the Most Massive Black Holes from Radio Observations: Observational Constraints on the Spin of SMBHs*, *Monthly Notices of the Royal Astronomical Society*, 414(3), 1937
- Massonneau, W., Dubois, Y., Volonteri, M., and Beckmann, R. S. (2023a), *How the Super-Eddington Regime Affects Black Hole Spin Evolution in High-Redshift Galaxies*, *Astronomy and Astrophysics*, 669, A143
- Massonneau, W., Volonteri, M., Dubois, Y., and Beckmann, R. S. (2023b), *How the Super-Eddington Regime Regulates Black Hole Growth in High-Redshift Galaxies*, *Astronomy & Astrophysics*, 670, A180
- McConnell, N. J. and Ma, C.-P. (2013), *REVISITING THE SCALING RELATIONS OF BLACK HOLE MASSES AND HOST GALAXY PROPERTIES*, *The Astrophysical Journal*, 764(2), 184
- McDonald, M., Bayliss, M., Benson, B. A., et al. (2012), *A Massive, Cooling-Flow-Induced Starburst in the Core of a Luminous Cluster of Galaxies*, *Nature*, 488, 349
- McDonald, M., McNamara, B. R., Voit, G. M., et al. (2019), *Anatomy of a Cooling Flow: The Feedback Response to Pure Cooling in the Core of the Phoenix Cluster*, *The Astrophysical Journal*, 885, 63

- McKinney, J. C., Tchekhovskoy, A., and Blandford, R. D. (2012), *General Relativistic Magnetohydrodynamic Simulations of Magnetically Choked Accretion Flows around Black Holes*, Monthly Notices of the Royal Astronomical Society, 423, 3083
- McKinney, J. C., Tchekhovskoy, A., and Blandford, R. D. (2013), *Alignment of Magnetized Accretion Disks and Relativistic Jets with Spinning Black Holes*, Science, 339(6115), 49
- McNamara, B. R. and Nulsen, P. E. J. (2007), *Heating Hot Atmospheres with Active Galactic Nuclei*, Annual Review of Astronomy and Astrophysics, 45, 117
- McNamara, B. R. and Nulsen, P. E. J. (2012), *Mechanical Feedback from Active Galactic Nuclei in Galaxies, Groups and Clusters*, New Journal of Physics, 14(5), 055023
- Merloni, A. and Heinz, S. (2007), *Measuring the Kinetic Power of Active Galactic Nuclei in the Radio Mode*, Monthly Notices of the Royal Astronomical Society, 381, 589
- Mezcua, M. and Prieto, M. A. (2014), *EVIDENCE OF PARSEC-SCALE JETS IN LOW-LUMINOSITY ACTIVE GALACTIC NUCLEI*, The Astrophysical Journal, 787(1), 62
- Mizuta, A. and Ioka, K. (2013), *Opening Angles of Collapsar Jets*, The Astrophysical Journal, 777, 162
- Murchikova, E. M., Phinney, E. S., Pancoast, A., and Blandford, R. D. (2019), *A Cool Accretion Disk around the Galactic Centre Black Hole*, Nature, 570, 83
- Nakamura, M., Tregillis, I. L., Li, H., and Li, S. (2008), *A Numerical Model of Hercules A by Magnetic Tower: Jet/Lobe Transition, Wiggling, and the Magnetic Field Distribution*, The Astrophysical Journal, 686, 843
- Narayan, R., Chael, A., Chatterjee, K., et al. (2022), *Jets in Magnetically Arrested Hot Accretion Flows: Geometry, Power and Black Hole Spindown*, Monthly Notices of the Royal Astronomical Society, 511(3), 3795
- Narayan, R. and Yi, I. (1995), *Advection-Dominated Accretion: Underfed Black Holes and Neutron Stars*, The Astrophysical Journal, 452, 710
- Nardini, E., Reeves, J. N., Gofford, J., et al. (2015), *Black Hole Feedback in the Luminous Quasar PDS 456*, Science, 347, 860
- Natarajan, P. and Armitage, P. J. (1999), *Warped Discs and the Directional Stability of Jets in Active Galactic Nuclei*, Monthly Notices of the Royal Astronomical Society, 309(4), 961
- Natarajan, P. and Pringle, J. E. (1998), *The Alignment of Disk and Black Hole Spins in Active Galactic Nuclei*, The Astrophysical Journal, 506(2), L97
- Nealon, R., Price, D. J., and Nixon, C. J. (2015), *On the Bardeen-Peterson Effect in Black Hole Accretion Discs*, Monthly Notices of the Royal Astronomical Society, 448, 1526

- Nemmen, R. S., Storchi-Bergmann, T., and Eracleous, M. (2014), *Spectral Models for Low-Luminosity Active Galactic Nuclei in LINERs: The Role of Advection-Dominated Accretion and Jets*, Monthly Notices of the Royal Astronomical Society, 438, 2804
- Netzer, H. (2015), *Revisiting the Unified Model of Active Galactic Nuclei*, Annual Review of Astronomy and Astrophysics, 53, 365
- Nomoto, K., Kobayashi, C., and Tominaga, N. (2013), *Nucleosynthesis in Stars and the Chemical Enrichment of Galaxies*, Annual Review of Astronomy and Astrophysics, 51(1), 457
- Novikov, I. D. and Thorne, K. S. (1973), *Astrophysics of Black Holes*.
- Ogilvie, G. I. (1999), *The Non-Linear Fluid Dynamics of a Warped Accretion Disc*, Monthly Notices of the Royal Astronomical Society, 304(3), 557
- Pacucci, F. and Loeb, A. (2020), *Separating Accretion and Mergers in the Cosmic Growth of Black Holes with X-Ray and Gravitational-wave Observations*, The Astrophysical Journal, 895, 95
- Padovani, P., Alexander, D. M., Assef, R. J., et al. (2017), *Active Galactic Nuclei: What's in a Name?*, The Astronomy and Astrophysics Review, 25(1), 2
- Padovani, P. and Matteucci, F. (1993), *Stellar Mass Loss in Elliptical Galaxies and the Fueling of Active Galactic Nuclei*, The Astrophysical Journal, 416, 26
- Pakmor, R., Springel, V., Coles, J. P., et al. (2022), *The MillenniumTNG Project: The Hydrodynamical Full Physics Simulation and a First Look at Its Galaxy Clusters*
- Palumbo, D. C. M., Wong, G. N., and Prather, B. S. (2020), *Discriminating Accretion States via Rotational Symmetry in Simulated Polarimetric Images of M87*, The Astrophysical Journal, 894, 156
- Papaloizou, J. C. B. and Pringle, J. E. (1983), *The Time-Dependence of Non-Planar Accretion Discs*, Monthly Notices of the Royal Astronomical Society, 202(4), 1181
- Peirani, S., Suto, Y., Beckmann, R. S., et al. (2024), *Cosmic Evolution of Black Hole-Spin and Galaxy Orientations: Clues from the NewHorizon and Galactica Simulations*
- Perego, A., Dotti, M., Colpi, M., and Volonteri, M. (2009), *Mass and Spin Co-Evolution during the Alignment of a Black Hole in a Warped Accretion Disc*, Monthly Notices of the Royal Astronomical Society, 399(4), 2249
- Peterson, B. (2006), *The Broad-Line Region in Active Galactic Nuclei*, in *Physics of Active Galactic Nuclei at All Scales*, edited by D. Alloin, R. Johnson, P. Lira, volume 693, 77–100, Springer Berlin Heidelberg

- Pillepich, A., Nelson, D., Springel, V., et al. (2019), *First Results from the TNG50 Simulation: The Evolution of Stellar and Gaseous Discs across Cosmic Time*, Monthly Notices of the Royal Astronomical Society, 490, 3196
- Planck Collaboration, Aghanim, N., Akrami, Y., et al. (2020), *Planck 2018 Results. VI. Cosmological Parameters*, Astronomy and Astrophysics, 641, A6
- Pringle, J. E. (1981), *Accretion Discs in Astrophysics*, Annual Review of Astronomy and Astrophysics, 19(1), 137
- Rafferty, D. A., McNamara, B. R., and Nulsen, P. E. J. (2008), *The Regulation of Cooling and Star Formation in Luminous Galaxies by Active Galactic Nucleus Feedback and the Cooling-Time/Entropy Threshold for the Onset of Star Formation*, The Astrophysical Journal, 687, 899
- Rafferty, D. A., McNamara, B. R., Nulsen, P. E. J., and Wise, M. W. (2006), *The Feedback-regulated Growth of Black Holes and Bulges through Gas Accretion and Starbursts in Cluster Central Dominant Galaxies*, The Astrophysical Journal, 652, 216
- Ressler, S. M., White, C. J., Quataert, E., and Stone, J. M. (2020), *Ab Initio Horizon-scale Simulations of Magnetically Arrested Accretion in Sagittarius A* Fed by Stellar Winds*, The Astrophysical Journal, 896, L6
- Reynolds, C. S. (2021), *Observational Constraints on Black Hole Spin*, Annual Review of Astronomy and Astrophysics, 59(1), 117
- Rezzolla, L., Barausse, E., Dorband, E. N., et al. (2008a), *Final Spin from the Coalescence of Two Black Holes*, Physical Review D, 78(4), 044002
- Rezzolla, L., Dorband, E. N., Reisswig, C., et al. (2008b), *Spin Diagrams for Equal-Mass Black-Hole Binaries with Aligned Spins*, The Astrophysical Journal, 679(2), 1422
- Ricarte, A., Narayan, R., and Curd, B. (2023), *Recipes for Jet Feedback and Spin Evolution of Black Holes with Strongly-Magnetized Super-Eddington Accretion Disks*
- Rupke, D. S. N. and Veilleux, S. (2011), *Integral Field Spectroscopy of Massive, Kiloparsec-scale Outflows in the Infrared-luminous QSO Mrk 231*, The Astrophysical Journal, 729, L27
- Russell, H. R., McNamara, B. R., Edge, A. C., et al. (2013), *Radiative Efficiency, Variability and Bondi Accretion on to Massive Black Holes: The Transition from Radio AGN to Quasars in Brightest Cluster Galaxies*, Monthly Notices of the Royal Astronomical Society, 432(1), 530
- Ryden, B. (2003), *Introduction to Cosmology*
- Sądowski, A. and Narayan, R. (2015), *Powerful Radiative Jets in Supercritical Accretion Discs around Non-Spinning Black Holes*, Monthly Notices of the Royal Astronomical Society, 453(3), 3214

- Sądowski, A., Narayan, R., McKinney, J. C., and Tchekhovskoy, A. (2014), *Numerical Simulations of Super-Critical Black Hole Accretion Flows in General Relativity*, Monthly Notices of the Royal Astronomical Society, 439(1), 503
- Sala, L., Cenci, E., Capelo, P. R., et al. (2020), *Non-Isotropic Feedback from Accreting Spinning Black Holes*, Monthly Notices of the Royal Astronomical Society, 500(4), 4788
- Sala, L., Valentini, M., Biffi, V., and Dolag, K. (2023), *Supermassive Black Hole Spin Evolution in Cosmological Simulations with OpenGadget3*
- Sanders, J. S., Fabian, A. C., and Taylor, G. B. (2009), *Feedback through Multiple Outbursts in the Cluster 2A 0335+096*, Monthly Notices of the Royal Astronomical Society, 396, 1449
- Schaye, J., Crain, R. A., Bower, R. G., et al. (2015), *The EAGLE Project: Simulating the Evolution and Assembly of Galaxies and Their Environments*, Monthly Notices of the Royal Astronomical Society, 446, 521
- Schaye, J., Kugel, R., Schaller, M., et al. (2023), *The FLAMINGO Project: Cosmological Hydrodynamical Simulations for Large-Scale Structure and Galaxy Cluster Surveys*, Monthly Notices of the Royal Astronomical Society, 526(4), 4978
- Scheuer, P. and Feiler, R. (1996), *The Realignment of a Black Hole Misaligned with Its Accretion Disc*, Monthly Notices of the Royal Astronomical Society, 282(1), 291
- Schmidt, M. (1963), *3C 273 : A Star-Like Object with Large Red-Shift*, Nature, 197, 1040
- Sesana, A., Barausse, E., Dotti, M., and Rossi, E. M. (2014), *Linking the Spin Evolution of Massive Black Holes to Galaxy Kinematics*, The Astrophysical Journal, 794, 104
- Shakura, N. I. and Sunyaev, R. A. (1973), *Black Holes in Binary Systems. Observational Appearance.*, Astronomy and Astrophysics, 24, 337
- Shapiro, S. L., Lightman, A. P., and Eardley, D. M. (1976), *A Two-Temperature Accretion Disk Model for Cygnus X-1: Structure and Spectrum.*, The Astrophysical Journal, 204, 187
- Shapiro, S. L. and Teukolsky, S. A. (1983), *Black Holes, White Dwarfs and Neutron Stars. The Physics of Compact Objects*
- Shen, X., Hopkins, P. F., Faucher-Giguère, C.-A., et al. (2020), *The Bolometric Quasar Luminosity Function at $z = 0-7$* , Monthly Notices of the Royal Astronomical Society, 495, 3252
- Shlosman, I., Begelman, M. C., and Frank, J. (1990), *The Fuelling of Active Galactic Nuclei*, Nature, 345, 679
- Sijacki, D., Springel, V., Di Matteo, T., and Hernquist, L. (2007), *A Unified Model for AGN Feedback in Cosmological Simulations of Structure Formation*, Monthly Notices of the Royal Astronomical Society, 380, 877

- Sijacki, D., Vogelsberger, M., Genel, S., et al. (2015), *The Illustris Simulation: The Evolving Population of Black Holes across Cosmic Time*, Monthly Notices of the Royal Astronomical Society, 452, 575
- Sikora, M., Stawarz, Ł., and Lasota, J.-P. (2007), *Radio Loudness of Active Galactic Nuclei: Observational Facts and Theoretical Implications*, The Astrophysical Journal, 658, 815
- Silk, J. and Rees, M. J. (1998), *Quasars and Galaxy Formation*, Astronomy and Astrophysics, 331, L1
- Sisk-Reynés, J., Reynolds, C. S., Matthews, J. H., and Smith, R. N. (2022), *Evidence for a Moderate Spin from X-ray Reflection of the High-Mass Supermassive Black Hole in the Cluster-Hosted Quasar H1821+643*, Monthly Notices of the Royal Astronomical Society, 514, 2568
- Soltan, A. (1982), *Masses of Quasars.*, Monthly Notices of the Royal Astronomical Society, 200, 115
- Springel, V. (2005), *The Cosmological Simulation Code Gadget-2*, Monthly Notices of the Royal Astronomical Society, 364(4), 1105
- Springel, V. (2010a), *E Pur Si Muove: Galilean-invariant Cosmological Hydrodynamical Simulations on a Moving Mesh*, Monthly Notices of the Royal Astronomical Society, 401, 791
- Springel, V. (2010b), *Smoothed Particle Hydrodynamics in Astrophysics*, Annual Review of Astronomy and Astrophysics, 48(1), 391
- Springel, V., Di Matteo, T., and Hernquist, L. (2005a), *Modelling Feedback from Stars and Black Holes in Galaxy Mergers*, Monthly Notices of the Royal Astronomical Society, 361, 776
- Springel, V. and Hernquist, L. (2003), *Cosmological Smoothed Particle Hydrodynamics Simulations: A Hybrid Multiphase Model for Star Formation*, Monthly Notices of the Royal Astronomical Society, 339(2), 289
- Springel, V., White, S. D. M., Jenkins, A., et al. (2005b), *Simulations of the Formation, Evolution and Clustering of Galaxies and Quasars*, Nature, 435, 629
- Springel, V., White, S. D. M., Tormen, G., and Kauffmann, G. (2001a), *Populating a Cluster of Galaxies - I. Results at $Z=0$* , Monthly Notices of the Royal Astronomical Society, 328, 726
- Springel, V., Yoshida, N., and White, S. D. M. (2001b), *GADGET: A Code for Collisionless and Gasdynamical Cosmological Simulations*, New Astronomy, 6, 79
- Steinborn, L. K., Dolag, K., Hirschmann, M., et al. (2015), *A Refined Sub-Grid Model for Black Hole Accretion and AGN Feedback in Large Cosmological Simulations*, Monthly Notices of the Royal Astronomical Society, 448(2), 1504

- Steinwandel, U. P., Beck, M. C., Arth, A., et al. (2019), *Magnetic Buoyancy in Simulated Galactic Discs with a Realistic Circumgalactic Medium*, Monthly Notices of the Royal Astronomical Society, 483(1), 1008
- Sturm, E., González-Alfonso, E., Veilleux, S., et al. (2011), *Massive Molecular Outflows and Negative Feedback in ULIRGs Observed by Herschel-PACS*, The Astrophysical Journal, 733, L16
- Talbot, R. Y., Bourne, M. A., and Sijacki, D. (2021), *Blandford-Znajek Jets in Galaxy Formation Simulations: Method and Implementation*, Monthly Notices of the Royal Astronomical Society, 504(3), 3619
- Talbot, R. Y., Sijacki, D., and Bourne, M. A. (2023), *Simulations of Spin-Driven AGN Jets in Gas-Rich Galaxy Mergers*
- Tamburini, F., Thidé, B., and Della Valle, M. (2020), *Measurement of the Spin of the M87 Black Hole from Its Observed Twisted Light*, Monthly Notices of the Royal Astronomical Society: Letters, 492(1), L22
- Tchekhovskoy, A. (2015), *Launching of Active Galactic Nuclei Jets*, in *The Formation and Disruption of Black Hole Jets*, edited by I. Contopoulos, D. Gabuzda, N. Kylafis, volume 414 of *Astrophysics and Space Science Library*, 45
- Tchekhovskoy, A., Narayan, R., and McKinney, J. C. (2011), *Efficient Generation of Jets from Magnetically Arrested Accretion on a Rapidly Spinning Black Hole: Jets from Magnetically Arrested BH Accretion*, Monthly Notices of the Royal Astronomical Society: Letters, 418(1), L79
- Tegmark, M. and Zaldarriaga, M. (2002), *Separating the Early Universe from the Late Universe: Cosmological Parameter Estimation beyond the Black Box*, Physical Review D, 66, 103508
- Teyssier, R. (2002), *Cosmological Hydrodynamics with Adaptive Mesh Refinement. A New High Resolution Code Called RAMSES*, Astronomy and Astrophysics, 385, 337
- Thielemann, F.-K., Argast, D., Brachwitz, F., et al. (2003), *Supernova Nucleosynthesis and Galactic Evolution*, in *From Twilight to Highlight: The Physics of Supernovae*, edited by W. Hillebrandt, B. Leibundgut, 331–343, Springer-Verlag, Berlin/Heidelberg
- Thorne, K. S. (1974), *Disk-Accretion onto a Black Hole. II. Evolution of the Hole*, The Astrophysical Journal, 191, 507
- Tombesi, F., Cappi, M., Reeves, J. N., et al. (2013), *Unification of X-ray Winds in Seyfert Galaxies: From Ultra-Fast Outflows to Warm Absorbers*, Monthly Notices of the Royal Astronomical Society, 430, 1102

- Tornatore, L., Borgani, S., Dolag, K., and Matteucci, F. (2007), *Chemical Enrichment of Galaxy Clusters from Hydrodynamical Simulations: Chemical Enrichment of Galaxy Clusters*, Monthly Notices of the Royal Astronomical Society, 382(3), 1050
- Tornatore, L., Borgani, S., Matteucci, F., et al. (2004), *Simulating the Metal Enrichment of the Intracluster Medium*, Monthly Notices of the Royal Astronomical Society, 349, L19
- Tremaine, S., Gebhardt, K., Bender, R., et al. (2002), *The Slope of the Black Hole Mass versus Velocity Dispersion Correlation*, The Astrophysical Journal, 574, 740
- Tremmel, M., Governato, F., Volonteri, M., and Quinn, T. R. (2015), *Off the Beaten Path: A New Approach to Realistically Model the Orbital Decay of Supermassive Black Holes in Galaxy Formation Simulations*, Monthly Notices of the Royal Astronomical Society, 451(2), 1868
- Tremonti, C. A., Moustakas, J., and Diamond-Stanic, A. M. (2007), *The Discovery of 1000 Km S-1 Outflows in Massive Poststarburst Galaxies at Z=0.6*, The Astrophysical Journal, 663, L77
- Urry, C. M. and Padovani, P. (1995), *Unified Schemes for Radio-Loud Active Galactic Nuclei*, Publications of the Astronomical Society of the Pacific, 107, 803
- Valentini, M., Murante, G., Borgani, S., et al. (2020), *Impact of AGN Feedback on Galaxies and Their Multiphase ISM across Cosmic Time*, Monthly Notices of the Royal Astronomical Society, 491, 2779
- Vandenbroucke, B. and De Rijcke, S. (2016), *The Moving Mesh Code Shadowfax*, Astronomy and Computing, 16, 109
- Visser, M. (2008), *The Kerr Spacetime: A Brief Introduction*
- Volonteri, M. (2010), *Formation of Supermassive Black Holes*, Astronomy and Astrophysics Review, 18, 279
- Volonteri, M., Madau, P., Quataert, E., and Rees, M. J. (2005), *The Distribution and Cosmic Evolution of Massive Black Hole Spins*, The Astrophysical Journal, 620, 69
- Volonteri, M., Sikora, M., and Lasota, J.-P. (2007), *Black Hole Spin and Galactic Morphology*, The Astrophysical Journal, 667(2), 704
- Von Der Linden, A., Best, P. N., Kauffmann, G., and White, S. D. M. (2007), *How Special Are Brightest Group and Cluster Galaxies?*, Monthly Notices of the Royal Astronomical Society, 379, 867
- Walton, D. J., Baloković, M., Fabian, A. C., et al. (2021), *Extreme Relativistic Reflection in the Active Galaxy ESO 033-G002*, Monthly Notices of the Royal Astronomical Society, 506, 1557
- Wang, Y. and Zhang, B. (2024), *Evidence of a Past Merger of the Galactic Center Black Hole*

- Weinberger, R., Springel, V., Hernquist, L., et al. (2017), *Simulating Galaxy Formation with Black Hole Driven Thermal and Kinetic Feedback*, Monthly Notices of the Royal Astronomical Society, 465(3), 3291
- Weinberger, R., Springel, V., Pakmor, R., et al. (2018), *Supermassive Black Holes and Their Feedback Effects in the IllustrisTNG Simulation*, Monthly Notices of the Royal Astronomical Society, 479, 4056
- White, S. D. M. and Rees, M. J. (1978), *Core Condensation in Heavy Halos: A Two-Stage Theory for Galaxy Formation and Clustering.*, Monthly Notices of the Royal Astronomical Society, 183, 341
- Wiersma, R. P. C., Schaye, J., Theuns, T., et al. (2009), *Chemical Enrichment in Cosmological, Smoothed Particle Hydrodynamics Simulations*, Monthly Notices of the Royal Astronomical Society, 399(2), 574
- Wilkins, D. C. (1972), *Bound Geodesics in the Kerr Metric*, Physical Review D, 5(4), 814
- Xie, F.-G. and Yuan, F. (2012), *Radiative Efficiency of Hot Accretion Flows*, Monthly Notices of the Royal Astronomical Society, 427, 1580
- Yuan, F. and Narayan, R. (2004), *On the Nature of X-Ray-Bright, Optically Normal Galaxies*, The Astrophysical Journal, 612, 724
- Yuan, F. and Narayan, R. (2014), *Hot Accretion Flows around Black Holes*, Annual Review of Astronomy and Astrophysics, 52(1), 529
- Zhang, T., Liao, S., Li, M., and Gao, L. (2019), *The Optimal Gravitational Softening Length for Cosmological N-body Simulations*, Monthly Notices of the Royal Astronomical Society, 487, 1227
- Zhang, X. and Lu, Y. (2019), *On Constraining the Growth History of Massive Black Holes via Their Distribution on the Spin-Mass Plane*

List of Figures

1.1	The distribution of galaxies in the Two Degree Field Galaxy Redshift Survey (2dFGRS) (Colless et al., 2001).	5
1.2	Different probes for the matter power spectrum (Tegmark & Zaldarriaga, 2002).	8
1.3	On the left, an illustration of the tree technique used to partition the computational domain into nodes, grouping particles recursively. On the right, the criterion to group particles and compute their combined gravitational effect at a given point, using a multipole expansion around their centre of mass. Adapted from Springel et al. (2001b).	11
1.4	Smoothing kernels for SPH estimate. Adopted from Dehnen & Aly (2012).	15
1.5	Stellar mass function at redshift zero, from the hydrodynamical simulations performed by Crain et al. (2009).	20
1.6	M_*/M_{halo} plotted as a function of M_{halo} , as predicted by Behroozi et al. (2013).	21
2.1	Schematic view of the components of an AGN. Credits: A. Merloni, ESO, 2010	24
2.2	Adopted from Padovani et al. (2017), credits C. M. Harrison.	25
2.3	Experimental correlations between BH mass and the bulge mass M_{bulge} (left panel) and bulge velocity dispersion (right panel). Adopted from Kormendy & Ho (2013).	27
2.4	Observational determination of the quasar luminosity functions. Adopted from Shen et al. (2020).	28
2.5	Observational collection of AGN feedback from jets. Adopted from Hlavacek-Larrondo et al. (2022).	30
2.6	Schematic illustration of the process of jet generation. In this analogy, the BH is represented as a perfectly conducting sphere, whose surface rotates with an angular frequency Ω . Moreover, the field lines are anchored to a perfectly conducting "ceiling", representing the ambient medium. From Davis & Tchekhovskoy (2020).	31
2.7	Inference of the BH spin from the observed shape of the Fe K lines in the spectra of AGN. Image credit: NASA/JPL-Caltech	33
2.8	Efficiencies model adopted in Steinborn et al. (2015).	37
2.9	Dataset for the new efficiency prescription, with the power-law fit superimposed to the data.	39

2.10	M_{BH} as a function of stellar mass M_* , at $z = 0$, for the BH sample in the simulation using the empirically-motivated model for efficiencies. Each point is colour-coded according to the number of mergers of the BH (including their progenitors). The dashed line shows the experimental fit by McConnell & Ma (2013), while crosses with associated uncertainties show data from Kormendy & Ho (2013).	40
3.1	Horizons and ergosurfaces of a rotating BH, in the Boyer–Lindquist coordinates. From Visser (2008).	46
3.2	Effective potential for a Schwarzschild BH. Each curve shows the potential for a different value of \tilde{L}	47
3.3	Curves of accretion rate \dot{M} versus Σ , defining different solutions for the accretion disc equations, plotted for a BH of $M_{\text{BH}} = 10 M_{\odot}$, $a = 0.1$ and $r/R_{\text{BH}} = 5$. Solutions on the left (right) of the dashed line are optically thin (thick). The LHAF is found to be internally inconsistent in the optically thick case (hence the dashed line). From Yuan & Narayan (2014).	53
3.4	Radiative efficiency of hot accretion flows, as a function of f_{Edd} . The insets present a summary of the main properties of each accretion flow type, as a function of f_{Edd} . The red (blue) boxes represent hot (cold) solutions. Adapted from Yuan & Narayan (2014).	55
3.5	Illustration of the structure of a warped thin disc. From Nealon et al. (2015).	59
3.6	Radiative efficiency – Eq. (3.64) – (top panel) and radius of the innermost stable circular orbit – Eq. (3.61) – (bottom panel), as a function of the BH dimensionless spin parameter. Some reference values of these quantities are also highlighted: $a = -1$, for a counter-rotating orbit around a maximally spinning BH; $a = 0$, for a non-spinning BH; $a = 0.998$, for the maximum spin allowed in our simulations.	64
3.7	Schematic of the steps that compose a single accretion episode. The vector schemes in the upper part of the figure represent the initial and final configurations of the angular momenta, in a case similar to the one shown in Fig. 1b by King et al. (2005). <i>Left</i> : an accretion disc settles around the BH, in a misaligned configuration. <i>Centre</i> : a warp develops, and the innermost part is forced to rotate in the BH equatorial plane and either co- or counter-align. <i>Right</i> : the BH spin changes in magnitude when gas is accreted at the innermost stable orbit.	65
3.8	Final BH spin dimensionless parameter after a single accretion episode as a function of M_{ratio} as defined in Eq. (3.60). The solid, dotted, dashed and dot-dashed lines represent a^{f} for the initial spin values -1, -0.5, 0, and 0.5 respectively. The solid and dotted lines represent the event of an accretion episode in which the accretion disc is counter-rotating with respect to the BH.	67
4.1	Gas density map of the ICs for the galaxy merger. The black arrows trace the local gas projected velocity field, while the white arrows indicate the initial direction of the CM of each galaxy. The arrows are scaled arbitrarily for visualisation purposes.	73

- 4.2 Spin alignment process in the idealised Milky Way galaxy. Top panels: angle subtended by the BH angular momentum and the z-axis θ_z . Bottom panels: BH spin parameter a . Quantities are plotted as a function of time (left panels) and of the ratio between accreted and initial BH mass $M_{\text{BH}}/M_{\text{BH},0}$ (right). Each line represents one simulation of the set summarised in Table 4.1. Dotted lines represent the instant after which condition (3.56) is no longer satisfied. 76
- 4.3 Time evolution of a few properties of the two BHs (each of them is depicted by either blue solid or orange dotted lines) in the idealised galaxy merger simulation. From top to bottom: separation distance between the two BHs; BH dimensionless spin parameter; BH mass; x, y, z component of the unit vector of the BH angular momentum. *Left panel*: entire simulated timespan. *Right panel*: timespan of 2 Myr, centred on the time of the merger (grey, dotted vertical line). The vertical green dash-dotted and purple dashed lines mark the instants in time illustrated in the top and bottom panel of Fig. 4.4, respectively. 78
- 4.4 3D perspective volumetric rendering of the gas density in the idealised galaxy merger simulation. The field of view depicted in the figure spans a width of 55 kpc and a height of 31 kpc, as measured along a plane that intersects the centre of the rendering volume. *Top panel*: last snapshot before the merger. *Bottom panel*: first snapshot after merger. The arrows mark the instantaneous direction of the BH spin vector. 80
- 4.5 Gas surface density maps at $z = 0$ for the ASIN (top) and DFROGIN (bottom) runs. The white circle indicates a spherical region of radius $5R_{200}$, centred on the target halo of the zoom-in region (i.e. the most massive at $z = 0$). The white dots mark the positions of the BHs in the simulation. 81
- 4.6 M_{BH} as a function of stellar mass M_* , at $z = 0$. Diamonds and stars represent BHs in ASIN and DFROGIN, respectively. The dashed line shows the experimental fit by McConnell & Ma (2013), while crosses with associated uncertainties show data from Kormendy & Ho (2013). 83
- 4.7 BH spin parameters a of the selected BH sample in ASIN (diamonds) and DFROGIN (stars) as a function of M_{BH} , at $z = 0$. The squares and pentagons show the collection of observational measurements of the BH spin parameter by Reynolds (2021) (with updates from Bambi et al. 2021) and Mallick et al. (2022), respectively. The hexagon represents the spin estimate reported by Walton et al. (2021) and the diamond represents the measurement obtained by Sisk-Reynés et al. (2022). 84
- 4.8 Summary of properties related to the most massive BH in the DFROGIN run, as they evolve across time. From top to bottom: z-component of the BH spin direction $j_{\text{BH},z}$ (black, solid line) and direction of the angular momentum of the gas in the BH kernel $j_{g,z}$ (orange, dashed line); cosine of the angle between the accretion disc and the BH spin at the beginning of each accretion episode $\cos \theta_{\text{BH-d}}$ (i.e. left-hand side of Eq. (3.56), black solid line) and $-J_d/(2J_{\text{BH}})$ (i.e. right-hand side of Eq. (3.56), orange dashed line); ratio of the magnitudes of the disc and BH angular momenta J_d/J_{BH} ; BH dimensionless spin parameter a ; radiative efficiency of the accretion disc ϵ_r ; Eddington ratio f_{Edd} ; BH mass M_{BH} 85

- 4.9 M_{BH} as a function of stellar mass M_* for the Box4 run. Circles represent the simulated sample at $z = 0$, while the observational points are as in Fig. 4.6. The points are colour-coded according to the number of mergers BH have undergone. 87
- 4.10 Distribution of BH spin parameters as a function of the BH mass in Box4 (circles), at $z = 0$. The points are colour-coded according to the number of mergers BH have undergone. The squares and pentagons show the collection of observational measurements of the BH spin parameter by Reynolds (2021) (with updates from Bambi et al. 2021) and Mallick et al. (2022), respectively. The hexagon represents the spin estimate reported by Walton et al. (2021) and the diamond represents the measurement obtained by Sisk-Reynés et al. (2022). 88
- 4.11 BH dimensionless spin parameter a as a function of M_{BH} , for the five most massive BHs at $z = 0$, for the Box4 run. Each line corresponds to one BH and is colour-coded by redshift. The symbols mark the position of each BH in the plot at a few specific instants in time, corresponding to $z = 0, 1, 2, 3, 4$, colour-coded accordingly. 89
- 4.12 Statistical analysis of a few key properties of the accretion episodes occurred in the Box4 run. The entire set of accretion episodes occurred during the simulation has been considered (i.e. for every BH and at every redshift). The top (middle) panel shows a 2D histogram of the values of $J_{\text{d}}/J_{\text{BH}}$ ($\theta_{\text{BH-d}}$) as a function of mass. Each bin is colour-coded by the number of accretion episodes in that bin (N_{bin}), normalised to the total number of episodes per mass bin ($N_{\text{mass bin}}$). In the top panel, the dashed line pinpoints $J_{\text{d}}/J_{\text{BH}} \propto M_{\text{BH}}^{-37/45}$ (for the self-gravitating case, Eq. 3.73); the dotted line shows $J_{\text{d}}/J_{\text{BH}} \propto M_{\text{BH}}^{23/16}$ (non self-gravitating case, Eq. 3.69). $a = 0.998$ and $f_{\text{Edd}} = 1$ are assumed to plot these reference lines. The bottom panel shows the fraction of counter-rotating accretion episodes over the total, per BH mass bin. 90
- 4.13 BH spin direction variation per accretion episode (i.e. $\Delta\theta_{\text{BH}} = \mathbf{j}_{\text{BH}} \cdot \mathbf{j}_{\text{BH}}^f$) as a function of $J_{\text{d}}/J_{\text{BH}}$, colour-coded by $\theta_{\text{BH-d}}$, the misalignment angle between disc and BH angular momenta at the beginning of the episode. The dashed lines illustrate the analytical dependence of $\mathbf{j}_{\text{BH}} \cdot \mathbf{j}_{\text{BH}}^f$ on $J_{\text{d}}/J_{\text{BH}}$, computed using Eq. 3.55. 92
- 4.14 Radiative efficiencies of the BH populations at redshift $z = 0$, as a function of mass, for the Box4 run. The triangles show the collection of empirical estimates of the radiative efficiency by Daly (2021). The dotted, dashed and dash-dotted lines mark the values of the efficiency corresponding to $a = -1, 0, 0.998$, respectively, for reference. The population in the bottom part of the figure represents the BH that are accreting in counter-rotating conditions. 93
- 6.1 Schematic representation of jet propagation in an ambient medium. Adopted from Begelman & Cioffi (1989). 103

List of Tables

4.1	Parameter summary for the idealised tests. $M_{\text{BH},0}$ is the BH mass in the ICs, $\theta_{z,0}$ is the angle subtended by the initial BH spin direction and the positive z axis, $f_{\text{Edd}} = \dot{M}_{\text{BH}}/\dot{M}_{\text{Edd}}$ is the Eddington ratio.	72
4.2	Parameter summary of the cosmological simulations. a_{seed} is the BH spin parameter at seeding; ϵ_f is the feedback coupling efficiency (Sec. 3.2.3); $M_{\text{BH,seed}}$ is the BH mass at seeding; $M_{*,\text{seed}}$ is the stellar mass considered for BH seeding (Sec. 2.3); m_{DM} is the DM particle mass; m_g is the initial gas particle mass; m_* is the star particle mass; ϵ_{DM} , ϵ_g , and ϵ_* are the DM, gas, and stellar and BH softening length, respectively.	74

Acknowledgements

I would like to express my gratitude to Klaus Dolag, my PhD supervisor, for his constant encouragement, guidance and patience throughout this research journey. I thank my supervising team members and co-authors, Milena Valentini and Veronica Biffi, for their insights and feedback throughout my doctorate. I also thank Eric Emsellem for his support and his role as the second revisor of my Thesis. I extend my sincere appreciation to the 'BiD4BEST' European Innovative Training Network (ITN) funded by the Marie Skłodowska-Curie Actions (860744) in Horizon 2020 that made this PhD endeavour possible, and to all the principal investigators, especially Francesco Shankar, coordinator of the project, as well as Joop Schaye and Silvia Bonoli, who supervised me during the project's secondments. It has been an extremely enriching experience, in terms of both professional and personal growth.

I also wish to thank all my USM colleagues and peers for their camaraderie, discussions, and encouragement throughout this academic endeavour. I am especially grateful to my colleagues and good friends Elena, Laura, Ilaria, Stephan, Freddy, Tirso, Anna, Stefan, Matteo and Zsofi. Moreover, I want to thank the BiD4BEST crew: Carolina, Brivael, Blessing, Giovanna, Mathilda, Iván M. R., Iván L., Nischal, Alex, Evgenii, Alba and Hao. My dear friends, we had a lot of fun, you were always there for me and I would not have been able to make it without you.

I want to thank Ludwig and Nadia, with whom I created many amazing memories. Thank you for sharing with me significant moments of your life and making me feel always welcome in your home. Your support and company during this journey have been invaluable.

Huge thanks also to Christian, for the adventures, the great evenings out eating good food, the amazing discussions and in general lots of fun. Your presence and friendship made everything lighter and more enjoyable.

To Mert, who entered my life along the way and made me feel I am the luckiest man in the world: it is an honour to have you by my side. For your constant presence, support, patience and encouragement I deeply thank you.

Special thanks go to my dear siblings Michela and Francesco and my aunt, Gabriella. I also want to thank my uncle, Luigi and his wife, Morena. Thank you all for being there for me during this journey. I would also like to express my gratitude for the friendship and support of Barbara Badetti, Barbara Guzzi and Andrea Angelelli, Alessandra and Nicola Thurner, Paola Riva, my long-time friends from Monza Ale, Nico, Ciro, Giuse, Miki, Gaia and Andrea and my long-distance PhD fellow students in Milano Alberto, Ludovica and Elisabetta.

Finally, my deepest gratitude goes to my mom, Giovanna, and my dad, Andrea. I will be forever thankful for your unconditional support and love and for your constant encouragement to pursue my dreams.